Pressure Gradient as an Independent Variable in Heterogeneous Bubble Nucleation

The members of the Committee approve the dissertation
of Brett A. Lindeman for the degree of Doctor of Philosophy.

Jaal Ghandhi
Advisor _____

Gregory Nellis _____

Franklin Miller _____

Scott Sanders _____

Riccardo Bonazza _____

Date _____

Pressure Gradient as an Independent Variable in Heterogeneous Bubble Nucleation

by

Brett A. Lindeman

A dissertation submitted in partial fulfillment of
the requirements for the degree of

Doctor of Philosophy
(Mechanical Engineering)

at the

UNIVERSITY OF WISCONSIN-MADISON

2020

Pressure Gradient as an Independent Variable in Heterogeneous Bubble Nucleation

Brett A. Lindeman
Department of Mechanical Engineering
University of Wisconsin-Madison, 2020
Professor Jaal B. Ghandhi, Advisor

Two-phase cooling with dielectric fluids of direct-to-silicon devices is hampered by the poor boiling performance resulting from lid removal and poor nucleation behavior of ideally smooth heater surfaces. In an effort to maintain thermal capacitance of the working fluid, while maximizing two-phase heat transfer, this study investigates whether liquid pressure gradients near the liquid-heater-interface can be used to increase the active nucleation site density (N_a''). Such behavior is preferable to using upstream throttling controls to flash the liquid to saturation as such behavior decreases the available downstream thermal capacitance.

A test section and flow boiling loop were built, and could provide an adjustable pressure gradient. Polished float glass, partially coated with ITO, was used for ohmic heating of the fluid while allowing for high-speed imaging of the nucleation behavior. Fluid passing over the glass traveled beneath a converging nozzle, with integrated pressure taps, used to create a linear pressure profile. This nozzle was adjusted to create a range of flow conditions that enabled the effects of Reynolds number and pressure gradient to be separated. Evaluation of the flow loop showed that constant pressure gradients as high as 245 kPa/m could be generated at flow rates approaching 1 L/min.

Results showed N_a'' to be a strong, positive function of the applied heat flux and weak, negative function of pressure gradient. Interestingly, the Reynolds number was shown to be unrelated to N_a'' for a constant heat flux. No correlation could be found that related the wall superheat to N_a'', differing from a significant quantity of existing research based on classical nucleation theory (CNT). These results confirm that CNT does not accurately predict nucleation behavior on ideally smooth surfaces. This research also shows that active nucleation sites are suppressed by 10% at a heat flux of 27 W/cm^2 and 34% at 21 W/cm^2 when the magnitude of the negative pressure gradient increases from 163 kPa/m to 240 kPa/m. From the perspective of N_a'', minimization of negative pressure gradients should increase the performance of two-phase cooling systems.

Acknowledgments

I am incredibly thankful for the current and previous faculty at this university, having supported and encouraged me throughout the years. First among them is my current adviser, Professor Jaal Ghandhi; I couldn't be more thankful for his generous support, mentorship, and showing that success and humanity are not mutually exclusive (you should see his gardening skills). Second, my previous adviser, Professors Tim Shedd, for fostering my creativity and giving me the opportunity to research in the Multiphase Flow Visualization Laboratory. I would like to extend my sincere thanks to Professors Franklin Miller, Greg Nellis, David Rothamer, Scott Sanders, and Mario Trujillo for your willingness to always provide advice and their encouragement, despite your busy schedules and own advisees. Lastly, to each member of my committee, thank you for your time and guidance throughout this process. I could not do this without you.

Second, I'd like to thank my parents for instilling a mindset of being able to do anything I put my mind to. Though my father isn't here to see it, I'm sure he'd be proud of how far I've come.

I'd like to thank my colleagues in the Multiphase Flow Visualization and Analysis Lab for all of their assistance over the years; both current: Arganthael, Dressler, Jason, Roman, Zach, Sydney, & Gunnar; and past: Rob, Dan, Mark, Sam, Ciara, Lorraine, Caitlin, & Xiaohui. In addition, I would also like to thank the staff of the TEAM Lab (nee Machine shop) for advising me on the development of my test section and providing significant training. Becoming the #1 all-time user of the machine shop shows how much assistance they provided.

Finally, I would like to thank the ME department, in addition to WARF, ASHRAE, and Professor Jaal Ghandhi, for their generous financial support throughout my MS and PhD programs.

Table of Contents

List of Tables

List of Figures

Nomenclature

Symbol		Description	Units
Abbreviations			
A	=	area	[m^2]
A	=	amperage	[A]
abs	=	absolute	
C_1, C_2	=	correlation constant	
c_p	=	specific heat capacity at constant pressure	[J/kg-K]
cdf	=	cumulative distribution function	
CI	=	confidence interval	
$CRAC$	=	computer room air conditioner	
d_h	=	hydraulic diameter, $= 4A/per$	[m]
d	=	diameter	[m]
DAQ	=	data acquisition system	
df	=	number of degrees of freedom	
$diff$	=	differential	
$dPdx$	=	spatial pressure gradient in x-direction	[Pa/mm]
DS	=	data set	
EV	=	experimental variable	
FA	=	Factor Analysis	
f	=	friction factor	
f_b	=	frequency of bubble departure	[Hz]
G	=	mass flux	[kg/s-m^2]
g	=	specific Gibbs free energy	[J/kg]
g_c	=	gravitational constant	[m/s^2]
GWP	=	global warming potential	
$\bar{h}$	=	heat transfer coefficient	[W/m^2-K]
h_{ch}	=	channel height	[m]
h_f	=	frictional head	[m]
h_{fg}	=	specific enthalpy of vaporization	[J/kg]
IHS	=	integrated heat sink	

k	=	thermal conductivity	[W/m-K]
L	=	length	[m]
m	=	mass	[kg]
$MFVAL$	=	Multiphase Flow Visualization and Analysis Laboratory	
N_p	=	number of physical values	
N_r	=	number of repeating values	
NI	=	National Instruments	
NV	=	new variable	
P	=	pressure	[Pa]
PCA	=	Principal component analysis	
per	=	perimeter	[m]
pdf	=	probability density function	
px	=	pixel	
$\dot{q}$	=	heat transfer rate	[W]
q''	=	heat flux	[W/m^2]
R	=	thermal resistance	[K/W]
R^2	=	coefficient of determination	
R_a	=	surface roughness	[m]
R_c	=	critical radius, $= \frac{2\sigma T_{sat}}{\rho_g h_{fg} \Delta T_{sat}}$	[m]
R_g	=	universal gas constant, 8.3145	[J/mol-K]
s	=	sample standard deviation	
s	=	specific entropy	[J/kg-K]
SLM	=	Stepwise linear model	
T	=	temperature	[K]
t	=	time	[s]
TC	=	thermocouple	
TS	=	test section	
TDP	=	thermal design power	[W]
u	=	velocity	[m/s]
V	=	volume	[m^3]
V	=	voltage	[V]
v	=	specific volume	[m^3/kg]
w	=	width	[m]
x	=	streamwise position, quality	
y	=	transverse position, independent variable	[m]

z_{st}	=	zero point stability	[kg/s]

Dimensionless groups

Ar	=	Archimedes Number, $= \frac{g}{\nu_f^2}\left(\frac{\sigma}{\rho_f g_c}\right)^{3/2}$	[-]
Bd	=	Bond number, $= \frac{(\rho_f - \rho_g) g d_h^2}{\sigma}$	[-]
Bi	=	Biot number, $= R_{cond}/R_{nc}$	[-]
Bo	=	Boiling number, $= \frac{q''}{G h_{fg}}$	[-]
Ca	=	Capillary number, $= \frac{\mu_f u}{\sigma}$	[-]
Ec	=	Eckert number, $= \frac{u^2}{c_{p,f}\Delta T_{sat}}$	[-]
Eu	=	Euler number, $= \frac{P_{ref} - P_h}{\frac{1}{2}\rho_f u^2}$	[-]
f_f	=	Friction factor, $= \frac{\mathrm{d}P}{\mathrm{d}x}\frac{d_h}{\frac{1}{2}\rho_f u^2}$	[-]
Hg	=	Hagen number, $= -\frac{\mathrm{d}P}{\mathrm{d}x}\frac{d_h^3}{\nu_f^2 \rho_f}$	[-]
Ja_1	=	Jakob number, $= \frac{\rho_f c_{p,f}\Delta T_{sat}}{\rho_g h_{fg}}$	[-]
Ja_2	=	Jakob number, $= \frac{c_{p,f}\Delta T_{sat}}{h_{fg}}$	[-]
Ja_{sub}	=	subcooled Jakob number,$= \frac{\rho_f c_{p,f}\Delta T_{sub}}{\rho_g h_{fg}}$	[-]
$Ja*$	=	Jakob number, based on abs. T, $= \frac{\rho_f c_{p,f} T_{sat}}{\rho_g h_{fg}}$	[-]
N_{conf}	=	confinement number, $= \frac{1}{d_h}\sqrt{\frac{\sigma}{g_c(\rho_f - \rho_g)}}$	
$Nu_{L_{char}}$	=	Nusselt number, $= \bar{h} L_{char}/k_f$	[-]
Pr	=	Prandtl number, $= \frac{\nu_f}{\alpha_f}$	[-]
Ra	=	Rayleigh number, $= \frac{g L^3 \beta (T_s - T_\infty)}{\nu\alpha}$	[-]
$Re_{L_{char}}$	=	Reynolds number, $= \frac{\rho v L_{char}}{\mu}$	[-]
$\rho*$	=	density scaling factor, $= \frac{\rho_f - \rho_g}{\rho_g}$	[-]
ρ^+	=	density scaling factor, $= \log_{10}\rho^*$	[-]
We	=	Weber number, $= \frac{\rho_f u^2 d_h}{\sigma}$	[-]

Greek symbols

α	=	thermal diffusivity	[m^2/s]

β	=	thermal expansion coefficient	[1/K]
Δ	=	difference	
δ	=	uncertainty	
ν	=	kinematic viscosity	[m^2/s]
ρ	=	density	[kg/m^3]
$\rho*$	=	density scaling factor, $= \frac{\rho_f - \rho_g}{\rho_g}$	[-]
ρ^+	=	density scaling factor, $= \log_{10}(\rho^*)$	[-]
σ	=	surface tension	[N/m]
θ	=	contact angle	[deg]

Subscripts and Superscripts

$\overline{a}$	=	average value of variable a
$\dot{a}$	=	rate of variable a
a''	=	flux of variable a
$1ph$	=	single-phase
$2ph$	=	two-phase
abs	=	absolute pressure
al	=	aluminum
∞	=	ambient, free stream
b	=	bubble
bot	=	bottom surface
$baro$	=	barometric
bp	=	back pressure
ch	=	channel
$cond$	=	conduction
$conv$	=	convection
$crit$	=	critical value
$diff$	=	differential
e	=	entrance
el	=	electrical
f	=	fluid
fc	=	forced convection
fd	=	fully developed
fm	=	flow meter
g	=	gas phase

ga	=	gauge pressure
gt	=	glass-liquid interface
gl	=	glass
gb	=	glass-air interface
H, h	=	heater
L, l	=	liquid phase
nc	=	natural convection
np	=	data set containing non-physical data
nom	=	nominal
p	=	physical data
R	=	reduced value, normalized by the critical value
r	=	number of repetitions in non-physical data
res	=	reservoir
$s, surf$	=	surface
sat	=	saturation
sub	=	subcooled
w	=	wall

Chapter 1

Introduction

This research began as a search for the optimal boiling surface for two-phase liquid cooling of high-performance microelectronics. Optimum performance in the microelectronics cooling industry means maintaining low surface temperatures (less than 95ºC) and low spatial temperature gradients, while being able to remove a significant amount of heat. For example, the IBM Power9 microprocessor has a die area of 6.9 cm^2 and has a thermal design power (TDP) of 190 W, or 27.5 W/cm^2. The NVIDIA Titan RTX, the latest high-performance GPU at $2,500 each, has a TDP of 280 W, and a 7.5 cm^2 die–a rated heat flux of 37 W/cm^2. An integrated heat sink (IHS), also known as a lid, typically interfaces between the silicon die and an external cooling solution using a thermal interface material (TIM). Unfortunately, the thermal resistance of the TIM is also one of the largest thermal resistances when designing a cooling solution for such devices. Leading cooling technologies for these processors typically have three forms:

1. Forced air cooling: heat pipes embedded in a bank of fins or vapor chambers with integral fins

2. Water cooling: pumped-liquid, planar jet-impingement

3. Two-phase, pumped-liquid cooling, using dielectric fluid

Forced air cooling has long been the standard for electronics cooling for reasons of resilience, simplicity, and technological inertia. Consumer-level performance is typically limited by acceptable fan noise and geometric constraints of the heat sink. In a data center application, servers can be cooled via computer room air-conditioners (CRACs) that

are located on the periphery of the data center; performance in this instance is typically limited by the large distance between heat generation in a server and cooling from the CRAC; performance can be improved by separating air-streams into hot and cold aisles. While the CRAC is an inefficient vapor-compression cycle, they have existed for many years and are the standard in data center cooling.

Water cooling excels due to its relative simplicity and the high thermal capacitance of forced convection to water[1]. The fluid is confined to tubing connecting each heat sink to a pumped-liquid flow loop. The heat sinks typically contain a planar jet, impinging liquid upon a skived surface, which is used to increase the surface area of the cooling surface; high fin densities result in low fluid velocities due to viscous drag and less heat transfer, while low fin densities result in high fluid velocities, but less heat transfer due to limited surface area. The temperature at the surface (T_s) of each chip is proportional to the heat rate ($\dot{q}$), mass flow rate ($\dot{m}$), specific heat of the fluid (c_f) and the incoming fluid temperature (T_f) in the form of Equation 1.1.

$$T_s = \frac{\dot{q}}{\dot{m} c_f} + T_f \tag{1.1}$$

Because T_f increases at each device, the overall system performance can be tuned so that the last device in series can dissipate its TDP to a fluid at a low enough temperature. Water cooling benefits from the high thermal capacitance of water, in comparison to air, but suffers from temperature variation between devices on a given flow loop, and fluid loss resulting in hardware failure[2].

Two-phase, pumped-liquid cooling typically uses a dielectric fluid, such as R245fa or HFE7000, because these fluids boil at pressures near atmospheric pressure and have low

[1]The fluid is called water, though it is typically a mix of glycol, water, and fungicides to prevent microbial growth.

[2]The primary method of fluid loss in pumped liquid systems is the slow diffusion through the wall of the tubing. It can typically be topped off with no ill effects.

global warming potentials (GWP). In a two-phase system, the pumped fluid is impinged upon a heat transfer surface at each device, where it absorbs energy through sensible and/or latent heating, depending on fluid inlet state. Local system pressure increases as a result of bubble formation in the sealed flow loop, but decreases as it flows along the fluid loop due to the imposed pressure difference between the pump and the downstream reservoir. The performance of a two-phase system can be chosen based upon an acceptable outlet fluid quality, which is determined by the TDP of each device being cooled, and the fluid flow rate, though the modeling of pumped, two-phase, jet impingement systems is more involved than single-phase water cooling. The benefits of two-phase cooling are that more components can be cooled on a single flow loop, in comparison to water cooling at a given pumping power, and the fluid temperature does not rise as significantly when absorbing thermal energy; due to the pressure drop along the flow path, the boiling point decreases and can result in outlet fluid temperatures lower than the inlet fluid temperature, despite absorbing significant amounts of thermal energy. The starting condition of a two-phase system can be chosen with more flexibility than air or water cooling and is the focus of this research. The inlet fluid in a two-phase system is subcooled (i.e., $T_{f,in} < T_{sat}$) as it leaves the pump due to the increased pressure. With no further conditioning, this fluid would reach the first device, in this subcooled state where it would likely result in purely single-phase convection. This is suboptimal as the thermal capacitance of dielectric fluids is less than that of water. Forcing the fluid through an orifice is an easy way to decrease the pressure to a saturated state, but diving too far inside the vapor dome decreases the available system capacitance, for a given outlet quality.

Ideal behavior for a two-phase system is one where the fluid reaches saturation at the heated surface so as to not lose any thermal capacitance upstream of the heater. Evidence that saturation has been reached is the nucleation of bubbles, unfortunately it is not straight-forward to predict *a priori* the conditions at which bubbles will form. Surface

temperatures can be 30°C above the saturation temperature without nucleation or 5°C below saturation with nucleation, while large negative pressures (i.e., below saturation pressure) will often not cavitate.

Optimizing heat transfer in a two-phase system requires predictive models with knowledge of the components shown in Figure 1.1[3]. The heat transfer behavior of two-phase flow involves knowledge about transient conduction to understand the state of the liquid surrounding the bubble. With the state of the film known, the next challenge is understanding the mass transfer occurring along the bubble surface as well as at the contact line (i.e., the three-phase boundary between liquid-solid-vapor). Evaporation along these surfaces increases the pressure within the bubble while also inducing capillary convection as the three-phase boundary evaporates. All of these behaviors are confounded when the bubble is in motion and the thickness of the three-phase boundary, and surrounding fluid state, is a function of position around the bubble.

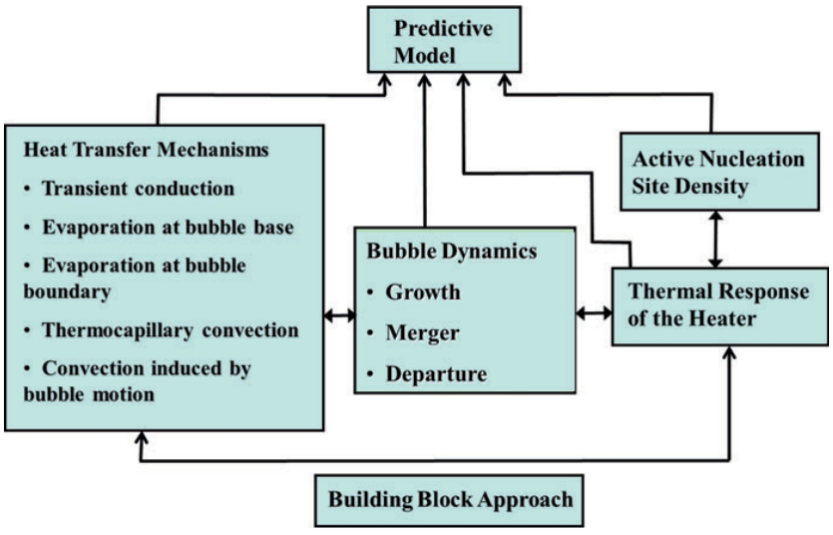

Figure 1.1: Reproduction of Figure 2 from Dhir [1] showing the subprocesses of predictive models for nucleate boiling

The energy absorbed by the bubble nucleation process typically originates in the heated

[3]Appendix E presents a history of boiling theory as it developed during the twentieth century

surface[4]. The absorbed energy leaves the surface locally subcooled relative to the fluid saturation temperature. Understanding the thermal response of the heater surface and its role in maintaining stable nucleation helps inform the previous heat transfer mechanisms.

The need for more research on active nucleation site density will be discussed in Chapter 2. The aim of this research is to determine whether pressure and pressure gradients can be used to influence the active bubble nucleation site density as a step in closing the mechanistic models described in Figure 1.1. Pressure and the local change in pressure are two of few variables that can be tuned by the designer of a two-phase flow systems, and little evidence in the literature has described the influence of these variables on the active bubble nucleation site density.

The experimental setup used to evaluate pressure gradients in flow boiling will be described in Chapter 3. This experimental setup details a new experiment that was designed and fabricated for visualization and heat transfer studies of flow boiling. Experimental uncertainties will describe the benefits and limitations of this particular flow loop design. Finally, a description of the flow loop operation will be discussed.

Experimental results are provided in Chapter 4 for the active nucleation site density, N_a'', bubble nucleation density, N_b'', and pressure relations. A discussion of these results is provided in Chapter 6.

[4]Exceptions include nucleation assisted by light, acoustic energy, and electro-hydrodynamics

Chapter 2

Literature Review

Consideration of what it meant to be a locus of bubble nucleation has existed at least as far back as the late 1920s [2], when it was noticed that bubbles, "originate at only a few small places.... these not being distinguished by any peculiarities whatsoever from the rest of the surface". Today, there are two variables most frequently correlated with the active bubble nucleation site density, N_a'' [sites/cm^2]: the surface heat flux, q'', and the surface superheat, $\Delta T_w = T_w - T_{sat}$, where T_w is the wall temperature and ΔT_{sat} the surface superheat.

2.1 Temperature Dependence of N_a''

Temperature dependence of N_a'' is typically modeled by equating the change in Gibbs free energy for a system before and after a bubble is formed, where the system is that region of liquid that will be fully occupied by vapor after formation.

$$\mathrm{d}g_f = \mathrm{d}g_g \tag{2.1}$$

After substituting Equation 2.2 into Equation 2.1, for both the liquid and gas phases, Equation 2.3 is produced.

$$\mathrm{d}g = -s\mathrm{d}T + v\mathrm{d}P \tag{2.2}$$

$$-s_f\mathrm{d}T + v_f\mathrm{d}P = -s_g\mathrm{d}T + v_g\mathrm{d}P \tag{2.3}$$

Equation 2.3 can be rearranged as shown in Equation 2.4

$$\left(\frac{\mathrm{d}P}{\mathrm{d}T}\right)_{sat} = \frac{s_g - s_f}{v_g - v_f} \tag{2.4}$$

Discretizing the derivative in Equation 2.4, and recognizing that $v_g - v_f \approx v_g$ leads to:

$$\left(\frac{\Delta P}{\Delta T}\right)_{sat} = \frac{s_g - s_f}{v_g} \tag{2.5}$$

Integrating Equation 2.6 across the phase change produces Equation 2.7,

$$\mathrm{d}h = T\mathrm{d}s + v\mathrm{d}P \tag{2.6}$$

$$\Delta h_{fg} = T_{sat}\Delta s_{fg} \tag{2.7}$$

Substituting Equation 2.7 into Equation 2.5 for $\Delta s_{fg} = s_g - s_f$, and solving for ΔP leads to

$$(\Delta P)_{sat} = \frac{\Delta h_{fg}\Delta T_{sat}}{T_{sat} v_g} \tag{2.8}$$

where ΔT_{sat} represents the change in saturation temperature with an incremental change in ΔP_{sat} from Equation 2.5.

The system being solved is that of a spherical bubble. The pressure difference between the inside and outside of the bubble is related using the simplified Laplace Equation, shown in Equation 2.9, where σ is the surface tension between the liquid and vapor phases, and R_b is the radius of the spherical bubble

$$\Delta P = \frac{2\sigma}{R_b} \tag{2.9}$$

Substituting Equation 2.9 into Equation 2.8 and solving for R_b produces Equation 2.10,

where R_b has been replaced by R_c known as the critical radius.

$$R_c = \frac{2\sigma T_{sat}}{\rho_g h_{fg} \Delta T_{sat}} \tag{2.10}$$

The Laplace equation provided a mechanical stability whereby any bubble larger than R_c will grow, while a bubble smaller than R_c will collapse.

If one assumes that bubbles form at defects in the surface, then the size of such bubble will largely correspond to the size of the defect due to the contact line being pinned to the defect. Therefore, R_c not only defines the critical size of the bubble, but also the critical size of the surface features capable of producing bubbles. For this reason, many correlations for N_a'' depend upon the critical radius R_c to varying degrees of success, the contact angle, θ, defined as the angle formed between the solid surface and the liquid/vapor interface of a sessile drop, measured through the liquid. A low contact angle implies the fluid is highly wetting (for water this would imply the surface is hydrophillic). At high contact angles the fluid is non-wetting.

Table 2.1 provides the functional forms for many of the correlations between N_a'' and temperature, T, or R_c, which is itself a function of temperature. The full correlations and their supplemental relations can be found in Appendix D.

Basu et al. [3], Hibiki and Ishii [5], and Ren et al. [8] studied flow boiling of water under the experimental conditions shown in Table 2.2. Notably, the Hibiki and Ishii [5] correlation is valid for a much larger range of N_a'' than the others; it also is applicable for much larger pressures, at which bubbles are expected to be smaller due to the Laplace relationship in Equation 2.9. The $f(\rho^+)$ term in the Hibiki and Ishii [5] correlation is a fitting parameter, based on the density of water, where

$$\rho^+ = \log_{10}(\rho^*) = \log\left(\frac{\rho_f - \rho_g}{\rho_g}\right) \tag{2.11}$$

Table 2.1: Functional form of $N_a'' = f(T)$ correlations

Source	**Functional Form of Correlation**
Basu et al. [3]	$N_a'' \propto (1-\cos\theta)\Delta T_w^{2.0}$ for $\Delta T_w \leq 15$ K
	$N_a'' \propto (1-\cos\theta)\Delta T_w^{5.3}$ for $\Delta T_w > 15$ K
Benjamin and Balakrishnant [4]	$N_a'' \propto \gamma^{-1}\{f(R_a P/\sigma)\}^{-0.4}\mathrm{Pr}^{1.63}(\Delta T_w)^3$
Hibiki and Ishii [5]	$N_a'' \propto \left[1-\exp\left(\frac{-\theta^2}{C_1}\right)\right]\left[\exp\left(C_2\frac{f(\rho^+)}{R_c}\right)-1\right]$
Kocamustafaogullari and Ishii [6]	$N_a'' \propto f(\rho^*)\ (\rho^*)^{2.16}\left[\frac{\sigma}{g(\rho_f-\rho_g)}\right]^{1.2}\theta^{2.4}R_c^{-4.4}$
Lie and Lin [7]	$N_a'' \propto \left(C_1 + N_{conf}^{0.51}\Delta T_w^{1.67}\right)$
Ren et al. [8]	$N_a'' \propto \exp\left[-C_1 Ja_{sub}\right]\mathrm{Re}_{d_h}^{-0.93}\Delta T_w^{4.19}$
Wang and Dhir [9]	$N_a'' \propto (1-\cos\theta)R_c$
Zhokhov [10]	$N_a'' \propto R_c^{-3}$

The fluid properties were accounted for in the Ren et al. [8] correlation by a Jakob number based on the degree of subcooling in the free stream,

$$Ja_{sub} = \frac{\rho_f c_{p,f}\Delta T_{sub}}{\rho_g h_{fg}} \tag{2.12}$$

and by the Reynolds number, Re_{d_h}[1].

Table 2.2: Experimental parameters of $N_a'' = f(T)$ correlations using flow boiling with water

	P	G	θ	N_a''	ΔT_{sub}	ΔT_{sat}	q''
	[kPa]	[kg/s-m^2]	[deg]	[sites/cm^2]	[K]	[K]	[W/cm^2]
Basu et al. [3]	104	124 - 886	30 - 90	1 - 230	26 - 53	9 - 17	17.4 - 70
Hibiki and Ishii [5]	101 - 19800	0 - 886	5 - 90	1 - 1.5e6		2 - 25	
Ren et al. [8]	200 - 300	300 - 1660		1 - 500	13 - 33	1 - 22	

The correlation by Lie and Lin [7] was developed for annular flow of R134a and incorporates a confinement number, N_{conf}, which can be thought of as the capillary length

[1] Ren et al. [8] defines the length scale used in the Reynolds number as an equivalent diameter, De, but no definition is provided. This analysis assumes the equivalent diameter is the hydraulic diameter, d_h.

normalized by the hydraulic diameter, d_h.

$$N_{conf} = \frac{1}{d_h}\sqrt{\frac{\sigma}{g_c(\rho_f - \rho_g)}} \tag{2.13}$$

The experimental ranges for the Lie and Lin [7] correlation are shown in Table 2.3.

Table 2.3: Experimental parameters of $N_a'' = f(T)$ correlation by Lie and Lin [7] for flow boiling of R134a.

	P	G	θ	N_a''	ΔT_{sub}	ΔT_{sat}	q''
	[kPa]	[kg/s-m^2]	[deg]	[sites/cm^2]	[K]	[K]	[W/cm^2]
Lie and Lin [7]	424 - 488	200 - 300		9 - 45	6 - 13	1 - 30	1.5 - 4.8

The remainder of the correlations in Table 2.1, namely Benjamin and Balakrishnan [11], Kocamustafaogullari and Ishii [6], Wang and Dhir [9], pertained to pool boiling. Both Benjamin and Balakrishnan [11] and Kocamustafaogullari and Ishii [6] included data from other researchers to broaden the applicability of their correlations to other fluids, while Wang and Dhir [9] studied pool boiling of water.

Benjamin and Balakrishnan [11] included a couple of parameters to account for fluid and solid properties. The solid-liquid property factor, γ, is shown in Equation 2.14, and was referred to as the ratio of *thermal assimilability* of the solid to that of the liquid by Pioro et al. [12];

$$\gamma = \sqrt{\frac{k_w \rho_w c_{p,w}}{k_f \rho_f c_{p,f}}} \tag{2.14}$$

The surface roughness, R_a, was non-dimensionalized with pressure and surface tension to produce the quadratic fitting parameter shown in Equation 2.15.

$$f\left(\frac{R_a P}{\sigma}\right) = 14.5 - 4.5 \times 10^6 \left(\frac{R_a P}{\sigma}\right) + 4 \times 10^{11} \left(\frac{R_a P}{\sigma}\right)^2 \tag{2.15}$$

The functional form of the Kocamustafaogullari and Ishii [6] correlation has been sim-

plified from the form shown in Appendix D by substituting relations and collecting terms. From Table 2.1 one can see the property fitting using ρ^*, which was previously defined in Equation 2.11. The direct relationship with contact angle is unique given that it is not a operand to a trigonometric function.

The experimental ranges for which these correlations are valid are shown in Table 2.4. Minimal ranges were provided in Kocamustafaogullari and Ishii [6] except that the correlation is valid for water, carbon disulfide, carbon tetrachloride, n-Hexane, acetone, and nickel-salt solutions; nucleating on stainless steel, monel, carbon steel, brass, copper, and platings of chromium, silver, zinc, and nickel.

Table 2.4: Experimental parameters of $N_a'' = f(T)$ correlations for pool boiling

	P	Pr	θ	N_a''	ΔT_{sat}	R_a
	[kPa]	[-]	[deg]	[sites/cm^2]	[K]	[μm]
Benjamin and Balakrishnan [11]		1.7 - 5	2.2 - 14	0.6 - 20	2 - 25	0.02 - 1.17
Kocamustafaogullari and Ishii [6]	100 - 19800			0 - 100		
Wang and Dhir [9]	101	1.7	18 - 90	0 - 200	3 - 12	¡ 0.02

The Zhokhov [10] paper was reported by Pioro et al. [12], as it was in Russian and from 1969. No further details were provided.

2.2 Heat Flux Dependence of N_a''

There is another branch of nucleation site density research that has been unable to replicate the results of the previous studies. For example Zeng and Klausner [13] mentioned that R_c is, "insufficient for predicting N_a''" and that "pool boiling correlations based on R_c are not applicable to flow boiling"; suggesting instead the velocity of the vapor, u_v, heat flux, q'', and T_{sat} are more appropriate independent variables. While several of the correlations in Table 2.1 use the contact angle of the fluid, other researchers have found the contact angle to be insignificant in correlating N_a'' [14].

Instead of correlating with surface superheat, the applied heat flux, q'' has been more successful. Such correlations have generally followed the form in Equation 2.16,

$$N_a'' \propto (q'')^n \tag{2.16}$$

where the exponent ranges from 1 to 3. Table 2.5 summarizes these correlations. In all cases the units for N_a'' and q'' are [sites/cm^2] and [W/cm^2], respectively.

Table 2.5: Exponents used in $N_a'' \propto (q'')^n$ correlations.

Reference	**Functional Form of Correlation**
Aoki [15]	$N_a'' = 2.79\ q''$
Dhir and Liaw [16]	$N_a'' \propto (q'')^{1.5}$
Gaertner and Westwater [17]	$N_a'' = 1.48 \times 10^4 (q'')^{2.13}$
Hahne and Barthau [18]	$N_a'' = 1.45 \times 10^3 (q''/Ja)^{3.0}$ for $q'' < 0.5$ W/cm^2
	$N_a'' = 4.53 \times 10^2 (q''/Ja)^{1.6}$ for $q'' > 0.5$ W/cm^2
Kurihara and Myers [19]	$N_a'' = 1.804 \times 10^{-3} \frac{\mu_f \bar{h}^3}{\rho_g k_f^3} \mathrm{Pr}^{2.67}$
Luke and Cheng [20]	$N_a'' \propto (q'')^n$ for $1.2 < n < 2.55$
Mikic and Rohsenow [21]	$N_a'' \propto\ q''$

All of the correlations in Table 2.5 were developed for pool boiling of the fluids in Table 2.6 on either a flat surface or, in the case of Hahne and Barthau [18] and Luke and Cheng [20], the outside diameter of a tube.

The correlation from Hahne and Barthau [18] was of the form $N_a'' \propto (q''/Ja)^n$, where Ja was defined by Equation 2.17.

$$Ja = \frac{\rho_f c_{p,f} \Delta T_{sat}}{\rho_g h_{fg}} \tag{2.17}$$

The correlation by Kurihara and Myers [19] is conspicuous in comparison to the others as it was derived from dimensional analysis using the Nusselt, Nu, Prandtl, Pr, and

Table 2.6: Test fluids applicable for correlations in Table 2.5.

Reference	**Fluids Studied**
Aoki [15]	Water
Dhir and Liaw [16]	*Ordinary liquids* in fully developed nucleate boiling
Gaertner and Westwater [17]	Aqueous solution of nickel salts
Hahne and Barthau [18]	R134a, R114
Kurihara and Myers [19]	Water, acetone, n-hexane, carbon-tetrachloride, and carbon-disulfide
Luke and Cheng [20]	Propane
Mikic and Rohsenow [21]	Meta-analysis with water, n-pentane, ethyl alcohol, benzene, and aqueous solution of nickel salts

Reynolds, Re, numbers of the form

$$Nu = C_1^i Re^j Pr^w \tag{2.18}$$

$$\text{where} \quad Nu = \frac{\bar{h} d_b}{k_f} \tag{2.19}$$

$$Re = \frac{G_b d_b}{\mu_f} \tag{2.20}$$

$$Pr = \frac{c_{p,f} \mu_f}{k_f} \tag{2.21}$$

Here, $\bar{h}$ is the mean heat transfer coefficient, d_b the bubble departure diameter, and G_b the mass flux due to bubble generation defined by Equation 2.22.

$$G_b = \frac{\pi}{6} d_b^3 \rho_g f_b N_a'' \tag{2.22}$$

The mass flux is equal to the number of active nucleation sites N_a'' producing spherical bubbles departing at a frequency f_b. Substituting $d_b f_b \approx$ const. and simplifying[2], pro-

[2] A relatively recent review of nucleate pool-boiling heat transfer by Pioro et al. [12] estimates this relation to be the following: $d_b f_b = 0.6 \left[\frac{\sigma g (\rho_f - \rho_g)}{\rho_f^2} \right]^{1/4}$

duces

$$\frac{\bar{h}}{k_f} = C_1^i d_b^{3j-1} \left(\frac{\rho_g N_a''}{\mu_f} \right)^j \left(\frac{c_{p,f}\mu_f}{k_f} \right)^w \tag{2.23}$$

Assuming that $\bar{h} \approx (N_a'')^{1/3}$, exponent j is known. Empirical data was then used to determine the exponent on the Prandtl number, which simplified to produced the final equation shown in Table 2.5 and Equation 2.24 in its published form.

$$\frac{\bar{h}}{k_f} = 820\ (N_a'')^{1/3} \left(\frac{\rho_g}{\mu_f} \right)^{1/3} \mathrm{Pr}^{-0.89} \tag{2.24}$$

Less is known about the variables that affect N_a'' when correlated with q'' and not ΔT. Zeng and Klausner [13] found that the critical radius, R_c, was important but not sufficient for predicting nucleation in flow boiling; while also noting the importance of T_{sat} and vapor velocity u_v when studying nucleation in a film above which was a flowing vapor.

2.3 Potential Pressure Gradient Dependence of N_a''

Dimensional analysis has so far proven ineffective for predicting heterogeneous bubble nucleation density for flow boiling on surfaces without artificial cavities. Evidence of this can be seen by the mismatch in correlations shown in Table 2.1 and Table 2.5, brought together in Table 2.7, with R_c having been replaced by the proportional temperature relationship shown on the right of Equation 2.25.

$$R_c \propto \frac{T_{sat}}{\Delta T_{sat}} = \frac{T_{sat}}{\Delta T_w} \tag{2.25}$$

The exponent, n, for $N_a'' \propto \Delta T_w^n$ is in the range $-1 < n < 5.3$ in addition to the $\exp(\Delta T_w / T_{sat})$ term in the Hibiki and Ishii [5] correlation. The exponent, m, for $N_a'' \propto (q'')^m$ is in the range $1 < m < 3$. As it will be seen later, it was not the case that previous

Table 2.7: Summary of N_a'' correlations

Source	**Functional Form of Correlation**
Basu et al. [3]	$N_a'' \propto (1-\cos\theta)\Delta T_w^{2.0}$ for $\Delta T_w \leq 15$ K
	$N_a'' \propto (1-\cos\theta)\Delta T_w^{5.3}$ for $\Delta T_w > 15$ K
Benjamin and Balakrishnant [4]	$N_a'' \propto \gamma^{-1}[f(R_a P/\sigma)]^{-0.4}\mathrm{Pr}^{1.63}\Delta T_w^3$
Hibiki and Ishii [5]	$N_a'' \propto \left[1-\exp\left(\frac{-\theta^2}{C_1}\right)\right]\left[\exp\left(C_2\frac{f(\rho^+)\Delta T_w}{T_{sat}}\right)-1\right]$
Kocamustafaogullari and Ishii [6]	$N_a'' \propto f(\rho^*)\,(\rho^*)^{2.16}\left[\frac{\sigma}{g(\rho_f-\rho_g)}\right]^{1.2}\theta^{2.4}\left[\frac{\Delta T_w}{T_{sat}}\right]^{4.4}$
Lie and Lin [7]	$N_a'' \propto \left(C_1 + N_{conf}^{0.51}\Delta T_w^{1.67}\right)$
Ren et al. [8]	$N_a'' \propto \exp\left[-C_1 Ja_{sub}\right]\mathrm{Re}_{d_h}^{-0.93}\Delta T_w^{4.19}$
Wang and Dhir [9]	$N_a'' \propto (1-\cos\theta)T_{sat}/\Delta T_w$
Zhokhov [10]	$N_a'' \propto \left(\frac{\Delta T_w}{T_{sat}}\right)^3$
Aoki [15]	$N_a'' = 2.79\,q''$
Dhir and Liaw [16]	$N_a'' \propto (q'')^{1.5}$
Gaertner and Westwater [17]	$N_a'' = 1.48\times10^4(q'')^{2.13}$
Hahne and Barthau [18]	$N_a'' = 1.45\times10^3(q''/Ja)^{3.0}$ for $q'' < 0.5$ W/cm^2
	$N_a'' = 4.53\times10^2(q''/Ja)^{1.6}$ for $q'' > 0.5$ W/cm^2
Kurihara and Myers [19]	$N_a'' = 1.804\times10^{-3}\frac{\mu_f\tilde{h}^3}{\rho_g k_f^3}\mathrm{Pr}^{2.67}$
Luke and Cheng [20]	$N_a'' \propto (q'')^n$ for $1.2 < n < 2.55$
Mikic and Rohsenow [21]	$N_a'' \propto q''$

authors chose to correlate N_a'' with temperature when they could have chosen to correlate results with heat flux. Results often could not be correlated with temperature, resulting in correlations with heat flux.

Relatively recent research has studied the impact of overlooked variables and their potential impact on nucleate boiling. Local surface temperature variation at individual nucleation sites was studied for its impact on bubble nucleation behavior [22]; a three temperature model was proposed that provided threshold temperatures that demarcate different nucleation behaviors. Other research has investigated the bubble nucleation behavior as it could be influenced by planar density of surface molecules (i.e., crystallographic orientation) [23–26]; though, opposing results have been produced [27].

Pressure gradients in a fluid were recently shown to be a predictor of bubble collapse behavior, where previously it had not been considered [28], through analysis of the Rayleigh-Plesset equation governing bubble dynamics. This opens the possibility that pressure gradients may have been overlooked elsewhere. Though Qi and Klausner [29] studied the role of nanobubbles, their concluding remarks are telling of the current state of boiling research:

> *The reliable prediction of nucleation site density in boiling systems based on first principles has been elusive. Some limited success has been achieved by Wang and Dhir [9, 30] with water on copper and with water on brass from this study shown in Fig. 8. However, these cases are the exception. Kenning [31] remarked, "At any time, a research community has a set of what should be working hypotheses, but which may become so firmly accepted that they are rarely questioned." This assumption that vapor trapping cavities are exclusively responsible for seeding heterogeneous boiling nucleation sites is one such hypothesis. The fact that pool boiling nucleation sites are easily formed using ethanol, a highly wetting fluid that floods cavities, is suggestive that another mechanism other than heterogeneous nucleation is responsible for the formation of nucleation sites. The existence of nanobubbles offers a plausible mechanism for seeding nucleation sites and requires extensive further scrutiny. Other mechanisms that can explain the collection of experimental observations should also be sought after.*

Chapter 3

Experimental Facility

A flow loop and test section (TS) were designed, fabricated, and constructed for this research. A significant amount of knowledge from previous experiments in the Multiphase Flow Visualization and Analysis Lab (MFVAL) informed the decisions about overall flow loop design as well as practicality of the test section.

3.1 Flow Loop

A schematic of the overall flow loop is presented in Figure 3.1. A magnetically driven screw pump (Micropump, Model GC-M35.PF5SE) was used. The pump had a rated capacity was 13.9 L/min of water at a rotational speed of 4,000 rpm. A DC motor with attached magnetic rotor was used to drive the pump; a DC motor driver was used to adjust the motor speed and thus the pump flow rate. The increased pressure downstream of the pump produced a slightly subcooled fluid; the degree of subcooling delivered to the test section could be controlled using rope heaters with a heating capacity of 125 W (Omega, Model FGR-030), which were wrapped around the stainless tubing and are depicted in red in Figure 3.1. The exact fluid state at the inlet of the test section could be determined from the liquid inlet thermocouple and the test section pressure transducers.

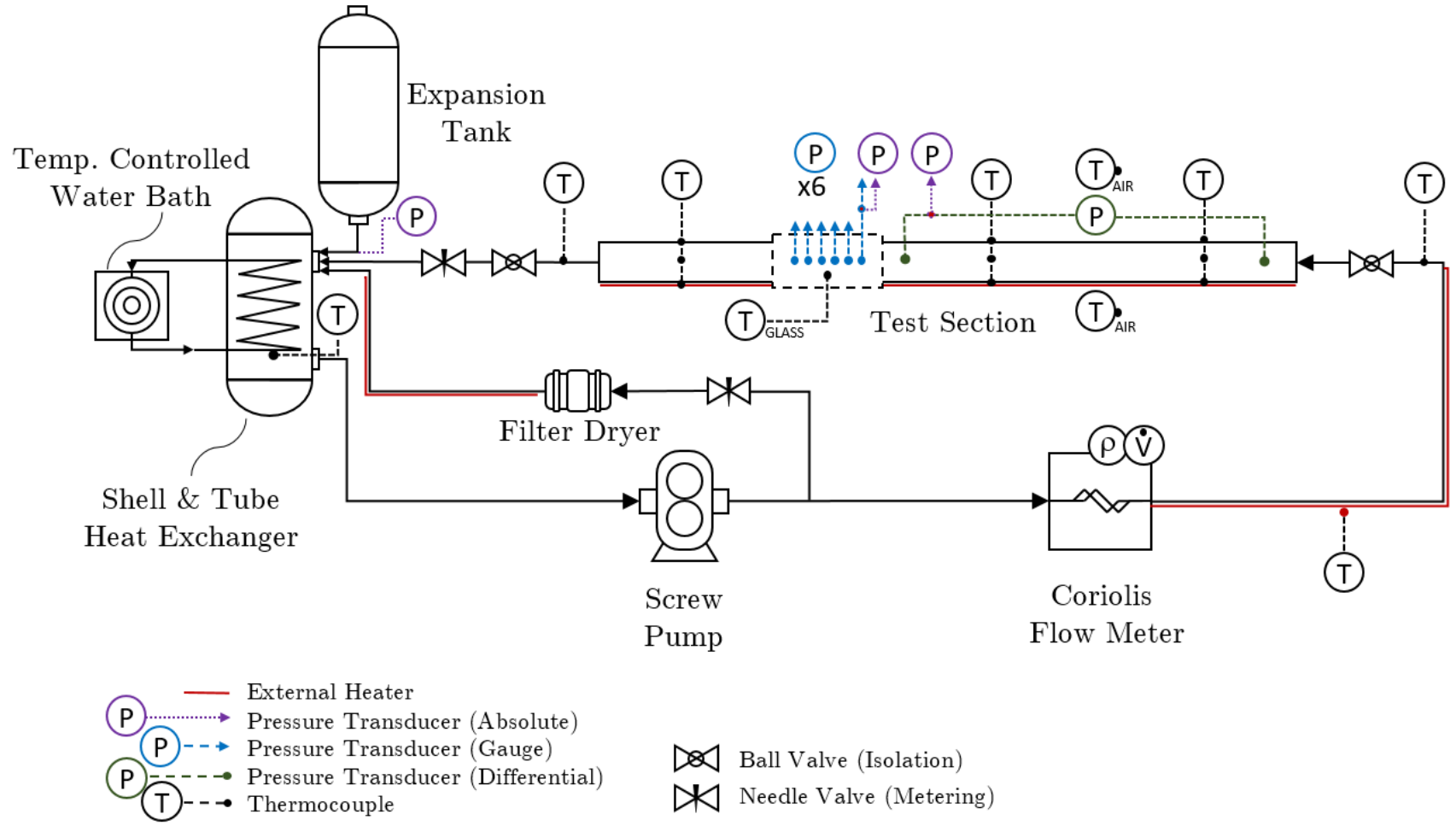

Figure 3.1: Simplified flow loop schematic depicting all major components for analyzing flow boiling performance.

Flow from the pump was metered using a Coriolis flow meter (Micro Motion Elite, Model CMFS040M) that provided two current-output signals corresponding to the fluid density and volumetric flow rate. The reservoir was a once-through shell-and-tube heat exchanger (Brazetek, Model BT-ST-155-B), with an internal volume of approximately 0.7 L. A vapor space was maintained at the top of the reservoir by controlling the amount of fluid in the flow loop; this enabled the fluid state to be determined by the reservoir pressure or reservoir temperature. The shell-side of the heat exchanger was the fluid reservoir, while the tube-side was in contact with the water. The overall system pressure was controlled by setting the temperature in the reservoir, via the temperature-controlled water bath (Cole-Parmer, Model 12101-41). This water bath had a refrigerant loop to heat or cool a 13 L reservoir of water to a desired temperature; the water was then pumped at 5 psi through the tube-side of the reservoir in a counterflow orientation.

An expansion tank was used to accommodate changes in fluid volume associated with changes in system temperature. For refrigerants this was not an issue since the fluid density was largely insensitive to temperature changes.[1] The expansion tank was located above the reservoir to ensure it contained exclusively vapor; lowering the expansion tank while enabling liquid to enter would have decreased the suction head on the pump and increased the chance of vapor entrapment in the pump. To further decrease the likelihood of vapor entrapment or cavitation in the pump, the outside diameter of the tubing from the reservoir to the pump inlet was 12.7 mm; all other tubing was 6.35 mm.

A bypass loop was located after the pump and connected to the top of the reservoir. This bypass loop had two primary functions: cleaning the fluid of particulate and water using a filter-dryer (molecular sieve by Parker, Model LLD-032), and fine metering of flow using the bypass needle valve. A needle valve was located at the outlet of the test section

[1]For example, R245fa density changes by -0.01 %/°C at a fluid temperature of 20°C. For a nominal fluid volume of 1 L, a 30°C rise in temperature corresponds to an additional 67 mL of fluid volume; this volume could be accommodated by the head space in the reservoir.

to control the amount of back pressure in the test section.

Material compatibility was a major concern in the design of this flow loop. The loop was designed to contain refrigerants and ethanol. For this reason all of the tubing in this flow loop was made of stainless steel, except for a few short lengths of copper (each shorter than 10 cm) attached to devices such as the filter-dryer due to the difficulty in obtaining a proper SAE flare in stainless steel tubing. Stainless steel compression fittings (Swagelok) were used wherever possible; one exception being the Coriolis flow meter, which had sanitary fittings with PTFE gaskets. The material composition of the O-rings was chosen from a set of specific formulations of EPDM (there are more than 30 such compositions of EPDM made by Parker, the exact components in each formulation being proprietary) that were known to perform best with refrigerants similar to R245fa and HFE7000.[2,3]

All fluid-contacting components were insulated (R-value ≈ 5.7 K-m^2/W) to limit losses to the environment; the tubing was wrapped in flexible EPDM pipe insulation while the pump, flow meter, reservoir, and expansion tank were wrapped in sheets of polyolefin insulation; and the aluminum test section was encapsulated in a box of rigid foam. The entire flow loop, save for the water bath, was assembled on top of an optical table and supported by a T-slotted structure. The vibration-isolation legs of the optical table were used to limit room vibrations to the test section. To decrease conductive heat loss to the T-slot frame, sheets of Ultem (polyetherimide) were used as washers between the test section and its supports.

[2]Typically the O-ring formulation cannot be specified when purchasing small quantities; Zatkoff Seals and Packings was found to be the most useful when sourcing specific formulations. To the author's knowledge, the formulations best suited for R245fa and HFE7000 have not been published.

[3]The industry standard test for O-ring compatibility uses a soxhlet condenser to heat the test fluid and O-ring pieces (the O-ring having been cut up to increase surface area) for a chosen amount of time. During the test, components of the O-ring's formulation may dissolve, resulting in shrinkage, or swelling if that mass was replaced with the test fluid. After the proscribed time has elapsed, the O-ring pieces are weighed to measure change in mass, and the liquid in the soxhlet condenser is boiled off to allow for weighing of the dissolved solids.

3.2 Test Section

The fabricated test section is shown in its exploded state with all major components labelled in Figure 3.2. The base was made from aluminum and contained thermocouple

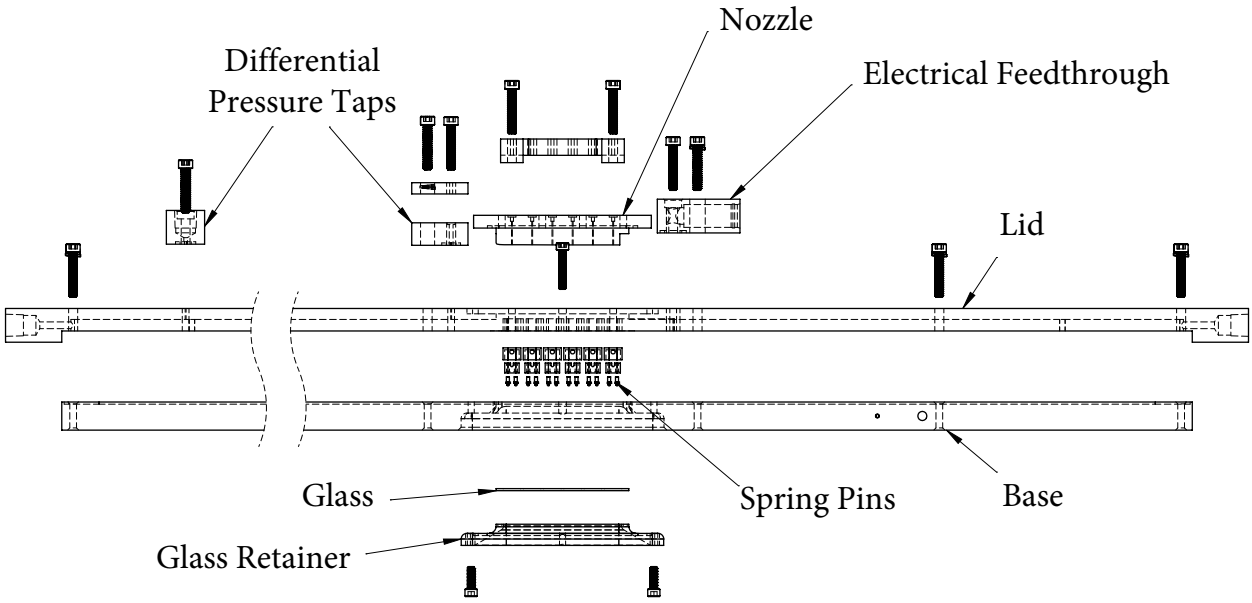

Figure 3.2: Exploded view of the test section with all major components labelled. For ease of fitting on the page, the entrance length has been removed; flow is from left to right.

wells, mounting holes, a large opening for the glass and its retainer, as well as the O-ring to seal between the base and the lid. For a sense of scale, the test-section base had dimensions of 15.9 mm x 63.5 mm x 1.05 m. The lid was also machined from aluminum and had dimensions of 19 mm x 63.5 mm x 1.12 m. The fluid channel was machined in the lid, was 6.35 mm deep and 12.4 mm wide, and can be seen as the dashed line traveling the length of the lid (flow moves from left to right, in Figure 3.2). Using these channel dimensions the hydraulic diameter (d_h) of 8.4 mm, was calculated using Equation 3.1,

$$d_h = \frac{4A_{ch}}{per_{ch}} \tag{3.1}$$

with A_{ch} being the cross-sectional area of the channel and per_{ch} the perimeter of the channel's rectangular cross-section. The entrance length (L_e) of the channel was 0.66 m. Equations 3.2a and 3.2b could be used to find the maximum Reynolds number (Re) for the flow that would be capable of becoming fully developed in an entrance length of 0.66 m.

$$\frac{L_e}{d_h} \approx 0.06Re \qquad \text{Laminar} \tag{3.2a}$$

$$\frac{L_e}{d_h} \approx 4.4Re^{1/6} \qquad \text{Turbulent} \tag{3.2b}$$

The calculated maximum Re for laminar and turbulent flow are 1310 and 32×10^6, respectively. This implies that laminar flow in the test section will become fully developed so long as it has a Re less than 1310; the same interpretation applies to the turbulent case. Both the entrance and exit of the test section channel were tapered from the sides of the channel as can be seen in Figure 3.3. The inlet was tapered to ease the transition to fully

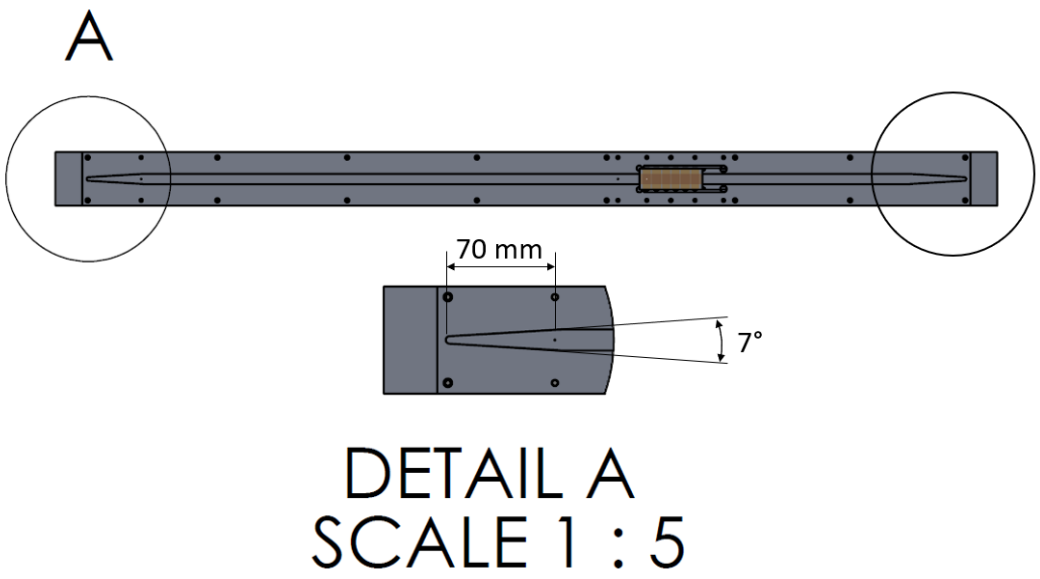

Figure 3.3: View of the underside of the lid, showing the entrance and exit tapers. Flow travels from left to right.

developed flow while the outlet was tapered to help force any vapor out of the test sec-

tion and minimize pressure losses between the nozzle and the reservoir. Both tapers were identical, with a total included angle of 7 degrees and length of 70 mm.

The nozzle portion of the test section defined the end of the entrance length. A prototypical nozzle is shown in Figure 3.4 where the flow direction is from left to right. The

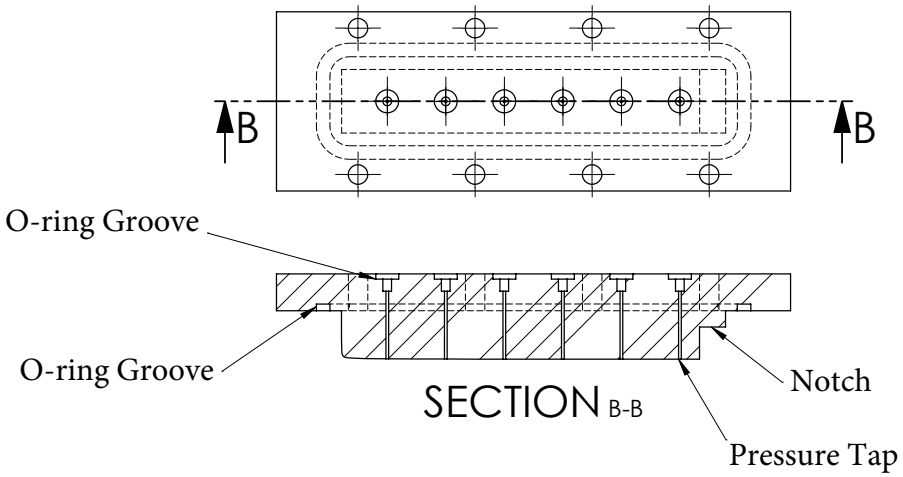

Figure 3.4: Top view and section of typical nozzle used to accelerate flow and decrease static pressure. Flow direction is from left to right.

nozzles were machined from aluminum to have a transitional, tight fit into the lid of the test section, to limit flow bypassing around the nozzle, and were sealed using an EPDM face seal. Pressure taps of 0.5 mm diameter were drilled through the nozzle; their size was chosen to be minimal so as not to disrupt the flow passing under the nozzle. Each pressure tap had an O-ring at the top to receive stainless steel tubing (1.5 mm outside diameter), which enabled the pressure transducers to be removed from the immediate vicinity of the test section (to allow space for insulation). These O-rings were compressed by the nozzle clamp located above the nozzle in Figure 3.2 and can be more clearly seen in Figure 3.5. The clamp was designed such that fully tightening the screws (between the clamp to the lid) would provide full compression of all O-rings in the nozzle. Further discussion of the nozzle's design is presented in Section 3.3.

When the nozzle was fully compressed there existed a small gap between the lower

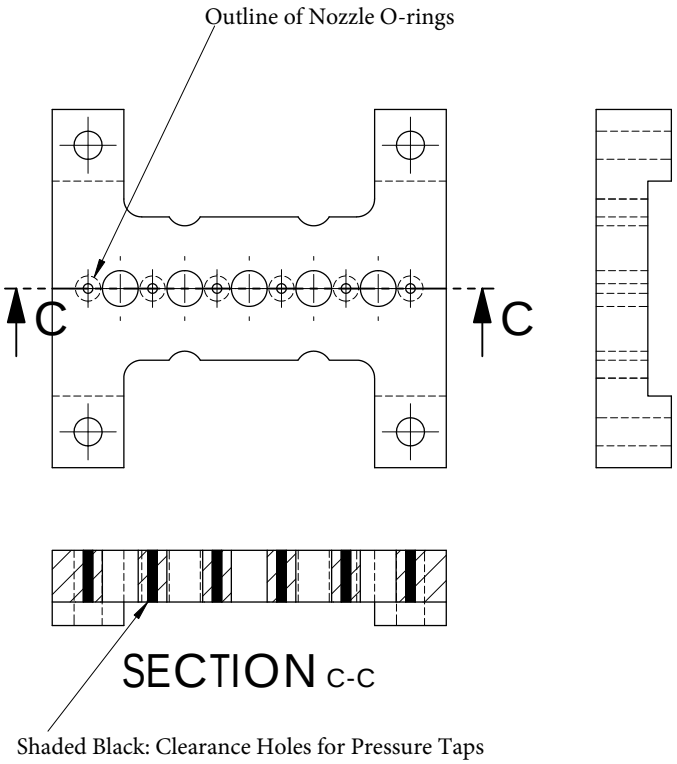

Figure 3.5: Top view and section of nozzle clamp used to compress the nozzle O-rings.

edge of the nozzle and the top surface of the glass, as shown in Figure 3.6, which defines the edges of the fluid channel wherein the nozzle is brown for contrast (all nozzles were made of aluminum) and the flow is once again flowing from left to right. The horizontal unhatched region is the fluid channel in Figure 3.6. The nozzle clamp is atop the nozzle, which is installed in the lid.

The bottom surface of the fluid channel was the top surface of the base. Parallel to the top surface of the base was the glass window. The glass used was float glass (soda-lime glass) of dimensions 25 mm x 75 mm x 1.1 mm (more detail to follow).

The bottom surface of the nozzle was machined to obtain the desired pressure gradient across the glass. For example, with R245fa as the design fluid, a linear pressure drop of 25 kPa across the 75 mm of glass is obtained from a nozzle whose fluid channel exit height was 0.14 mm. With a channel width of 12.4 mm, the channel is 88 times wider than it is

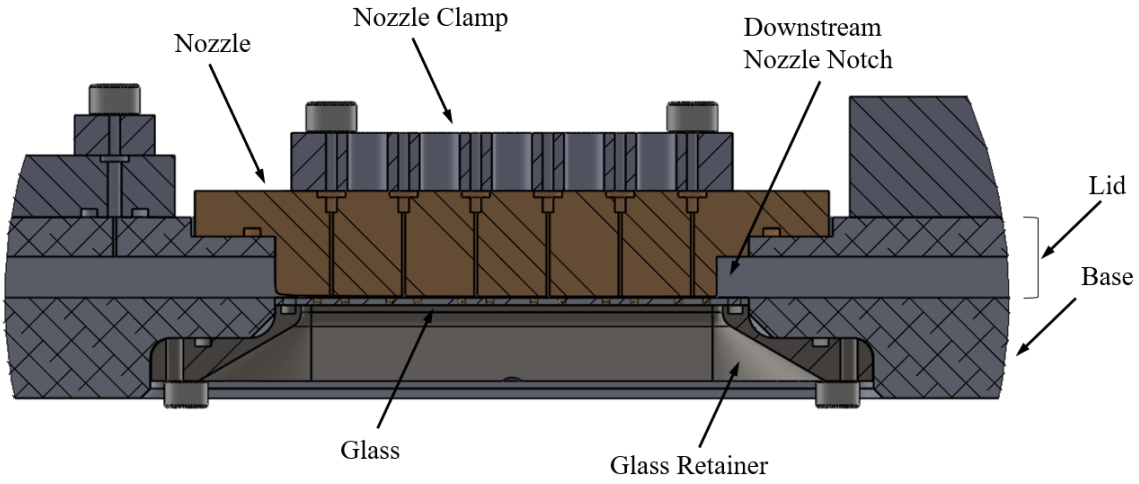

Figure 3.6: Section view of test section at the location of the nozzle. Nozzle shown as brown for contrast, but was made from aluminum. Flow travels from left to right between the nozzle and the glass.

tall, for this particular case.

The glass was sealed from beneath by the glass retainer, which was fabricated from steel to minimize deflections caused by the glass retainer being 2 mm thick at its thinnest point. Side and section views of the glass retainer were seen in Figures 3.2 and 3.6, respectively, and a perspective view is shown in Figure 3.7 for more clarity. The glass retainer pressed the glass against Ultem insulators used in the electrical circuit described below. The Ultem insulators can be seen in Figure 3.8.

The two channels on the top surface of the glass retainer are O-ring grooves; one to seal against the bottom of the glass, and the other to seal against the bottom of the test section's base. The retainer contains a large rectangular through-hole in the middle for visualization from beneath. The O-ring grooves were designed for 30% compression, which produces an average compressive load of 3.5 N/mm. This meant that the glass retainer would exert a force of approximately 600 N against the bottom of the glass; for this reason, the tolerance between the top of the glass retainer and the bottom of the lid was kept to within 25 μm to prevent excessive force on the glass caused by a larger

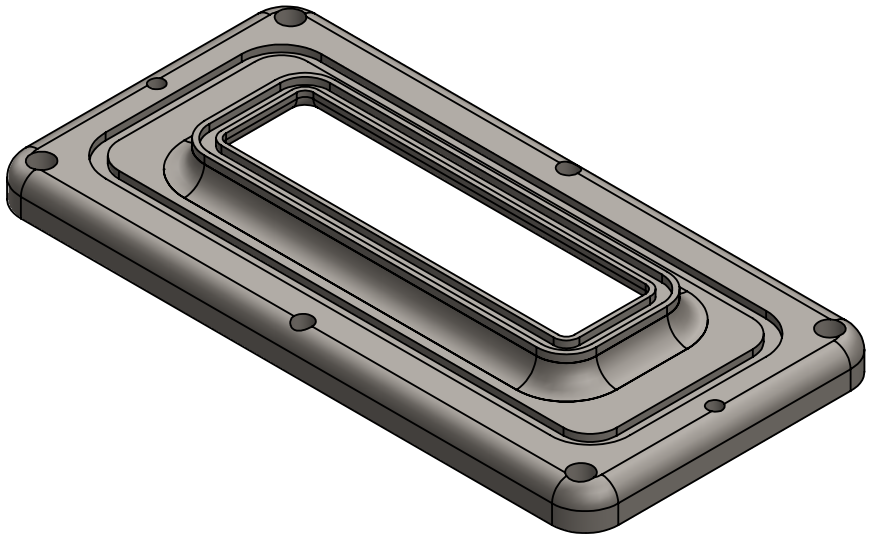

Figure 3.7: Perspective view of glass retainer.

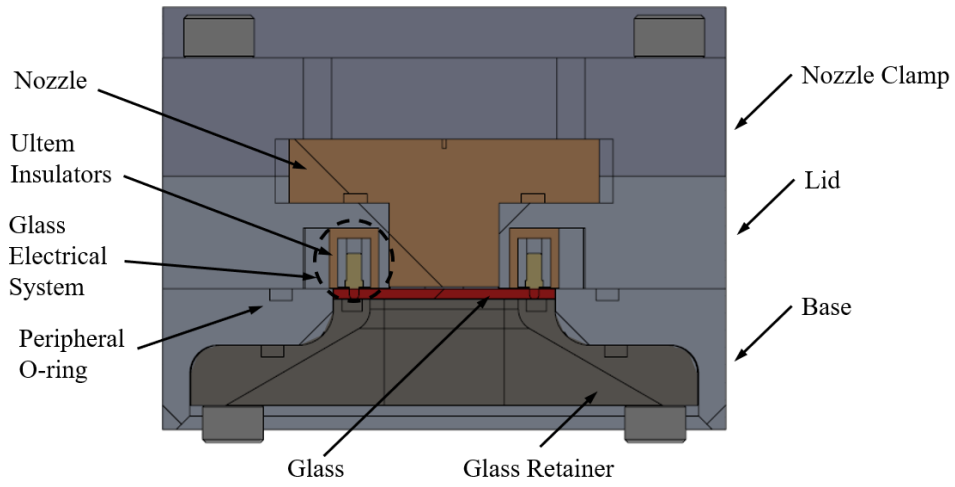

Figure 3.8: Section view through test section to show mating surfaces when the glass retainer is installed. The top surface of the glass (the glass is red for clarity) is pressed gainst Ultem insulators that form part of the electrical circuit to be described later.

tolerance. The baseline fluid channel height could be measured using a depth micrometer or calipers when the nozzle was installed, and with the glass and retainer removed. From this baseline, fine adjustments of the fluid channel height were achieved by inserting

stainless steel shims between the nozzle and the test section lid (in increments of 0.076 mm) prior to tightening the nozzle clamp, as shown in Figure 3.9.

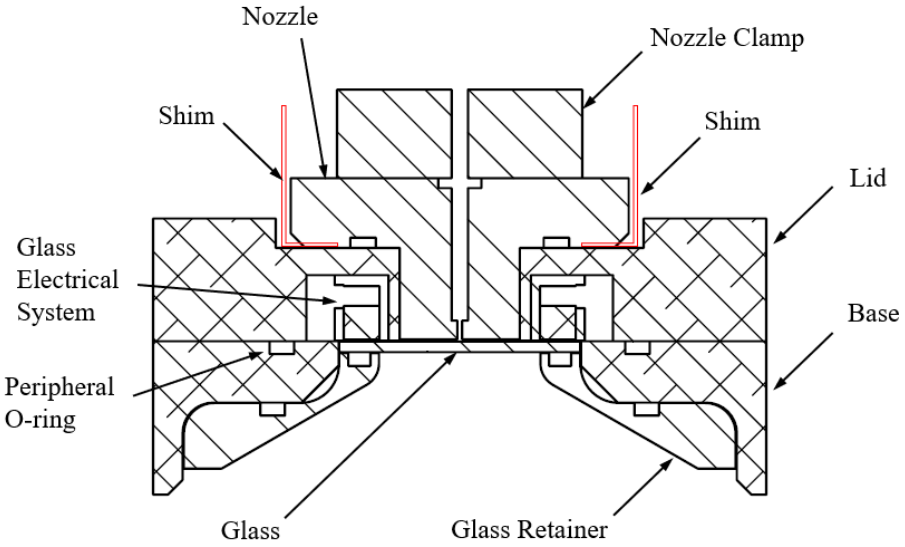

Figure 3.9: Section view through test section, only showing cut surfaces, showing location of shims when nozzle is raised.

Besides being a window into the test section for observing flow boiling, the glass was also an ohmic heater, with two gold pads acting as bus bars in a similar manner as McHale and Garimella [32]. As purchased from Delta-Technologies (Part CG-811N-S115), the glass was coated with a SiO_2 passivation layer followed by a coating of indium-tin oxide (ITO) until the surface resistivity was between 30 Ω/□ and 60 Ω/□. Discussion regarding the units ohms per square (Ω/□) can be found in Appendix A. The ITO coating was patterned to provide control of where heat was applied to the fluid. To prepare the glass for partial removal of the ITO, a mask was made from laser-cut Kapton tape and applied to the ITO surface after the glass had been cleaned in acetone and subsequently ethanol. The glass substrate then spent one minute in an etchant solution (an aqueous solution of 20% HCl, 5% HNO_3, heated to 55°C [33]) to dissolve any exposed ITO. After washing the surface with acetone and then ethanol to clean residue from the etching process, an-

other mask was used to prepare the glass for the attachment of the electrical busses. The busses were applied in two layers via e-beam metallization: the first layer was 10 nm of titanium to act as an adhesive for the second layer that was 100 nm of gold. The gold extends from the edge of the glass to the nearest edge of the fluid channel and provided a robust substrate for making electrical contact to the ITO. The edges of glass in contact with gold were then sanded to remove gold that could cause electrical short circuits to the aluminum test section.[4] Photos of the glass after gold deposition and finished glass ready for the test section are shown in Figure 3.10. The mostly transparent, slightly dark

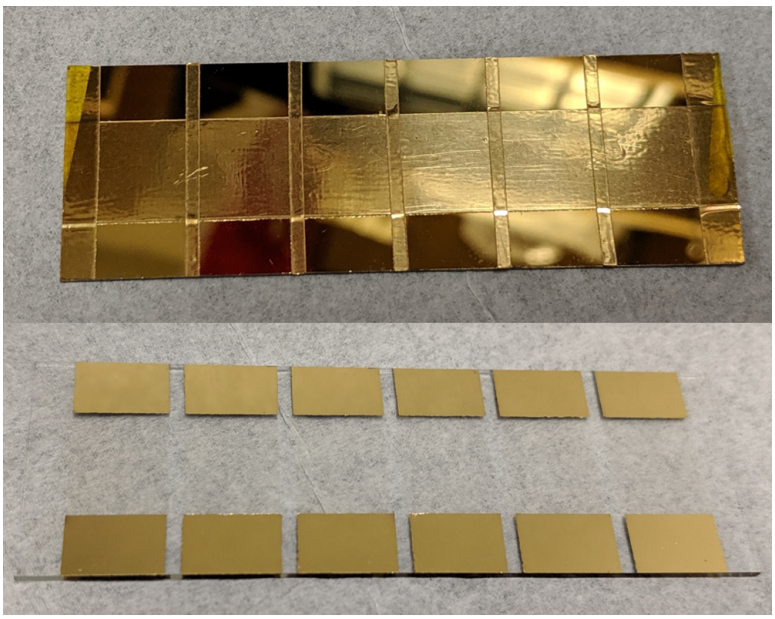

Figure 3.10: Top: glass substrate after gold deposition, with mask still applied. Bottom: Glass with deposition mask removed. The six ITO heaters (barely visible) run from the six gold pads on the lower and upper edges of the glass.

paths between opposing gold pads are the six ITO strips that remain after etching and are

[4]Conductive epoxies were initially used to create an electrical bus on the ITO coating, as suggested by the glass manufacturer [33]. It was found that the conductive epoxy changed resistivity as the porous matrix of epoxy absorbed liquid; this behavior was later confirmed to be possible by contacting the manufacturer of the silver epoxy. Both bare silver epoxy pads, and using a minimal volume of silver epoxy to adhere copper shim stock to the ITO film, were attempted without success. As the heat flux increased, liquid that wet between the solid particles of the epoxy could boil; breaking the bond between the ITO and epoxy and/or copper pad, or merely causing some of the matrix to dry out and change resistance.

roughly 9.5 mm by 12.4 mm (or 1.3 □). This formed independent heaters that were used to assess performance at different static pressures while at the same pressure gradient and flow rate.

Power was provided by a Xantrex XDC600-10 programmable DC power supply. Connecting the power supply to the glass were 1 mm diameter, spring pins (Mill-Max, Model 0921-1-15-20-75-14-11-0), each containing a gold piston with an internal spring capable of axially deflecting 1 mm while providing 0.9 N of force and electrically conducting up to 2 A. Each gold pad in Figure 3.10 had two spring pins, allowing for up to 4 A per heater. Figure 3.11 shows a section view through the test-section to display the electrical system used to power the glass heaters. For reference, the fluid channel passes just behind the section view in Figure 3.11, and flow moves from left to right.

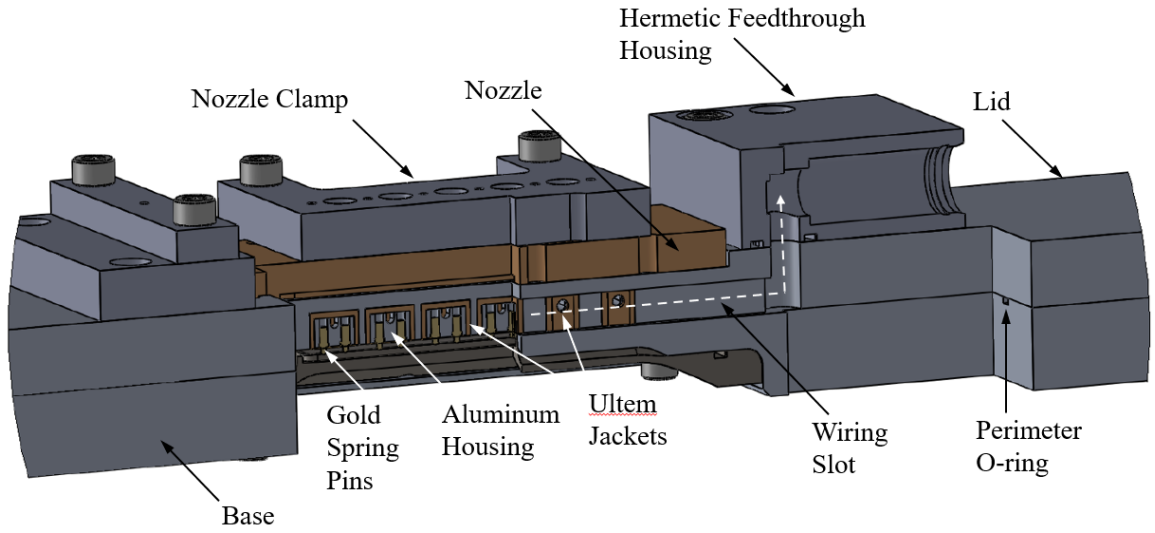

Figure 3.11: Cut-away view of test section to show the electrical circuit for the glass heaters.

The gold spring pins can be seen grouped in pairs, and are pressed inside aluminum housings. Each aluminum housing electrically connected pairs of spring pins together while providing a more sizeable surface for soldering wires. The aluminum housings were mounted inside Ultem jackets to prevent electrical contact to the aluminum test

section. Wires were directed to the spring pin assemblies via slots cut into the underside of the test section lid; these slots can be seen as two long, horizontal features in Figure 3.12, terminating at large diameter holes. There is a perimeter O-ring in the test section base that encircles the perimeter of the test section and seals between the lid and the base. In Figure 3.12, that O-ring would contact the lid between the spring pin wiring slots and the adjacent four screws.

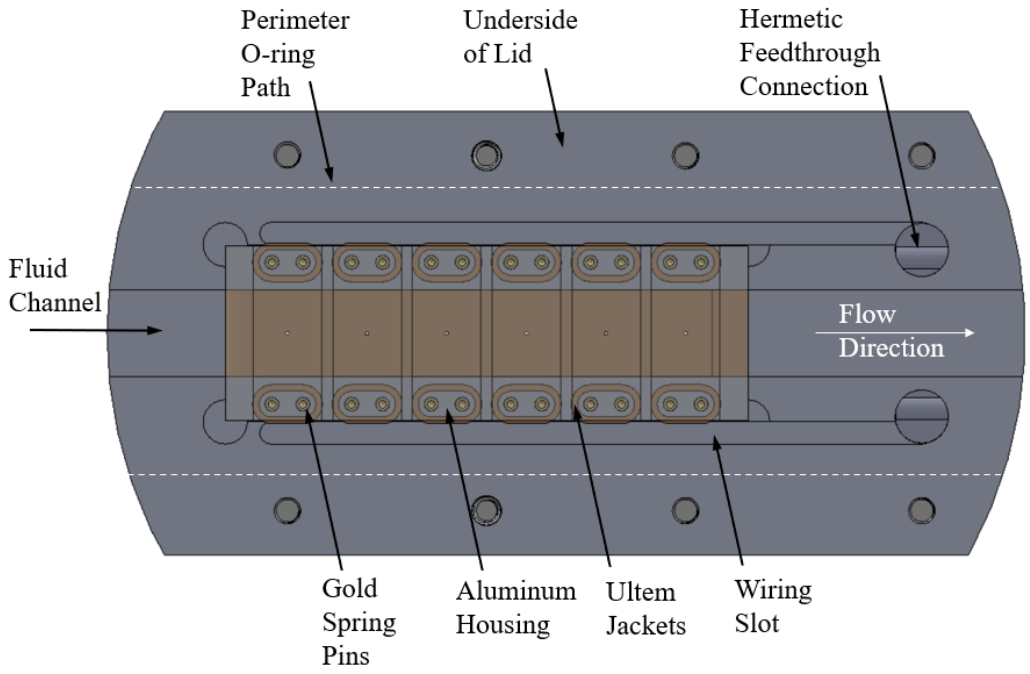

Figure 3.12: View of test section from below, having removed the base and glass retainer to display the placement of electrical components relative to the glass.

Previous experience has shown wiring to be one of the main causes of leaks in fluid systems.[5] For this reason, a hermetic feedthrough, wire-seal was purchased from Pave Technologies (Model 0597), rated at 550 kPa; this was an epoxy plug, with dual piston seals (replaced with the correct formulation of EPDM), containing nine, 70 cm long, 22 AWG, PTFE-insulated wires extending from each side of the plug. One side of the

[5]Braided wire can cause fluid to leak between the braids and refrigerants can react with pvc typically used to insulate wiring, causing leaks.

feedthrough wires was soldered to the six spring pin housings, while the opposite ends were routed to electrical connections for the power supply. The feedthroughs were mounted in an aluminum block, per the manufacturer's specification, and can be seen in Figure 3.11 and Figure 3.2.

Prior to installation, an electrically insulating layer of Kapton film (without adhesive) was applied to the top surface of the glass (between the spring pins and the fluid channel) to provide a 50 μm gap between the gold pads and the aluminum test section. This additional thickness was previously accommodated by machining 50 μm from the test section lid, resulting in the fluid-contacting surface of the glass being level with the top surface of the test section base, that is the bottom of the fluid channel. This can be seen in Figure 3.13. In addition, 100 μm of Kapton tape was added to each of the short sides of the glass retainer to decrease the compression force on the glass out of an abundance of caution. Repeated measurements between experiments were taken to confirm the ab-

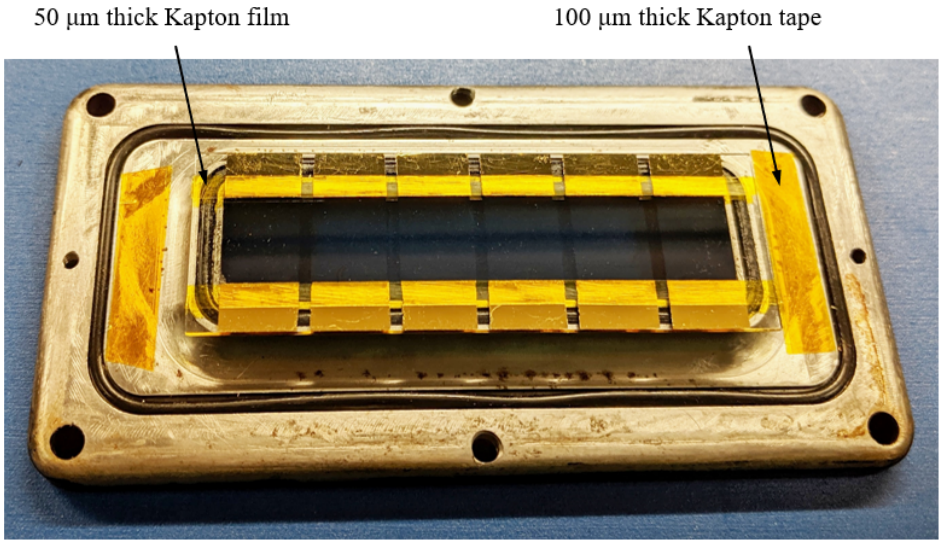

Figure 3.13: Photo of glass retainer prior to installation with Kapton film applied to prevent damage to the glass.

sence of a short circuit between the glass and the aluminum test section. The resistance

of each heater was also recorded to track the behavior of the ITO coating and associated electrical connections throughout the experiment.

A bottom view of the test section is shown in Figure 3.14 with the glass retainer and base installed. This view clearly shows the area for visualization provided by the 120 degree included taper on the underside of the glass retainer. The circles in the background are the pressure taps in the nozzle shown in Figure 3.6. For convention, heater 1, H1, was the most upstream heater; downstream heaters were named sequentially from H1.

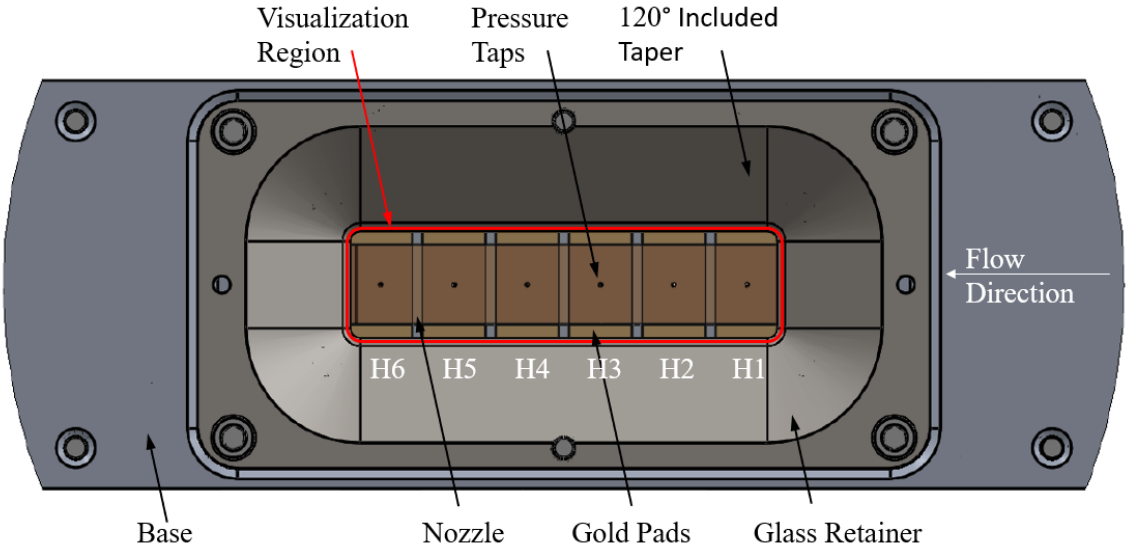

Figure 3.14: View of test section from below with the glass retainer and glass in their installed configuration. Note, flow now travels from right to left.

3.3 Nozzle Design

Each nozzle was designed to produce a linear pressure drop along the flow path, i.e., a constant, negative pressure gradient. The contour of the nozzle was initially designed using a modified version of the Bernoulli equation to include frictional head losses (Δh_f)

while neglecting gravitational head,

$$\frac{P_1}{\rho g} + \frac{v_1^2}{2g} = \frac{P_2}{\rho g} + \frac{v_2^2}{2g} + \Delta h_f \tag{3.3}$$

where the friction head (Δh_f) was calculated using the upstream velocity, v_1, and discretized fluid element of width Δx.

$$\Delta h_f = f_{duct} \frac{\Delta x}{d_h} \frac{v_1^2}{2g} \tag{3.4}$$

The friction factor was found using the correlation for turbulent flow through a smooth duct from Petukhov [34], shown in Equation 3.5.

$$f_{duct} = [0.790 \ln(Re_{d_h}) - 1.64]^{-2} \qquad \text{for } 3000 < Re_{d_h} < 5 \times 10^6 \tag{3.5}$$

Equation 3.3 was solved numerically. For a fluid element under the nozzle, spanning the width of the fluid channel, all upstream properties were known (including pressure, velocity, flow area, and fluid properties). The downstream pressure and fluid properties were also known. The downstream channel height could be iterated upon until the friction coefficient produced the correct downstream pressure. The downstream fluid velocity would thus be known. The nozzle was logarithmically discretized into 200 points, starting from its upstream edge, to accurately capture the significant change in geometry at the beginning of the nozzle. Typical nozzle profiles, calculated using this analysis are shown in Figure 3.15, where the lines represent the top of the fluid channel as fluid passes beneath the nozzle from left to right. The roundness of the leading edge can be seen in the section view of Figure 3.6.

The flow was assumed to be incompressible, turbulent, and of constant properties. The primary nozzle used for experimentation was designed for R245fa with a pressure

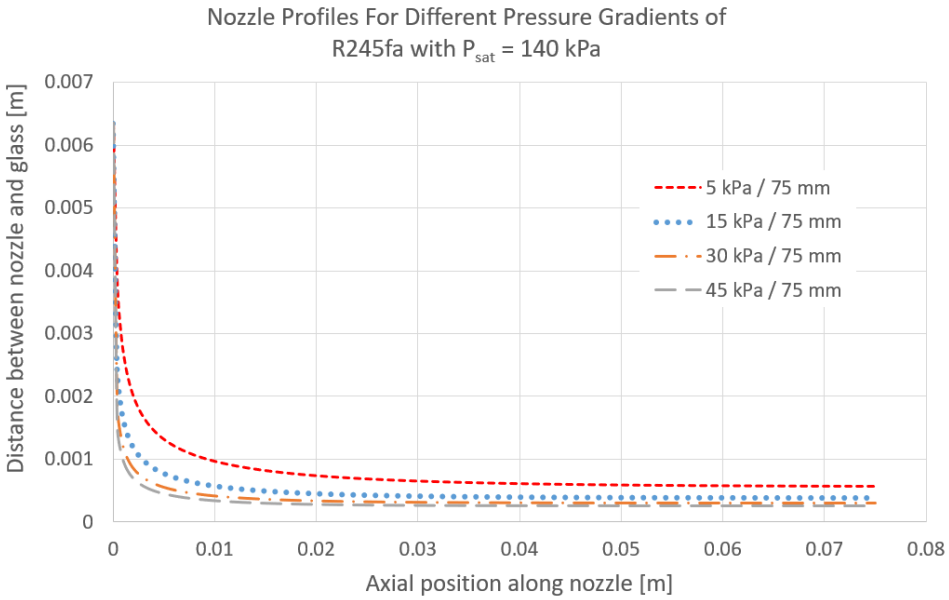

Figure 3.15: Typical nozzle profiles for linear pressure gradients as calculated using Equation 3.3.

change along the nozzle of -25 kPa, at a flow of 0.75 L/min, nominal fluid temperature of 30°C, and a subcooling of 10°C to ensure the calculation did not reach saturation. The calculated nozzle profile and design criteria are shown in Figure 3.16(a). Note the y-scale of Figure 3.16(a) is logarithmic and exaggerates the amount of curvature present in the nozzle. For a channel width of 12.4 mm, the channel width to height ratio of the primary-design nozzle shown in Figure 3.16(a) is greater than 20:1 for all but the initial 3.7 mm of the 75 mm long nozzle. In addition, the fluid contacting surface of the nozzle was sanded to 3000 grit to obtain a smooth, matte finish.

An example of the performance for this primary nozzle is shown in Figure 3.16(b) for R245fa for a flow rate of 0.7 L/min. Excellent linearity is seen in the pressure profile. For three different fluids (R245fa, HFE7000 & R123), with shim thicknesses, th_{shim}, (76 μm & 152 μm) and unshimmed nozzles, the average value for R^2 of the linear regression was 0.997, with a minimum of 0.989 and a maximum of 1.000. The maximum shim thickness used was 0.15 mm; this was limited by the amount of unloading of the O-ring between

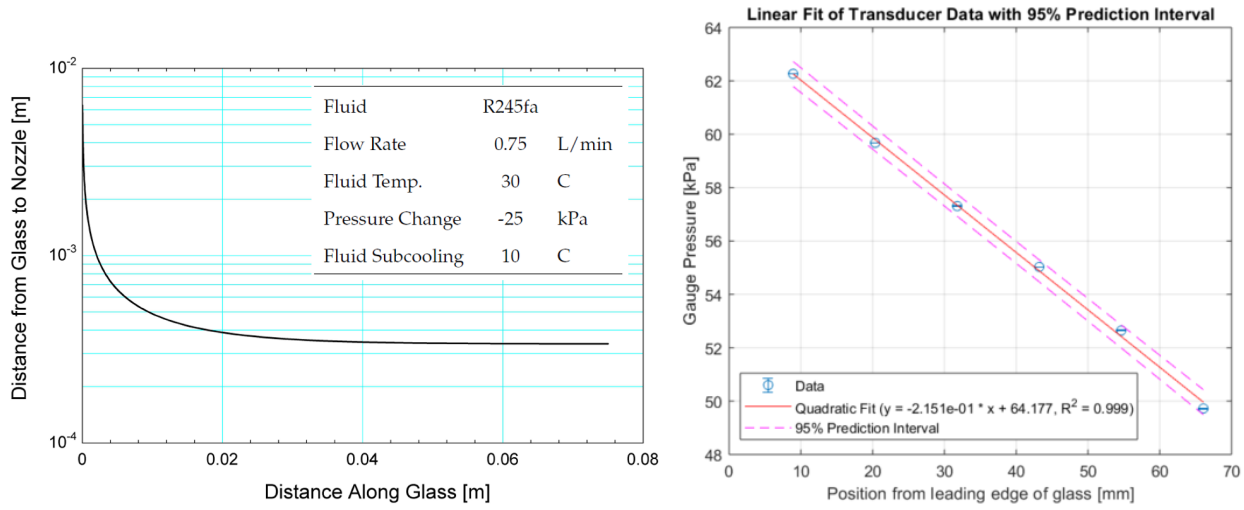

(a) (b)

Figure 3.16: Primary nozzle (a) design and (b) example performance with R123 at 0.7 L/min

the nozzle and the lid before fluid leakage. This O-ring groove was specifically fabricated shallower than designed to accommodate shimming; at the cost of decreased O-ring life. From this it could be determined that the nozzle was consistent in producing linear pressure gradients across multiple fluids and also maintained linearity when shimmed by up to 0.15 mm from the design nozzle height. To put this in perspective, the channel height at the middle of an unshimmed nozzle is 0.19 mm tall; thus a 0.15 mm shim doubles the channel height. The spatial extent of each heater along the profile of the nozzle is bracketed by pairs of red data points in Figure 3.17. Fluid flow above H1 experiences the majority of the contraction imposed by the nozzle. For this reason, boiling behavior on H1 was not prioritized during this study. Nozzle height, at the center of each heater, for all shim thicknesses, is shown in Figure 3.18. The nozzle is nearly flat for locations beyond H3.

Fluid entered the test section in stainless steel tubing with an inner diameter of 5 mm; the fluid left the nozzle in a channel with a d_h of about 0.2 mm; it then experienced a

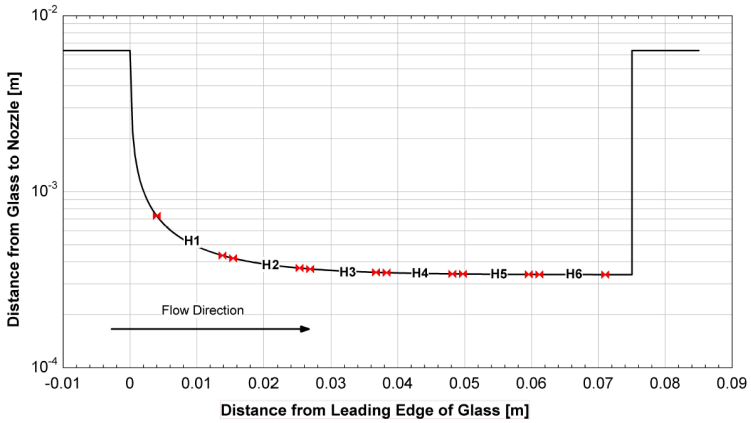

Figure 3.17: Heater locations along nozzle profile.

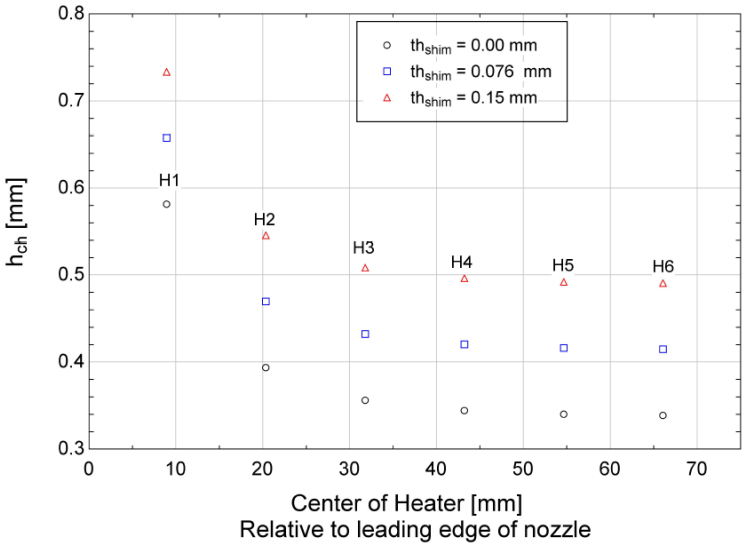

Figure 3.18: Nozzle heights for each heater and all shim thicknesses.

moderate amount of pressure drop before exiting the test section. A summary of the pressure changes caused by changes in channel geometry can be seen in Figure 3.19. The flow condition used for the calculations in Figure 3.19 assumed R245fa flowing at 0.75 L/min with a temperature and pressure of 20°C and 130 kPa, respectively.

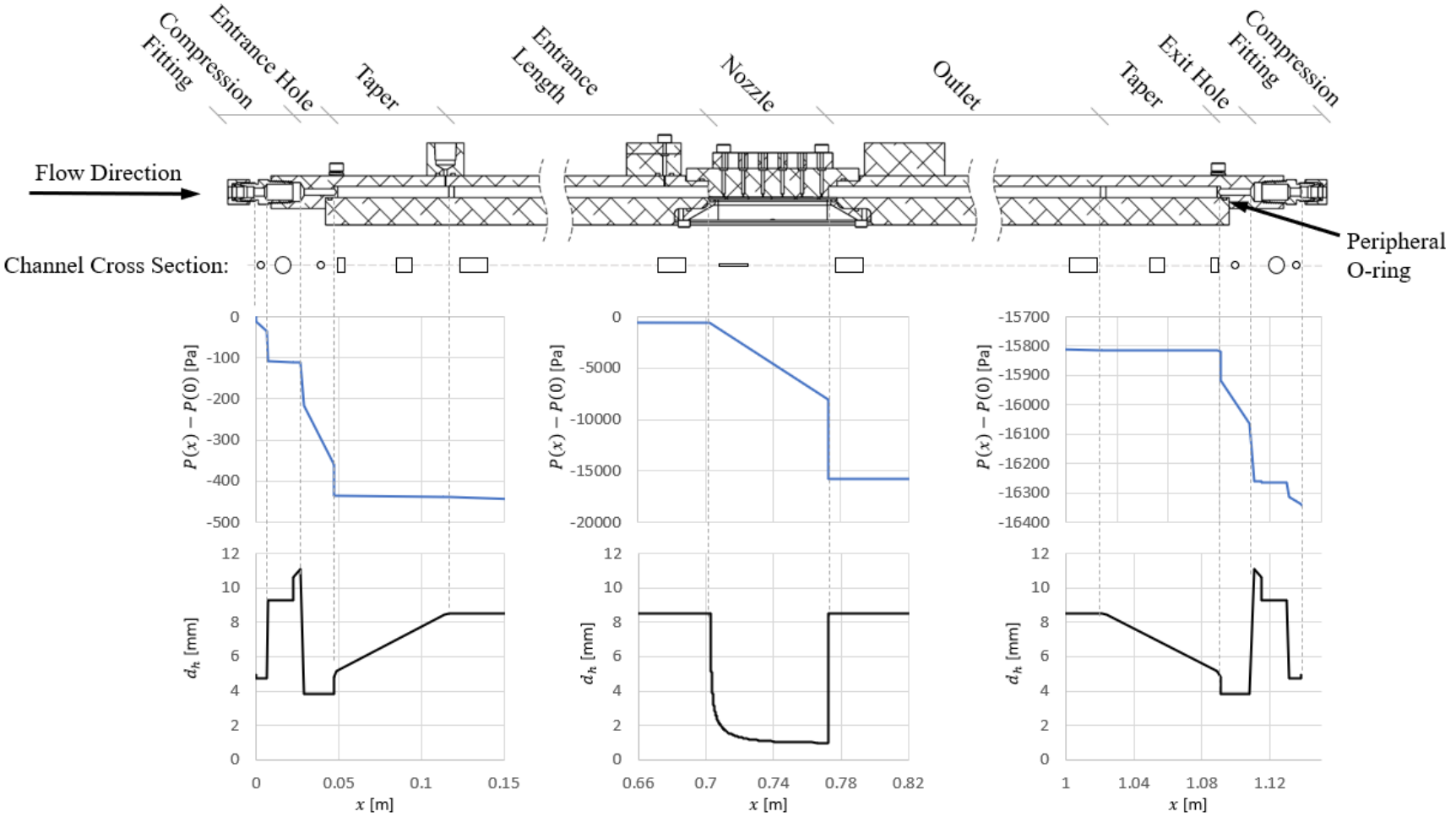

Figure 3.19: Section view through test section depicting pressure drops, changes in d_h, and shape of the fluid-channel cross section for R245fa, at 20°C, 130 kPa, and flow rate of 0.75 L/min.

The largest contributor to entrance pressure loss was the entrance hole that allowed fluid to bypass the peripheral O-ring. The diameter of the entrance hole was limited by the clearance needed to support the O-ring groove in the base, and by the depth of the fluid channel (nominally 6.35 mm). The nearly 300 Pa pressure loss is insignificant in comparison to the pressure drop beneath and following the nozzle. The linear pressure drop under the nozzle was chosen by design; 7.5 kPa pressure drop along the glass in Figure 3.19. The downstream edge of the nozzle did not extend to the downstream edge of the glass; this can easily be seen in Figure 3.6. This enabled visual verification that bubbles were not present in the vortex immediately downstream of the nozzle, causing pressure fluctuations in the nozzle. The sudden expansion of the fluid following the nozzle resulted in an additional 7.7 kPa of pressure drop.

3.4 Visualization

A schematic of the high-speed visualization setup can be seen in Figure 3.20.

The camera lens[6], shown in Figure 3.20, had high power LEDs above and below to provide sufficient lighting for high speed imaging. The LEDs were 12 Vdc modules from Cree (model XHP70) and had a maximum current of 2.4 A each. Three LEDs were mounted on each heat sink and typically saw currents of 2 A when in use, for a total of 144 W; this was sufficient for imaging a 304 x 400 pixel image at 19,000 frames per second, with an exposure of 2 μs, at f/5.6. Several methods were used for decreasing stray reflections that would decrease the image quality:

- Light stops made from black hardboard were placed between the lens and LEDs prevented reflections from the environment
- The underside of the glass retainer was painted black

[6]Nikon, model AF Micro-Nikkor 200mm f/4D IF-ED

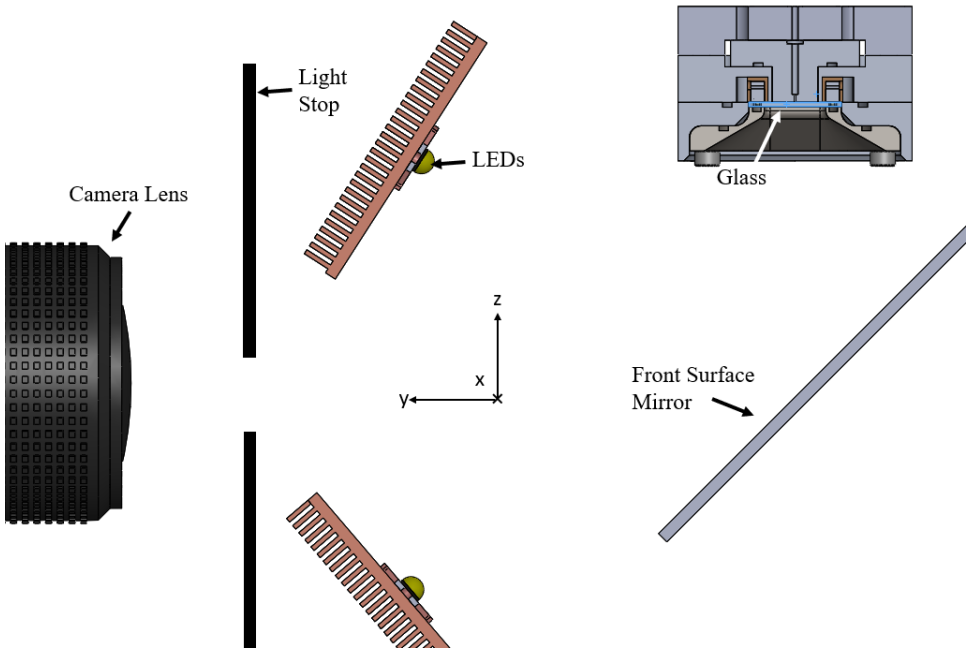

Figure 3.20: Cross-section view of test section, looking toward the test section outlet, showing the setup for high speed imaging.

- All exposed aluminum from the test section was masked with tape and covered black hardboard
- The bottom surface of the nozzle was progressively sanded up to 3000-grit to provide a uniformly matte surface

A front-surface aluminum mirror was mounted at 45° to facilitate horizontal camera placement with imaging from beneath the test section. The camera lens was attached to a Vision Research, Phantom v311, high speed camera and was mounted on a manual z-axis stage to support the use of a motorized, x-axis linear stage. The z-axis was set once and rarely needed adjustment. The camera image magnification was set to show only one full heater of the glass; this allowed full use of the camera sensor without having to crop the image. The x-axis stage allowed for repeatable camera placement when switching between heaters. Moving between adjacent heaters required moving the camera by 11.4

mm

A typical camera image (304 x 400) is shown in Figure 3.21. The active heater is located on the right side of Figure 3.21, bracketed between two gold pads (a) that appear dark due to their specular reflection; the dark circle (b) in the middle of the active heater is a 0.5 mm diameter pressure tap. The image extends in width downstream of the active heater until the adjacent pressure tap (c) can be seen. The pressure taps were fabricated using CNC to ensure exact placement ($\pm$ 0.013 mm)[7]; as a result, the distance between neighboring pressure taps was 11.43 mm and could be used to calibrate each image in terms of mm/pixel during the video processing algorithm.

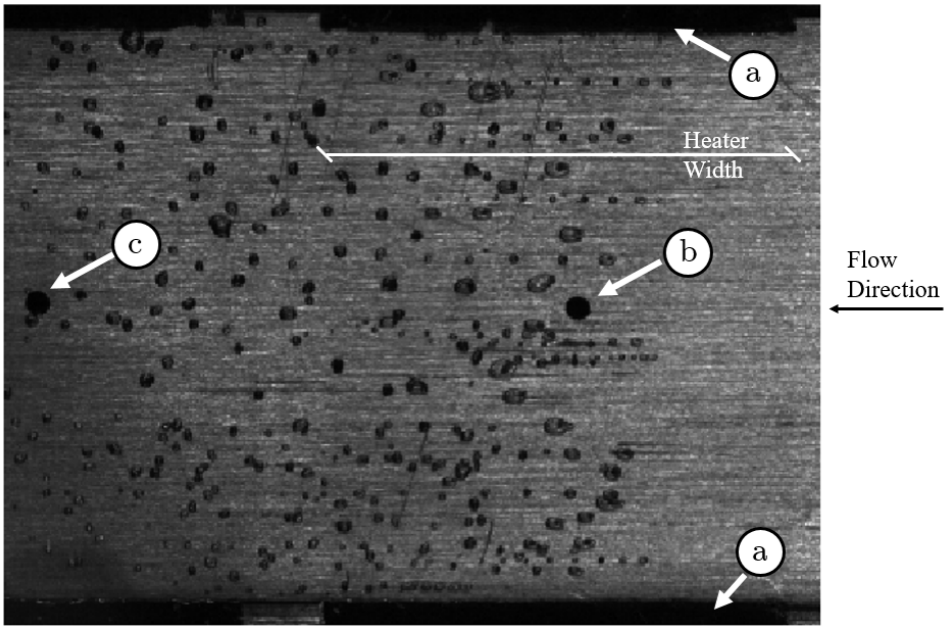

Figure 3.21: Example image from Phantom camera showing (a) gold pads, (b) pressure tap for observed heater, (c) downstream pressure tap

Appendix B describes the design and performance of a video processing algorithm that was created to automate the identification of bubble parameters: centroid locations, diameters, tracks between frames. This algorithm worked by converting the raw video

[7] A Trak DPM CNC vertical milling machine was used with a typical positional accuracy and repeatability of 0.013 mm [35].

file into a series of binary images showing only the bubbles to be tracked. The centroids of each bubble were input into a particle-tracking routine by Blair and Dufresne [36], as adapted for Matlab from the method proposed by Crocker and Grier [37] and Crocker and Weeks [38]. After significant analysis, it was determined that the automated processing was not accurate over a sufficient range of bubble density. Therefore, manual processing of the data was required. See Appendix B for details.

Manual video analysis used the Phantom Camera Control (PCC) software by Vision Research to play back each video at between 2 frames per second and 40 frames per second. Between 200 and 10,000 frames were analyzed for each video; the exact number was chosen such that the median number of nucleation events per video was around 20 bubbles/second at any given nucleation site. Each video was played in ping-pong mode (i.e., the video played forward until it reached a stop, at which time it played the video in reverse, and repeated when the first stop was reached) until the nucleation frequency at all nucleation sites was recorded.

A polymer sheet was overlaid on the viewing screen such that a marker could be used to identify nucleation sites that were already analyzed. For each nucleation site the video was played at a speed that enabled an accurate count of how many bubbles were generated at that site. This method produced an accurate count of the average number of bubbles generated at a given nucleation site over the number of analyzed frames; the spatial locations of each nucleation site; and the number of nucleation sites. An example of these data is shown in Figure 3.22.

Between-experiment measurement repeatability of N_a'' was assessed for three different experiments; results are shown in Figure 3.23. The maximum percent deviation was 10%, with an average of 4%. Calculating the uncertainty in the repeated measurements, given the data points in Figure 3.23, results in N_a'' being known to within $\pm 10\%$ for a 95% confidence level. Repeated measurement of the same video, showed no significant differences;

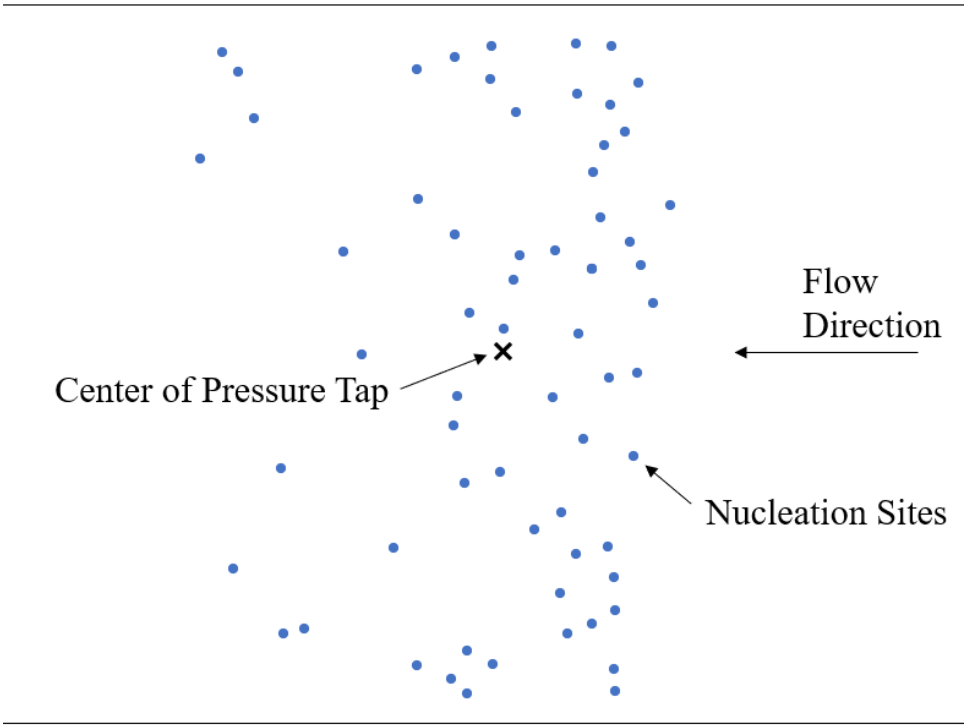

Figure 3.22: Example image of nucleation site location data, showing location relative to the pressure tap.

repeated measurements were within two nucleation sites.

Overall, 254 videos were manually analyzed with a total of 8717 nucleation sites and a total of 176,982 counted bubbles. These results were combined with the collected sensor data corresponding to each video.

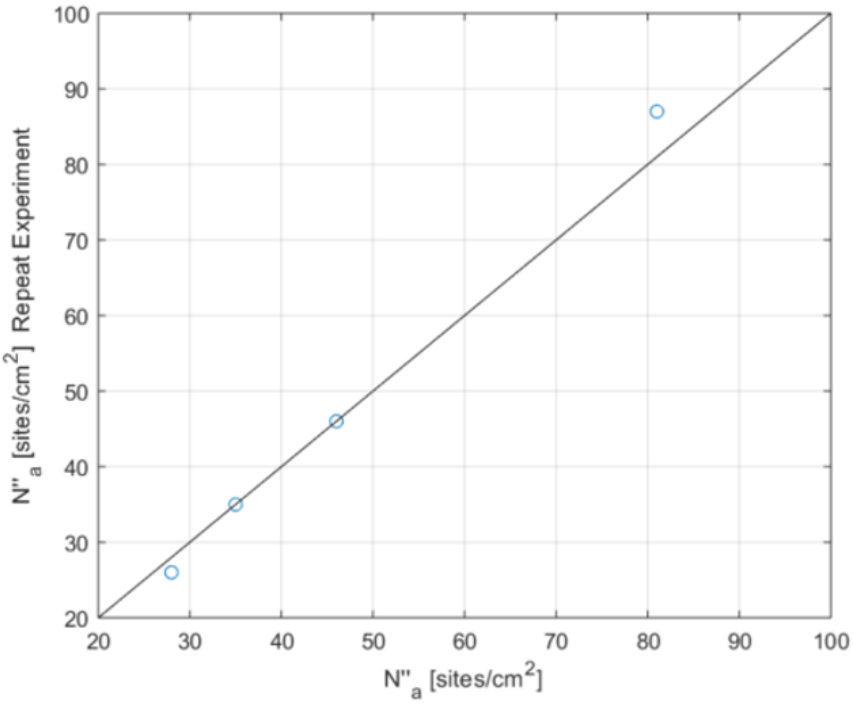

Figure 3.23: Between-experiment repeatability of N_a'' measurements.

3.5 Low-Speed Data Acquisition

During the acquisition of each high-speed video, corresponding data files were recorded for low-speed sensor measurements. NI-DAQmx was used to generate *.tdms files of all sensor signals; Table 3.1 summarizes these sensors. Placement of each sensor can be found in Figure 3.1.

Details of the accuracy of each measurement is provided in Section 3.6, along with the uncertainty of values calculated from each measurement.

The temperature of the test section was monitored at three locations along the length of the channel. At each location, there were three thermocouples: one located on the top surface of the test section, another recessed 8 mm into the base of the test section, and a third thermocouple on the outside surface of the test section heaters; these can be seen in Figure 3.24. The nine test section thermocouples were used in combination with the fluid

Table 3.1: Input sensors being recorded by NI-DAQmx

Temperatures	Pressures	Other
Reservoir	Reservoir (abs)	6 x Heater Current
Fluid Inlet	Entrance Length (diff)	Flow Rate
Fluid Outlet	Entrance Length (abs)	Fluid Density
3 x TS Top Surface	6 x Heater (gauge)	
3 x TS Base	Heater 1 (abs)	
3 x TS Heaters	Barometric	
2 x TS Ambient		
Ambient		
Water Bath		
Glass		
Rope Heater		

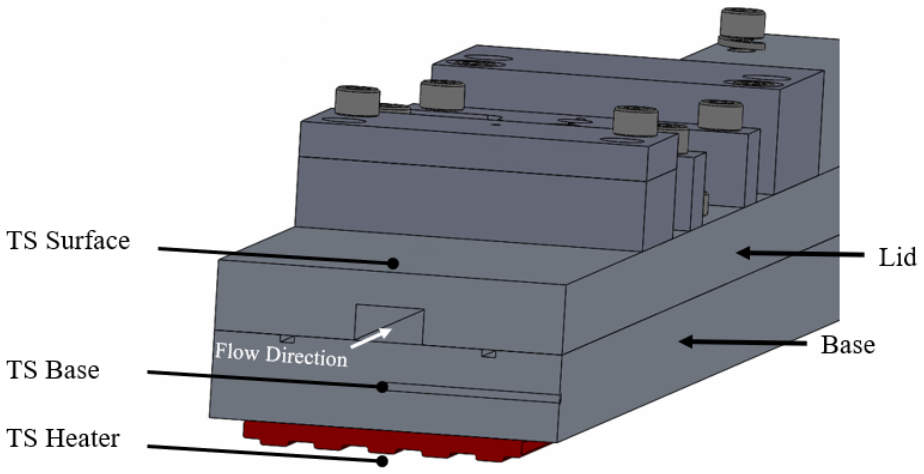

Figure 3.24: Cross-section of test section showing vertical position of thermocouples, for one of the three locations along the length of the test section.

inlet thermocouple to verify that the system had reached steady state prior to recording video. There were two thermocouples located within the insulated envelope of the test section, but not touching the aluminum; these were used in combination with the ambient room temperature to estimate thermal losses from the test section. A thermocouple was pressed on the outside of the glass using a thin layer of thermal interface material; this thermocouple was either located in the middle of the active heater, or in the middle of H6.

Every data trial was run twice: once with the glass thermocouple located at H6 concurrent with high-speed video of the active heater, and another trial with the glass thermocouple in the middle of the active heater.

Table 3.2 summarizes the capabilities of the data acquisition hardware used to record the sensor values.

Table 3.2: Data acquisition hardware specifications

				No. of Channels				
DAQ	Sampling			Voltage		Current		TC
Modules	Bits	Rate	Units	In	Out	In	Out	In
NI 9207	24	500	S/s-Ag	8		8		
NI 9211	24	14	S/s-Ag					4
NI 9214	24	68	S/s-Ag					16
NI 9215	16	100	kS/s/ch-Sim	4				
NI 9263	16	100	kS/s/ch-Sim	4				
NI USB-6008	12	100	kS/s-Ag	4	4	2	2	

During an experiment three *.tdms data files were generated:

1. Master file compiling data from all cDAQ channels at all times, sampling continuously

2. A cDAQ-Video file for storing 3 seconds of data recorded simultaneously with each recorded video in a data run

3. An NI USB-6008 file for storing 3 seconds of heater shunt resistor voltages recorded simultaneously with each recorded video in a data run

While the programmed sampling rate was 10 Hz, the DAQ hardware limited this to 2 Hz for the NI 9207, NI 9211, and NI 9214. The aggregate sampling nature of these three DAQs meant that they took a total of 0.55 seconds to record one sample, or 1.8 Hz. To illustrate this, Table 3.3 shows the first 10 data points for the measured gauge pressure at heater 1 ($P_{ga,H1}$) The repeated values are non-physical as the DAQ repeated the previous data

Table 3.3: Example data: first 10 values of gauge pressure as measured at H1, when sampled at 10 Hz.

t [s]	$P_{ga,H1}$ [kPa]
0.0	36.767
0.1	36.767
0.2	36.767
0.3	36.767
0.4	36.767
0.5	36.839
0.6	36.839
0.7	36.839
0.8	36.839
0.9	36.839

point until the next sample was available. This slightly complicated the analysis. The sample average of the whole data set ($\bar{x}$) can be shown to be equal to the sample average of the physical values ($\bar{x}_p$), as shown in Equation 3.6,

$$\begin{aligned} \bar{x} &= \frac{\sum N_r x_{p,i}}{N_{total}} \\ &= \frac{N_r N_p}{N_{total}} \frac{\left(\sum x_{p,i}\right)}{N_p} \\ &= \frac{\sum x_{p,i}}{N_p} \\ \bar{x} &= \bar{x}_p \end{aligned} \tag{3.6}$$

where the i'th physical value of x is $x_{p,i}$, the number of repetitions[8] is N_r , and the number of physical values is N_p . In reference to Table 3.3, $x_{p,1} = 36.767$, $x_{p,2} = 36.839$, $N_r = 5$, and $N_p = 2$. Note that by definition, $N_{total} = N_r N_p$.

The sample standard deviation of the physical values of x, $s_{x,p}$, can be calculated in a

[8]The number of repetitions is simply the ratio of frequencies: $N_r = 10\text{Hz}/2\text{Hz} = 5$, in this instance

similar way. Equation 3.7 shows the typical form of the sample standard deviation.

$$s_x = \sqrt{\frac{\sum_i (x_i - \bar{x})^2}{N-1}} \tag{3.7}$$

For the over-sampled data with N_{total} number of data points, the sample standard deviation, s_x can be written as,

$$\begin{aligned} s_x &= \left[\frac{\sum N_r (x_{p,i} - \bar{x})^2}{N_{total} - 1}\right]^{1/2} \\ &= \left[\frac{N_r \sum (x_{p,i} - \bar{x})^2}{N_{total} - 1}\right]^{1/2} \\ &= \left[\frac{N_r (N_p - 1)}{N_{total} - 1} \frac{\sum (x_{p,i} - \bar{x})^2}{N_p - 1}\right]^{1/2} \\ &= \left[\frac{N_r (N_p - 1)}{N_{total} - 1}\right]^{1/2} s_{x_p} \\ s_x &= \left[\frac{(N_{total} - N_r)}{N_{total} - 1}\right]^{1/2} s_{x_p} \end{aligned} \tag{3.8}$$

which implies that the standard deviation of the physical data points in variable x (s_{x_p}) can be derived from the standard deviation of the over-sampled data (s_x) according to Equation 3.9, where N_{total} and N_r have been set to 30 and 5, respectively, for the 3 seconds of video data.

$$\begin{aligned} s_{x_p} &= s_x \left[\frac{N_{total} - N_r}{N_{total} - 1}\right]^{-1/2} \\ s_{x_p} &= 1.077 s_x \end{aligned} \tag{3.9}$$

The results show that the standard deviation of the physical data is 7.7% higher than that of the whole data set.

This procedure was used to find the standard deviation for data channels measured by

the NI 9207, NI 9211, and NI 9214 DAQs. The remaining DAQs recorded unique samples at a rate of 10 Hz. For the remainder of this document the standard deviation will always refer to only the physical data points calculated from either Equation 3.9 or Equation 3.7.

3.6 Experimental Uncertainty

Experimental uncertainties were calculated using the framework of Kline and McClintock [39], as summarized by Moffat [40], where the uncertainty of F, a function of independent variables X_i, can be computed using the root-sum-of-squares method shown in Equation 3.10.

$$\delta F = \left[\sum_{i=1}^{N} \left(\frac{\partial F}{\partial X_i} \delta X_i \right)^2 \right]^{1/2} \tag{3.10}$$

Here, the partial derivative corresponds to the sensitivity of F to variable X_i, and is scaled by the magnitude of the uncertainty δX_i. All of the scaled uncertainties are then added in quadrature to compute the total uncertainty of F.

3.6.1 Measurement Uncertainty

The measurement uncertainty of a random variable, δX, was calculated according to Equation 3.11,

$$\delta X = \frac{t_{CI:\nu} s_X}{\sqrt{N}} \tag{3.11}$$

where $t_{CI:\nu}$ is the Student's t-statistic, s_X is the standard deviation of X, and N is the number of measurements. The t-statistic is the value of x at which the area under the Student's t probability density function (pdf) is equal to the confidence level, c_t, where df is the number of degrees of freedom. The Student's t-distribution is shown in Equation

3.12.

$$y_{pdf} = f(x|df) = \frac{\Gamma(\frac{df+1}{2})}{\Gamma(\frac{df}{2})\sqrt{df\pi}}\left(1+\frac{x^2}{df}\right)^{-\frac{df+1}{2}} \tag{3.12}$$

Figure 3.25 shows the positive half of the Student's t pdf and cumulative density function, cdf, for varying degrees of freedom. As the number of degrees of freedom increases, the maximum value of the pdf increases; correspondingly, at a given value of x, the cdf is higher for higher values of df. For quantities whose summary statistic is the average of

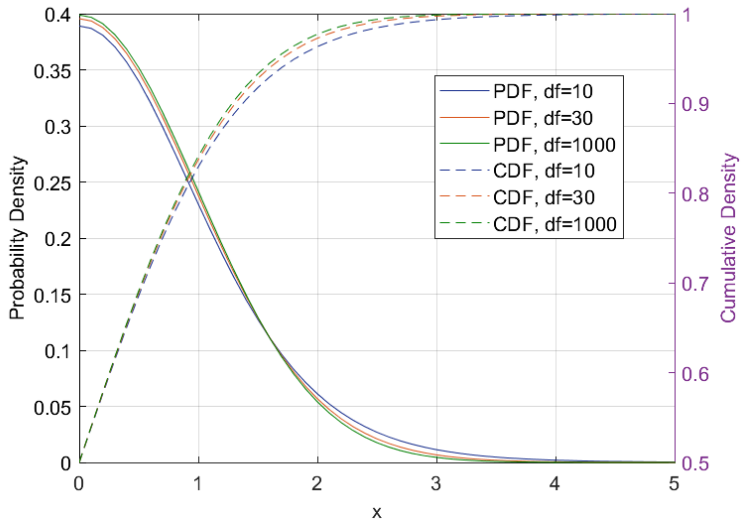

Figure 3.25: Student's t-distribution pdf and cdf for varying degrees of freedom

many replicated observations, the number of degrees of freedom is equal to one less than the number of replications (i.e., $df = N - 1$).

The total uncertainty was calculated by adding the measurement uncertainties in quadrature with the fixed, device uncertainties described next.

3.6.2 Device Uncertainty

The device uncertainties were obtained from data sheets and calibration results. Figure 3.26 shows these uncertainties overlaid on the flow schematic. A description of each

device uncertainty follows Figure 3.26.

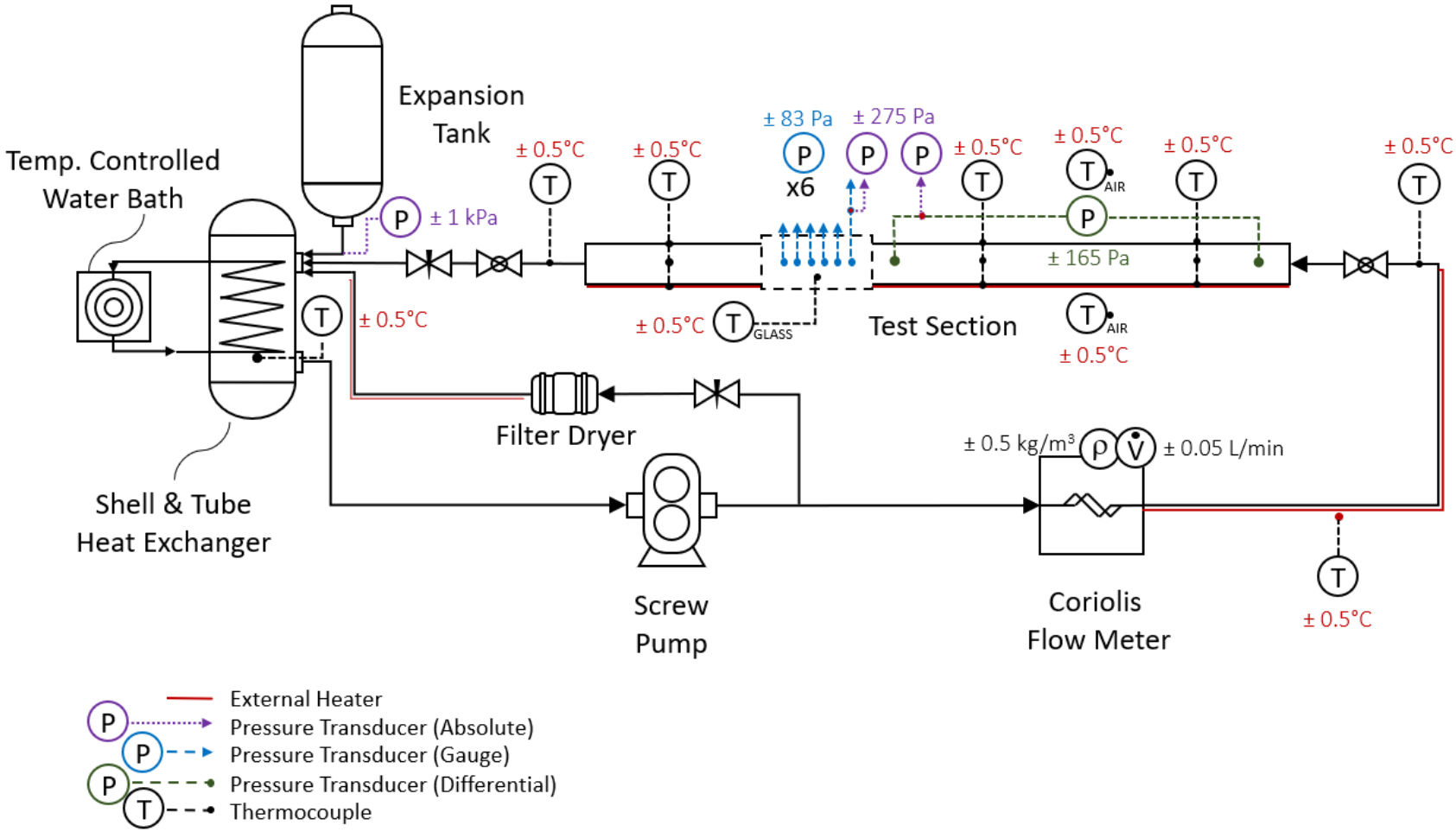

Figure 3.26: Flow loop schematic with labelled device uncertainties.

Flow Meter

The Coriolis flow meter was programmed to output signals from 4 - 20 mA for flow rates less than 5 L/min and densities between 100 kg/m^3 and 3000 kg/m^3. This flow rate range is significantly lower than the nominal flow rate of 38.7 L/min, which causes an increased device uncertainty. Equation 3.13 shows the volume flow rate uncertainty, δQ_{fm}, as a function of the flow meter's zero point stability, ($z_{st} = 1.4 \times 10^{-5}$ kg/s), the liquid mass flow rate ($\dot{m}_l$), and the nominal volumetric flow rate of the Coriolis flow meter ($Q_{fm,nom} = 38.7$ [L/min]).

$$\delta Q_{fm} = \frac{z_{st}}{\dot{m}_l} Q_{fm,nom} \tag{3.13}$$

The volume flow rate uncertainty is shown in Figure 3.27 in addition to the markers corresponding to experimental trials. The average volume flow uncertainty was ± 0.05 L/min, with a low of ± 0.03 L/min and a maximum of ± 0.12 L/min.

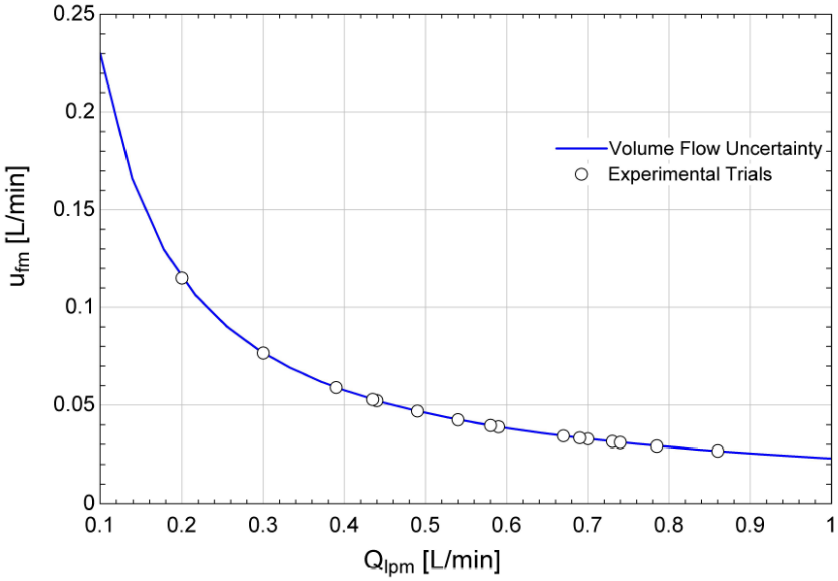

Figure 3.27: Flow rate device uncertainty

Pressure Transducers

All of the flow loop pressure transducers had a relative uncertainty of 0.08% of their full scale ranges. The absolute pressure transducers, Omega PX409 series sensors, had a range of 0 kPa to 344 kPa resulting in an absolute uncertainty of $\pm$0.275 kPa. The differential transducers had a range that went up to 207 kPa resulting in an absolute uncertainty of $\pm$0.166 kPa. The most accurate transducers were the six gauge pressure transducers in the nozzle, with a range of 103 kPa and a corresponding uncertainty of $\pm$0.083 kPa. Not shown in Figure 3.26 is the barometric pressure transducer with a nominal uncertainty of $\pm$1.5%. These values are summarized in Table 3.4.

Table 3.4: Summary of pressure transducer accuracy

Transducers	Range [kPa]	Device Uncertainty [kPa]
$P_{ga,H}$	103	0.083
P_{baro}	115	1.7
P_{diff}	207	0.166
$P_{abs,H1}$, $P_{diff,abs,low}$, P_{res}	344	0.275

Thermocouples

The thermocouples used in this experiment were either Type-T (copper/constantan), or Type-E (nickel-chromium/constantan) thermocouples. They were calibrated using an automated water bath that ramped the liquid temperature between 10°C and 70°C, in increments of 5°C, raising and lowering the temperature between this range twice, before fitting calibration curves for each thermocouple. The water bath temperature was monitored using a liquid thermometer to verify accuracy of the calibration. Every thermocouple not in contact with the liquid had Arctic Silver AS5 thermal paste applied to decrease its contact resistance. Every thermocouple in the loop was insulated to mitigate axial conduction.

Heaters

The heat rate in the ITO film, q_H, was calculated from measurement of the ITO film resistance, R_{ITO}, and the current passing through a 0.1 Ω, 1% accuracy, shunt resistor, i_{shunt} according to Ohm's Law shown in Equation 3.14.

$$q_H = i_{shunt}^2 R_{ITO} \tag{3.14}$$

The NI USB-6008 DAQs, with a working range of ±1 V, measured the voltage across each shunt resistor. For example, a measured shunt voltage of 0.05 V, gives a calculated shunt current of 0.5 ±0.016 A, showing that the NI USB-6008 DAQs had sufficient resolution to resolve the current passing through the shunt resistors. The resistance of each ITO heater was measured before and after each experiment using a Agilent 34401A Multimeter. The resistance of each ITO heater was approximately 60 Ω; at this range, the multimeter uncertainty was ±0.01 Ω. Figure 3.28 shows the circuit used to calculate q_H. The shunt current, i_{ITO} was equal to the current through the heater i_H. The resistance between points A and B (R_{AB}) in Figure 3.28, with the supply voltage, $V_{sup} = 0$ V, was used as the resistance of the ITO heater. This assumption was justified by measuring $R_{AB} < 0.1$ Ω with the glass replaced with an aluminum plate, which shorted the spring pins; in this arrangement, R_{AB} represented the resistance due to wires, solder joints between the wire and the aluminum housing, connection between the aluminum housing and the gold spring pins, and ultimately the contact resistance between the gold spring pins and the aluminum. This agreed with the 20 mΩ (max) rated contact resistance of the gold spring pins. For a measured shunt voltage of 0.05 V and nominal $R_{ITO} = 60$ Ω, the calculated ITO power, (q_H), is 15 ±1 W. The uncertainty in the shunt voltage measurement was responsible for

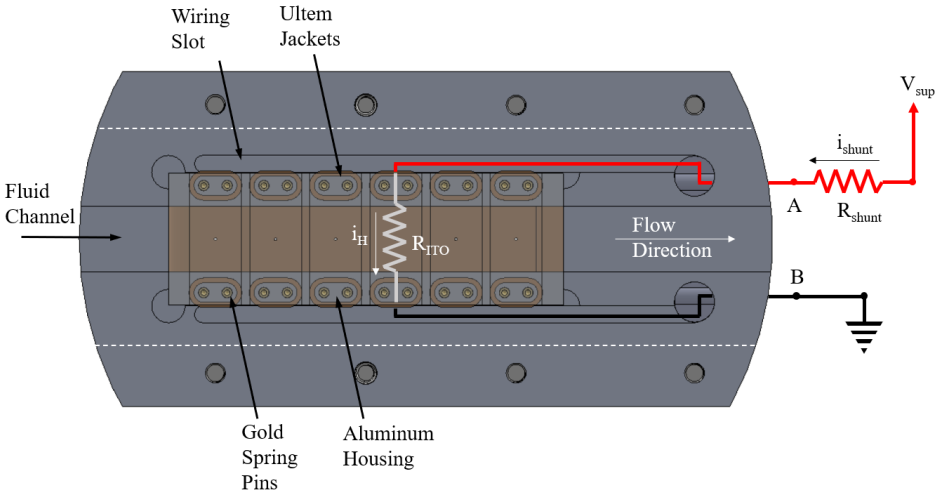

Figure 3.28: Circuit used to measure heat rate in ITO film. The measured resistance from A to B was used as an estimate of R_{ITO} when $V_{sup} = 0$ V.

90% of the uncertainty in q_H[9].

The temperature coefficient of resistance for the ITO was 2×10^{-4} per °C [41]. This implies that for a nominal $R_{ITO} = 60\ \Omega$, an 80°C increase in temperature would increase R_{ITO} by 1 Ω. Recalculating the uncertainty in q_H for $\delta R_{ITO} = \pm 1\ \Omega$ results in $\delta q_H = \pm 1$ W; this is identical to the previous case, showing that the accuracy of measuring R_{ITO} was not critical in estimating q_H.

Table 3.5 summarizes the device uncertainties.

Table 3.5: Device uncertainty specifics

					Uncertainty	
Type	Type	Model	Range	Units	Relative	Absolute
Pressure (gauge)	Omega	MMG015V5P3C0T4A5	0 - 103	kPa	0.08%	0.083
Pressure (abs.)	Omega	PX409-050A5V	0 - 344	kPa	0.08%	0.275
Pressure (diff.)	Omega	PX409-030DWU5V	0 - 207	kPa	0.08%	0.166
Pressure (baro.)	Apogee Inst.	SB-100	15 - 115	kPa	1.5%	
Flow Rate	Micro Motion Elite	CMFS040M	0 - 5*	L/min		0.02
Density	Micro Motion Elite	CMFS040M	100 - 3000*	kg/m^3		0.5
Temperature	Thermocouple	Type-T	10 - 80*	°C		0.5

*This range brackets the calibrated range of the device, not the device's absolute range

[9]This uncertainty could be improved by either decreasing the resistance and increasing the accuracy of the shunt resistor, or increasing the accuracy of the DAQ used to measure the voltage drop across the shunt resistor.

Temperature at Heater Surface

Knowing the temperature at the liquid-glass interface was important for characterizing the boiling process and comparing results with existing literature. Previously the heat generated at the ITO was calculated, but there was no analysis of how much of that heat was delivered to the fluid rather than being lost to the surroundings. A 1D thermal model was developed to estimate the wall temperature and is shown in Figure 3.29. The heat flux at the ITO, q''_H, had two paths for dissipation: forced convecting to the liquid, q''_{fc}, or conducting through the glass, q''_{gl}, and then transferred to the ambient environment through natural convection q''_{nc}. An additional source term, q''_{LED} was added to account for the thermal energy radiated from the LED assembly.

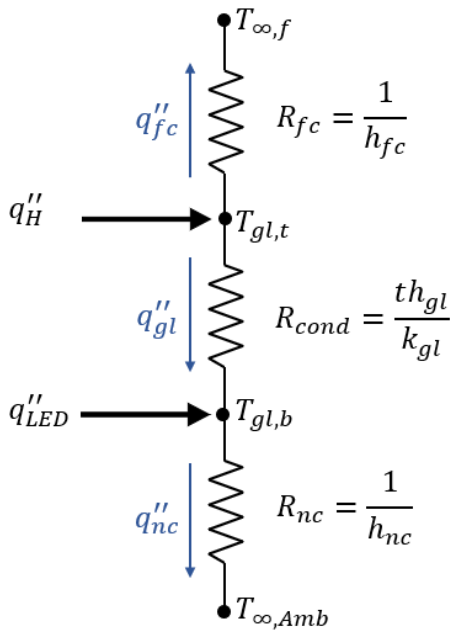

Figure 3.29: 1D Resistance network for heat transfer through glass.

The heat transfer coefficient for forced convection through a rectangular duct was calculated using the DuctFlow_N correlation in EES [42], which fit data from Kakaç et al. [43] to correlate the laminar flow Nusselt number in a duct, and used the Gnielinski [44]

correlation for the turbulent flow Nusselt number in a pipe. Laminar flow was defined as flow with $Re_{d_h} < 2300$, while turbulent flow was define as flow with $Re_{d_h} > 3000$. The Nusselt was interpolated for transitional flow defined as $2300 < Re_{d_h} < 3000$. The Nusselt number provided by these correlations was based on d_h as shown in Equation 3.15, where k_f is the thermal conductivity of the liquid and h_{fc} is the heat transfer coefficient due to forced convection.

$$Nu_{d_h} = \frac{h_{fc} d_h}{k_f} \tag{3.15}$$

Conduction through the glass was modeled using soda-lime glass with a nominal thermal conductivity, $k_{gl} = 0.937$ W/m-K and thickness, $th_{gl} = 1.1$ mm. From these values, the conduction resistance, R_{cond}, was calculated to be 0.0012 K-m^2/W.

Natural convection was initially modeled using Equation 3.16, from Raithby and Hollands [45], to find the heat transfer coefficient, h_{nc}, where the characteristic length (L_{char}) was defined as the ratio of the glass surface area to its perimeter,

$$\frac{\overline{h_{nc}} L_{char}}{k_f} = \frac{2.5}{\ln\left\{1 + \frac{2.5}{0.527 Ra_{L_{char}}^{0.20}}\left[1 + \left(\frac{1.9}{Pr}\right)^{0.9}\right]^{2/9}\right\}} \tag{3.16}$$

and the Rayleigh number was defined by Equation 3.17;

$$Ra_L = \frac{g L^3 \beta (T_s - T_\infty)}{\nu \alpha} \tag{3.17}$$

however, the Rayleigh number for this flow was lower than the range applicable to Equation 3.16 for surface temperatures as high as 60°C, whereupon $h_{nc} = 10.5$ W/m^{2}K. A conservative estimate of $h_{nc} = 15$ W/m^{2}K was made until it was more finely tuned in the LED model.

An experiment was conducted to measure the effects of q''_{LED} by measuring $T_{gl,bot}$ with

the LEDs on and off, at the known flow conditions shown in Table 3.6. The channel height was equal to the entrance length channel height of 6.35 mm. This well-defined geometry meant that a good estimate of R_{fc} could be made. Additionally, the properties of the glass window were well known and varied little with temperature, meaning that R_{gl} was accurately estimated. The only variable to be tuned in the 1D model was R_{nc}, assuming there was little conduction from the glass to the aluminum of the test section.

Table 3.6: 1D Model inputs for q''_{LED} trials

Flow Geometry			Fluid Parameters			Glass Parameters		
h_{ch}	6.35	mm	Fluid	R123		$L_{gl,nc}$	66.7	mm
w_{ch}	12.4	mm	Q_{lpm}	0.56	L/min	$w_{gl,nc}$	16.7	mm
			Re_{d_h}	3100		th_{gl}	1.1	mm
			Pr	0.70		k_{gl}	0.937	W/m-K

The temperature of the outside surface (bottom) of the glass window $T_{gl,bot}$ was measured using a 0.5 mm diameter, bare thermocouple that was placed on the outside of the glass window, using a thin layer of thermal paste to decrease contact resistance. Figure 3.30 shows the results of the 1D analysis after tuning the values for q''_{LED} and h_{nc}. Figure 3.30(a) shows the change in glass temperature (bottom surface) resulting from turning on the LEDs at different fluid temperatures, in addition to the values predicted by the 1D model. The 'LED Off' points in Figure 3.30(b) were used to iterate h_{nc} until the predicted $T_{gl,bot}$ equaled the measured $T_{gl,bot}$; this occurred when $h_{nc} = 20$ W/m^{2}K. This is higher than the value predicted using Equation 3.16 indicating that the natural convection was likely aided by circulation from the LED fans. The 'LED On' points in Figure 3.30(b) were then tuned by changing q''_{LED} until the predicted $T_{gl,bot}$ equaled the measured $T_{gl,bot}$; this occurred when $q''_{LED} = 200$ W/m^2. The tuned 1D model is shown in Figure 3.31. A Biot number ($Bi_{gl,th}$) comparing conduction through the thickness of the glass to natural

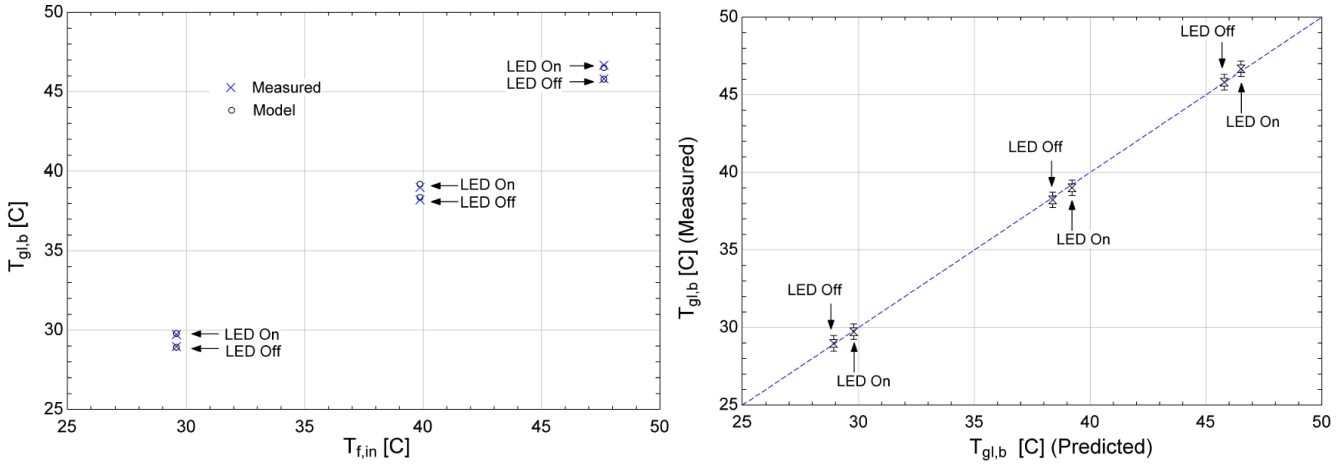

(a) (b)

Figure 3.30: Results of 1D model showing (a) the effects of turning the LEDs on at different fluid inlet temperatures, and (b) the ability of the 1D model to predict experimental results.

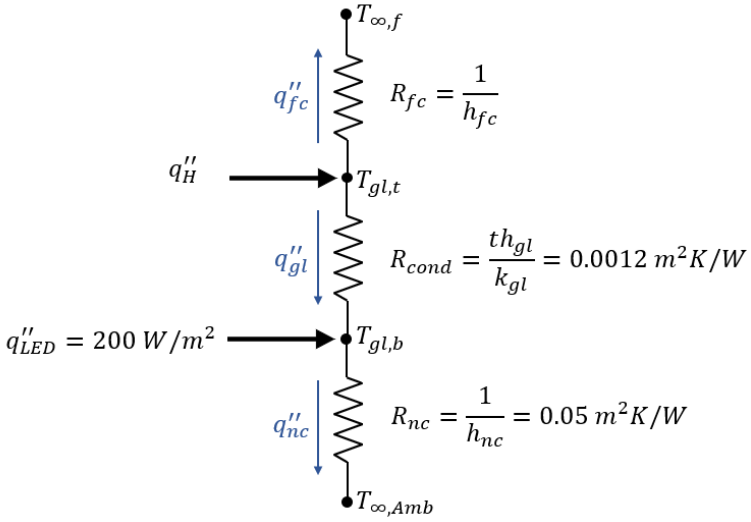

Figure 3.31: 1D Resistance network after tuning q''_{LED} and h_{nc}.

convection was calculated as shown in Equation 3.18, based on the values in Figure 3.31.

$$Bi_{gl,th} = \frac{R_{cond}}{R_{nc}} = \frac{0.0012\ \text{m}^2\text{K/W}}{0.05\ \text{m}^2\text{K/W}} = 0.02\ [\text{-}] \tag{3.18}$$

Because $Bi_{gl} << 1$, the glass window was assumed to be isothermal through the thickness of the glass.

3.7 Flow Loop Operation

Prior to experimentation, the system was degassed to bring the system pressure as close as possible to the partial pressures predicted by the fluid data sheet. To degas the fluid, the reservoir temperature was changed until the saturation pressure of the pure fluid was slightly below atmospheric pressure. Fluid was pumped through both the bypass loop and test section–each flow path being heated to produce a two-phase mixture returning to the reservoir. The pure fluid recondensed in the reservoir leaving the vapor space at the top of the reservoir (and all of the expansion tank) rich with dissolved gas. The top of the expansion tank was then vented, which released the accumulating dissolved gasses, thereby decreasing the system pressure. This process continued, gradually increasing the reservoir temperature, ending when the saturation pressure of the fluid was equal to both the fluid data sheet and atmospheric pressure. Typical starting conditions for a newly filled flow loop were partial pressures between 10 kPa and 40 kPa above the pure fluid saturation pressure. Ending conditions often resulted in reservoir pressures less than 1 kPa above the pure fluid saturation pressure.

Occasionally the system needed to be cooled to 15°C and held for ten minutes before returning the system to test conditions; this process took approximately an hour. This cycling was required any time the system had been idle for more than a couple hours, or if pressure oscillations were evident in the test section. It was hypothesized that the cooling cycle condensed any vapor trapped in the pump, leading to smooth operation thereafter.

Recording a full set of data required performing two experiments. An example full set

of data is shown in Table 3.7. The first experiment (Test #5 in Table 3.7) recorded video at each heater for different electrical powers while the glass thermocouple was located at heater 6; in this case T_{gl} is measuring the outlet fluid temperature. The second experiment (Test #6 in Table 3.7). recorded the videos at the same test conditions as experiment 1, except with T_{gl} being measured in the middle of the active heater. Each full set of data (two experiments) was conducted for a given fluid, nozzle height (determined by th_{shim}), $dPdx$, Q_{lpm}, and $T_{f,in}$. The data sets could be combined to form a full data set.

Table 3.7: Example of manually recorded data for a full data set.

12/17/2019	H	V_H [V]	A_H [A]	Vid. #	File
	2	36	0.621	62	5_2_36_1
Test #5	2	40	0.690	63	5_2_40_1
	2	38	0.655	64	5_2_38_1
	2	42	0.725	65	5_2_42_1
	2	34	0.586	66	5_2_34_1
	3	40	0.688	67	5_3_40_1
	3	34	0.585	68	5_3_34_1
	3	38	0.654	69	5_3_38_1
	3	42	0.723	70	5_3_42_1
	3	36	0.620	71	5_3_36_1
	4	36	0.632	72	5_4_36_1
	4	34	0.598	73	5_4_34_1
	4	42	0.740	74	5_4_42_1
	4	40	0.704	75	5_4_40_1
	4	38	0.669	76	5_4_38_1

	H	V_H [V]	A_H [A]	Vid. #	File
	2	40	0.690	77	6_2_40_T
Test #6	2	34	0.588	78	6_2_34_T
	2	36	0.622	79	6_2_36_T
	2	42	0.727	80	6_2_42_T
	2	38	0.657	81	6_2_38_T
	3	42	0.723	82	6_3_42_T
	3	38	0.655	83	6_3_38_T
	3	34	0.586	84	6_3_34_T
	3	40	0.689	85	6_3_40_T
	3	36	0.620	86	6_3_36_T
	4	36	0.632	87	6_4_36_T
	4	34	0.599	88	6_4_34_T
	4	42	0.740	89	6_4_42_T
	4	38	0.670	90	6_4_38_T
	4	40	0.706	91	6_4_40_T

Fluid	R245fa	
Nozzle	2	
Shim	0.1524	mm
ΔP	6	kPa
Q_{lpm}	0.73	L/min
$T_{f,in}$	28	C
T_{gl}	H6	

Time:	12:48 AM
H	R_H [Ω]
1	56.0
2	54.7
3	54.6
4	54.4
5	54.6
6	57.6

Each experiment had a standard procedure for start-up and operation for a given test condition:

Start-up

1. Verify that the bypass loop is closed. This allowed the pump to run more slowly, decreasing the chance of vapor entrapment.

2. Set the water bath temperature. This determined the reservoir pressure.

3. With the pump stopped, adjust the nozzle to the appropriate height by adding or removing 0.013 mm thick, stainless steel shims beneath the edge of the nozzle (shown in Figure 3.9).

4. Turn on the pump and set the flow rate to 50% of the test flow rate, while the system reached the desired temperature

5. Measure the electrical resistance for each ITO heater at the beginning and end of each day's experiments.

6. Reconfigure the Agilent 34401A Multimeter as an ammeter to measure the total current delivered from the power supply

7. Adjust the Phantom camera, mirror, and LEDs until the glass is square with the camera and the image is focused and bright in the PCC software.

8. As the water bath temperature increases, adjust the heat flux from the inlet-tubing rope heaters and the test-section silicone heaters so that the inlet and test section temperatures slightly lagged the water bath.

9. When the water bath reached the test point, the rope and silicon heaters were adjusted until the fluid temperature at the inlet to the test section ($T_{f,in}$) was 2°C higher than the reservoir temperature.

10. Steady state operation is reached when the fluid inlet thermocouple nominally equalled the test section surface and base thermocouples ($T_{f,in}$, 3 x $T_{TS,surf}$, 3 x $T_{TS,base}$, see Figure 3.24)

Operation

1. Place the glass thermocouple in the middle of H6
2. Start the main LabVIEW program that continuously records data
3. Move the Phantom camera to focus on the desired heater.
4. Set the power supply to the desired power condition
5. Enable the power supply output
6. When the glass thermocouple reaches steady state, trigger LabVIEW to write additional data to file. This step records 3 seconds of data, sampled at 10 Hz, to a *.tdms file corresponding to the given flow condition. This $*$.tdms file accumulates data for every heat flux, at every heater, for which a video is recorded at a given flow rate, system temperature, back pressure, nozzle height, and fluid.
7. In the 3 seconds it took LabVIEW to record data, the Phantom camera gets triggered to record video at 19,000 frames/second (recording ceases automatically when the camera memory is filled at 30,000 frames)
8. Manually record the power supply current from the Agilent multimeter
9. About 5 seconds after LabVIEW finishes recording data for that video, disable the power supply output.
10. In the PCC software, save 3000 frames of video to a *.cine file

11. Record the video filename and the corresponding incremented video number for that day

12. Return to Step 3 until the first set of experiments is complete

13. Stop the main LabVIEW program.

The operation steps were then repeated for the second experiment where the glass thermocouple was placed at the center of each active heater in Step 3.

The system was shut down by setting the water bath temperature to room temperature and turning the pump off when the system pressure reached atmospheric pressure. As the fluids cooled down they became more dense and could pull a vacuum. The pressure transducers measuring gauge pressure at each heater were not designed for negative pressure. With the pump off and the flow loop slightly below atmospheric pressure, the expansion tank was minimally vented to allow air into the expansion tank thereby preventing excessive vacuum.

3.8 Experimental Trials

The constant variables used for each experiment are shown in Table 3.8, where ΔP is the pressure change along the nozzle, and P_{bp} is the additional back pressure caused by metering the needle valve immediately downstream of the test section. The nozzle could be raised by a maximum of 0.15 mm without removing liquid from the flow loop, as the nozzle could be loosened enough to insert shims without fluid leakage. The maximum pressure difference across the nozzle was limited by the full scale range of the pressure transducers in the nozzle (i.e., 103.4 kPa); the static pressure measured at each heater was a function of the reservoir temperature, which determined $P_{res,sat}$, the nozzle height, the flow rate, and the imposed back pressure. The flow rate varied between 0.2 L/min

and 0.86 L/min; these limits were set by uncertainty at low flow rates (shown in Figure 3.27) and by vapor entrapment in the pump at high flow rates. For the remainder of this document, the first column of Table 3.8 will be condensed to *DSn:Hm* when referring to the data corresponding to the n'th row of Table 3.8, and m'th heater.

Table 3.8: Test matrix summarizing constants for all experiments. Two sets of data were recorded for each data set, one with T_{gl} measured at H6, and another with T_{gl} measured at the center of each active heater.

Data Set	**Date**	**Run No.**	**Fluid**	**Shim** mm	ΔP kPa	Q_{lpm} L/min	$T_{f,in}$ C	P_{bp} kPa
1	12/16/20	1_*	R245fa	0	-6	0.44	23	0
2		3_*		0	-12	0.7	23	0
3		5_*		0	-6	0.49	28	0
4	12/17/20	1_*		0.15	-6	0.67	23	0
5		3_*		0.15	-6	0.69	23	25
6		5_*		0.15	-6	0.73	28	0
7	01/04/20	1_*	HFE7000	0.15	-6	0.67	39	0
8		3_*		0.15	-9	0.86	40	0
9		5_*		0.15	-6	0.69	40	25
10	01/06/20	2_*		0.15	-6	0.74	50	0
11		3_*		0	-6	0.435	40	0
12	01/07/20	3_*	R123	0	-6	0.39	30	0
13	01/08/20	1_*		0	-13.6	0.59	30	0
14	01/11/20	2_*		0	-12	0.54	30	0
15		3_*		0	-3	0.2	30	0
16	01/12/20	2_*		0.076	-9.3	0.58	30	0
17	01/13/20	1_*		0.076	-3.7	0.3	30	0
18		4_*		0.076	-14	0.785	30	0

The results of these experiments are discussed in the following chapter. The data set number in Table 3.8 will be used to refer to specific experimental runs; for example, DS12 refers to the experimental runs conducted on 01/07/2020.

Chapter 4

Experimental Results

A range of heat fluxes was applied to different heaters (see Table 3.8; this was also shown in Table 3.7 as an applied voltage). The lowest heat flux approximately corresponded to the onset of nucleate boiling (point A in Figure 4.1), and was increased until bubble generation reached the fully developed regime of nucleate boiling (point B in Figure 4.1). This corresponded to an experimental range of heat flux of 9 to 34 W/cm^2 . Heat fluxes

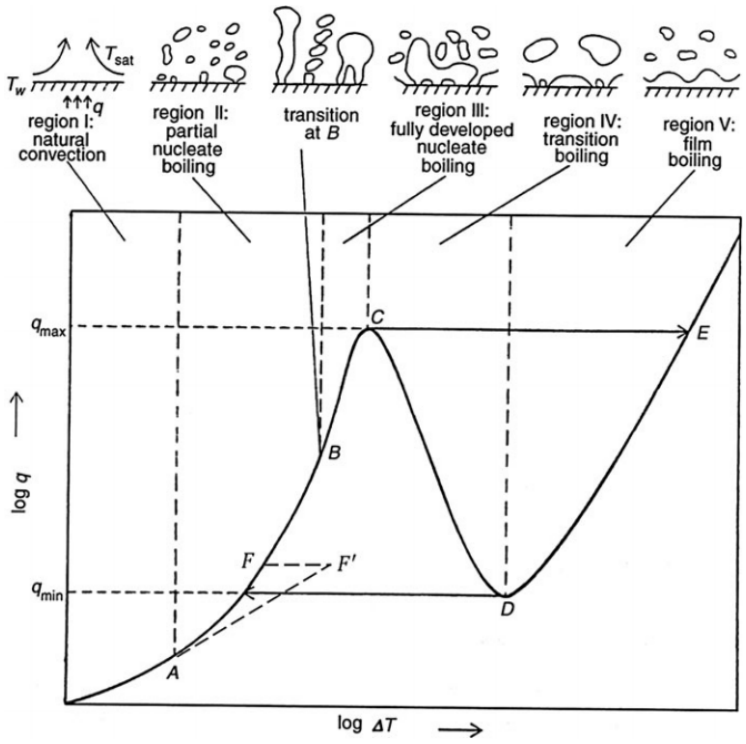

Figure 4.1: Boiling curve reproduced from Dhir [1] depicting the bubble generation characteristics during each flow regime.

below this range caused superheating of the fluid, $\Delta T_w = T_h - T_{sat} > 0$, without bubble nucleation. An example of nucleate boiling at point B in Figure 4.1 can be seen in Figure

4.2. The upper limit of q''_h occurred when the fluid reached the fully developed regime of nucleate boiling; this limit was chosen because the characteristic long streams of bubbles were not described well by a unique nucleation site, or series of nucleation sites.

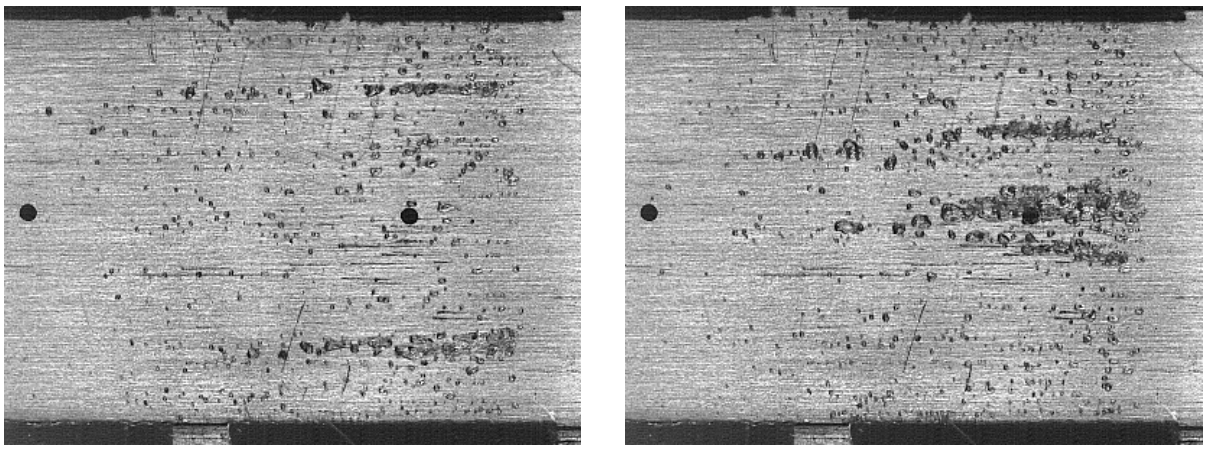

(a) (b)

Figure 4.2: Characteristic images of transitional nucleate that marked the upped edge of heat fluxes of this study. Frame (a) was recorded 26 ms before frame (b).

Density gradients within the flow of R123 could be observed for $h_{ch} = 6.35$ mm, as shown in Figure 4.3[1]. The temporal separation of each frame in Figure 4.3 is 80 ms, with $Q_{lpm} = 0.58$ L/min, $q''_h = 4$ W/cm^2, $Re_{d_h} = 3700$, $T_{f,in} = 30°$C, $T_h = T_{gl,t} = 74°$C, $\Delta T_w = 41°$C. The same behavior was not seen for $h_{ch} = 0.3$ mm.

[1]The background is out of focus in Figure 4.3 as the camera lens was focused on the glass surface, while the background was 6.35 mm beyond the focal plane.

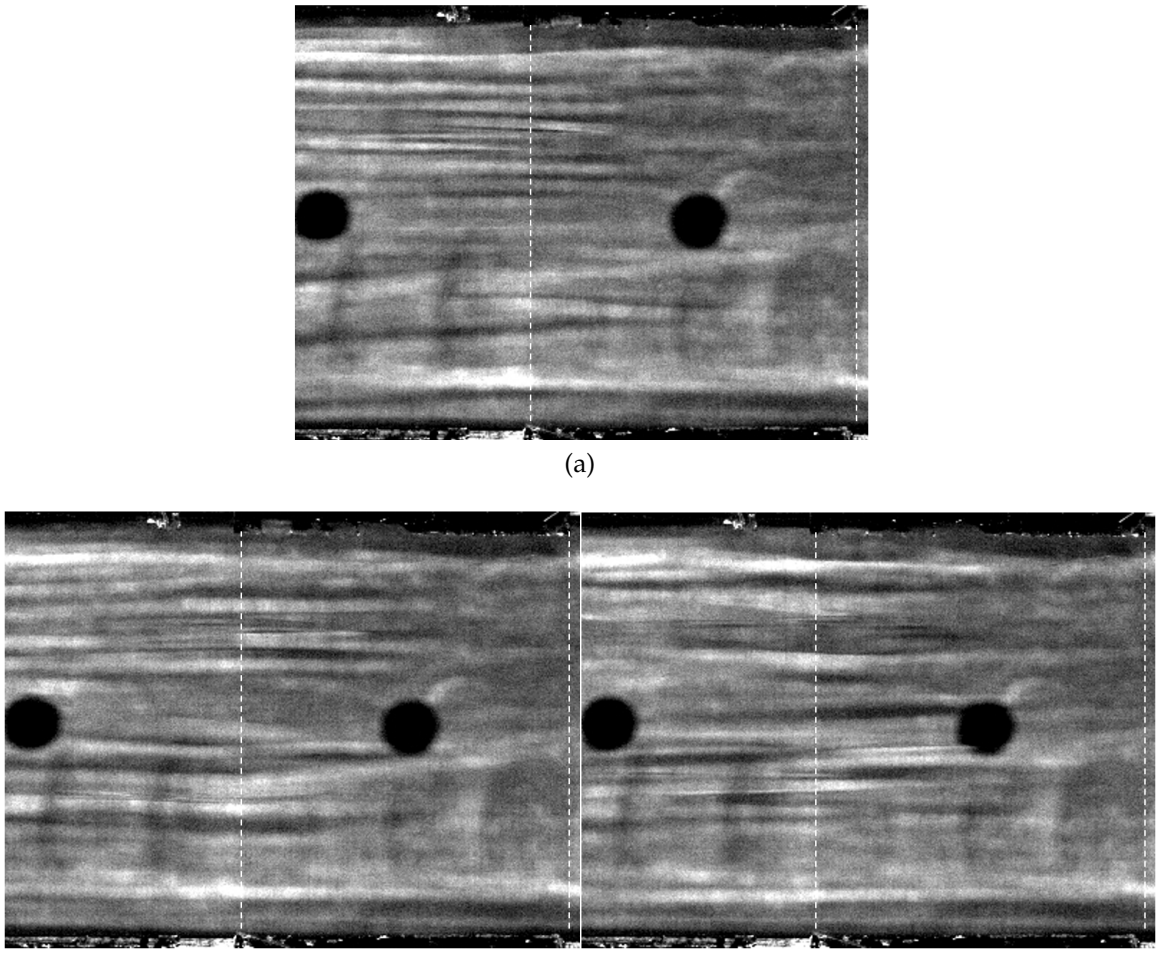

(a)

(b) (c)

Figure 4.3: Density gradients within the fluid. The camera lens was focused on the glass surface, leaving the background out of focus, since h_{ch} was 6.35 mm. Each frame (a), (b), (c), is separated by 80 ms

4.1 Flow Loop Behavior

Behavior common to all measurements are described in this section using data from DS2 in Table 3.8. The pressures measured at each heater, during the entirety of DS2 are shown in Figure 4.4. The steep increases of pressure indicate the presence of bubble nucleation; this does not necessarily coincide with the heater being turned on, as single-phase heat transfer resulted in minimal change in fluid pressure. This steep rise in pressure is caused

by the increased friction of the two-phase mixture and also by the acceleration of the fluid due to rapidly expanding bubbles. In the first two minutes of Figure 4.4 there is a gentle rise in pressure present in all $P_{ga,H}$, without a step change; this behavior is characteristic of the absence of bubble nucleation and is the result of heating a subcooled fluid. There

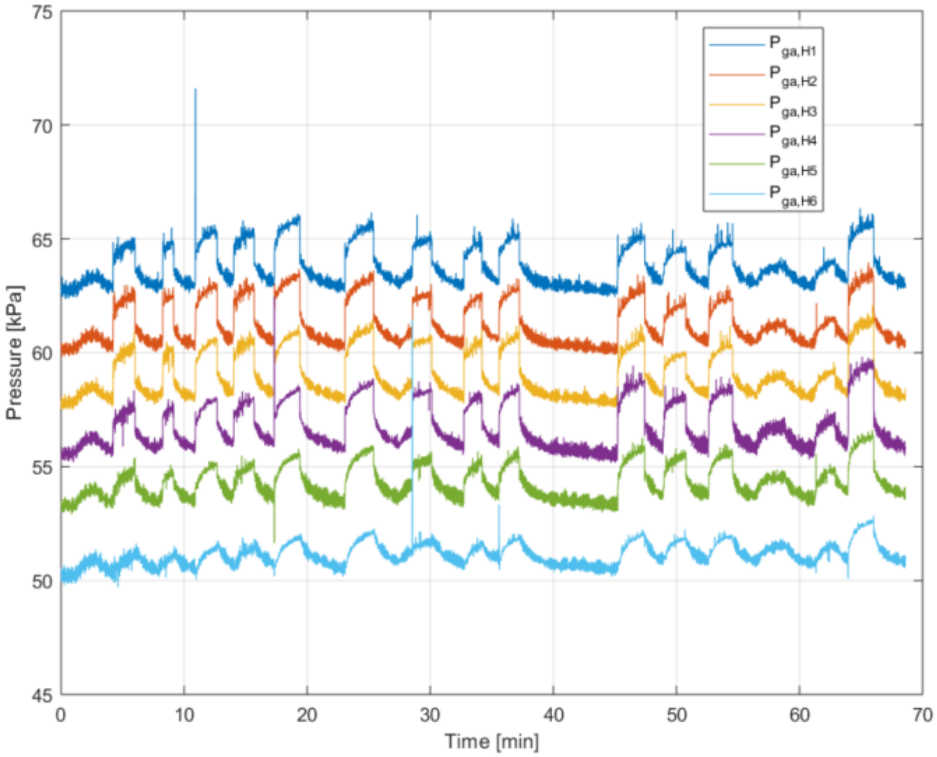

Figure 4.4: DS2 nozzle pressures

are several instances of spikes in pressure (e.g., $P_{ga,H1}$ at $t = 11$ min, $P_{ga,H4}$ at $t = 17$ min, $P_{ga,H6}$ at $t = 28$ min, etc.). These spikes are evidence of explosive boiling, where a large surface of the heater was suddenly covered in bubbles. An example of this behavior can be seen in Figure 4.5 where the flow is moving from right to left as a vapor explosion spans the width of the channel within 2 ms. Eventually the flow returns to either transitional or isolated-bubble nucleate boiling, depending on the magnitude of the applied heat flux.

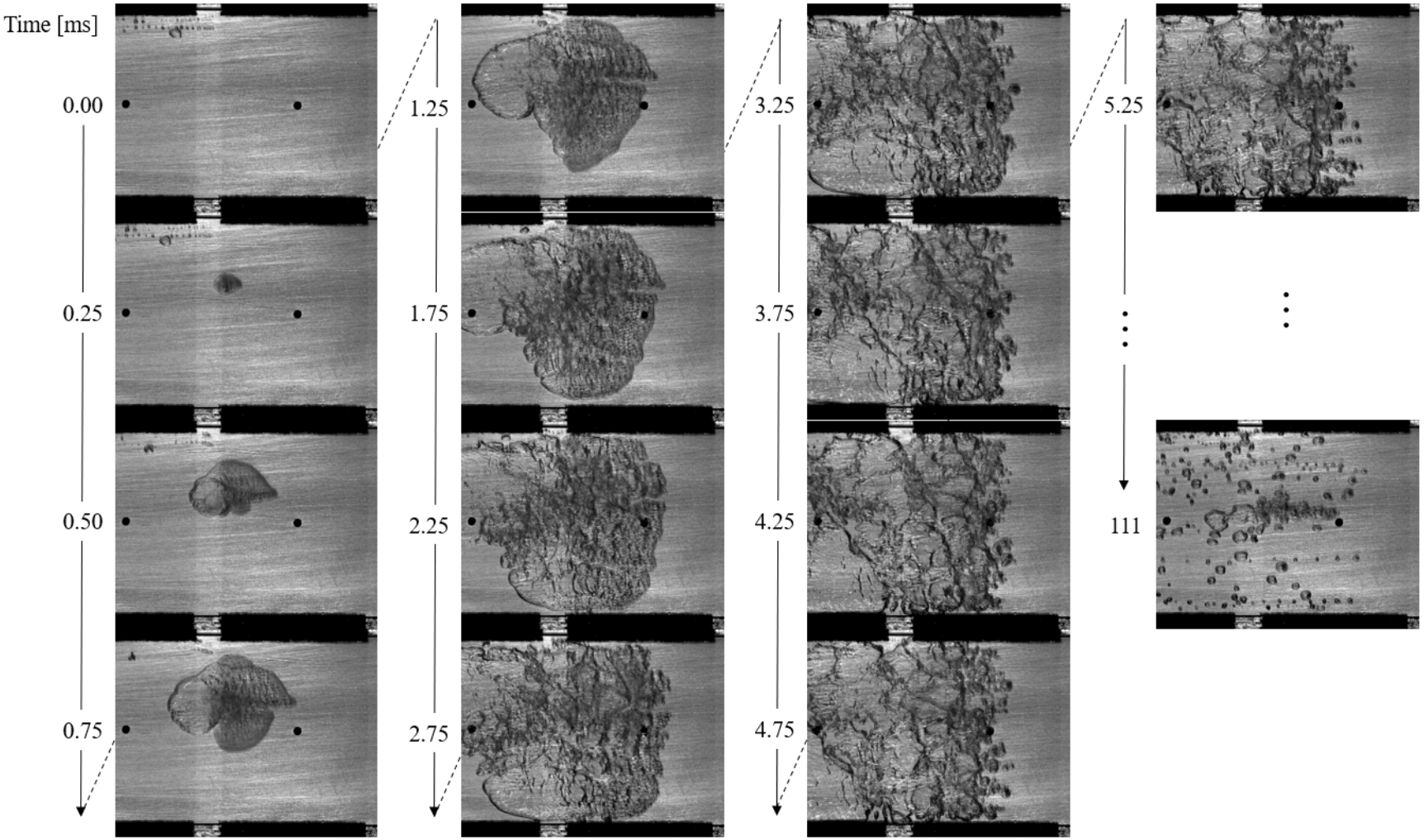

Figure 4.5: Time evolution of explosive boiling with R245fa. Flow moves from right to left

The vertical separation between pressure measurements in Figure 4.4 is indicative of the pressure gradient in the nozzle. The temporal variation in pressure gradient is presented in Figure 4.6, where the steady state pressure gradient without an applied heat flux was approximately -215 Pa/mm. Application of a heat flux, caused bubble nucleation, which affected the pressure profile along the nozzle; it was not practical to manually adjust the flow rate during the experiment in an effort to return the pressure gradient to the pre-heating value. Additionally, changes in flow rate would alter the nucleation behavior, adding a difficult-to-control variable. In general, the linearity of the pressure

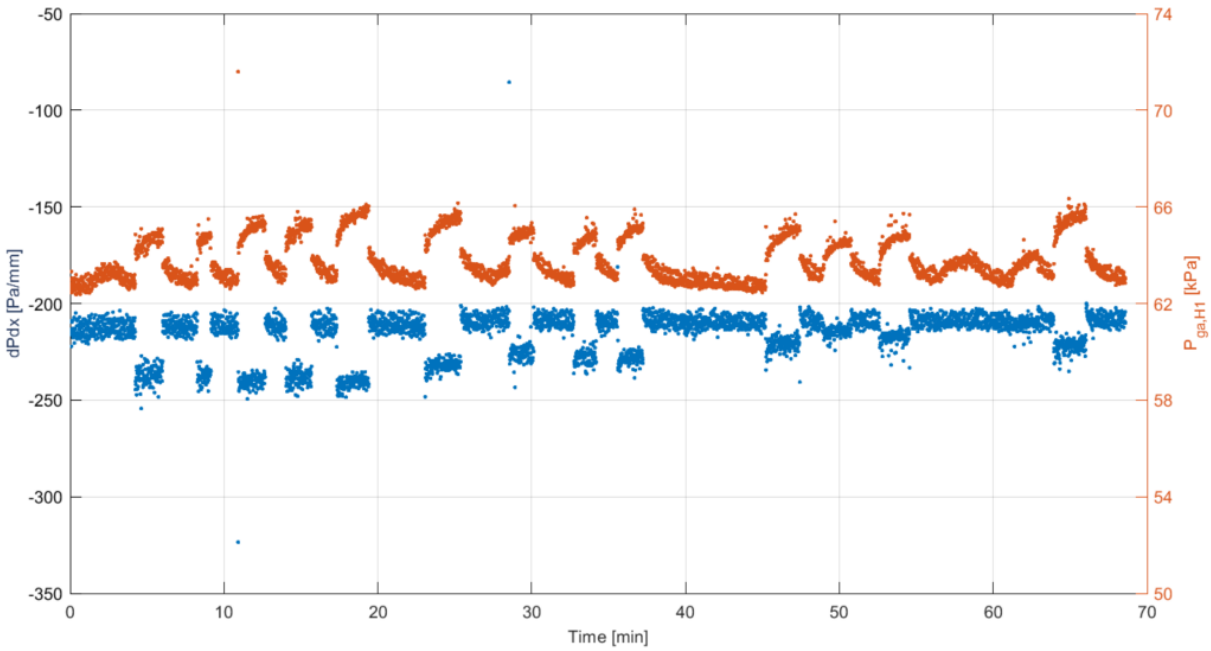

Figure 4.6: DS2 nozzle pressure gradient

gradient was minimally affected by nucleation, as shown in Figure 4.7. It's unclear why the linearity decreased in time.

Figure 4.8 shows that the measured back-pressure, P_{bp} throughout DS2. The average value was predicted well by the single-phase analysis in Figure 3.19. The average, measured back pressure of 10.7$\pm$1.5 kPa includes all pressure drops between $H6$ and the

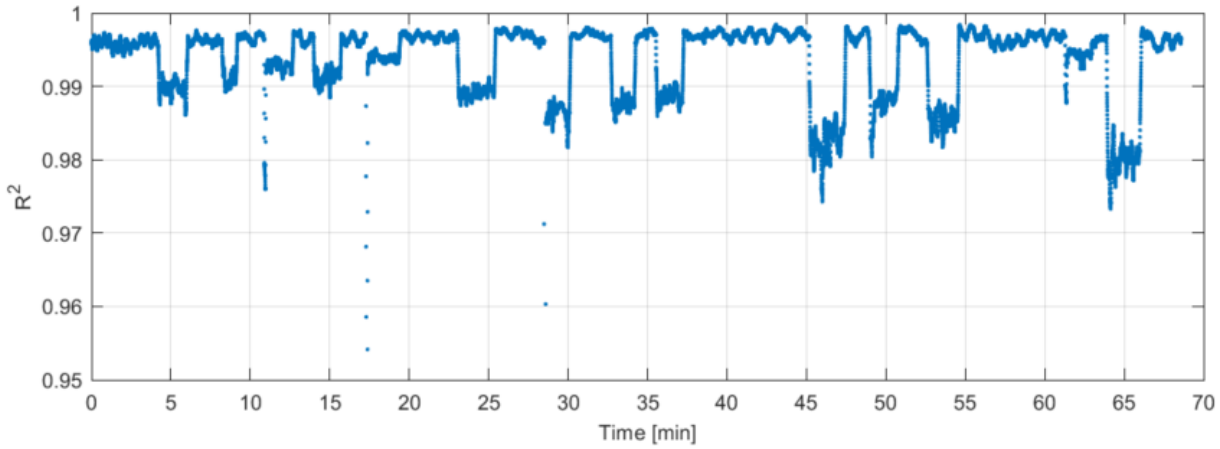

Figure 4.7: DS2 pressure gradient linearity, shown as a moving average of the coefficient of determination, R^2.

reservoir. The predicted back pressure was 8.3 kPa when calculated between *H6* and the outlet of the test section. It is likely that adding pressure drops for the tubing, fittings, and elevation change between the exit of the test section to the reservoir would raise the predicted value to the measured back pressure.

The test section temperature showed minimal variation throughout the experiment, save for the outlet thermocouples, as shown in Figure 4.9, where T_s refers to the thermocouples in contact with the external-top surface of the test section, with the most upstream thermocouple being $T_{s,1}$. Similarly, $T_{al,1}$ refers to the most upstream thermocouple embedded in the base of the test section; see Figure 3.24 for more detail on thermocouple placement. The first four thermocouples, $T_{s,1}$,$T_{al,1}$,$T_{s,2}$, and $T_{al,2}$, were within ± 0.5°C of each other throughout the experiment. The fluid inlet temperature was one degree cooler than the test section; this coincides with the acceptable limit through all experiments. The downstream base and surface thermocouples, gray in Figure 4.9, were monitored to prevent a large temperature difference along the length of the test section. The pause in trials between 38 minutes and 45 minutes in Figure 4.4 allowed for the test section to marginally cool down prior to further tests. The temperature of the aluminum test sec-

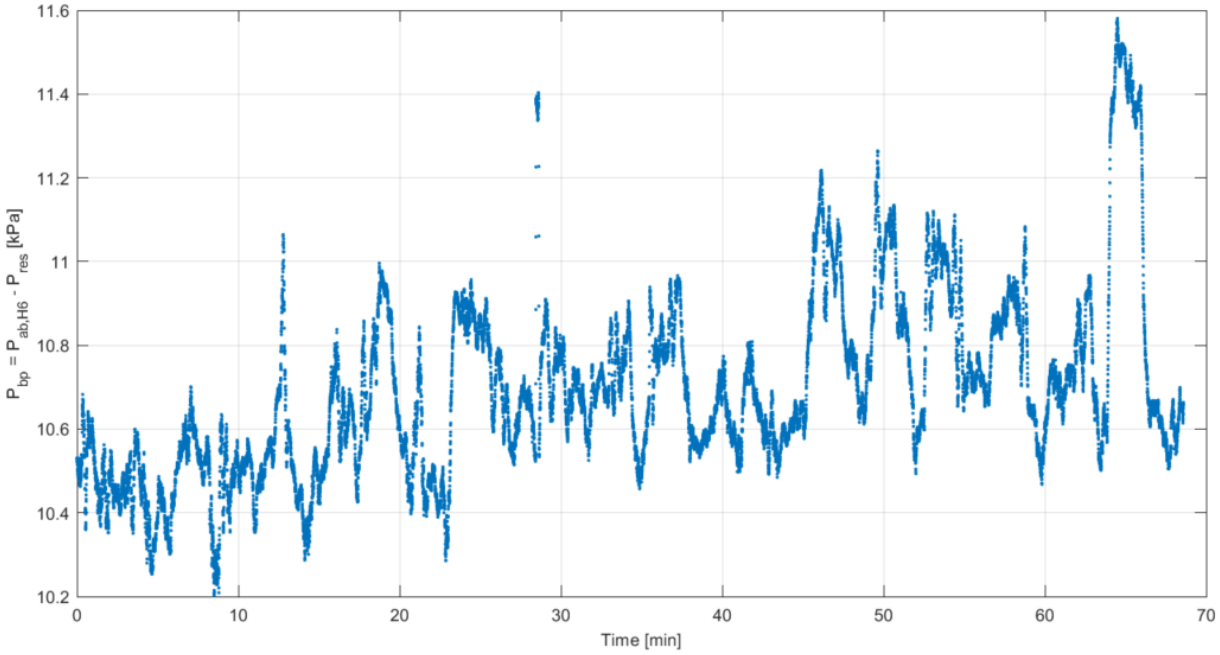

Figure 4.8: DS2 back-pressure

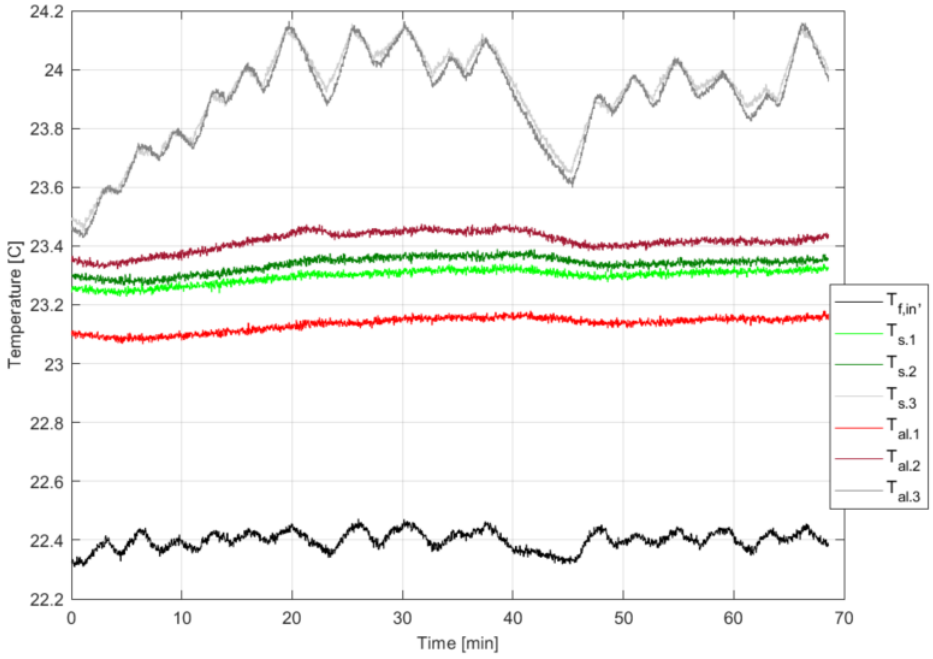

Figure 4.9: DS2 test section temperatures

tion, downstream of the glass, was elevated due conduction from the fluid having been heated by q''_h.

The temporal variation of heater temperature can be seen in Figure 4.10. The reported measurement of T_h is accurate for steady state measurements based on the isothermal assumption previously discussed. Due to the low-speed data acquisition, the measured T_h was unable to resolve the fast transient when the heater was first turned on. The temperature overshoot present in T_h at 8 minutes is characteristic of the sudden nucleation shown in Figure 4.5. Temperature overshoot is a common occurrence when the heated surface is very smooth or when the fluid is highly wetting; common enough that it was indicated as point F' in Figure 4.1. Steady state was decided based on the measurement of T_{gl}; for this data set $T_{gl} = T_h$, however the companion data set used $T_{gl} = T_{H6}$.

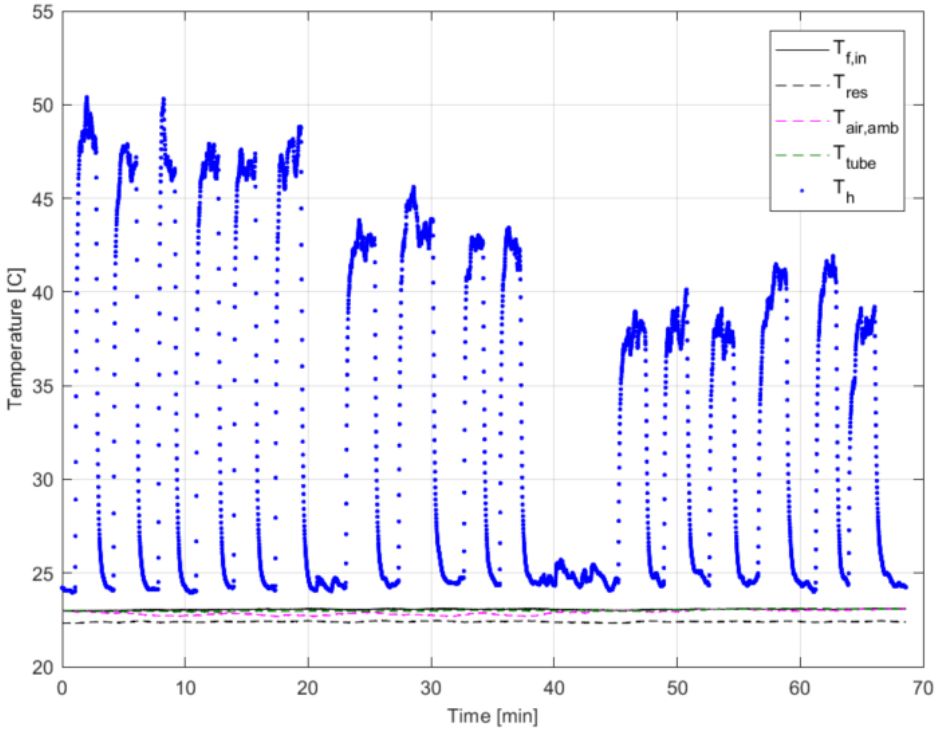

Figure 4.10: DS2 fluid-related temperatures

4.2 Active Nucleation Site Density, N_a''

Generally one would expect the number of bubbles nucleation sites to increase with the applied heat flux and/or surface temperature. Both of these conditions will be evaluated prior to exploring the effects of changing other parameters.

The active nucleation site density, N_a'' was strongly correlated with the applied heat flux, q_h'', as shown in Figure 4.11. R245fa and R123 had similar nucleation behavior, but HFE7000 was different. In all three fluids there appeared to be a threshold heat flux below which nucleation did not occur; this was approximately 10 W/cm^2 for R245fa and R123, and 8 W/cm^2 for HFE7000. The onset of nucleation began relatively gradually for R245fa, and R123, with fewer than 10 nucleation sites in many cases. In contrast,

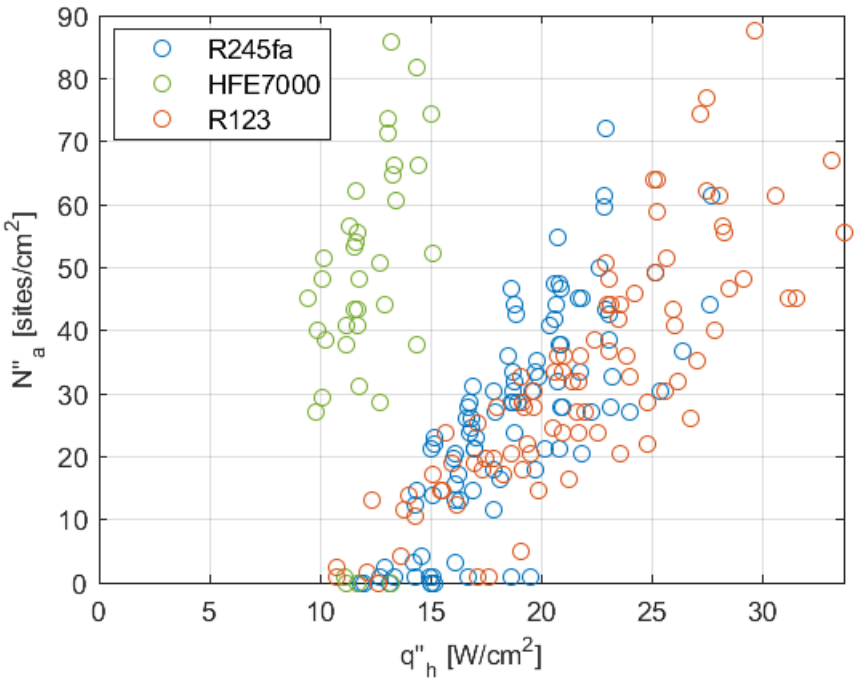

Figure 4.11: Comparison of N_a'' and q_h'' between different fluids, across all experimental data

HFE7000 didn't experience such low quantities of active nucleation sites; for example, the

difference between $N_a'' = 0$ sites/cm^2 and $N_a'' = 52$ sites/cm^2 was an increase in $q_h'' = 1.9$ W/cm^2, or 14%. For cases with bubble nucleation, at low heat fluxes, it took upwards of 30 seconds of surface heating before bubbles appeared; high heat fluxes produced bubbles almost immediately after the heat flux was applied.

Isolating the R123 data in Figure 4.12 shows the strong correlation between N_a'' and q_h'' as well as the tight grouping of data. The same behavior was observed with the other fluids, though not as tightly collapsed as in Figure 4.12; the results for all fluids, split by each heater, can be found in Appendix C, Figure C.1.

The direct correlation N_a'' and $\Delta T_w = T_h - T_{sat}$ is less strong, as shown in Figure 4.13. From Figure 4.11, HFE7000 had the steepest rate of increase in N_a'' with q_h''; Figure 4.13 shows that this was occurring at a relatively low superheat. Figure 4.13 shows an overall lack of correlation when comparing N_a'' data with ΔT_w for all fluids tested. No improvement in correlation was found by looking more specifically at the data for R245fa split between heaters. Figure 4.14 shows that N_a'' decreases as the heater is changed from H2 to H4, but also has a larger spread of ΔT_w. The spreading of N_a'' across a wider range of ΔT_w between H2 and H4 was not seen in both R123 and HFE7000, though a similar decreased in average ΔT_w was observed (see Figure C.2); this decrease corresponds to the expected change in T_{sat} over the range of P_h for each fluid.

The degree of subcooling, $dT_{sub} = T_{h,sat} - T_{f,in}$, was investigated for its impact on N_a'' as shown in Figure 4.15. It is clear that q_h'' has a significant affect on N_a'' due to the color changes in the vertical direction; however, the impact of dT_{sub} is less than initially expected. As the degree of subcooling increased, the lowest values for N_a'' also increased, indicating that the fluid exhibited explosive nucleation and less isolated bubble nucleation. To understand why subcooling had minimal affect on N_a'', it is helpful to consider the heat flux required to bring all of the fluid to saturation, $q_{1ph,sat}''$; this was calculated according to Equation 4.1, where $\dot{m} = Q_{m3s}\rho_l$ and all properties were calculated at the

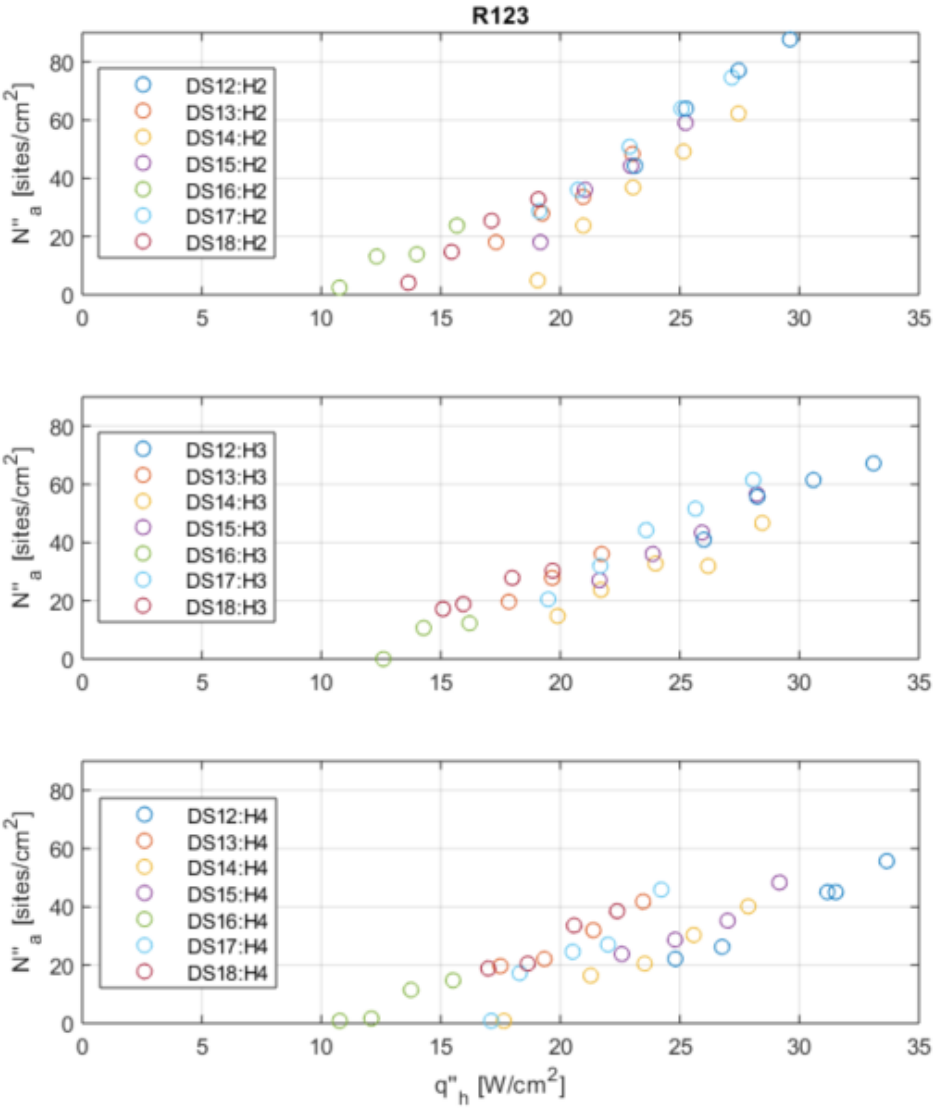

Figure 4.12: Comparison of N_a'' and q_h'' for R123, split between H2, H3, H4

inlet temperature, $T_{f,in}$.

$$q''_{1ph,sat} = \frac{\dot{m}c_p}{A_h}\left(T_{h,sat} - T_{f,in}\right) \tag{4.1}$$

For the R123 data, as an example, Figure 4.16 shows the heat flux required to raise the temperature of the fluid to saturation[2]. Comparing the predicted heat flux in Figure 4.16 with experimental heat flux in Figure 4.15 it is clear the bulk of the fluid is not being

[2]The corresponding figure with all three fluids is shown in Figure C.5

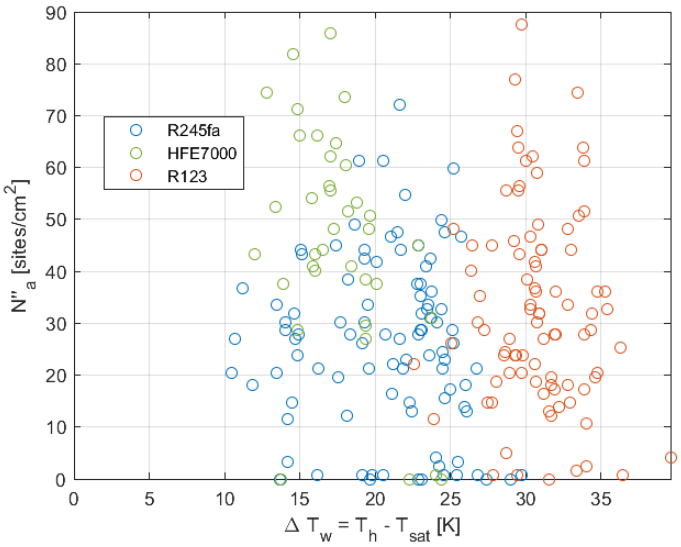

Figure 4.13: Comparison of N_a'' and ΔT_w between different fluids, across all experimental data

heated to saturation as the applied heat flux is significantly less than that shown in Figure 4.16. As the degree of subcooling increases, the amount of single-phase heat transfer required to heat the bulk fluid linearly increases; these values are significantly higher than those seen in Figure 4.15. This suggests the presence of a boundary layer below which the bulk fluid is being heated to saturation.

One might expect the single-phase heat transfer coefficient to increase with an increase in flow rate, decreasing the surface temperature, and thereby causing a decrease in bubble nucleation. Six data sets are compared in Figure 4.17 and no significant dependence on the volumetric flow rate is observed.

In turbulent flow, the shape of the duct does not significantly affect the heat transfer coefficient [46]; therefore, the Nusselt number correlation by Gnielinski [44], for turbulent flow in pipes, can be used to find the single-phase heat transfer coefficient for forced

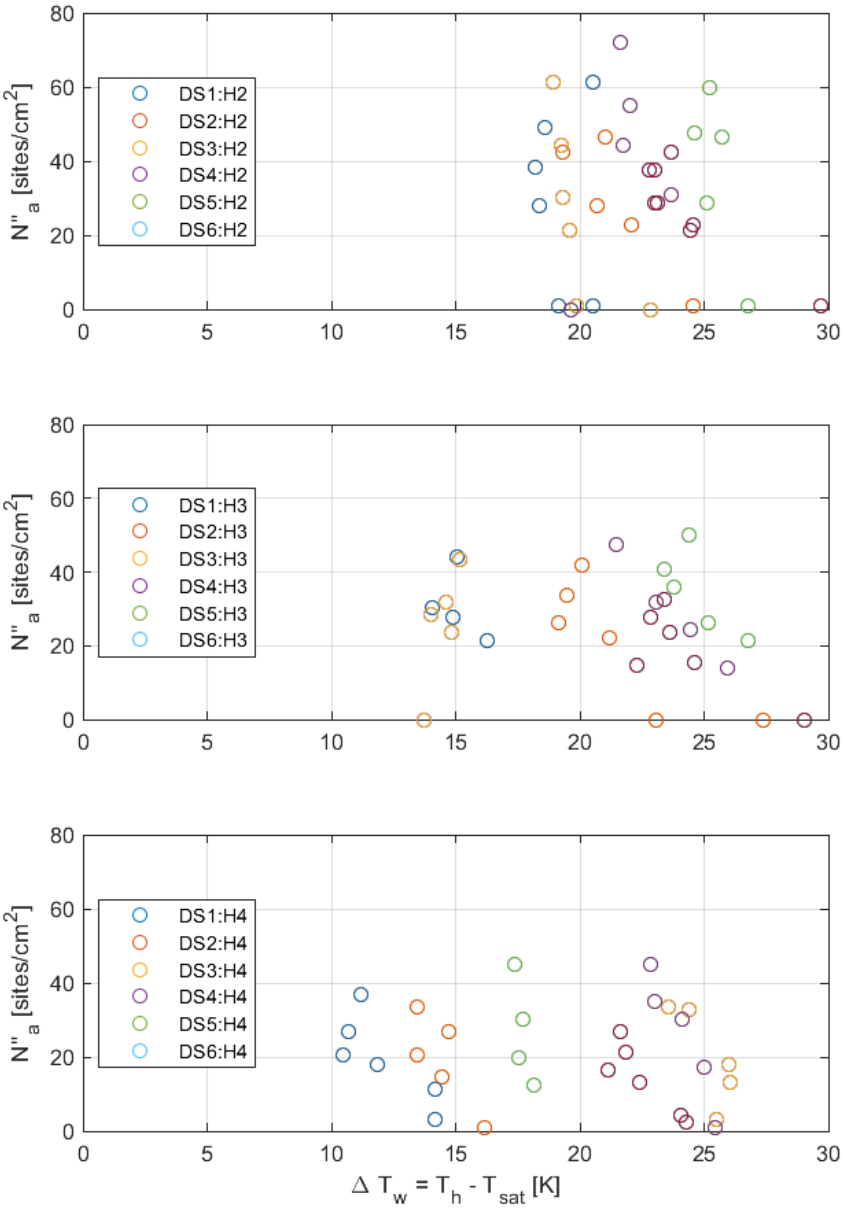

Figure 4.14: Comparison of N_a'' and ΔT_w for R245fa, split between (a) H2, (b) H3, and (c) H4

convection, h_{fc}, in a duct,

$$Nu_{d_h,fd} = \frac{h_{fc} d_h}{k_f} = \frac{(\frac{f_{fd}}{8})(Re_{d_h} - 1000)Pr)}{1 + 12.7(Pr^{2/3} - 1)\sqrt{\frac{f_{fd}}{8}}} \tag{4.2}$$

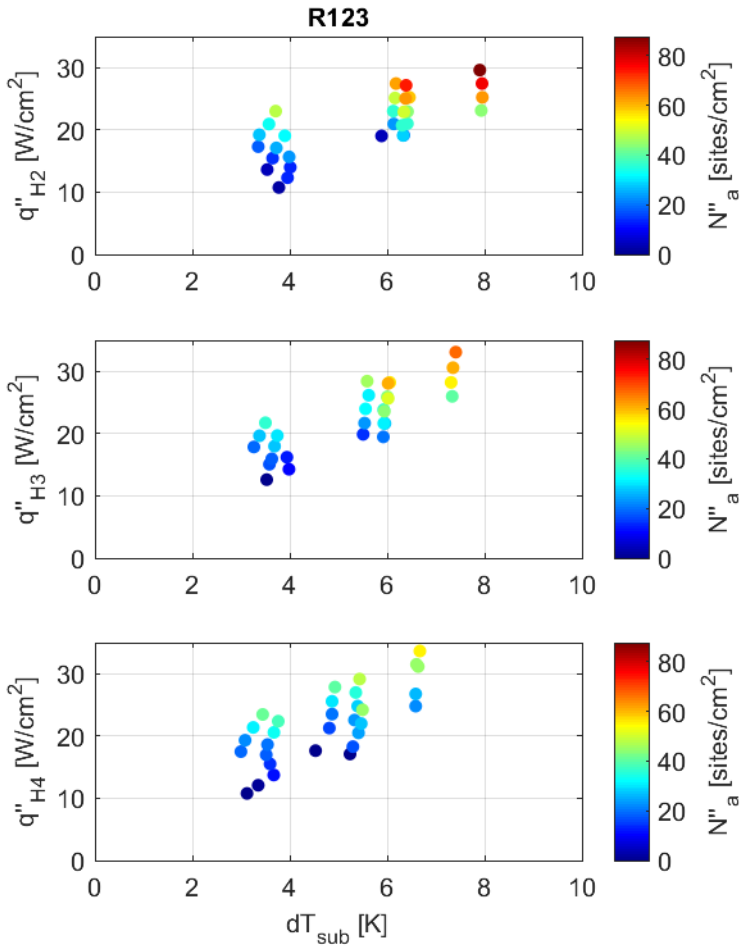

Figure 4.15: Effects of varying $dT_{sub} = T_{h,sat} - T_{f,in}$ on N_a'' for R123

where f_{fd} is the fully developed friction factor. For a smooth rectangular duct, the fully developed friction factor [46] is,

$$f_{fd} = [0.790 \ln(Re_{d_h}) - 1.64]^{-2} \qquad \text{for } 3000 < Re_{d_h} < 5 \times 10^6 \tag{4.3}$$

Assuming the two-phase heat transfer coefficient has a similar form to the single-phase value, this suggests that the Reynolds number might be more appropriate for correlating nucleation phenomena than Q_{lpm}. The results for R123 are shown in Figure 4.18,

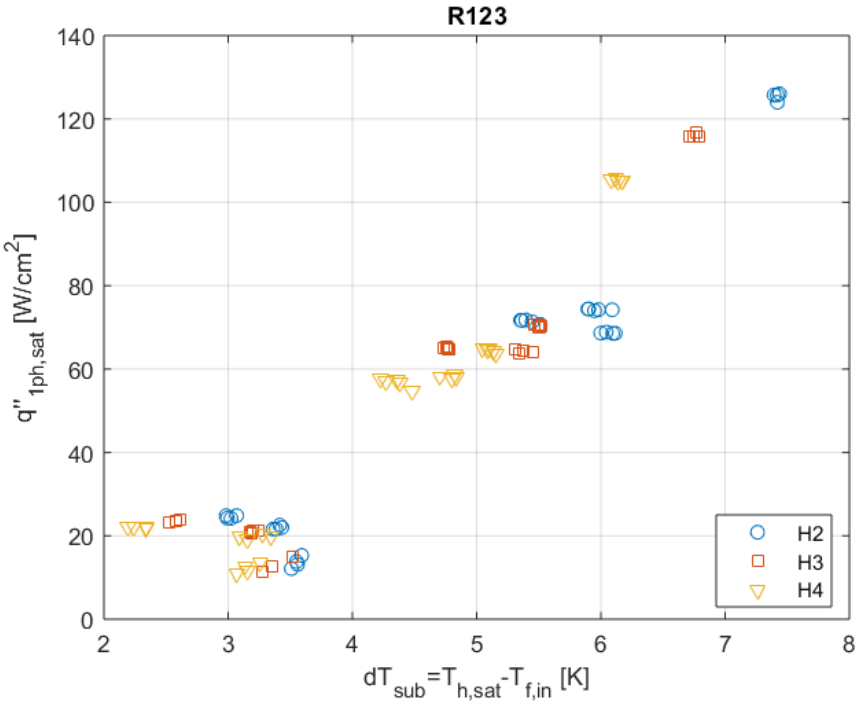

Figure 4.16: Experimental data for single-phase heat flux required to raise bulk fluid temperature to saturation

where Re_{d_h} has been calculated using the inlet temperature and saturation pressure at the center of each heater. It would appear that there is a steeply negative correlation between Re_{d_h} and N_a'', but the independent variable in Figure 4.18 was the heat flux. As the heat flux increased, more bubbles were generated, which increased the local pressure, thereby decreasing the flow rate, which resulted in the lower Reynolds number in Figure 4.18 . Additionally, Figure 4.18 shows that at high Re_{d_h}, the additional heat flux did not significantly decrease the Reynolds number of the flow; the arrows point to data for which sample images are shown in Figure 4.20 to illustrate this point. As Re increased, so too did the minimum q_h'' required to nucleated. Figure 4.19 depicts the heat flux dimension of Figure 4.18 side-by-side with the Reynolds number data . For Reynolds numbers corresponding to laminar flow ($Re_d < 3500$), the data from R123 seems to show similar results. As Re_d becomes turbulent, there begins to be separation of the data. This would seem to

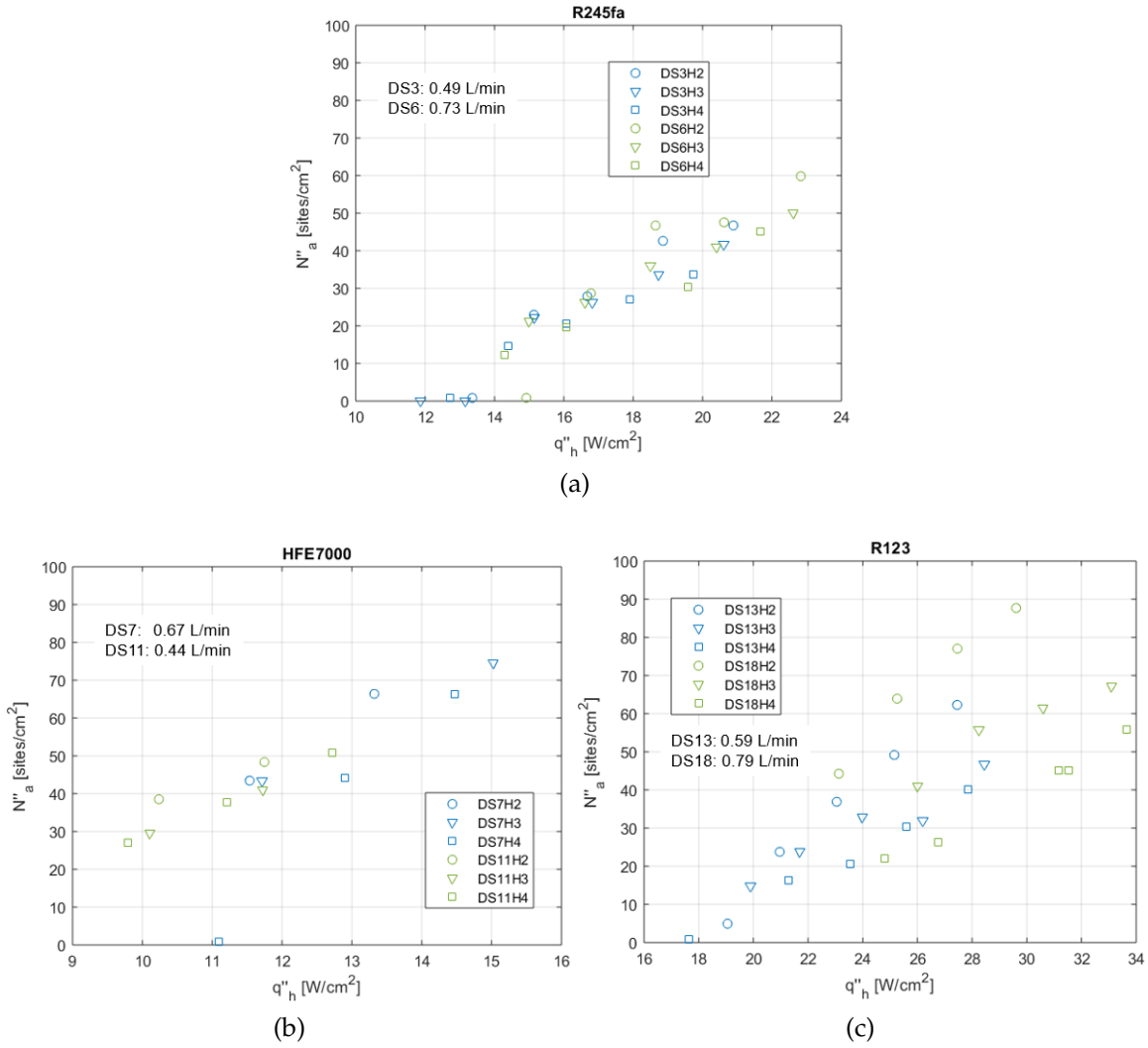

Figure 4.17: Comparison of N_a'' and q_h'' for changes in flow rate (a) R245fa (DS3 & DS6), (b) HFE7000 (DS7 & DS11), and (c) R123 (DS13 & DS18)

reflect a Reynolds number dependence, except that the results for H2, the circles, remains in line with the laminar data. This suggests that the pressure drop between the heaters is responsible for the difference, and not Re_d. R245fa, and HFE7000 did not display the same behavior as R123; these fluids showed no dependence on Re_d across all data sets. A figure of all three fluids can be seen in Figure C.4.

As the Re_{d_h} increased, Figure 4.20 makes it clear that the bubble diameter tended to decrease. This was partly due to bubbles having less residence time on a given nucleation

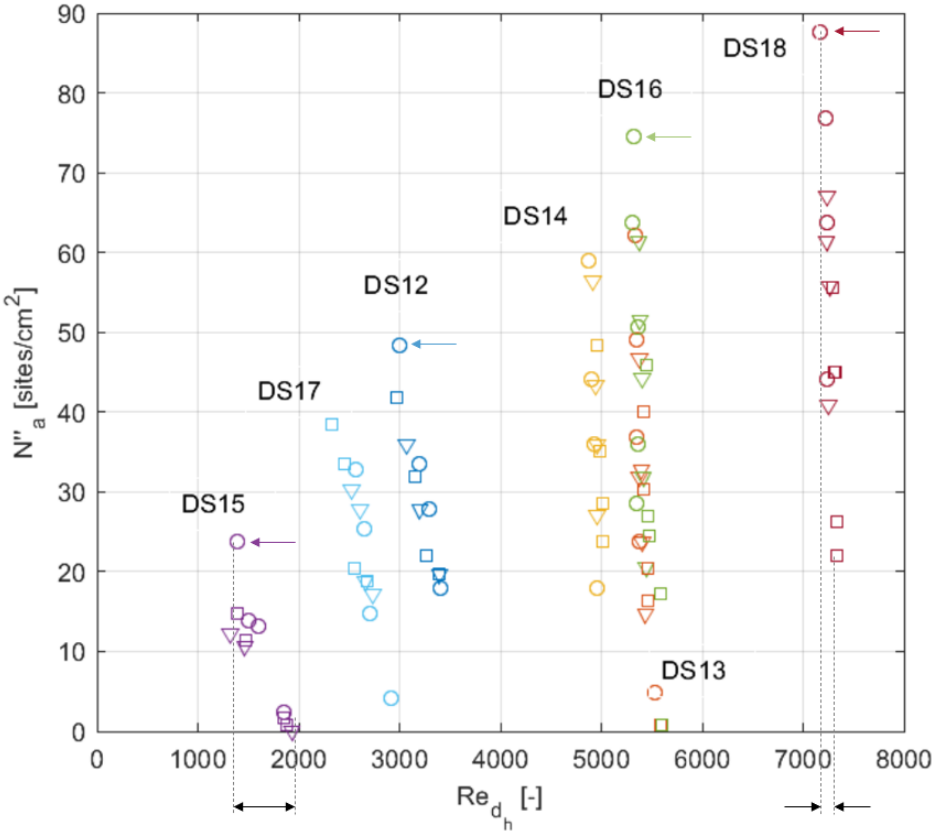

Figure 4.18: Comparison of N_a'' and Re_{d_h} for R123, split among H2 (circles), H3 (triangles), and H4 (squares). Arrows indicate data with snapshots shown in Figure 4.20

site, creating less vapor than at smaller Re_{d_h}, but also because higher Reynolds numbers caused higher local pressure, which decreased bubble diameters. Typically the higher heat flux would cause a bubble to be larger, as more vapor is generated at higher q_h'', but the increased pressure at higher Re_{d_h} overwhelms this effect.

Data from trials DS13 and DS16 had nominally the same Reynolds number (see Figure 4.18). Looking at these data sets more closely, Figure 4.21 shows that for each heater at a given Re_{d_h}, N_a'' and G are inversely related for all q_h''. The same trend can be seen when comparing between heaters; the mass flux increases along the nozzle and is accompanied by a decrease in N_a'' along the nozzle. Looking specifically at DS13, for $q'' = 25$ W/cm^2, a 47% increase in G, resulted in a -34% change in N_a''. DS13 had a pressure gradient of

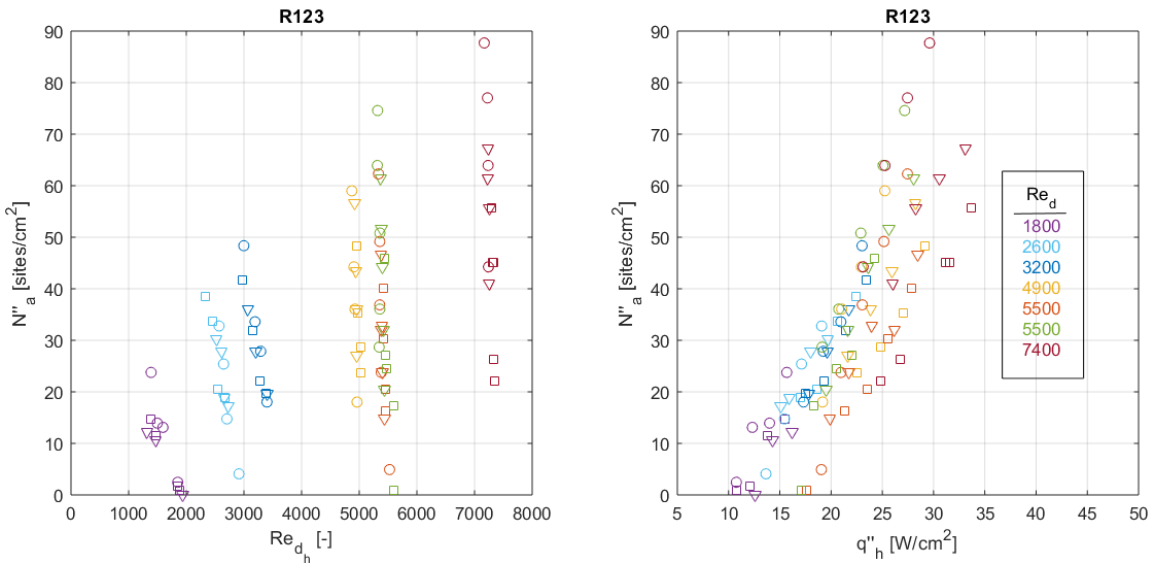

Figure 4.19: Comparison of N_a' and q'' for different Re_{d_h} for R123, split among H2 (circles), H3 (triangles), and H4 (squares). The values and colors of Re_{d_h} correspond to those in Figure 4.18

-238 kPa/m whereas DS16 had a pressure gradient of -163 kPa/m. The percent difference between N_a'' at DS16, relative to the DS13, is positive 10% at a $q_h'' = 27$ W/cm^2, and positive 34% at 21 W/cm^2.

Related to flow rate and Reynolds number is the pressure gradient. Two pressure gradients were used for comparison with N_a'': $dPdx_{heated}$ recorded during the time at which the video was being recorded, and $dPdx_{unheated}$ corresponding to pressure gradient present just prior to the heater being turned on. Figure 4.22 shows the results for R123, based on each pressure gradient; (a) $dPdx_{heated}$ and (b) $dPdx_{unheated}$.[3] Looking along the $q_h'' = 20$ W/cm^2 grid lines in each plot of Figure 4.22, it can be seen that N_a'' increases with decreasing $dPdx$.

[3]Figures for all fluids, based on each definition of $dPdx$ can be found in Figure C.6 and Figure C.7

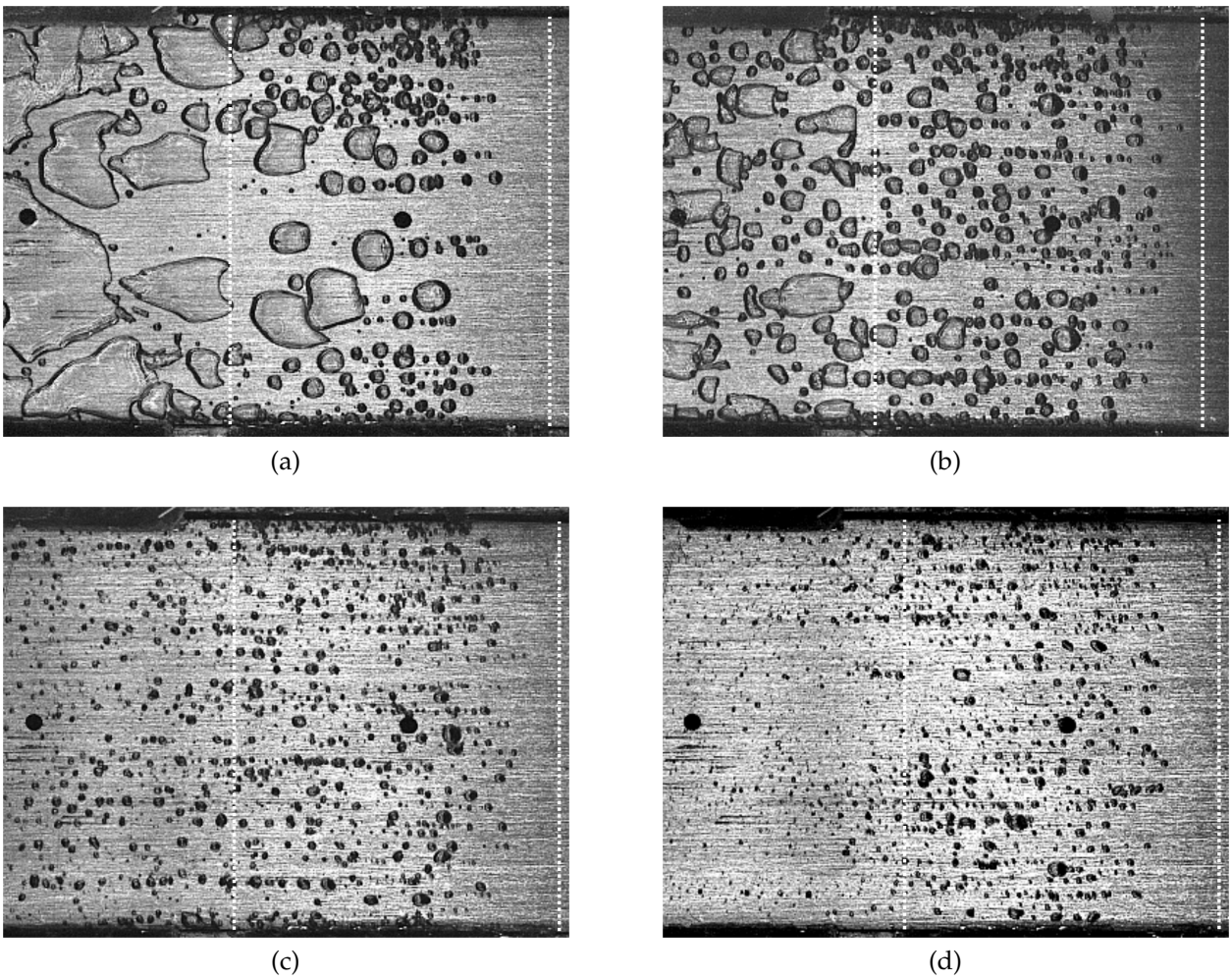

(a) (b)

(c) (d)

Figure 4.20: Comparison of R123 nucleation behavior at (a) $Re_{d_h} = 1390$, $q''_h = 16$ W/cm^2, DS15; (b) $Re_{d_h} = 2998$, $q''_h = 23$ W/cm^2, DS12; (c) $Re_{d_h} = 5319$, $q''_h = 27$ W/cm^2, DS16; and (d) $Re_{d_h} = 7168$, $q''_h = 29$ W/cm^2, DS18. Dashed lines approximate the heater width.

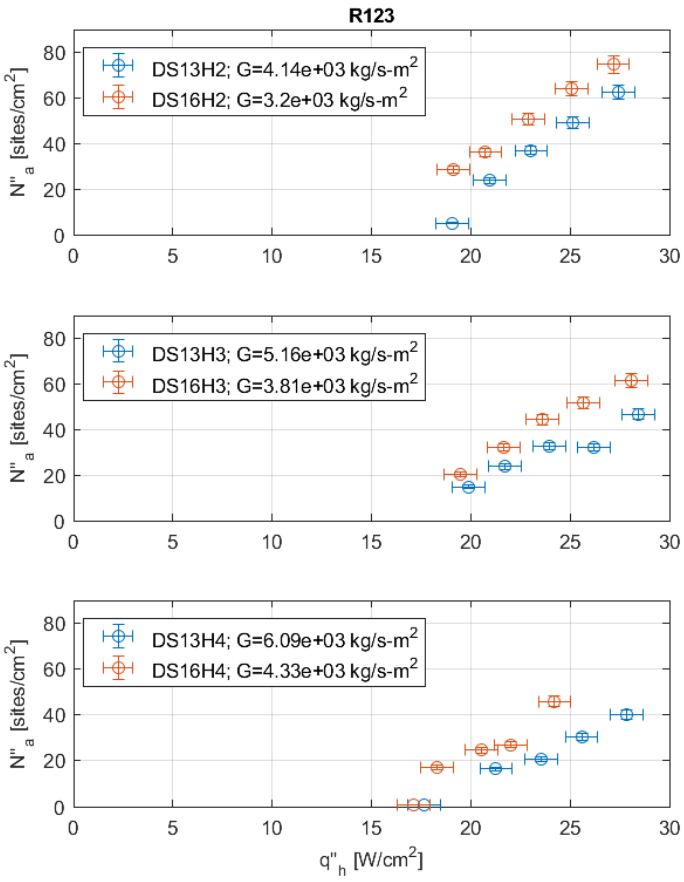

Figure 4.21: Comparison of N_a'' and q_h'' for R123 at nominally the same Re_{d_h}.

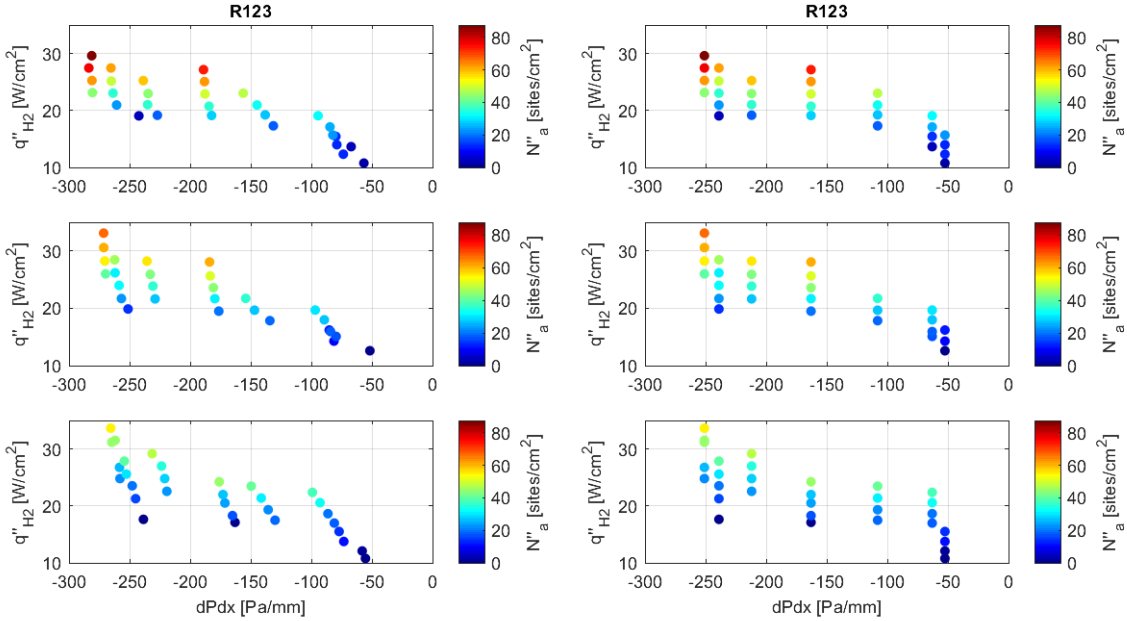

Figure 4.22: Comparison of q_h'' and N_a'' with (a) $dPdx_{vid}$ and (b) $dPdx_{pre,vid}$, for R123, split among H2, H3, and H4.

4.3 Bubble Nucleation Density, N_b''

The density of nucleating bubbles, N_b'', was proportional to the density of active nucleation sites, N_a'', as can be seen in Figure 4.23. The quadratic relationship suggests that nucleation rate at a given site is increasing as the number of active sites increases.

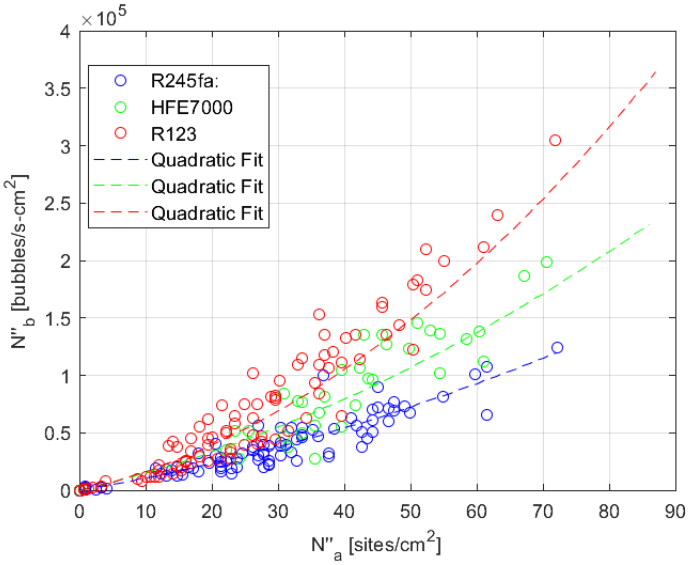

(a)

$N_b'' = a_1 N_a'' + a_2 (N_a'')^2$			
Fluid	a_1	a_2	$\mathbf{R^2}$
R245fa	961	9.78	0.86
HFE7000	1370	15.4	0.85
R123	1304	33.1	0.92

(b)

Figure 4.23: Comparison of (a) N_b'' and N_a'' for all experimental data with (b) associated quadratic regressions

Separating the results between each fluid and each heater, as in Figure 4.24, shows that each heater showed similar performance.

In general, bubbles first began to form at the region of lowest pressure (i.e., the trailing edge of the heater). With additional heat flux, the bubbles began to form further upstream; however, the additional convection of passing bubbles resulted in a lower surface temperature, which deactivated most downstream nucleation sites. this behavior continued until the front of bubbles neared the upstream-edge of the heater; at this point,

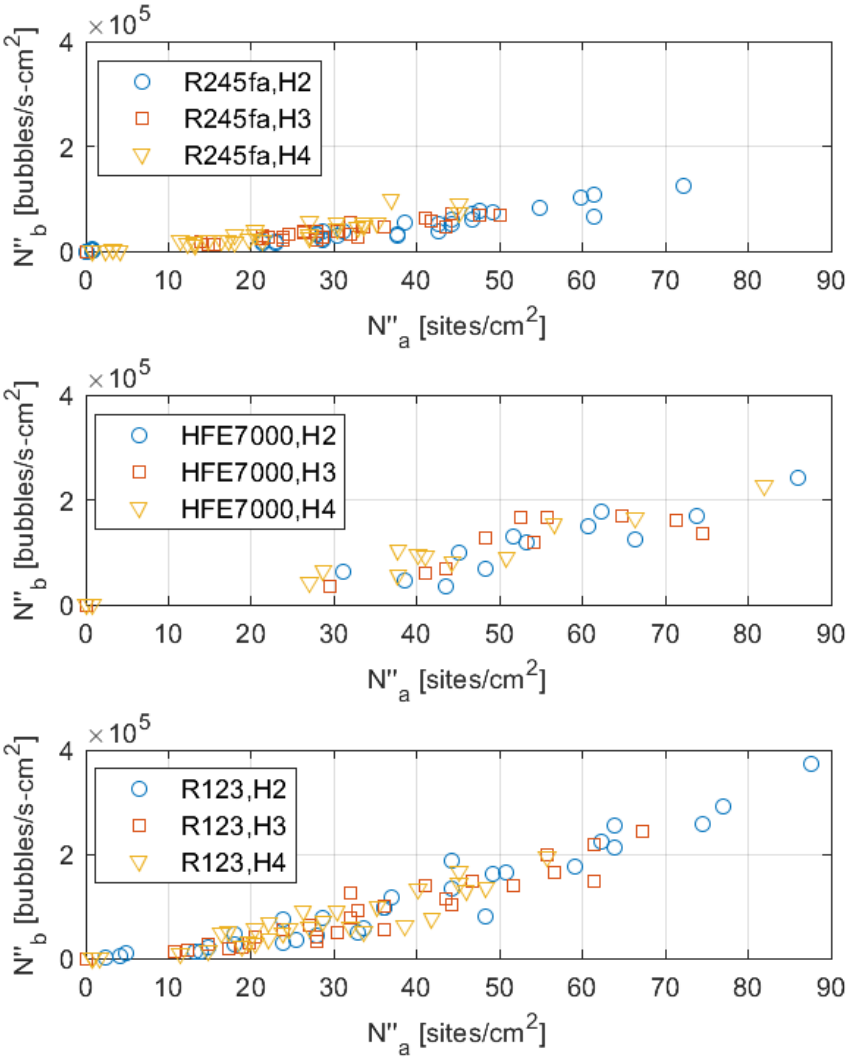

Figure 4.24: Comparison of N_b'' and N_a'', split between heaters and fluids

nucleation sites further downstream began to reactivate.

Chapter 5

Correlation Comparison

Comparing the experimental results with correlations in literature is informative. A summary of literature correlations from Chapter 2 has been repeated here as Table 5.1. The full correlations, with all terms filly defined, are summarized in Appendix D

Table 5.1: Summary of N_a'' correlations

Source	**Functional Form of Correlation**	Eq. No.
Basu et al. [3]	$N_a'' \propto (1-\cos\theta)\Delta T_w^{2.0}$ for $\Delta T_w \leq 15$ K	D.1
	$N_a'' \propto (1-\cos\theta)\Delta T_w^{5.3}$ for $\Delta T_w > 15$ K	
Benjamin and Balakrishnant [4]	$N_a'' \propto \gamma^{-1}[f(R_a P/\sigma)]^{-0.4}\mathrm{Pr}^{1.63}\Delta T_w^3$	D.2
Hibiki and Ishii [5]	$N_a'' \propto \left[1-\exp\left(\frac{-\theta^2}{C_1}\right)\right]\left[\exp\left(C_2\frac{f(\rho^+)\Delta T_w}{T_{sat}}\right)-1\right]$	D.3
Kocamustafaogullari and Ishii [6]	$N_a'' \propto f(\rho^*)\ (\rho^*)^{2.16}\left[\frac{\sigma}{g(\rho_f-\rho_g)}\right]^{1.2}\theta^{2.4}\left[\frac{\Delta T_w}{T_{sat}}\right]^{4.4}$	D.4
Lie and Lin [7]	$N_a'' \propto \left(C_1 + N_{conf}^{0.51}\Delta T_w^{1.67}\right)$	D.5
Ren et al. [8]	$N_a'' \propto \exp\left[-C_1 Ja_{sub}\right]\mathrm{Re}_{d_h}^{-0.93}\Delta T_w^{4.19}$	D.6
Wang and Dhir [9]	$N_a'' \propto (1-\cos\theta)T_{sat}/\Delta T_w$	D.7
Zhokhov [10]	$N_a'' \propto \left(\frac{\Delta T_w}{T_{sat}}\right)^3$	D.8
Aoki [15]	$N_a'' = 2.79\ q''$	D.9
Dhir and Liaw [16]	$N_a'' \propto (q'')^{1.5}$	D.10
Gaertner and Westwater [17]	$N_a'' = 1.48\times10^4 (q'')^{2.13}$	D.11
Hahne and Barthau [18]	$N_a'' = 1.45\times10^3 (q''/Ja)^{3.0}$ for $q'' < 0.5$ W/cm^2	D.12
	$N_a'' = 4.53\times10^2 (q''/Ja)^{1.6}$ for $q'' > 0.5$ W/cm^2	
Kurihara and Myers [19]	$N_a'' = 1.804\times10^{-3}\frac{\mu_f \bar{h}^3}{\rho_g k_f^3}\mathrm{Pr}^{2.67}$	D.13
Luke and Cheng [20]	$N_a'' \propto (q'')^n$ for $1.2 < n < 2.55$	D.14
Mikic and Rohsenow [21]	$N_a'' \propto\ q''$	D.15

Each of the $N_a'' \propto \Delta T_w$ correlations in Table 5.1 were evaluated for all experimental data points and the results are plotted in Figure 5.1. The most apparent difference between the correlations is the 10 order of magnitude variation observed. The correlations by Basu et al. [3], Hibiki and Ishii [5], and Wang and Dhir [9] were developed for water,

while the Kocamustafaogullari and Ishii [6] correlations was developed for a variety of fluids (e.g., water, carbon disulfide, carbon tetrachloride, n-hexane, acetone, and a nickel-salt solution). The Hibiki and Ishii [5] correlation was fit across a wide range of pressures; the data in Figure 5.1 correspond to the atmospheric pressure data.

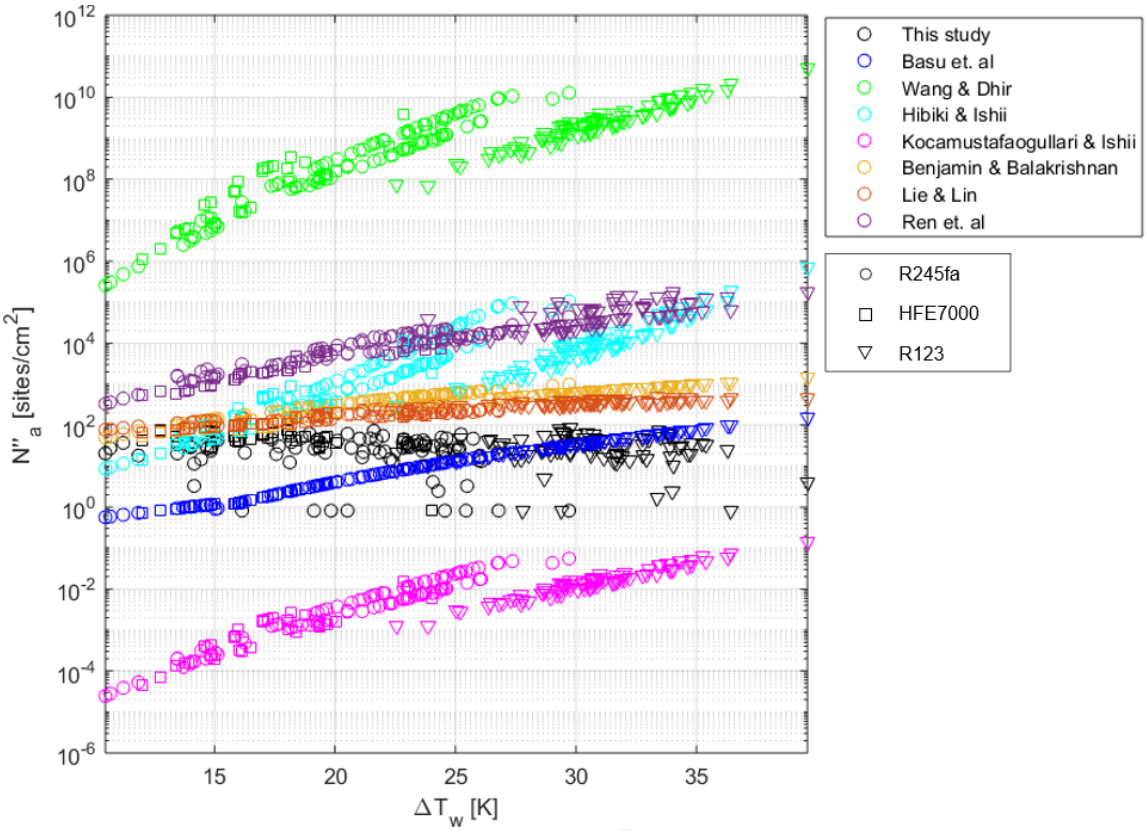

Figure 5.1: Comparison between Table 5.1 correlations for N_a'' and experimental data

Each correlation was used to predict the authors' own data, to verify that the correlations were implemented correctly. Reproducing four figures from these studies (Figure 5.2) shows that the correlations were correctly implemented and suggests that the significant variation between correlations was due to the fact that the fluids used in this study (R245fa, HFE7000, and R123) would give rise to significantly different constants than for the original fluid(s).

The difference in fluid properties between water and the fluids used in this experiment

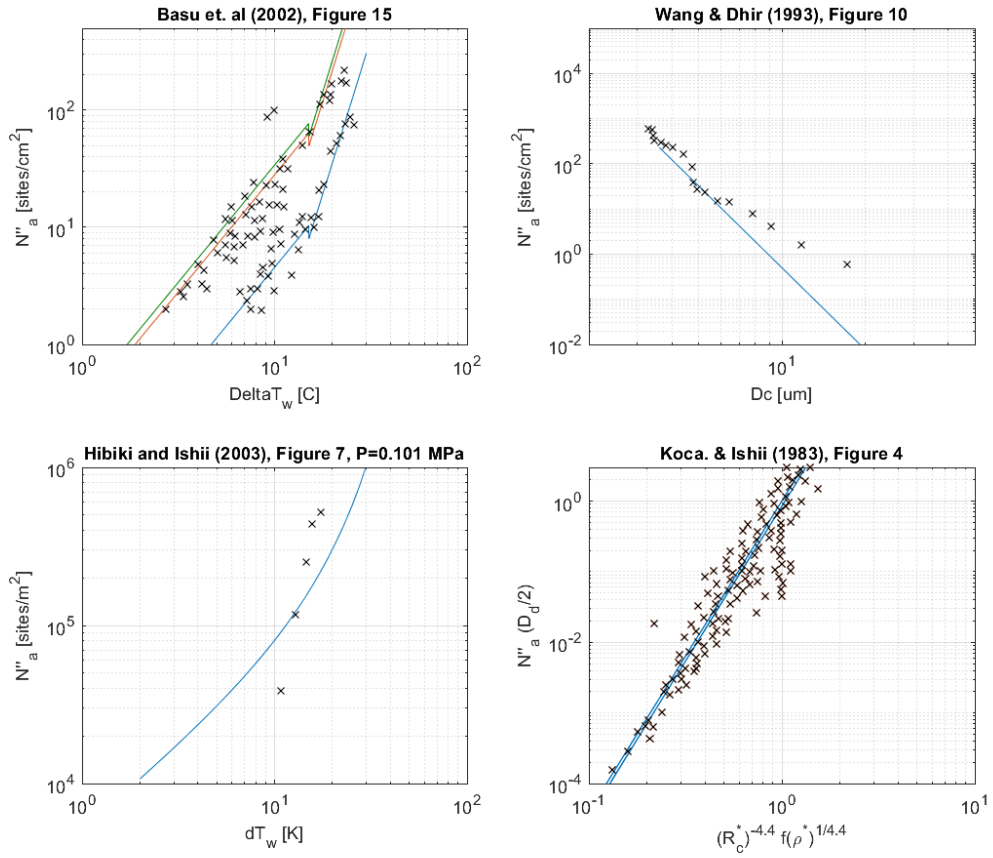

Figure 5.2: Reproduced figures from authors' papers using the N_a'' correlations from Appendix D, to verify correct implementation of each correlation.

can be seen in Table 5.2. The critical radius, R_c, shown in Equation 5.1,

Table 5.2: Fluid property differences within N_a'' correlations.

Fluid	T_{sat} [K]	R_c [μm]	Pr [-]	Re_{d_h} [-]	ρ^* [-]	σ [N/m]	N_{conf} [-]
Water	373	33	1.7	4463	1603	0.059	4.3
R245fa	288	7.4	7.2	3844	228	0.015	1.8
HFE7000	307	6.2	6.6	4775	163	0.011	1.6
R123	301	8.1	5.5	4728	224	0.015	1.7

$$R_c = \frac{2\sigma T_{sat}}{\rho_g h_{fg} \Delta T_s} \tag{5.1}$$

and calculated at $P = 1$ atm and $\Delta T_s = 1$ K in Table 5.2, was an explicit function of temperature. Comparing the critical radius between the fluids is more informative when plotted against the reduced temperature, $T_R = T_{sat}/T_{crit}$, as shown in Figure 5.3. Water and the three test fluids from this experiment have similar trends–the main difference being that water is more further from its critical temperature than the other fluids. The range of reduced temperatures shown in Figure 5.3 correspond to pressures in the range of 1.0 to 1.8 atm.

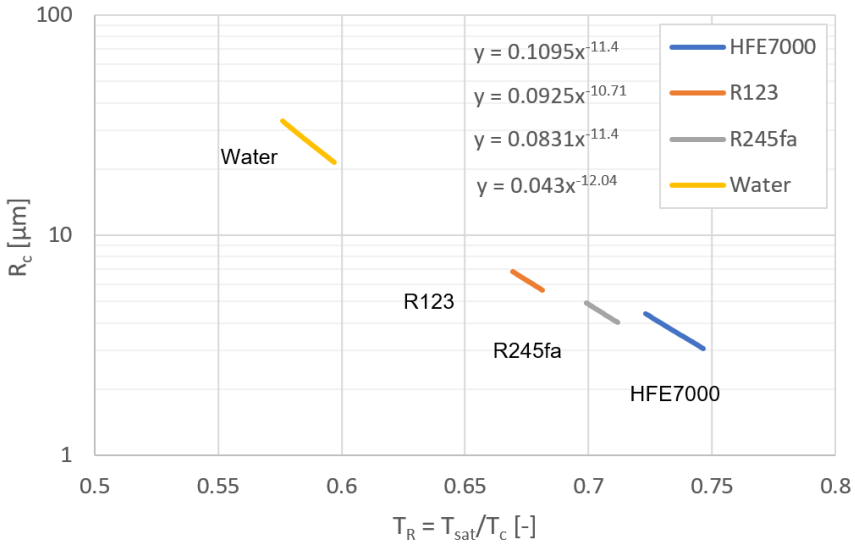

Figure 5.3: Critical radius comparison between water and test fluids

The Prandtl number, Pr, for water was 30% or less than that of the test fluids; this difference is amplified in the Benjamin and Balakrishnant [4] correlation with the term $\mathrm{Pr}^{1.63}$. The Reynolds number, Re_{d_h} was calculated at saturation conditions for a fluid pressure of 1 atm and a volumetric flow of 0.5 L/min through a 0.3 mm x 12.4 mm channel; the largest percent difference in Re_{d_h} was a 14% deviation from water. Several of the correlations are functions of a dimensionless density, $\rho^* = \frac{\rho_f - \rho_g}{\rho_g}$, or $\rho^+ = \log(\rho^*)$; this fitting parameter has the largest difference between water and the experimental fluids with the experimental fluids being less than 14% of ρ^* for water. The surface tension, σ, and confinement

number, $N_{conf} = \frac{1}{d_h}\sqrt{\frac{\sigma}{g(\rho_f - \rho_g)}}$, show nearly the same percent difference between the test fluids and water, with the test fluids being 30% that of water.

The experimental data from this study failed to show any significant correlation between N_a'' and ΔT_w, as was shown in Figure 4.13 and seen in Figure 5.1. Better correlation was found between N_a'' and q''. Wang and Dhir [9] presented the general correlation in Equation 5.2, where the nucleation rate is a strong function of heat flux, q'',

$$N_a'' \propto (q'')^2 \tag{5.2}$$

and supported by Figure 5.4

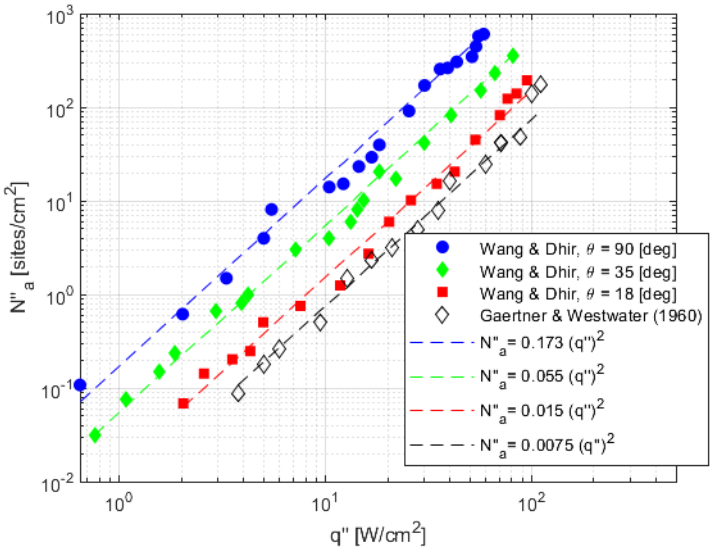

Figure 5.4: Reproduction of Figure 7 from Wang and Dhir [9] showing a general correlation between N_a'' and q''.

The experimental data for N_a'' were plotted in Figure 5.5 against q'' to investigate regressions of the type shown in Equation 5.3,

$$N_a'' \approx (q'')^n \tag{5.3}$$

for which the exponents were between 1 and 3 in Table 5.2. The rows in Figure 5.5 represent individual heaters, while the columns show different fluids.

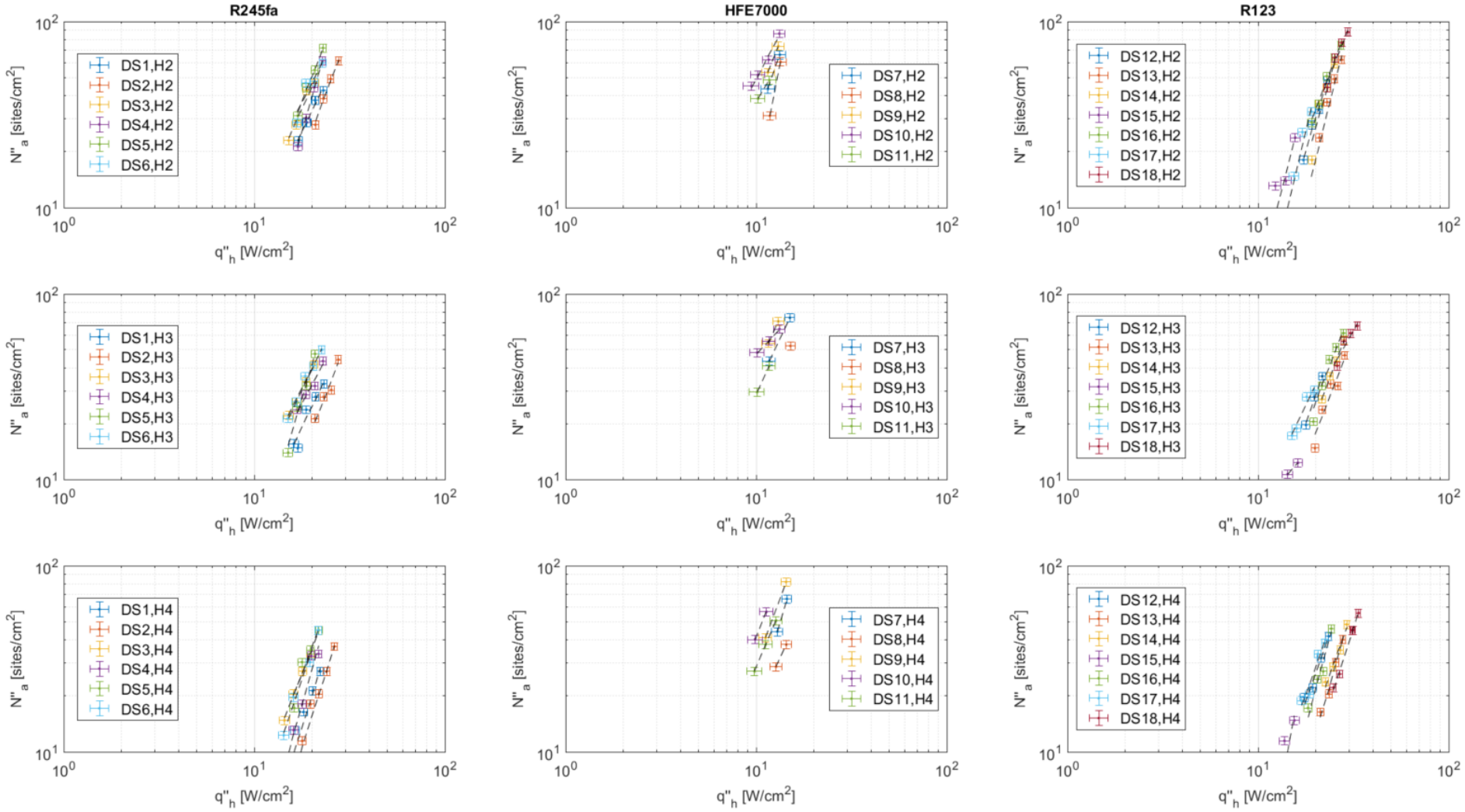

Figure 5.5: Experimental results for N_a'' plotted against q'', where the rows correspond to H2, H3, and H4, respectively, and the columns correspond to the fluids, R245fa, HFE7000, and R123, respectively.

Each data set was fit using the power regression in Equation 5.3 for N_a'' values greater than 10 sites/cm^2; nucleation densities lower than this value did not fit the regression for higher values. Hahne and Barthau [18] found similar behavior where lower nucleation densities were proportional to $(q''/Ja)^3$ in comparison to the higher nucleation densities being proportional to $(q''/Ja)^{1.6}$. The exponents for each curve are plotted in Figure 5.6. The mean values in Figure 5.6 are shown in Table 5.3. The uncertainty in q'' was 0.8

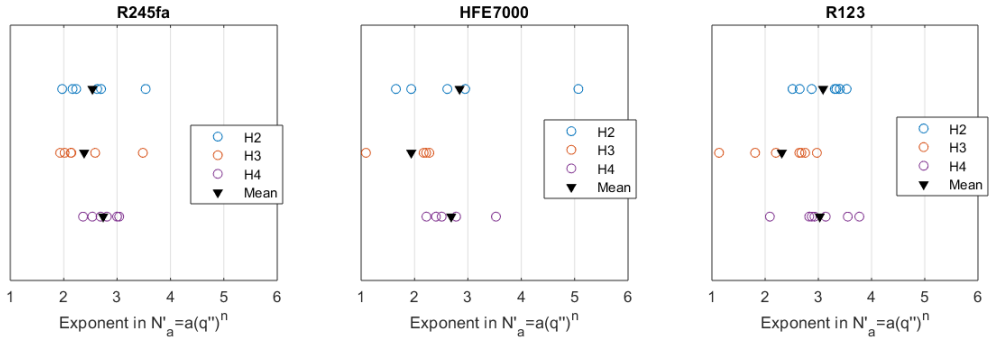

Figure 5.6: Exponent in Equation 5.3 for each data set in Figure 5.5. Each data set is spatially arranged in the same grid as Figure 5.5, with the x-axis being the exponent and vertical alignment relating to the 3x3 grid of Figure 5.5.

W/cm^2, while the uncertainty in N_a'' was 10% of the reading. In all three fluids, the expo-

Table 5.3: Mean values of each data set fluid-heater combination in Figure 5.6.

n	R245fa	HFE7000	R123
H2	2.5	2.8	3.1
H3	2.4	1.9	2.3
H4	3.7	2.7	3.0

nent is generally greater at H2 and H4 relative to H3. The consistency of this result across all three fluids suggests this is not due to random variation. In general, the exponent is between 1 and 4 for each fluid, though the limited number of data points used in the power regression of each data set makes each individual exponent uncertain.

Chapter 6

Discussion & Extension

It is clear that N_a'' is a strong function of the applied heat flux, q'' in a form similar to Equation 6.1. This was shown graphically in Figure 4.11 and Figure 5.5, and also by the plurality of existing correlations shown in Table 5.1 having this form.

$$N_a'' \propto (q'')^n \tag{6.1}$$

The results of this study found the exponent in Equation 6.1 to generally be between 1 and 4. Omitted-variable bias is likely responsible for the difficulty in determining the exact power-law relation between N_a'' and q''. This chapter will describe the development of a correlation to unify the experimental results from this study.

6.1 Dimensionless Correlations

Dimensionless variables were chosen to increase the scalability of this experiment. The heat flux was non-dimensionalized by defining the Boiling number, Bo, as the ratio of heat flux to latent heat capacity of the moving fluid,

$$Bo = \frac{q''}{Gh_{fg}} \tag{6.2}$$

The mass flux in the denominator matches the results from Figure 4.21 where it was shown that at a constant Re, the higher mass flux uniformly resulted in a decrease in N_a''.

Non-dimensionalizing the heat flux in this way helps to unify the HFE7000 results

with the other dielectric fluids as shown in Figure 6.1, where the coefficient of determination, R^2, was equal to 0.4 when regressing all of the data according to Equation 6.3.

$$N_a'' = C_1 Bo + C_2 \tag{6.3}$$

The spread of the data, at N_a'' equal to 40 sites/cm^2, is about 62% when measured from the regression line to the 95% prediction interval. This data point will be used as a reference to gauge future changes to the correlation. The exponent on Bo was initially set to one while investigating methods for accommodating fluid property differences.

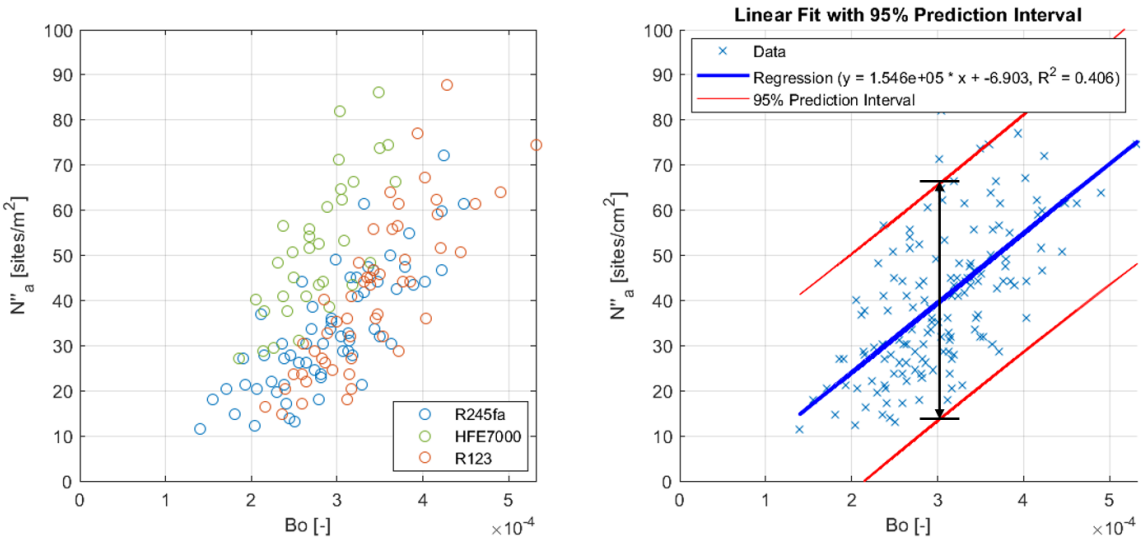

Figure 6.1: Correlation with Boiling number, Bo.

An exploratory search of dimensionless numbers was conducted to find a parameter that could bring the data for HFE7000 closer to the trends of results of R245fa and R123. Parameters were included in this search if they met any of three criteria:

1. Previously used in correlations for N_a''
2. Previously used by authors to describe their N_a'' data, even if it didn't end up in their correlation

3. Number contains parameters relevant to the bubble nucleation, or flow, parameters

This method was not ideal–a first principles approach would be preferred. However, first principle approaches have thus far failed to predict bubble nucleation behavior, as described at the end of Chapter 2. The dimensionless numbers considered in this analysis are defined in Table 6.1.

Table 6.1: Dimensionless numbers considered during correlation development

Name	Symbol	Definition	Evaluated At
Archimedes No.	Ar	$\frac{g}{\nu_f^2}\left(\frac{\sigma}{\rho_f g_c}\right)^{3/2}$	T_{film}
Bond No.	Bd	$\frac{(\rho_f-\rho_g)gd_h^2}{\sigma}$	T_{film}
Boiling No.	Bo	$\frac{q''}{Gh_{fg}}$	T_{film}
Capillary No.	Ca	$\frac{\mu_f u}{\sigma}$	T_{film}
Eckert No.	Ec	$\frac{u^2}{c_{p,f}\Delta T_{sat}}$	T_{film}
Euler No.	Eu	$\frac{P_{ref}-P_h}{0.5\rho_f u^2}$	$P_{ref} = P_{abs,diff,low}$ T_{film}
Friction factor	f_f	$\frac{\mathrm{d}P}{\mathrm{d}x}\frac{d_h}{\frac{1}{2}\rho_f u^2}$	$T_{f,in}$
Hagen No.	Hg	$-\frac{\mathrm{d}P}{\mathrm{d}x}\frac{d_h^3}{\nu_f^2\rho_f}$	T_{film}
Jakob No.	Ja_1	$\frac{\rho_f c_{p,f}\Delta T_{sat}}{\rho_g h_{fg}}$	T_{film}
	Ja_2	$\frac{c_{p,f}\Delta T_{sat}}{h_{fg}}$	T_{film}
	Ja_{sub}	$\frac{\rho_f c_{p,f}\Delta T_{sub}}{\rho_g h_{fg}}$	$T_{f,in}$
	$Ja*$	$\frac{\rho_f c_{p,f} T_{sat}}{\rho_g h_{fg}}$	T_{sat}
Confinement No.	N_{conf}	$\frac{1}{d_h}\left[\frac{\sigma}{g(\rho_f-\rho_g)}\right]^{1/2}$	T_{film}
Nusselt No.	Nu_{dh}	$\frac{hd_h}{k_f}$	T_{film}
Prandtl No.	Pr	$\frac{\nu_f}{\alpha_f}$	$T_{f,in}$
Reynolds No.	Re_{dh}	$\frac{\rho_f u d_h}{\mu_f}$	$T_{f,in}$
Density factor	ρ^*	$\frac{\rho_{fg}}{\rho_g}$	T_{film}
Weber No.	We	$\frac{\rho_f u^2 d_h}{\sigma}$	T_{film}

Histograms of each of these parameters, for all test conditions, are shown in Figure 6.2.

The equations for each dimensionless number are shown on the horizontal axes. Figure 6.2 was primarily used to predict the effect its inclusion would have on the behavior of the correlation. For example, the density factor, ρ^*, Hagen number, Hg, and Nusselt number show HFE7000 data being more separated from the other fluids, in comparison to the other dimensionless parameters. It was thus expected that including one or more of those would help unify the experimental data.

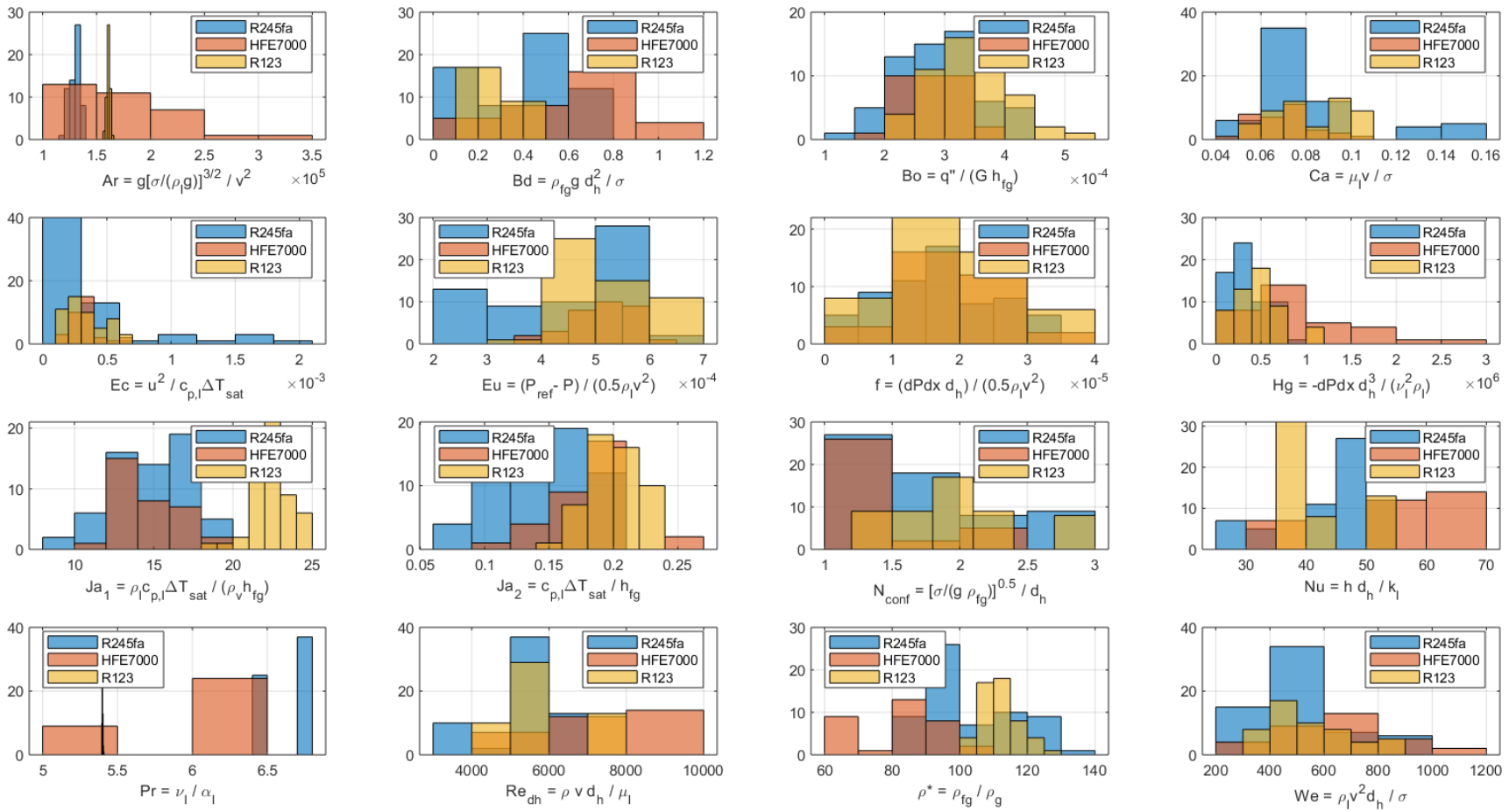

Figure 6.2: Histograms of dimensionless parameters considered during correlation development; this included the Archimedes, Bond, Boiling, Capillary, Eckert, Euler, Friction factor, Hagen, Jakob, Confinement, Nusselt, Prandtl, Reynolds, Density ratio, and Weber numbers.

Including the density factor, ρ^*, in the denominator of the correlation, as shown in Equation 6.4, moved the HFE7000 data in the intended direction, as shown in Figure 6.3.

$$N_a'' = \frac{C_1 Bo}{\rho^*} + C_2 \tag{6.4}$$

A linear regression of all data in Figure 6.3 showed that $R^2 = 0.534$. The error in predicting 40 sites/cm^2 is 55%.

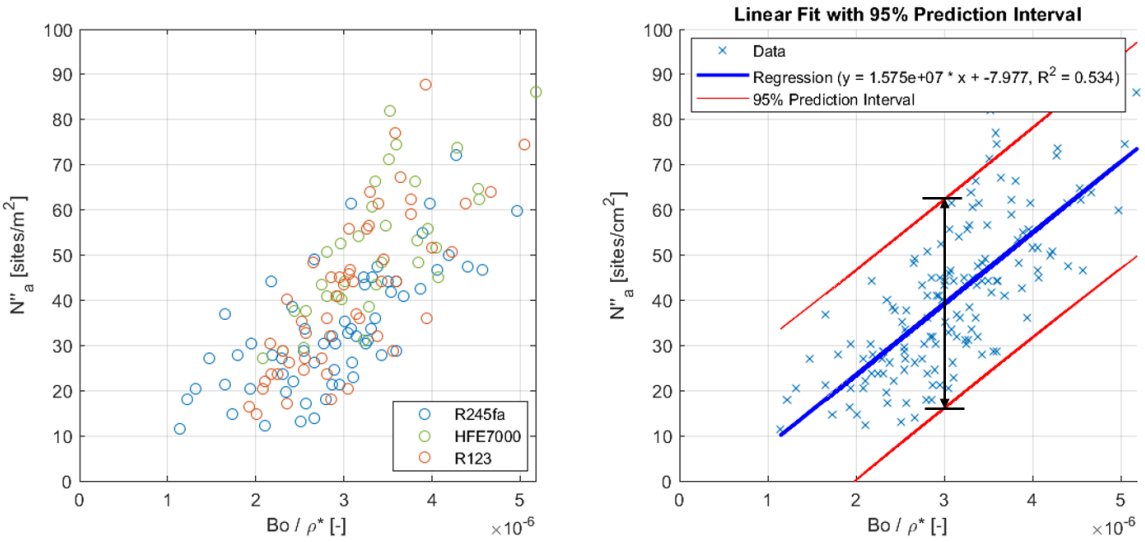

Figure 6.3: Correlation with Boiling number and density factor: Bo/ρ^*.

The Hagen number, Hg, represents a dimensionless pressure gradient and can also be used to correlate N_a'' with Bo as shown in Figure 6.4 and Equation 6.5.

$$N_a'' = C_1 Bo^{1.5} Hg^{0.5} + C_2 \tag{6.5}$$

Using Hg allows for the exponent on Bo to align more closely with the experimental results from this study. It also brings the scales of the axes closer to each other. At 40 sites/cm^2 the scatter in the data is about 50%. Changing Bo to $Bo^{1.5}$ improved R^2 to 0.516, and the addition of the Hagen number further improved it to 0.542.

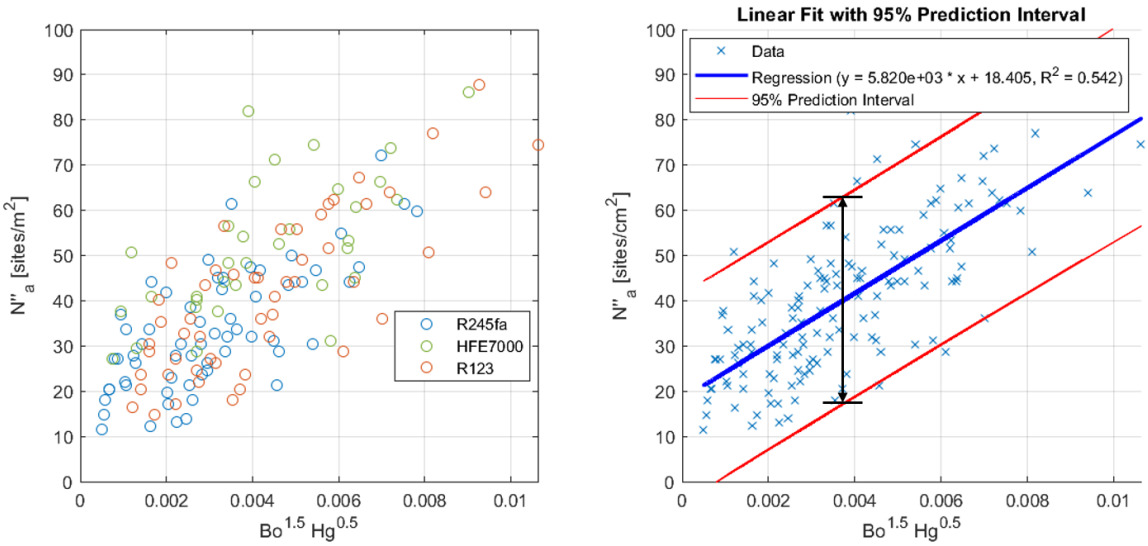

Figure 6.4: Correlation with Boiling and Hagen numbers: $Bo^{1.5}Hg^{0.5}$.

The Nusselt number, Nu is the only dimensionless number to include the heat transfer coefficient, h. While Bo implicitly depends upon h, because q'' could be rewritten as a $h\Delta T_{sat}$, including Nu in the correlation increased the coefficient of determination to 0.66, but the spread of data remained at 50% at 40 sites/cm^2 as shown in Figure 6.5.

$$N_a'' = C_1 \frac{Bo^{2.2} Nu^{1.4}}{(\rho^*)^{0.7}} + C_2 \tag{6.6}$$

The best-fitting regression took the form shown in Equation 6.7, with an $R^2 = 0.71$, and an uncertainty at 40 W/cm^2 of 44%.

$$N_a'' = \frac{Bo^{1.2} Nu^{0.5} Re^{0.4}}{(\rho^*)^{0.5} Pr^{0.9} Eu^{0.7}} \tag{6.7}$$

The results of this correlation are found in Figure 6.6. The Euler number was the only dimensionless parameter evaluated to condense the data toward the linear regression of each fluid individually. There remains a mismatch between HFE7000 and the other fluids

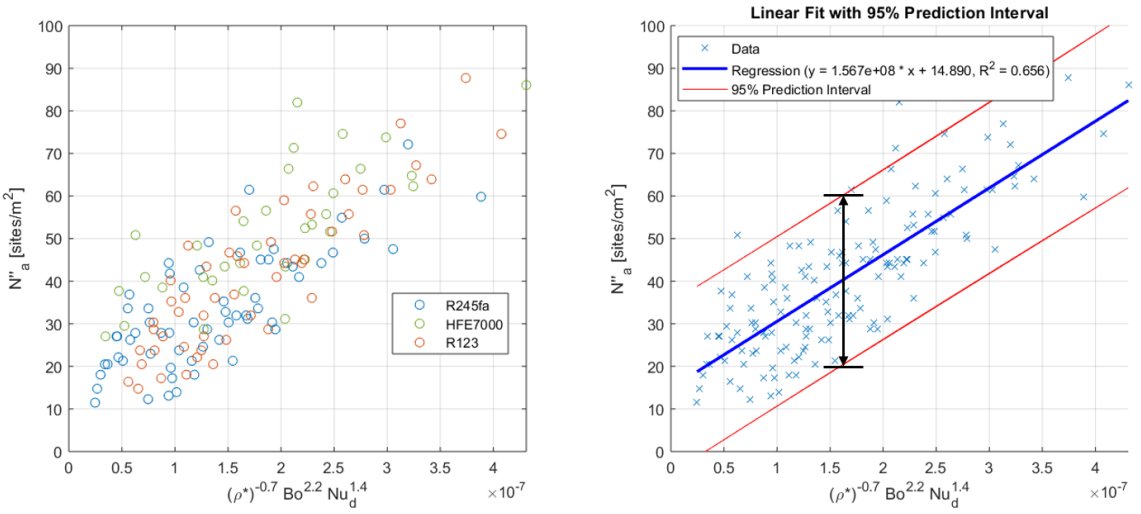

Figure 6.5: Correlation with Boiling and Nusselt numbers, with ρ^*: $Bo^{2.2}Nu^{1.4}(\rho^*)^{-0.7}$.

that could not be resolved using the existing dimensionless parameters. This regression

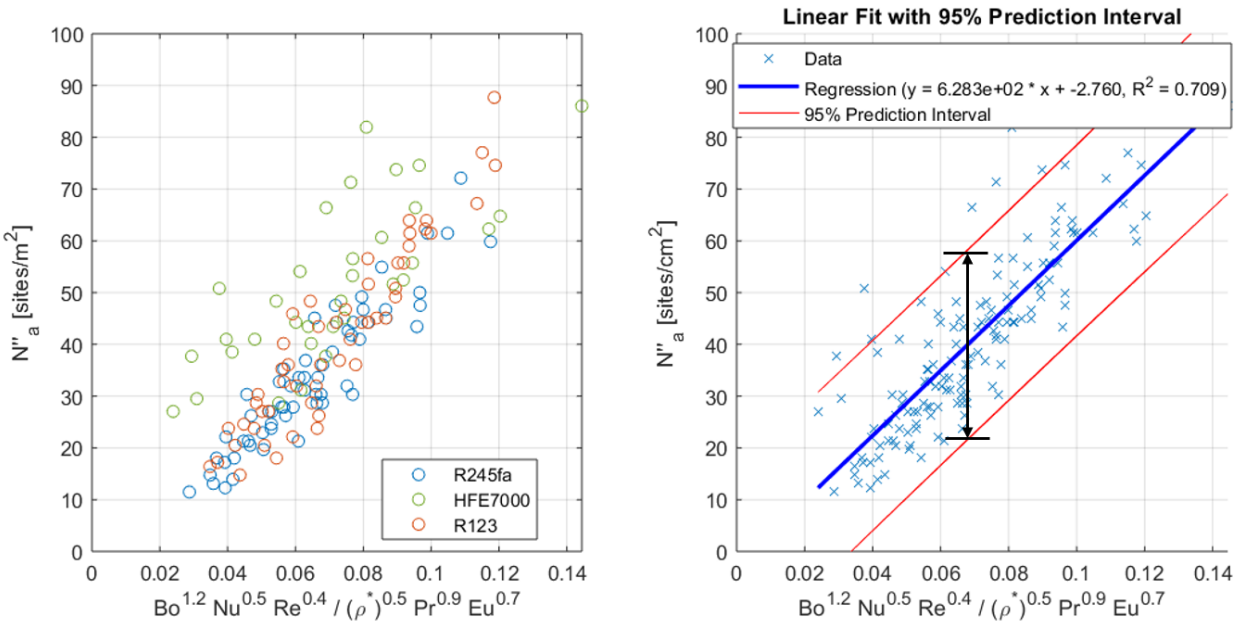

Figure 6.6: Highest R^2 regression, though overfit using non-physical exponents: $Bo^{1.2}Nu^{0.5}Re^{0.4}(\rho^*)^{-0.5}Pr^{-0.9}Eu^{-0.7}$.

was considered to be overfit, given the number of parameters and non-physical exponents.

After seeing the improvement that could be had by including the Euler number, a simpler correlation was created as Equation 6.8,

$$N_a'' = 3550 Bo^{1.5} Hg^{0.5} Eu^{-1} + 13.7 \tag{6.8}$$

resulting in an $R^2 = 0.58$ and an uncertainty at 40 sites/cm^2 of 54%. This regression is shown in Figure 6.7

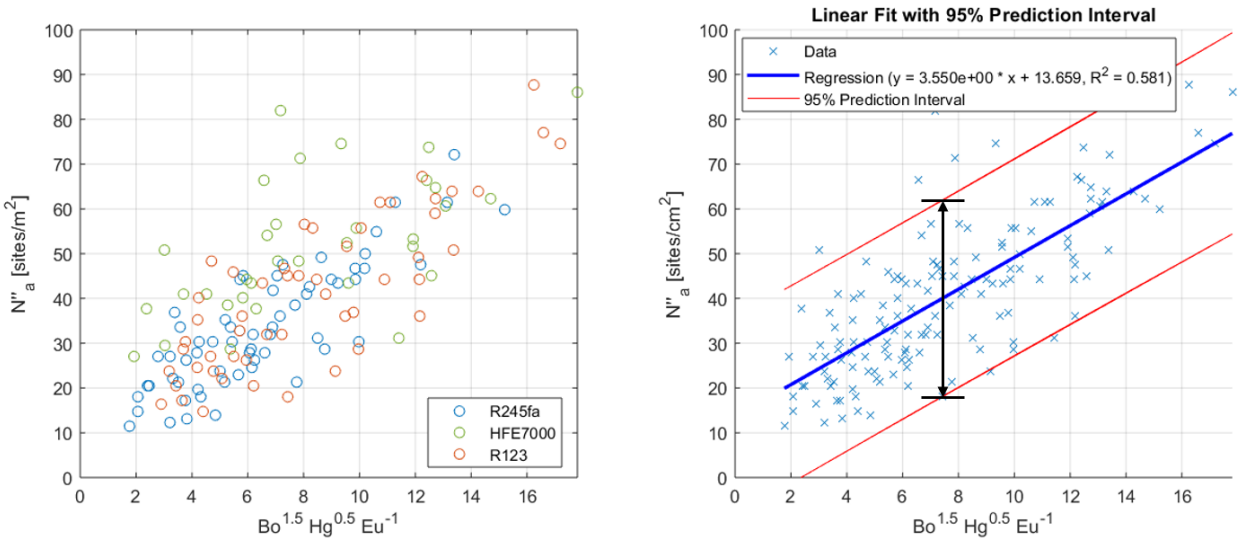

Figure 6.7: Simplified regression with N_a'' including the Euler number to account for the pressure drop in the nozzle: $Bo^{1.5} Hg^{0.5} Eu^{-1}$.

To summarize, the correlations developed here are presented in Table 6.2.

Table 6.2: Correlations of N_a'' for the experimental data of this study.

Equation	No.	R^2	$\delta N_a''$ at 40 sites/cm^2
$N_a'' = C_1 Bo + C_2$	6.3	0.40	62%
$N_a'' = \frac{C_1 Bo}{\rho^*} + C_2$	6.4	0.53	55%
$N_a'' = C_1 Bo^{1.5} Hg^{0.5} + C_2$	6.5	0.54	50%
$N_a'' = C_1 \frac{Bo^{2.2} Nu^{1.4}}{(\rho^*)^{0.7}} + C_2$	6.6	0.66	50%
$N_a'' = \frac{C_1 Bo^{1.2} Nu^{0.5} Re^{0.4}}{(\rho^*)^{0.5} Pr^{0.9} Eu^{0.7}} + C_2$	6.7	0.71	45%
$N_a'' = C_1 \frac{Bo^{1.5} Hg^{0.5}}{Eu} + C_2$	6.8	0.58	54%

6.2 Statistical Methods

During the process of developing these correlations, several techniques were explored; principal component analysis (PCA), factor analysis (FA), and a stepwise linear model (SLM). In PCA, the data are processed by subtracting the mean value of each experimental variable (EV), normalizing the data, and calculating the covariance between variables. A linear model is then optimized by scaling each EV and linearly combining them into a new set of variable (NV). Each NV can be plotted on a biplot to inspect their interaction, with the goal of learning which variables change together, and which variables have the most importance. An example of a PCA biplot is shown in Figure 6.8.

The blue vectors point in the direction of impacting each "Component". For example, Component 1 is positively influenced by Bo, and N_a'', while also negatively influenced by Bd and Re. Component 1 is additionally positively correlated with ρ^* and Nu_d, but to a lesser degree. More importantly, such a plot shows variables that are related; for example, Bo and Nu_d are positively correlated to a significant degree, while negatively correlated with Re as they are opposed to each other. Variables at right angles to another are predominantly agnostic to each other, when related by each component in Figure 6.8. After trying 30 different combinations of input EV to PCA, and plotting even more NV in a similar manner to Figure 6.8, no significant result could be realized.

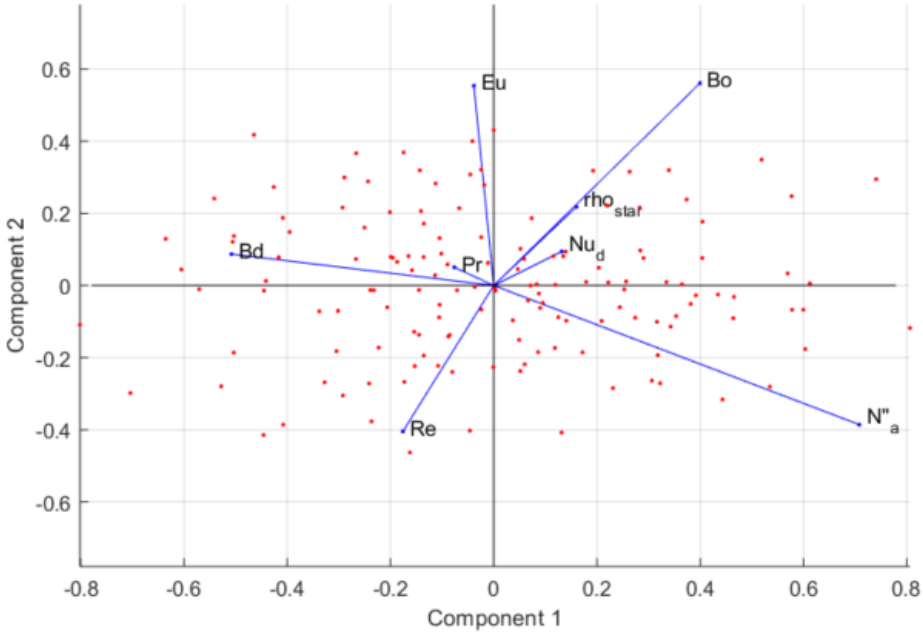

Figure 6.8: Principal component analysis example.

Factor analysis was used to find latent variables that are difficult to measure, but nothing new was found after a similar amount of expended effort trying a multitude of different experimental variables only to get insignificant results.

Lastly, a stepwise linear model was created, which is generated by fitting a given set of input variables and testing each term to see whether it has any meaningful affect on the output variable. Twenty-five variables were input into the SLM and the significance, or "effects" of each variable was plotted on the half-normal plot shown in Figure 6.9. The half-normal plot shows which variables have a normal, symmetric affect on the output variable, and which deviate from a normal distribution. Those variables at the top of the half-normal plot have deviated from the straight line produced by the lower end of the data. The suggestion from Figure 6.9 is that Eu, the interaction of Ja_{sub} and Eu, the Prandtl number, and the Bond number, Bd have an asymmetrical effect on N_a'' and deserve further investigation. It is suspect that Bo doesn't appear in the top 17 EV shown in Figure 6.9.

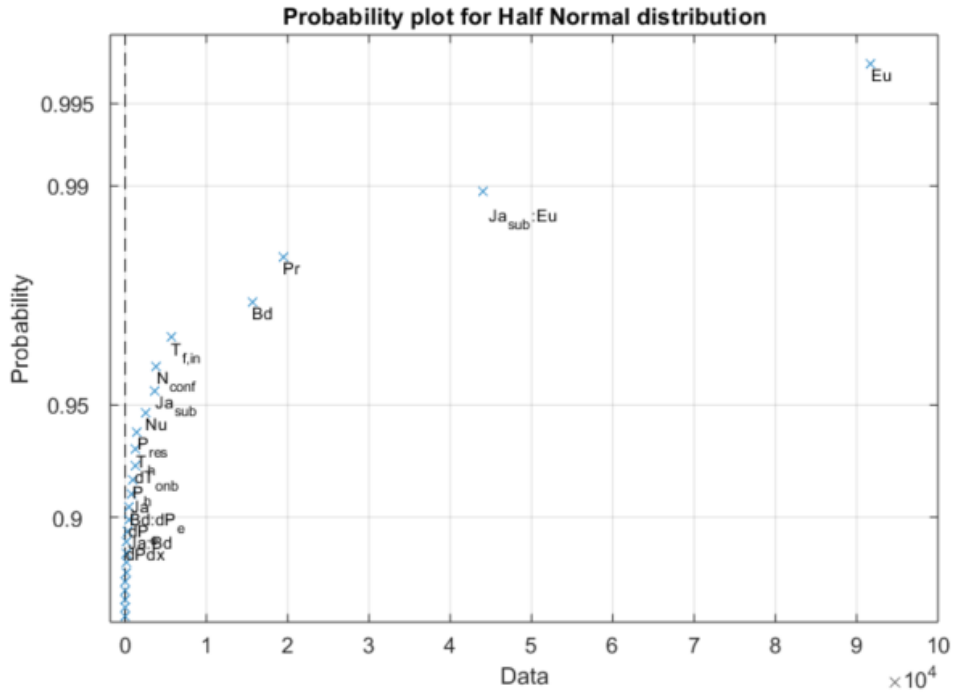

Figure 6.9: Principal component analysis example.

It appears that Nu, T_h, dT_{onb}, and Ja appear in place of Bo. For reference, dT_{onb} is the superheat required before bubble nucleation occurs.

The SLM was the inspiration for including Eu in Equation 6.7; it did condense the data to a degree, but it is clear that a more complex correlation is required to more precisely fit the experimental data.

6.3 Correlation Behavior with Water

Each of the correlations from Table 6.2 were evaluated with water, to examine whether they caused a spread in the data similar to what was shown in Figure 5.1. A flow condition similar to the comparison papers was chosen with the parameters shown in Table 6.3. A rectangular channel, through which water was flowing at 0.7 L/min was used as the basis for comparison. A heat flux between 0 and 25 W/cm^2 was simulated with a heater

Table 6.3: Parameters used when comparing water with generated correlations

	Variable	Value	Units
Geometry	w_{ch}	12.7	mm
	h_{ch}	6.35	mm
	d_h	8.4	mm
Flow	Q_{lpm}	0.7	L/min
	G	140	kg/s-m^2
	Re_d	3960	-

located 12 mm downstream of the reference condition ($P_{ref} = 1$ atm). At these conditions, the pressure drop, due to friction, was insignificant, which caused Eu to mostly be constant. A plot of all five correlations is shown in Figure 6.10, though two correlations produced approximately constant, but negative values and were omitted from the figure.

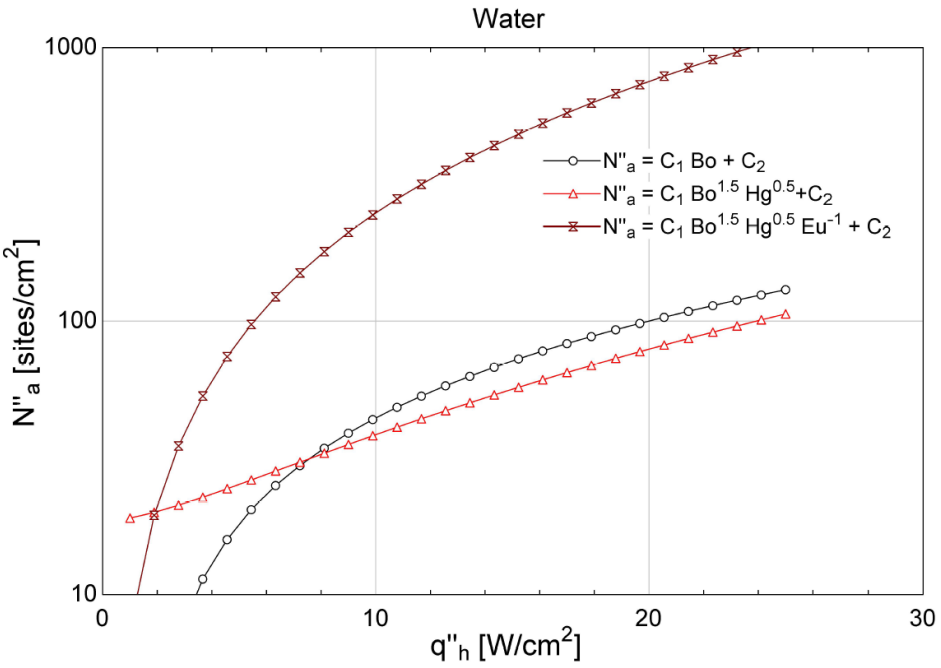

Figure 6.10: Evaluation of generated correlations with simulated flow conditions and water as a test fluid. Correlations not shown evaluated to approximately constant negative values.

It is evident that correlations that use ρ^* are not appropriate when predicting N_a'' across a range of fluids. The Nusselt number was calculated using correlations using the Shah

flow boing correlation as implemented in EES [42] to find the two-phase heat transfer coefficient. The length scale in Nu was chosen as d_h. The values for $N_a'' > 10$ sites/cm^2 shown in Figure 6.10 are within the range of being relevant for the correlations from Table 5.1, which suggests that Bo, Hg, and perhaps Eu are relevant parameters for predicting N_a'' across a range of fluids and heat fluxes.

6.4 Contact Angle

The contact angle, θ, was largely absent from much of the discussion. It is typically used to explain the stability of bubble formation, relate bubble departure diameter & bubble departure frequencies, and is generally understood to be inversely proportional to bubble formation. At low contact angles, cavities in a surface are less able to retain the vapor/gas phase requisite to the pre-existing vapor theory of boiling. This study is primarily interested in what can be done to improve boiling performance on ideally smooth surface, akin to silicon surfaces of a microprocessor die. As such, surface cavities are not present and the theory of pre-existing vapor is not applicable. As such, the contact angle, being mostly constant, can be absorbed into the leading constant multiplying each correlation.

For dielectric fluids like R245fa, HFE7000, and R123, the contact angle is typically below 10 degrees, meaning that they are highly wetting and likely to displace vapor from all but the sharpest of surface defects. The pre-existing vapor theory suggests that heterogeneous nucleation will cease once as the contact angle approaches zero, requiring liquids to boil homogeneously. This highlights one of the fundamental opportunities for research regarding bubble nucleation, because the pre-existing theory of boiling breaks down for situations similar to those in this study.

Chapter 7

Conclusions

This chapter summarizes the main conclusions and describes future work made possible by the new flow loop.

7.1 Flow Loop

The flow loop performance largely matched the intended design; the pressure gradient along the nozzle was constant near the design points, and remained nearly constant across a wide range of flow rates and shim thicknesses. At high flow rates, typically when the nozzle was removed from the test section and a blank nozzle inserted making it a straight channel, the flow rate of the system was limited by the net suction head of the pump causing vapor intake. When the nozzle was in-place, the flow rate was limited by the 103 kPa, gauge, full-scale range of the pressure transducers in the nozzle; in this case the maximum flow rate was determined by the system pressure and the desired pressure gradient along the nozzle.

Thermal stability of the flow loop was successfully achieved using the shell-and-tube heat exchanger as a reservoir with the temperature-controlled water bath providing cooling. Rope heaters around the stainless steel tubing, and silicone heaters beneath the test section, made it possible to have a nearly saturated fluid at the inlet to the nozzle, so long as care was taken to slowly reach steady state thereby preventing nucleation upstream of the nozzle.

The 1.1 mm thick, polished float glass, window performed better than expected, having no glass failures when heated to over 80°C and at absolute pressures up to 200 kPa.

The e-beam deposition process used in forming gold electrical busses worked sufficiently well. At 80°C, the gold/titanium film began to fail; it is unclear whether this occurred because ethanol was the working fluid at the time, or whether it was due to thermal expansion of the glass causing delamination. Electrodeposition methods have shown promise in adhering a wide variety of metals onto ITO [47], which may solve this issue.

High-speed videos (400 x 300 pixels) were recorded at 19,000 frames per second, which was fast enough for there to be at least two frames during the bubble formation process in all but the smallest, fastest bubbles. Bubbles forming in less than 53 μs could not accurately be resolved , but such bubbles appeared in less than 5 sites per video and only in the highest N_a'' cases. Imaging at these high speeds is a fairly recent addition to the research of N_a'', with most researchers filming between 3,000 and 8,000 frames per second; The results of this study could not have been possible at those speeds.

7.2 Active Bubble Nucleation Density, N_a'', [sites/cm^2]

The density of active nucleation sites, N_a'', was successfully measured for densities between 1 site/cm^2 and 107 sites/cm^2; the upper limit being imposed by the practicality of manual counting, and by the added uncertainty caused when upstream bubbles travel over a nucleation site, making it difficult to see if a bubble formed during the traversal. As the nucleation rate at each site was largely constant, nucleation sites that happened to coincide in frequency with upstream nucleation sites could increasingly be missed due to this overlap.

This study presented data for R245fa, HFE7000, and R123 across a range of flow rates, pressure gradients, back pressures and heat fluxes. Unlike a lot of research that is based on classical nucleation theory, this study failed to find a significant correlation between N_a'' and the superheat ΔT_w, as was shown in Figure 4.13. Instead, a strong correlation

with the applied heat flux, q'', of the form

$$N_a'' \propto (q'')^n \qquad \text{for} 1.9 < n < 3.7 \tag{7.1}$$

was found, as shown in Figure 5.5, where the average of exponent, n, for all data sets for a given fluid and heater, varied between 1.9 and 3.7, as shown in Table 5.3. This power-law form of the heat flux dependence agrees with the majority of the literature correlations in Table 5.1.

The conclusions in literature are sparing in regards to which other variables can reliably be included in Equation 7.2. The degree of subcooling was shown to have an insignificant correlation with N_a'', in Figure 4.15. The flow rate was shown to have an insignificant correlation with N_a'' in Figure 4.17, while the Reynolds number was shown to have no significant correlation with N_a'' in Figures 4.19 and C.4. The mass flux, and by extension pressure gradient, were shown to be important in Figure 4.21, as a negative correlation between G, or $dPdx$, with N_a''. Active nucleation sites were suppressed by 10% at a heat flux of 27 W/cm^2 and 34% at 21 W/cm^2 when the magnitude of the negative pressure gradient increases from 163 kPa/m to 240 kPa/m.

Sixteen dimensionless variables were evaluated for their ability to condense the experimental data as it pertains to the development of an improved N_a'' correlation. The heat flux was non-dimensionalized using Bo, which itself improved the correlation over Equation 7.2. Further improvement using ρ^*, Hg, and Nu were observed, however after comparing each correlation with a generic set of values for water, only the correlations with Bo and Hg continued to perform well. The final correlation that best fit the data, while being able to accommodate water as a fluid, is shown in Equation 7.2.

$$N_a'' = 3550 Bo^{1.5} Hg^{0.5} + 13.6 \tag{7.2}$$

Statistical analysis showed the Euler number to be important, and its inclusion did condense better than correlations with Bo alone. It also increased the water predictions by about an order of magnitude, which better matches with the predictions of water experiments shown in Figure 5.2.

Overall, these results show that pressure is a relevant parameter in the study of N_a'' as it relates to Hg, G, and Eu; however, this is a secondary influence relative to the effects of q''.

7.3 Future Work

Further extensions of this work includes looking more closely at the statistics of N_a'' to generate a more complex, broad correlation, than the linear regressions of this study. The spread of data, after correlation, implies there are some omitted variables that could further condense the results. The biggest drawback of this experiment was the manual analysis of bubble nucleation sites. Future work to automate that process would greatly increase the efficacy of this experiment. Once automation in video analysis is achieved, the versatility of the flow loop lends itself to a variety of experiments. The window is the size of a microscope slide, which lends itself to several other areas of research:

1. Application of additive structures (e.g., carbon nanotubes, nanowires, porous structures)

2. Wet chemistry techniques for functionalizing the surface in an effort to change the surface behavior at different temperatures or fluid concentrations

3. Inclusion of micro- and nano-sensing techniques via PVD, CVD, or lithography (e.g., glass-integrated surface thermocouples, multiplexed pixels capable of locally measuring transient heat flux at the base of a growing bubble)

Bibliography

[1] Vijay K Dhir. Handbook of Thermal Science and Engineering. In F. A. Kulacki, editor, *Handbook of Thermal Science and Engineering*, pages 1645–1694. Springer International Publishing AG, 2018. ISBN 9783319320038. doi: 10.1007/978-3-319-32003-8.

[2] Max Jakob. Heat Transfer in Evaporation and Condensation – I. *Mechanical Engineering*, 58:643–660, 1936.

[3] Nilanjana Basu, Gopinath R. Warrier, and Vijay K. Dhir. Onset of Nucleate Boiling and Active Nucleation Site Density During Subcooled Flow Boiling. *Journal of Heat Transfer*, 124(4):717, 2002. ISSN 00221481. doi: 10.1115/1.1471522.

[4] R. J. Benjamin and A R Balakrishnant. Nucleate pool boiling heat transfer of pure liquids at low to moderate heat fluxes. *International Journal of Heat and Mass Transfer*, 39(12):2495–2504, 1996.

[5] Takashi Hibiki and Mamoru Ishii. Active nucleation site density in boiling systems. *International Journal of Heat and Mass Transfer*, 46(14):2587–2601, 2003. ISSN 00179310. doi: 10.1016/S0017-9310(03)00031-0.

[6] G. Kocamustafaogullari and M. Ishii. Interfacial area and nucleation site density in boiling systems. *International Journal of Heat and Mass Transfer*, 26(9):1377–1387, sep 1983. ISSN 00179310. doi: 10.1016/S0017-9310(83)80069-6.

[7] Y. M. Lie and T. F. Lin. Subcooled flow boiling heat transfer and associated bubble characteristics of R-134a in a narrow annular duct. *International Journal of Heat and Mass Transfer*, 49(13-14):2077–2089, 2006. ISSN 00179310. doi: 10.1016/j.ijheatmasstransfer.2005.11.032.

[8] Tingting Ren, Zhiqiang Zhu, Meiyue Yan, Jiangwu Shi, and Changqi Yan. Experimental study on bubble nucleation and departure for subcooled flow boiling in a narrow rectangular channel. *International Journal of Heat and Mass Transfer*, 144: 118670, 2019. ISSN 00179310. doi: 10.1016/j.ijheatmasstransfer.2019.118670. URL `https://doi.org/10.1016/j.ijheatmasstransfer.2019.118670`.

[9] C. H. Wang and V. K. Dhir. Effect of Surface Wettability on Active Nucleation Site Density During Pool Boiling of Water on a Vertical Surface-. *Journal of Heat Transfer*, 115:659–669, 1993.

[10] K. A. Zhokhov. Number of vapour generating centers (in Russian). *Aerodynamics and Heat Transfer in Working Elements of Power Equipment. Publication of TsKT*, (91): 131–135, 1969.

[11] R. J. Benjamin and A. R. Balakrishnan. Nucleation Site Density in Pool Boiling of Saturated Pure Liquids: Effect of Surface Microroughness and Surface and Liquid Physical Properties. *Experimental Thermal and Fluid Science*, 15(1):32–42, 1997. ISSN 08941777. doi: 10.1016/S0894-1777(96)00168-9.

[12] I.L. Pioro, W. Rohsenow, and S.S. Doerffer. Nucleate pool-boiling heat transfer. I: review of parametric effects of boiling surface. *International Journal of Heat and Mass Transfer*, 47(23):5033–5044, nov 2004. ISSN 00179310. doi: 10.1016/j.ijheatmasstransfer.2004.06.019.

[13] L Z Zeng and J F Klausner. Nucleation Site Density in Forced Convection Boiling. *Journal of Heat Transfer*, 115(February):215–221, 1993. ISSN 00221481. doi: 10.1115/1.2910651.

[14] Hai Trieu Phan, Nadia Caney, Philippe Marty, Stéphane Colasson, and Jérôme Gavillet. How does surface wettability influence nucleate boiling?

Comptes Rendus Mécanique, 337(5):251–259, may 2009. ISSN 16310721. doi: 10.1016/j.crme.2009.06.032.

[15] Tadao Aoki. *The study of active sites and bubble formation frequency in nucleate boiling heat transfer*. Masters, Oregon State University, 1966.

[16] V. K. Dhir and S. P. Liaw. Framework for a unified model for nucleate and transition pool boiling. *Journal of Heat Transfer*, 111(3):739–746, 1989. ISSN 15288943. doi: 10.1115/1.3250745.

[17] R. F. Gaertner and J. W. Westwater. Population of Active Sites in Nucleate Boiling Heat Transfer. *Chemical Engineering Progress Symposium Series*, 56(30):39–48, 1960.

[18] Erich Hahne and Gerrit Barthau. Heat transfer and nucleation in pool-boiling. *International Journal of Thermal Sciences*, 45(3):209–216, mar 2006. ISSN 12900729. doi: 10.1016/j.ijthermalsci.2004.10.009.

[19] H. M. Kurihara and J. E. Myers. The effects of superheat and surface roughness on boiling coefficients. *AIChE Journal*, 6(1):83–91, mar 1960. ISSN 0001-1541. doi: 10.1002/aic.690060117.

[20] Andrea Luke and Da-chuan Cheng. High speed video recording of bubble formation with pool boiling. *International Journal of Thermal Sciences*, 45:310–320, 2006. doi: 10.1016/j.ijthermalsci.2005.06.011.

[21] B. B. Mikic and W. M. Rohsenow. A New Correlation of Pool-Boiling Data Including the Effect of Heating. *Journal of Heat Transfer*, 9:245–250, 1969.

[22] D. B. R. Kenning. Wall Temperature Variations and the Modelling of Bubble Nucleation Sites. In *Pool and external flow boiling : proceedings of the Engineering Foundation*

Conference on Pool and External Flow Boiling, pages 105–110, Santa Barbara, California, 1992.

[23] Bradley Bon and James Klausner. Pool Boiling Heat Transfer of Highly Wetting Fluids on Smooth Metallic Surfaces. *ASME/JSME 2011 8th Thermal Engineering Joint Conference*, pages T10182–T10182–10, 2011. doi: 10.1115/AJTEC2011-44045.

[24] Bradley Bon. *The role of surface microstructure and topography in pool boiling heat transfer*. Doctoral, University of Florida, 2011.

[25] Bradley Bon, James Klausner, and Edward McKenna. An Investigation of Pool Boiling Heat Transfer on Single Crystal Surfaces and a Dense Array of Cylindrical Cavities. *Journal of Heat Transfer*, 135(12):121501, sep 2013. ISSN 0022-1481. doi: 10.1115/1.4024652.

[26] W. B. Harrison and Zelvin Levine. Wetting effects on boiling heat transfer: The copper-stearic acid system. *AIChE Journal*, 4(4):409–412, dec 1958. ISSN 0001-1541. doi: 10.1002/aic.690040406.

[27] H. B. Clark, P. S. Strenge, and J.W. Westwater. Active Sites for Nucleate Boiling. *Chemical Engineering Progress Symposium Series*, 55(29):103–110, 1959.

[28] Raunak Bardia and Mario F. Trujillo. An improved categorization of vapor bubble collapse: Explaining the coupled nature of hydrodynamic and thermal mechanisms. *International Journal of Heat and Mass Transfer*, 145:118754, 2019. ISSN 00179310. doi: 10.1016/j.ijheatmasstransfer.2019.118754.

[29] Yusen Qi and James F. Klausner. Comparison of Nucleation Site Density for Pool Boiling and Gas Nucleation. *Journal of Heat Transfer*, 128

(January):13–20, 2006. ISSN 00221481. doi: 10.1115/1.2130399. URL http://heattransfer.asmedigitalcollection.asme.org/article.aspx?articleid=1448237.

[30] C. H. Wang and V. K. Dhir. On the Gas Entrapment and Nucleation Site Density During Pool Boiling of Saturated Water. *Journal of Heat Transfer*, 115:670–679, 1993.

[31] D. B. R. Kenning. What do we really know about nucleate boiling? In *IMechE 6th UK National Conference on Heat Transfer*, pages 143–167, 1999.

[32] John P. McHale and Suresh V. Garimella. Nucleate boiling from smooth and rough surfaces – Part 1: Fabrication and characterization of an optically transparent heater–sensor substrate with controlled surface roughness. *Experimental Thermal and Fluid Science*, 44:456–467, jan 2013. ISSN 08941777. doi: 10.1016/j.expthermflusci.2012.08.006.

[33] Delta-Technologies. Application Notes, 2011. URL http://delta-technologies.com/downloads/applicationnotes.pdf.

[34] B. S. Petukhov. Heat Transfer and Friction in Turbulent Pipe Flow with Variable Physical Properties. *Advances in Heat Transfer*, 6:503–564, 1970.

[35] Southwestern Industries. DPM V3, V5, V7 Safety, Installation, Maintenance, Service & Parts List, 2009. URL https://www.southwesternindustries.com/media/manuals/24949_Manual.pdf.

[36] D. Blair and E. Dufresne. Matlab Particle Tracking, 2005. URL http://site.physics.georgetown.edu/matlab/.

[37] John C. Crocker and David G. Grier. Methods of digital video microscopy for colloidal studies. *Journal of Colloid and Interface Science*, 179(1):298–310, 1996. ISSN 00219797. doi: 10.1006/jcis.1996.0217.

[38] John C Crocker and Eric R Weeks. Particle tracking using idl, 1996. URL `http://www.physics.emory.edu/faculty/weeks//idl/`.

[39] S. J. Kline and F. A. McClintock. Describing Uncertainties in Single-Sample Experiments. *Mechanical Engineering*, 75(January):3–8, 1953.

[40] Robert J. Moffat. Describing the Uncertainties in Experimental Results. *Experimental Thermal and Fluid Science*, 1:3–17, 1988.

[41] Indium Corporation. Indium Oxide and Indium-Tin Oxide (ITO) Coatings. Technical report, Indium Corporation, Chicago, IL, 2013.

[42] S A Klein. Engineering Equation Solver, 2019. URL `www.fchart.com`.

[43] S. Kakaç, R. K. Shah, and W. Aung, editors. *Handbook of Single-Phase Convective Heat Transfer*. Wiley-Interscience, New York, 1987. ISBN 9780471817024.

[44] V. Gnielinski. New Equations for Heat and Mass Transfer in Turbulent Pipe and Channel Flow. *International Chemical Engineering1*, 16:359–368, 1976.

[45] G. D. Raithby and K. G. T. Hollands. Natural Convection. In W. M. Rohsenow, J. P. Hartnett, and Y. I. Cho, editors, *The Handbook of Heat Transfer*. McGraw-Hill, New York, 3rd edition, 1998.

[46] Gregory Nellis and Sanford Klein. *Heat Transfer*. Cambridge University Press, Cambridge, 1st edition, 2009.

[47] Xiaowei Zhang, Baohua Lou, Dongyue Li, Wei Hong, You Yu, Jing Li, and Erkang Wang. A universal method for the preparation of functional ITO electrodes with ultrahigh stability. *Chemical Communications*, 51(31):6788–6791, 2015. ISSN 1364548X. doi: 10.1039/c5cc00906e.

[48] Van P. Carey. *Statistical Thermodynamics and Microscale Thermophysics*. Cambridge University Press, Cambridge, 1999.

[49] Carl S. Helrich. *Modern Thermodynamics with Statistical Mechanics*. Springer, Berlin, 2009.

[50] Jacob N. Israelachvili. *Intermolecular and Surface Forces*. Elsevier, Oxford, third edition, 2011. ISBN 978-0-12-391927-4.

[51] Pablo Debenedetti. *Metastable Liquids*. Princeton University Press, Princeton, 1996. ISBN 0-691-08595-1.

[52] J. Mitrovic. How to create an efficient surface for nucleate boiling? *International Journal of Thermal Sciences*, 45(1):1–15, jan 2006. ISSN 12900729. doi: 10.1016/j.ijthermalsci.2005.05.003.

[53] Sushil Bhavnani, Vinod Narayanan, Weilin Qu, Michael Jensen, Satish Kandlikar, Jungho Kim, and John Thome. Boiling Augmentation with Micro/Nanostructured Surfaces: Current Status and Research Outlook. *Nanoscale and Microscale Thermophysical Engineering*, 18(3):197–222, jul 2014. ISSN 1556-7265. doi: 10.1080/15567265.2014.923074.

[54] T. B. Drew and C. Mueller. Boiling. *Trans. AIChE*, 33:449–473, 1937.

[55] M. Jakob and W. Fritz. Versuche über den Verdampfungsvorgang (Experiments on the evaporation process). *Forschungsarbeiten auf dem gebiete des ingenieurwesens (Research in the field of Engineering)*, 2(12):435–447, 1931.

[56] Shiro Nukiyama. The Maximum and Minimum Values of the Heat Q Transmitted from Metal to Boiling Water under Atmospheric Pressure. *International Journal of Heat and Mass Transfer*, 9:1419–1433, 1966.

[57] Robert B. Dean. The Formation of Bubbles. *Journal of Applied Physics*, 15(5):446–451, 1944. ISSN 00218979. doi: 10.1063/1.1707453.

[58] S. G. Bankoff, W. J. Colahan Jr., and D. R. Bartz. Summary of Conference on Bubble Dynamics and Boiling Heat Transfer Held at the Jet Propulsion Laboratory. Technical report, California Institute of Technology, 1956.

[59] J. Frenkel. *Kinetic Theory of Liquids*. Clarendon Press, Oxford, 1946.

[60] John A. Clark. The Thermodynamics of Bubbles. Technical report, MIT, Cambridge, MA, 1956.

[61] Louis Bernath. Theory of Bubble Formation in Liquids. *Industrial & Engineering Chemistry*, 44(6):1310–1313, 1952. ISSN 0019-7866. doi: 10.1021/ie50510a037.

[62] Victor K Lamer and Victor K La Mer. Nucleation in Phase Transitions. *Industrial and Engineering Chemistry*, 44(6):1270–1277, 1952. ISSN 0019-7866. doi: 10.1021/ie50510a027.

[63] F. E. Bartell and J. W. Shepard. Surface roughness as related to hysteresis of contact angles. I. The system paraffin-water-air. *The Journal of Physical Chemistry*, 57(2):211–215, 1953.

[64] Claude Corty and Alan Foust. Surface Variables in Nucleate Boiling. *Chemical Engineering Progress Symposium Series*, 51(17):1–12a, 1953.

[65] S. G. Bankoff. Ebullition From Solid Surfaces in the Absence of a Pre-Existing Gaseous Phase. *Transactions of the ASME*, 79:735–740, 1957.

[66] John C. Fisher. The Fracture of Liquids. *Journal of Applied Physics*, 19(1948):1062–1067, 1948. ISSN 00218979. doi: 10.1063/1.1698012.

[67] S. G. Bankoff. Entrapment of gas in the spreading of a liquid over a rough surface. *AIChE Journal*, 4(1):24–26, mar 1958. ISSN 0001-1541. doi: 10.1002/aic.690040105.

[68] Peter Griffith and John D. Wallis. The Role of Surface Conditions in Nucleate Boiling. *Chemical Engineering Progress Symposium Series*, 56(30):49–63, 1960.

[69] a. S. Perkins and J. W. Westwater. Measurements of bubbles formed in boiling Methanol. *AIChE Journal*, 2(4):471–476, 1956. ISSN 0001-1541. doi: 10.1002/aic.690020411.

[70] Franklin D. Moore and Russell B. Mesler. The measurement of rapid surface temperature fluctuations during nucleate boiling of water. *AIChE Journal*, 7(4):620–624, dec 1961. ISSN 0001-1541. doi: 10.1002/aic.690070418.

[71] J. W. Westwater. Boiling Heat Transfer. *American Scientist*, 47(3):427–446, 1959.

[72] S S Kutateladze. Boiling heat transfer. *International Journal of Heat and Mass Transfer*, 4:31–45, 1961.

[73] Y. Y. Hsu. On the size range of active nucleation cavities on a heating surface. *Journal of Heat Transfer*, 84(3):207–213, 1962.

[74] W. M. Rohsenow. Nucleation with Boiling Heat Transfer. *Industrial and Engineering Chemistry*, 58(1):40–47, 1966.

[75] P. J. Marto and W. M. Rohsenow. Effects of surface conditions on nucleate pool boiling of sodium. *Journal of Heat Transfer*, 88(2):196–203, 1966.

[76] Ralph L. Webb. Donald Q. Kern Lecture Award Paper: Odyssey of the Enhanced Boiling Surface. *Journal of Heat Transfer*, 126(6):1051, 2004. ISSN 00221481. doi: 10.1115/1.1834615.

[77] M G Cooper and a J P Lloyd. The microlayer in nucleate pool boiling. *International Journal of Heat and Mass Transfer*, 12:895–913, 1969. doi: 10.1016/0017-9310(69)90154-9.

[78] W. M. Rohsenow. Boiling. *Annual Review of Fluid Mechanics*, 1971.

[79] Keith Cornwell. Naturally Formed Boiling Site Cavities. *Letters in Heat and Mass Transfer*, 4:63–72, 1977.

[80] M. Sultan and R. L. Judd. Interaction of the Nucleation Phenomena at Adjacent Sites in Nucleate Boiling. *Journal of Heat Transfer*, 105(1):3–9, 1983. ISSN 00221481. doi: 10.1115/1.3245556.

[81] a.D. D. Messina and E.L. L. Park. Effects of precise arrays of pits on nucleate boiling. *International Journal of Heat and Mass Transfer*, 24(1):141–145, jan 1981. ISSN 00179310. doi: 10.1016/0017-9310(81)90102-2.

[82] W. Nakayama, T. Daikoku, H. Kuwahara, and T. Nakajima. Dynamic Model of Enhanced Boiling Heat Transfer on Porous Surfaces, Part I : Experimental Investigation. *Journal of Heat Transfer*, 102(August):445–450, 1980.

[83] W. Nakayama, T. Daikoku, H. Kuwahara, and T. Nakajima. Dynamic Model of Enhanced Boiling Heat Transfer on Porous Surfaces, Part II: Analytical Modeling. *Journal of Heat Transfer*, 102(August):451–456, 1980.

[84] A Majumdar and B. Bhushan. Role of Fractal Geometry in Roughness Characterization and Contact Mechanics of Surfaces. *Journal of Tribology*, 112(April):205–216, 1990.

[85] V. K. Dhir. Boiling Heat Transfer. *Annual Review of Fluid Mechanics*, 30(1):365–401, jan 1998. ISSN 0066-4189. doi: 10.1146/annurev.fluid.30.1.365.

[86] Masahiro Shoji. Studies of boiling chaos: a review. *International Journal of Heat and Mass Transfer*, 47(6-7):1105–1128, mar 2004. ISSN 00179310. doi: 10.1016/j.ijheatmasstransfer.2003.09.024.

[87] T. N. Dinh, J. P. Tu, A. T. Dinh, and T. G. Theofanous. Nucleation Phenomena in Boiling on Nanoscopically Smooth Surfaces. In *41st Aerospace Sciences Meeting and Exhibit*, pages 1–11, Reno, Nevada, 2003. American Institute of Aeornautics and Astronautics.

[88] T G Theofanous, T N Dinh, J P Tu, and A T Dinh. The boiling crisis phenomenon Part II : dryout dynamics and burnout. *Experimental Thermal and Fluid Science*, 26: 793–810, 2002.

[89] Dong Liu, Poh-Seng Lee, and Suresh V. Garimella. Prediction of the onset of nucleate boiling in microchannel flow. *International Journal of Heat and Mass Transfer*, 48: 5134–5149, 2005.

[90] Weilin Qu and Issam Mudawar. Prediction and measurement of incipient boiling heat flux in micro-channel heat sinks. *International Journal of Heat and Mass Transfer*, 45(19):3933–3945, sep 2002. ISSN 00179310. doi: 10.1016/S0017-9310(02)00106-0.

[91] Ana V. Pesse, Gopinath R. Warrier, and Vijay K. Dhir. An experimental study of the gas entrapment process in closed-end microchannels. *International Journal of Heat and Mass Transfer*, 48(25-26):5150–5165, dec 2005. ISSN 00179310. doi: 10.1016/j.ijheatmasstransfer.2005.07.020.

[92] V.P. P. Carey and a.P. P. Wemhoff. Thermodynamic analysis of near-wall effects on phase stability and homogeneous nucleation during rapid surface heating. *International Journal of Heat and Mass Transfer*, 48(25-26):5431–5445, dec 2005. ISSN 00179310. doi: 10.1016/j.ijheatmasstransfer.2005.06.027.

[93] V Gerweck, G Yadigaroglu, V Gerweckf, and G Yadigaroglu. A local equation of state for a fluid in the presence of a wall and its application to rewetting. *International Journal of Heat and Mass Transfer*, 35(7):1823–1832, 1992.

[94] Yusen Qi and James F. Klausner. Heterogeneous Nucleation With Artificial Cavities. *Journal of Heat Transfer*, 127(11):1189, 2005. ISSN 00221481. doi: 10.1115/1.2039111.

[95] Yusen Qi and James F. Klausner. Comparison of Nucleation Site Density for Pool Boiling and Gas Nucleation. *Journal of Heat Transfer*, 128(January):13–20, 2006. ISSN 00221481. doi: 10.1115/1.2130399.

[96] Suriyan Laohalertdecha, Paisarn Naphon, and Somchai Wongwises. A review of electrohydrodynamic enhancement of heat transfer. *Renewable and Sustainable Energy Reviews*, 11(5):858–876, 2007. ISSN 13640321. doi: 10.1016/j.rser.2005.07.002.

[97] R. S. Neve and Y. Y. Yan. Enhancement of heat exchanger performance using combined electrohydrodynamic and passive methods. *International Journal of Heat and Fluid Flow*, 17(4):403–409, 1996. ISSN 0142727X. doi: 10.1016/0142-727X(95)00016-J.

[98] Mathieu Legay, Nicolas Gondrexon, Stéphane Le Person, Primius Boldo, and André Bontemps. Enhancement of heat transfer by ultrasound: Review and recent advances. *International Journal of Chemical Engineering*, 2011, 2011. ISSN 1687806X. doi: 10.1155/2011/670108.

[99] Sreenath Krishnan, Sarit K. Das, and Dhiman Chatterjee. Physics of the Interaction of Ultrasonic Excitation With Nucleate Boiling. *Journal of Heat Transfer*, 136(3): 031501, 2013. ISSN 0022-1481. doi: 10.1115/1.4025641.

[100] M. C. Chyu and A. M. Mghamis. Nucleate boiling on two cylinders in line contact. *International Journal of Heat and Mass Transfer*, 34(7):1783–1790, 1991.

[101] a. E. Bergles and W. M. Rohsenow. The Determination of Forced-Convection Surface-Boiling Heat Transfer. *Journal of Heat Transfer*, 8(3):365–372, 1964. ISSN 00221481. doi: 10.1115/1.3688697.

[102] Wade R Mcgillis, John S Fitch, William R Hamburgen, and Van P Carey. Pool Boiling Enhancement Techniques for Water at Low Pressure. Technical report, Western Research Laboratory, Palo Alto, 1990.

Appendix A

Sheet Resistivity, $\Omega/\square$

A few words could be said about the units $\Omega/\square$: The electrical resistance (R_{el}) of a material is the volumetric resistivity (ρ) divided by the cross sectional area (A) through which the electricity must travel, multiplied by the length of travel (l), or

$$R_{el} = \rho l / A \tag{A.1}$$

Letting the cross sectional area be rectangular ($A = w \cdot th$) and rearranging produces

$$R_{el} = \frac{\rho}{th}\frac{l}{w} \tag{A.2}$$

The first term on the right side of Equation A.2 technically has units Ω, but can be thought of as having units $\Omega/\square$. The second term is the length to width ratio, defining the rectangularity of the electricity's path. Because the width of the conductor decreases the resistance linearly, and the length increases the resistance linearly, the absolute units are of no consequence. For this reason, the ratio is considered to define a number of squares as a measure of rectangularity.

For example, if the width of a material is half the length, it would be considered to be 2 $\square$. If the width was 10 times the length, it would contain 0.1 $\square$. For the case of Figure 3.10, the width was 9.5 mm and the length was 12.4 mm, making each heater 1.3 $\square$. The measured resistance of each heater was nominally 60 Ω, which comports with the factory resistivity of the coating being between 30 $\Omega/\square$ and 60 $\Omega/\square$.

Appendix B

Bubble Tracking Algorithm

A bubble tracking algorithm was initially designed for identifying the quantity and spatial distribution of bubble nucleation sites, departure frequencies, and the evolution of bubble diameters through time. The algorithm was abandoned after considerable effort due to inherent inaccuracies, though certain changes to the experimental procedure or video conversion process may improve its accuracy for future research.

B.1 Bubble Tracking Algorithm

The goal of the video processing algorithm was to track bubbles as they moved between frames. The origin of each track could be used to pinpoint bubble nucleation sites, spatial distribution of nucleation sites, and departure frequency. Each recorded video consisted of 2,000 frames; 200 of those frames were imported to Matlab for analysis. Figure B.1 provides a high-level overview of the video analysis algorithm.

For reference, Figure B.2 shows a high level overview of the math used to convert a raw camera image to a cleaned binary image that could be used for further analysis to locate and track bubbles. Each step is described below.

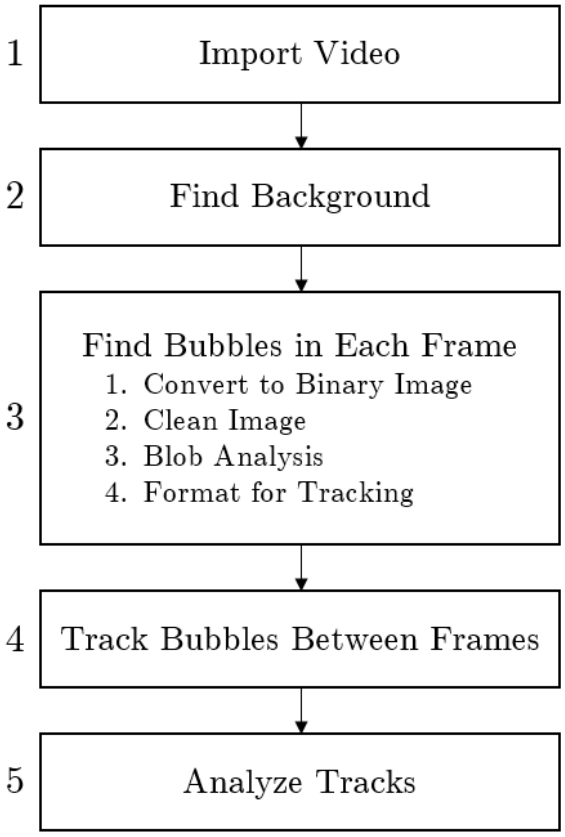

Figure B.1: Overview of video analysis algorithm

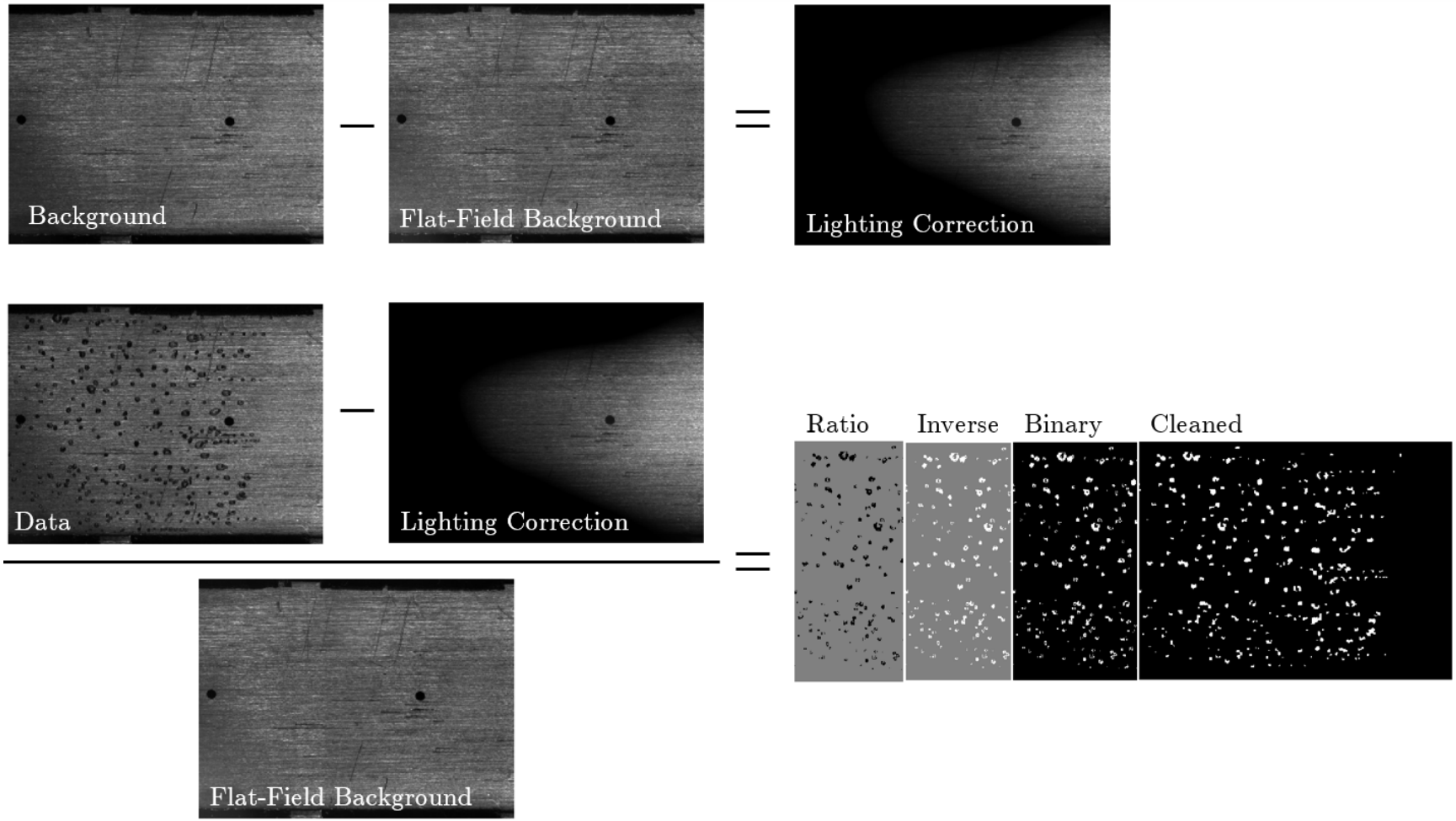

Figure B.2: High level math behind video processing algorithm to go from original image to cleaned binary image used for analysis.

B.1.1 Step 1: Convert raw camera file to 3-D unsigned 16-bit matrix

Converting the video from its native *.cine format (a file format proprietary to Vision Research) to a 3-dimensional *.mat array allowed for further processing in Matlab, where the first two dimensions (304 x 400) contain the spatial intensity of a given frame and the third dimension was the frame number. The resulting *.mat array contained unsigned 16-bit integer values corresponding to light intensity and was of size (304 x 400 x 200). An example image from the camera is shown in Figure B.3.

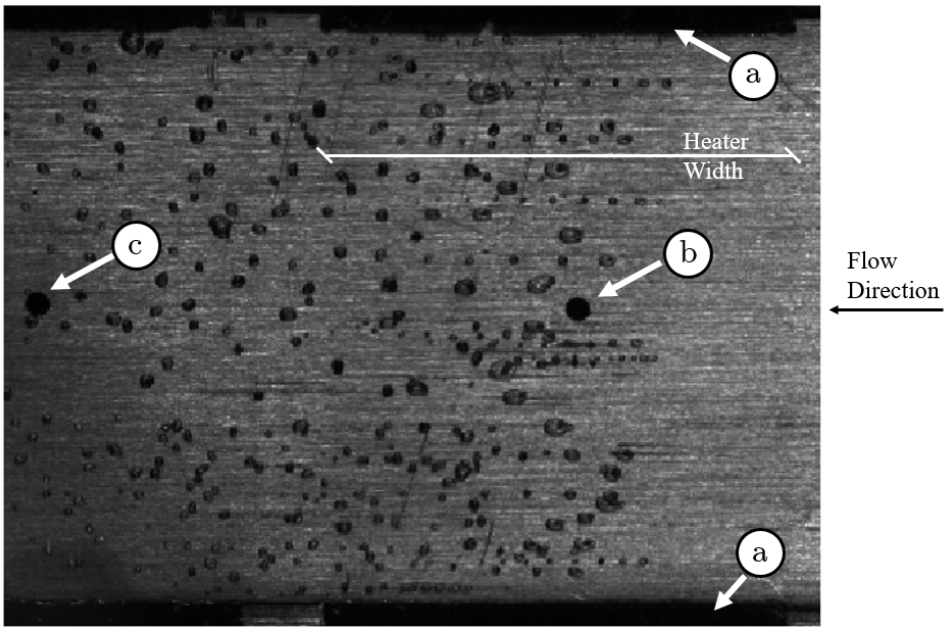

Figure B.3: Example image from the Phantom camera

B.1.2 Step 2: Define background images

Defining the background image was aided by noting that the bubbles in each image were darker than the background. At each pixel location, the brightness in all frames could be analyzed for the 95% quantile. The result was an array of pixel intensities representative of the background when no bubbles were present. Continuing with the data shown in

Figure B.3 whose first frame can be seen in Figure B.4(a) , the calculated background image is shown in Figure B.4(b).

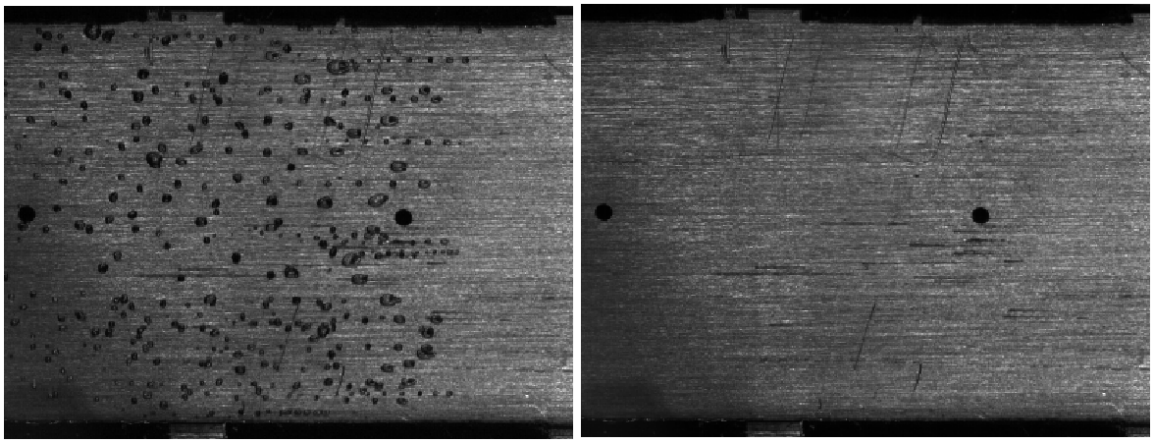

(a) (b)

Figure B.4: Example first frame (a), and the calculated background image (b)

A background image without lighting variations could be defined using 2-D image flat-field correction; the result of this process is shown in Figure B.5.

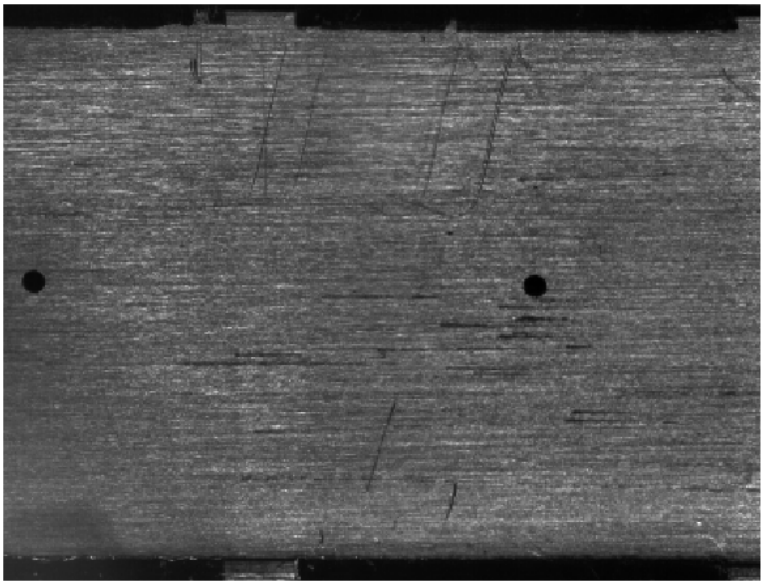

Figure B.5: 2-D flat-field corrected background image

Subtracting the flat-field background (Figure B.5) from the background image (Figure

B.4(b)) shows the effect of flat-field correction and is shown in Figure B.6. The bright regions of Figure B.6 indicate regions of the data frame that were brighter than other regions. Figure B.6 could subsequently be used as a mask for correcting the lighting in each data frame by subtracting the lighting correction image from each data frame.

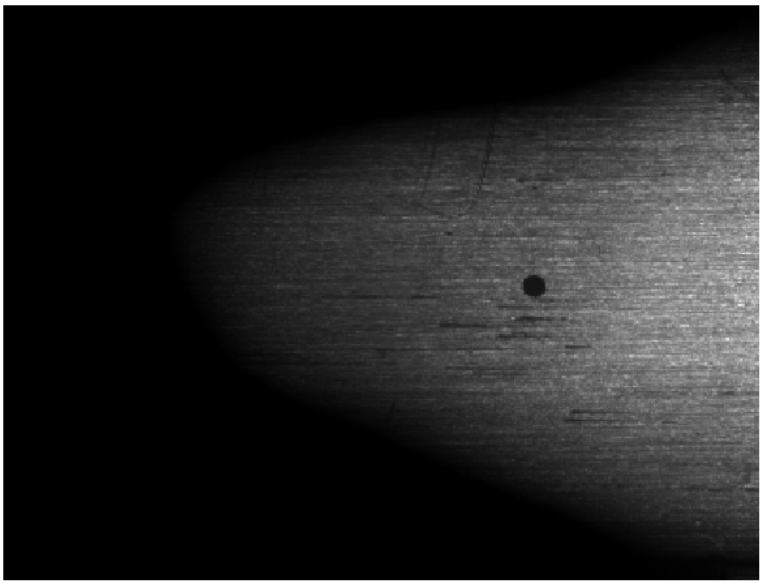

Figure B.6: Image of lighting correction formed by subtracting the flat-field background image from the background image.

B.1.3 Step 3.1: Generate binary images

The third step in the video processing algorithm was looping through every frame of the video, analyzing the frame, and storing bubble statistics in an array that could be input into the tracking algorithm in the subsequent step. Analyzing the frame first required converting it into a binary image, with bubbles being black and the rest of the image being white.

This process began by loading a frame of the data matrix (seen in Figure B.4(a)), correcting for lighting variation by subtracting Figure B.6, and then dividing by the flat-field

background image, Figure B.5. The subtraction identified those locations with significant brightness differences between the data frame and the 2-D flatfield corrected image. Locations with the same brightness were removed (e.g., the pressure taps, gold pads). Dividing by the 2-D flatfield image increased the contrast between the bubbles and the remainder of the image. A significant decrease in pixel brightness occurred after the subtraction in regions away from a bubble, while pixels at bubble locations saw less change due to the bubbles being dark. After division, locations away from bubbles saw their small pixel brightness divided by a relatively large value; locations at bubbles resulted in a value near one because the subtraction had little effect.

The result of this process was an image with only those features that were darker than the flat-field background image, see Figure B.7. These features represent the bubbles in the original data image (i.e., Figure B.4(a)).

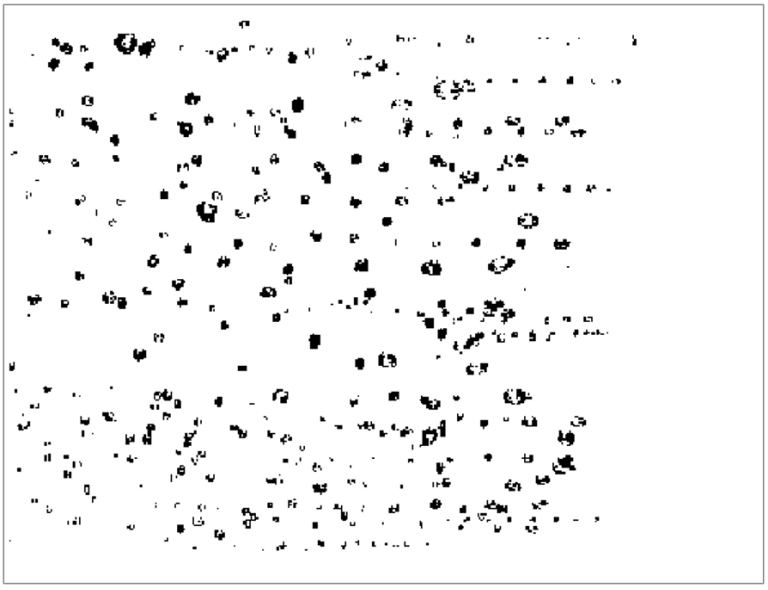

Figure B.7: Image of lighting correction formed by subtracting the flat-field background image from the background image.

Overlaying Figure B.7 in yellow onto the original data frame, Figure B.4(a), shows the ability of this process to separate dark regions from the background, as displayed in

Figure B.8.

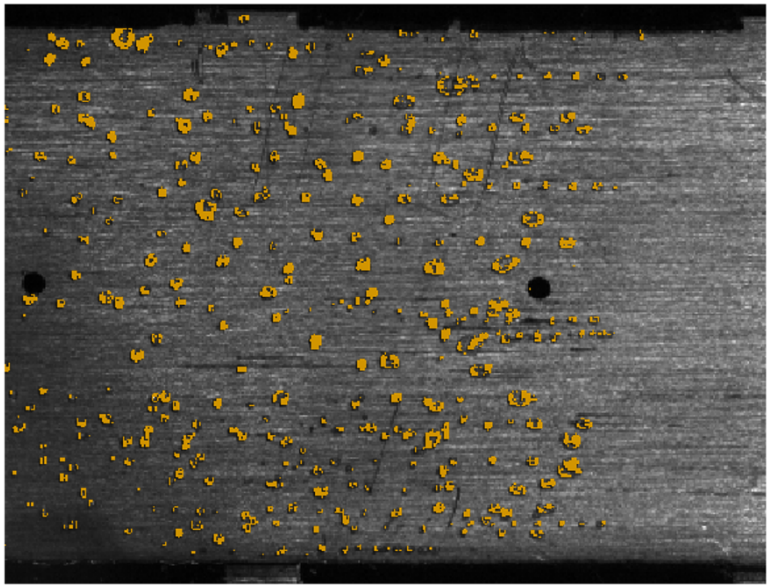

Figure B.8: Darker regions of the original data frame in yellow, overlaid on the original data frame.

This step was the most successful when there was a significant contrast between the bubble and the background surface. Locations circled in red in Figure B.9 show regions that were not identified by this process as a result of their brightness not being different enough from the original data frame. Overall, this step was successful because the vast majority of bubbles were correctly identified.

The Matlab toolbox for finding object areas, centroids, and feature shapes requires a binary image as the input. The bubble image in Figure B.7 was inverted to get an image where the objects of interest were white and the background was dark. The resulting image was converted into a binary image and can be seen in Figure B.10. There was no noticeable loss in image quality during this process since the grayscale image in Figure B.7 had a significant amount of contrast.

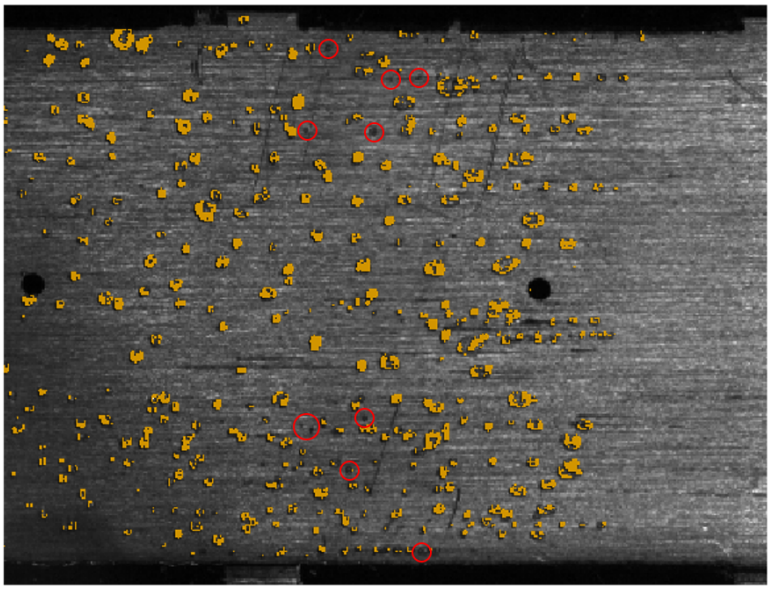

Figure B.9: Overlay image with red circles denoting locations of poor performance when identifying bubbles.

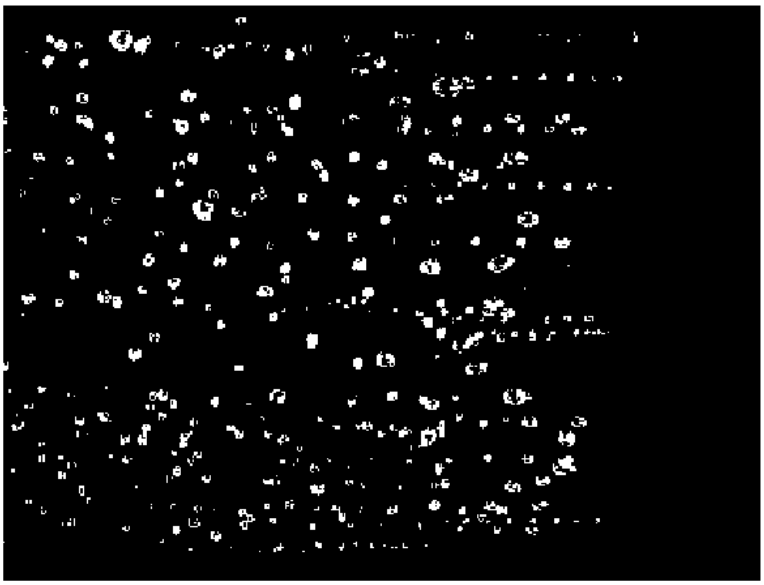

Figure B.10: Binary image of identified bubbles from original data frame.

B.1.4 Step 3.2: Clean image with morphological operations

Once the binary image was formed, morphological operations were used to bridge neighboring pixels separated by one dark pixel, delete areas with one lone white pixel, and fill

in regions of black completely surrounded by a white ring. The results of this process are shown in Figures B.11(a) and (b); where Figure B.10(b) has less roughness at the edges of each feature. Without the morphological operations, bubbles were often double or triple counted due to groups of white pixels being separated by even one black pixel. Over-application of morphological operations tended to cause the omission of small bubbles and merging of neighboring bubbles. The chosen algorithm was a compromise between these two options.

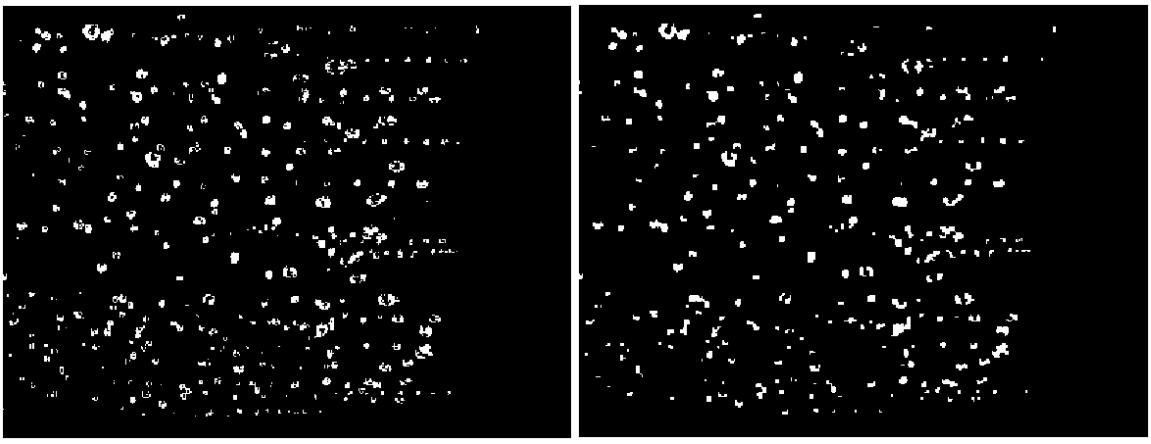

(a) (b)

Figure B.11: Data frame as a (a) binary image and the (b) cleaned version of the same image after morphological operations

B.1.5 Step 3.3: Blob Analysis

Matlab blob analysis could be used to obtain statistics for regions in a binary image. This analysis identified all groupings of white pixels and calculated spatial properties for each connected group of white pixels. This was used to return the area, centroid, and equivalent diameter of each grouping of white pixels in the morphologically cleaned image. Figure B.12 shows the results of the blob analysis for the first frame; the perfect circles qualitatively show the diameter of each detected feature, while the irregular pink objects

are those features detected after the import and cleaning processes. From these results, a table of all bubble centroid locations and their associated frame number could be tabulated as an input to the subsequent bubble-tracking algorithm.

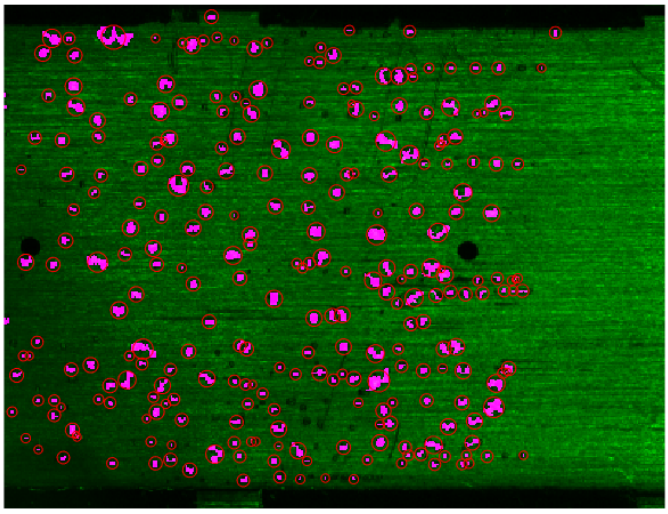

Figure B.12: Results of blob analysis overlaid on image showing difference between data frame and cleaned frame.

Figure B.13 shows the tradeoff between excessive and minimal morphological operations from Figure B.11. The white arrows in Figure B.13 point to two features joined by a small amount of pixels and could have benefited from more morphological operations. The white circles in Figure B.13 identify locations where bubbles were no longer detected due to a combination of poor identification during the image processing shown in Figure B.8 and morphological operations cleaning the features until they no longer existed. Morphological operations that would split adjoining bubbles also acted to further split bubbles that should have been connected. The compromise was chosen where the majority of bubbles were correctly identified, when comparing between a video with minimal bubbles and another video with roughly twice the number of bubbles present in Figure B.12.

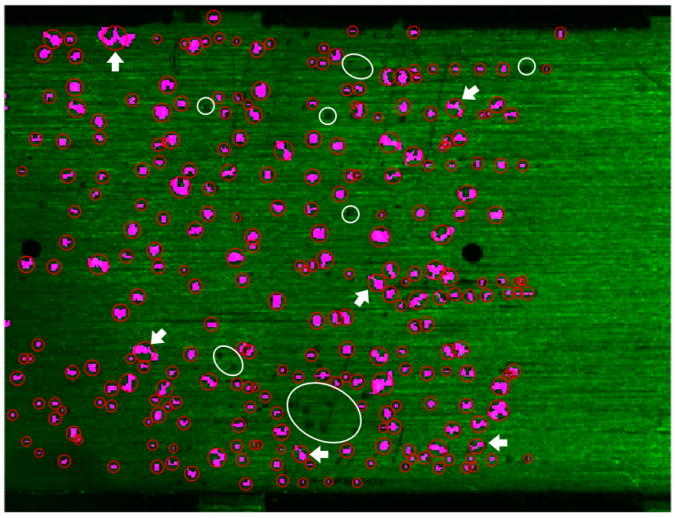

Figure B.13: Results of blob analysis overlaid on image showing difference between data frame and cleaned frame.

B.1.6 Step 4: Bubble tracking algorithm

The fourth step of the video analysis involved tracking bubbles from one frame to the next. This was accomplished using the Blair and Dufresne [36] particle-tracking routine, as adapted for Matlab from the method proposed by Crocker and Grier [37] and Crocker and Weeks [38]. Given the position of particles in a particular data frame, the tracking algorithm calculated all of the possible positions those particles could have moved to in the following frame; it then minimized the total squared displacement between those positions to link particles between the two frames. A particle was deemed *lost* if it was absent for more than 2 frames and short tracks were discarded if they were shorter than 5 frames long, to omit noise. Figure B.14 shows the raw image data frame with an overlay of the bubble tracks for the first 200 frames of the video.

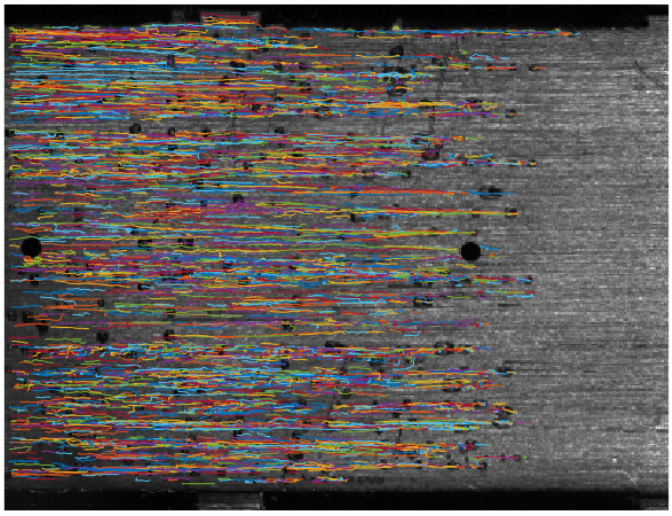

Figure B.14: Bubble tracking results

B.1.7 Step 5: Bubble track analysis

The fifth step included analyzing the tracks and extracting data. To limit the amount of poor data from the tracking algorithm, tracks shorter than 50 pixels in the streamwise direction were not considered in the subsequent analysis; each video frame was 400 pixels wide, which meant that a bubble had to be successfully tracked for 12.5% of the frame width to be considered a valid bubble track. Figure B.15 shows the results of this truncation of the data. This can be compared to Figure B.14 to see that particles starting near the left (downstream) edge of the image were omitted; these particles would have been those that started in the first frame.

Given the relevant tracks, the starting position of the remaining tracks could be calculated. A two-dimensional histogram was used to find all starting locations within 3 pixels of each other. The results of this can be seen in Figure B.16, where the color bar indicates the number of bubble tracks that started at the same location (within 3 pixels). The x-axis in Figure B.16 is relative to the upstream edge of the active heater, with positive x-values being downstream. The y-axis in Figure B.16 is relative to the centerline of the fluid chan-

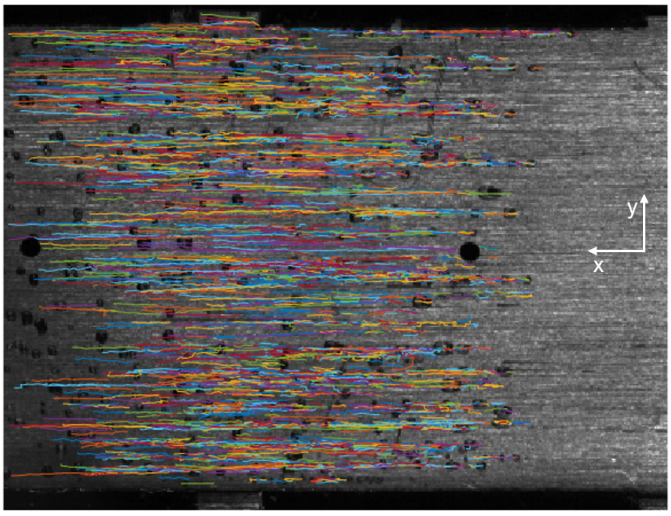

Figure B.15: Bubble tracking results, for tracks longer than 50 pixels

nel. The raw image from which this data was taken was 17.3 mm wide by 13.2 mm tall. Figure B.16 shows only those locations where bubble tracks started.

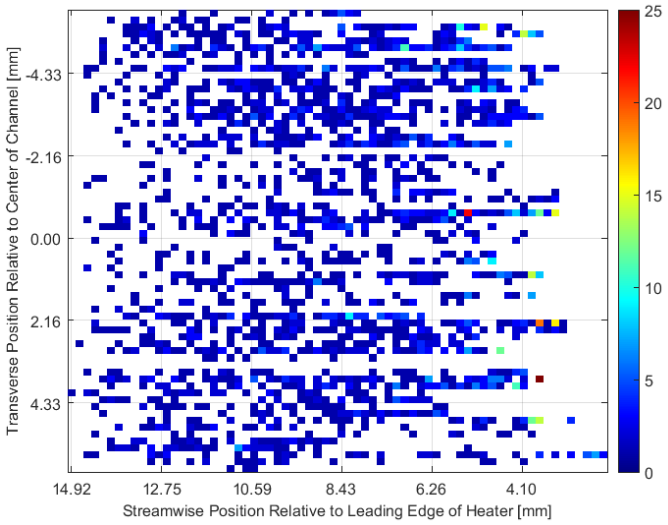

Figure B.16: Bubble track starting location density

Figure B.16 shows that the majority of identified bubble tracks began at the same spot less than five times. The locations where bubbles formed more than five times were located toward the leading edge of the heater. This was consistently seen and expected since the heat transfer coefficient associated with a sliding bubble acts to cool the surface

downstream of the nucleation front, thereby suppressing nucleation. Nucleation sites were considered for further analysis if they produced six or more bubbles within the analyzed frames. This value was chosen after manual analysis of videos showed bubble nucleation sites reliably nucleated at least that many times per video. Filming at 19,000 frames per second was fast enough for at least two frames to occur while each bubble was nucleating, and relatively stationary. For this reason, it was expected that there should be consistency among starting locations of bubble tracks. Occasionally bubbles would form at a frequency nearly equal to that of the camera; these bubbles were on the order of 0.25 mm in diameter.

The average nucleation rate at each location was calculated based upon the number of tracks that started at each location divided by the number of video frames in the analysis. A histogram for this sample video is shown in Figure B.17. The minimum bubble nucleation frequency that could be measured using this algorithm was 475 Hz assuming five nucleation events were seen in 200 frames, filmed at 19,000 frames per second. The maximum frequency observed was bubbles occurring every other frame, as previously noted, occurring at 9,500 Hz. Given the camera resolution, no bubbles were observed to nucleate faster than the frame rate of the camera.

As a characteristic of all nucleation events, the equivalent diameter could be summarized from the blob analysis as shown in Figure B.18. The shape and magnitude of diameters is more important than the absolute count across the 200 video frames.

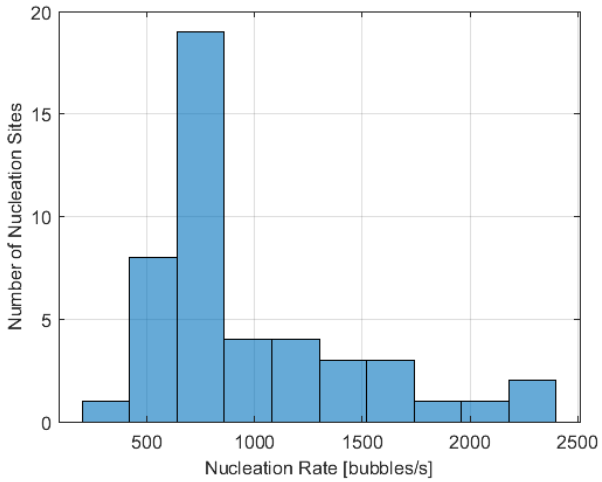

Figure B.17: Frequency of bubble tracks starting at same location

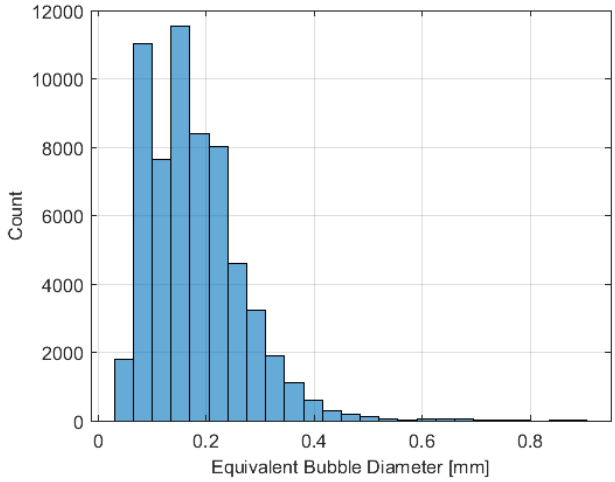

Figure B.18: Bubble diameter count across 200 video frames.

B.2 Results

A few videos were analyzed and verified to be approximately equal to a manual count. Subsequently, 277 videos were analyzed and it was clear that significant changes needed to be made to improve results. The decision was made to stop development of the bubble tracking algorithm and complete the analysis by manual count. Figure B.19 shows that the algorithm consistently under counted the number of bubbles nucleating in each video,

and was inconsistent in identifying nucleation sites. There are a number of reasons for this poor prediction.

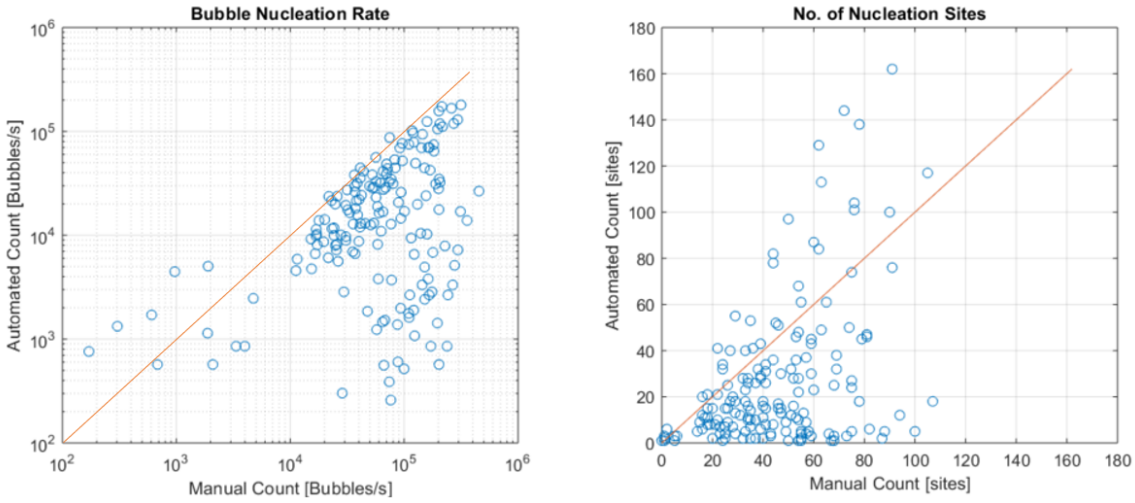

Figure B.19: Comparison of video processing algorithm against manual count.

B.2.1 Bubble Size Relative to Channel Size

The algorithm excelled when bubbles appeared as mostly solid dark circles; this occurred when bubbles were equal to or less than the fluid channel height. Bubbles with diameters larger than the channel dimension lost sphericity and developed flats on the glass and top surface of the channel. Flat facets on a bubble failed to specularly reflect light and returned bright patches; sometimes these features focused the light, other times the flat facets transmitted the background through the bubble.

The effects of this can more clearly be seen with larger bubbles. Figure B.21(a) shows a data frame for R123 prior to analysis. Figure B.21(b) shows the result of blob analysis for the morphologically cleaned image. The white arrows point to large bubbles with incomplete perimeters. This happened when the perimeter of a bubble was not uniformly dark and the non-uniformity was too large for morphological operations to close; only features

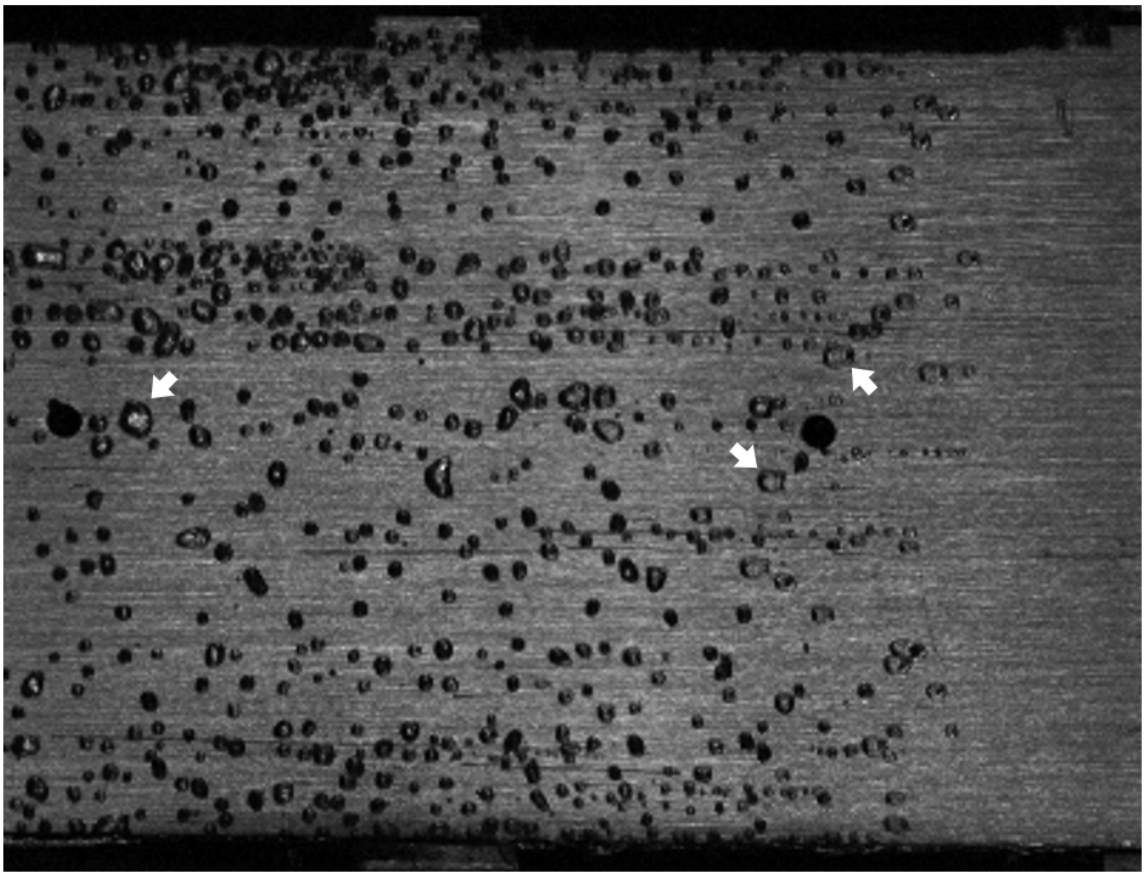

Figure B.20: Image of HFE7000 nucleation showing larger bubbles becoming brighter in the center.

with complete perimeters were filled. The blue arrows point to some of the bubbles that were either touching or so close that morphological operations filled in the missing pixel and joined them. The gold arrows show successfully identified bubbles that were a result of completely identified perimeters that could be filled and were not in contact with other bubbles.

The behavior of features described by the white arrows was an artifact of the morphological operations; several of these operations depended on the presence or absence of a single pixel joining or separating bubbles. The single pixel nature of this behavior led to noisy bubble tracks. When the split or joined bubble tracks lasted longer than 50 pixels,

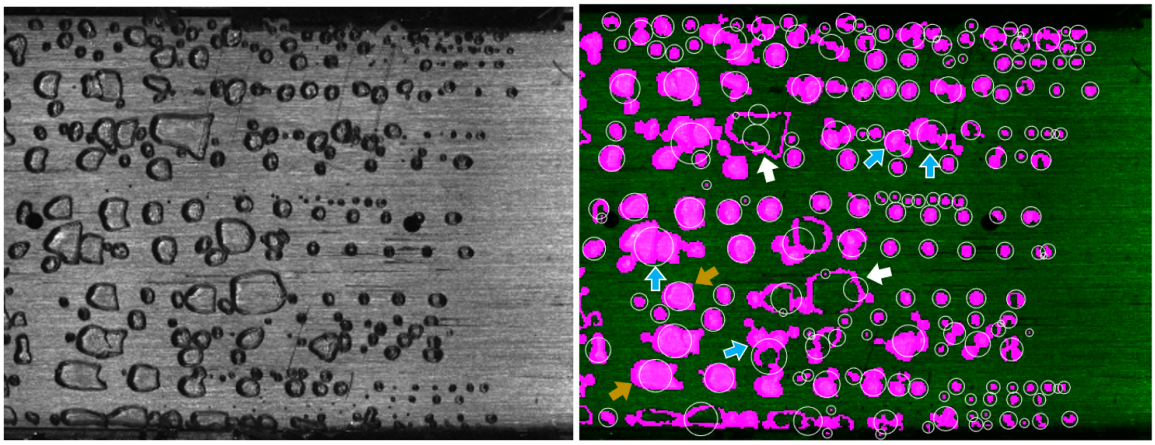

(a) (b)

Figure B.21: Image of HFE7000 frame (a) before analysis and (b) after analysis showing identified bubbles. White arrows show single bubbles that were identified as many bubbles; blue arrows show many bubbles that were identified as one bubble; and yellow arrows point to large bubbles that were successfully identified because they had complete perimeters after morphological operations.

they counted as a nucleation site despite being an artifact of morphological operations. This inflated the number of nucleation sites. The total bubble count was always low due to the low contrast between the background and the bubble as the bubble size decreased. The fastest nucleation frequencies (near 19 kHz) were from the smallest bubbles, which exaggerated the under count. This trend can be seen in Figure B.3, for example, and several of the previous figures.

Another cause for deviation in results from the algorithm was the tracking problems encountered when a bubble formed underneath another bubble. For example, Figure B.22 shows a sequence of images with a bubble nucleating at 26 μs, underneath part of a passing bubble. Such behavior is unable to be captured by the tracking algorithm. Most of the time bubbles nucleated from a site at a constant rate independent of passing bubbles.

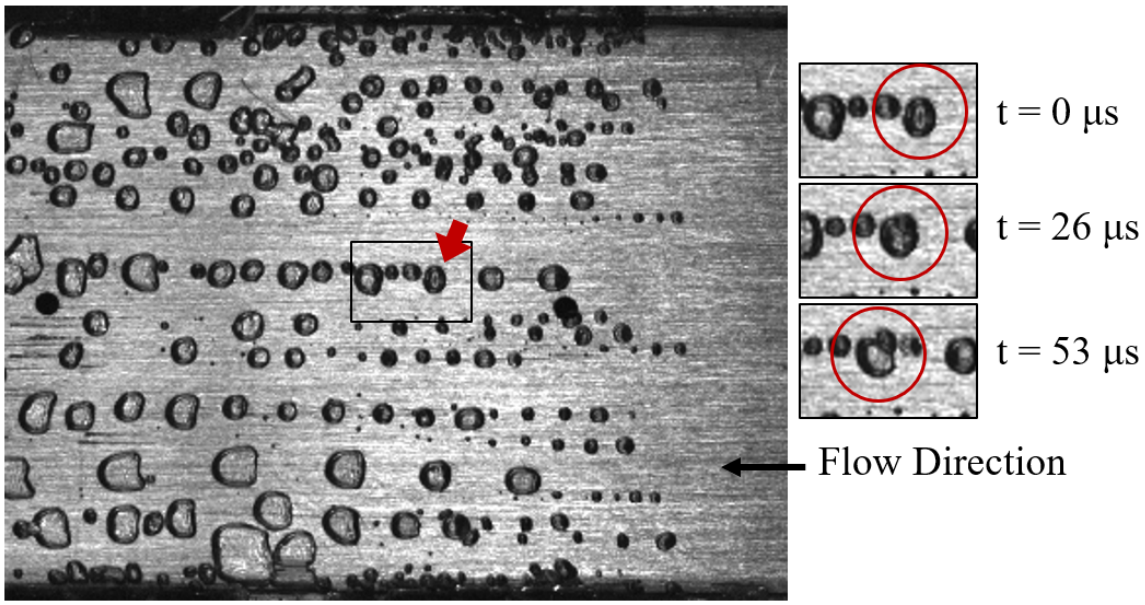

Figure B.22: Sequence of images showing a bubble nucleating from underneath a passing bubble

B.2.2 Spatial calibration of videos

The location of the pressure taps in each video were known to be 11.43 mm apart. A measurement of the number of pixels between the centers of each pressure tap could then be used to calibrate the length scales of each video. To locate each pressure tap, the flat-field background image was split into halves, one containing the right-most pressure tap, and the other the downstream pressure tap. Each image half could be analyzed using Sobel edge detection to find locations of maximum gradients in brightness. The pressure taps were the only circular features in the image halves. Knowing the distance between adjacent pressure taps to be 11.43 mm, this could be divided by the calculated distance between pressure taps in pixels, resulting in a calibration length of 43.3 μm/pixel in the x-direction.

The measured distance between the y-values at the edges of the nozzle measured 289 px. Each nozzle was machined to a width of 12.47 $\pm$ 0.01 mm. Dividing these values

results in a scaling length of 43.2 μm/pixel in the y-direction. This justified using the distance between pressure taps as the length calibration for both the x-direction and y-direction.

Appendix C

Supplemental Figures

The normal properties for each test fluid are shown in Table C.1.

Table C.1: Normal fluid properties for each test fluid

Fluid	Thermodynamic Properties							Transport Properties			
	P kPa	T_{sat} C	ρ_l kg/m^3	ρ_v kg/m^3	c_p J/kg-K	Δh_{fg} J/kg	σ N/m	k_l W/m-K	μ_l kg/m-s	α_l m^2/s	Pr -
HFE7000	101.325	34.2	1379	8.40	1259	133,640	0.01131	0.072	3.79E-4	4.18E-8	6.58
R123	101.325	27.8	1457	6.47	1039	170,585	0.01485	0.076	4.04E-4	5.05E-8	5.49
R245fa	101.325	15.2	1365	5.96	1302	196,028	0.0149	0.084	4.66E-4	4.73E-8	7.21

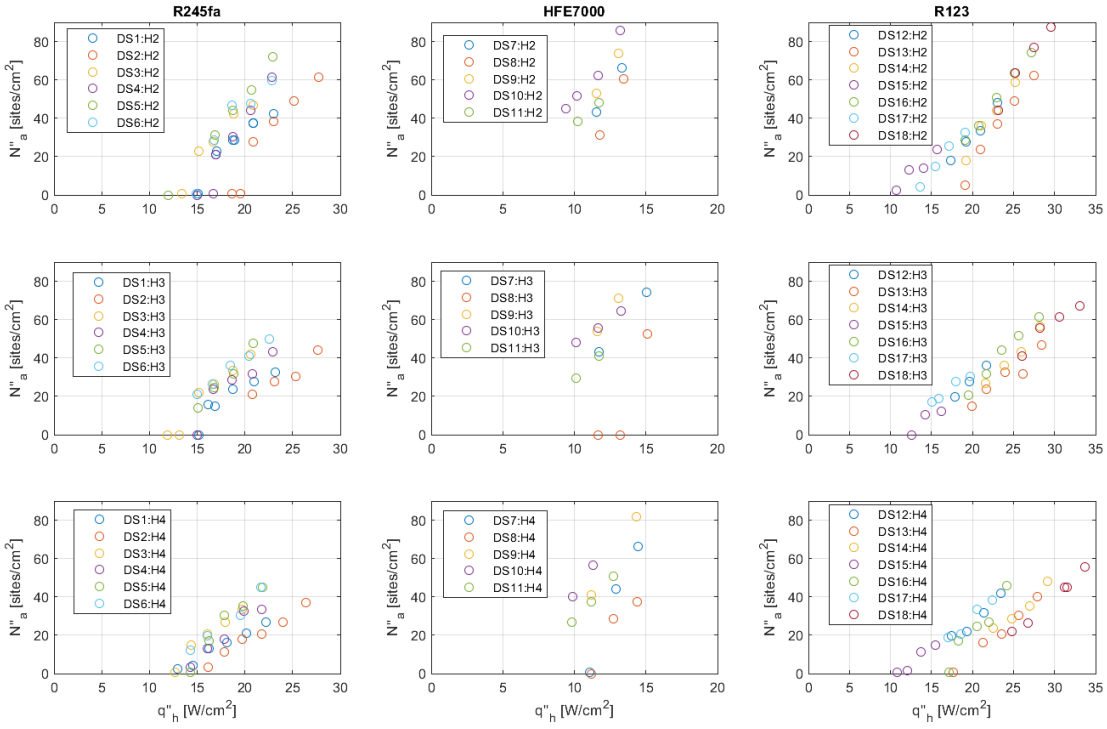

Figure C.1: Comparison of all N_a'' and q_h'' data where the columns split between fluids–R245fa, HFE7000, R123; and the rows split between heaters–H2, H3, H4

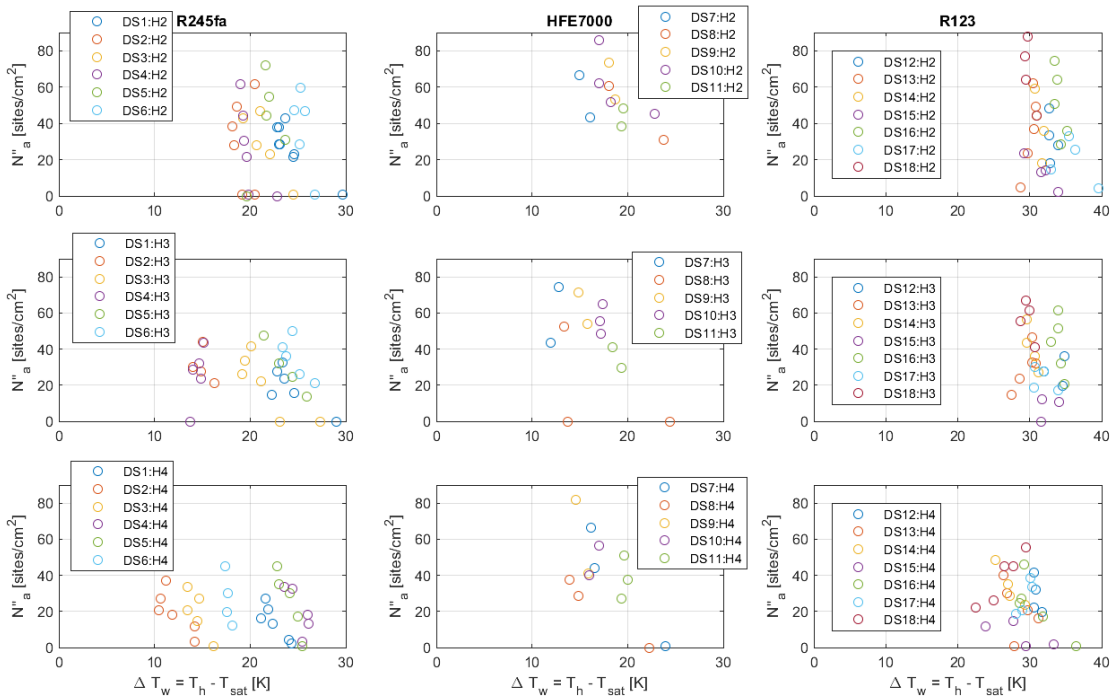

Figure C.2: Comparison of all N_a'' and ΔT_w data where the columns split between fluids–R245fa, HFE7000, R123; and the rows split between heaters–H2, H3, H4

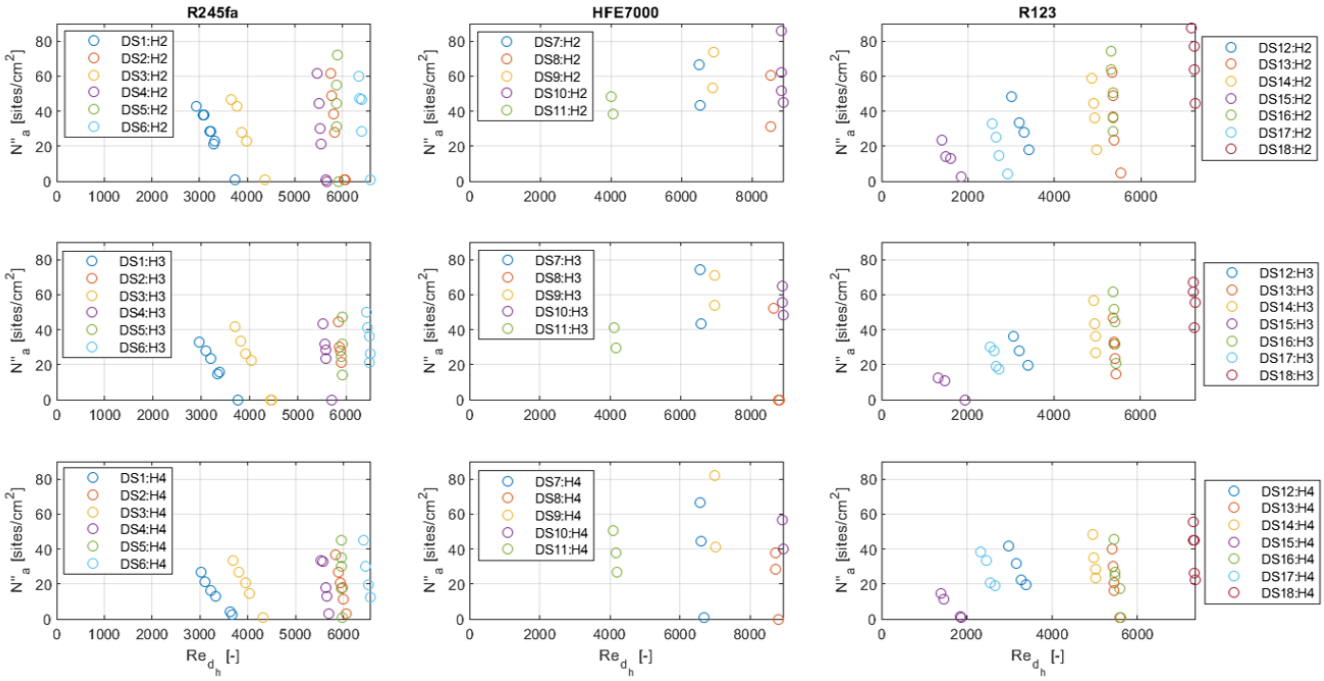

Figure C.3: Comparison of all N_a'' and Re_{d_h} data where the columns split between fluids–R245fa, HFE7000, R123; and the rows split between heaters–H2, H3, H4

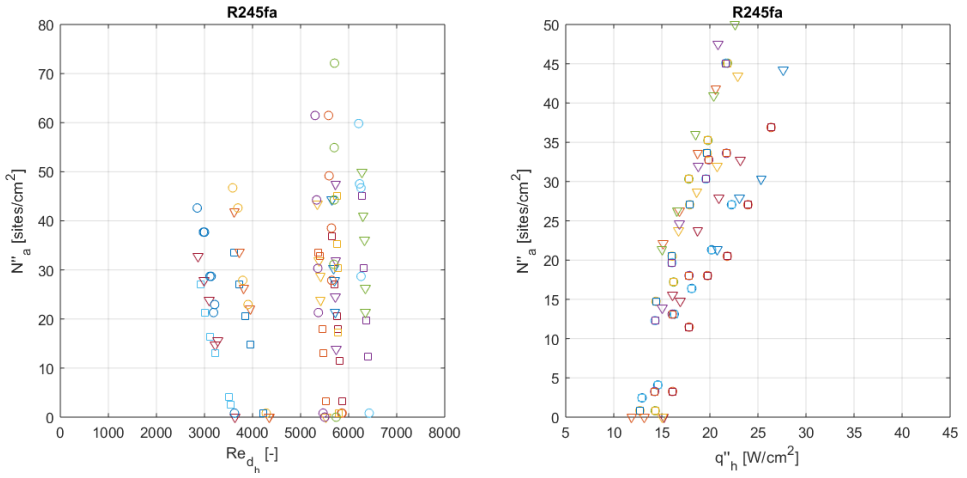

(a)

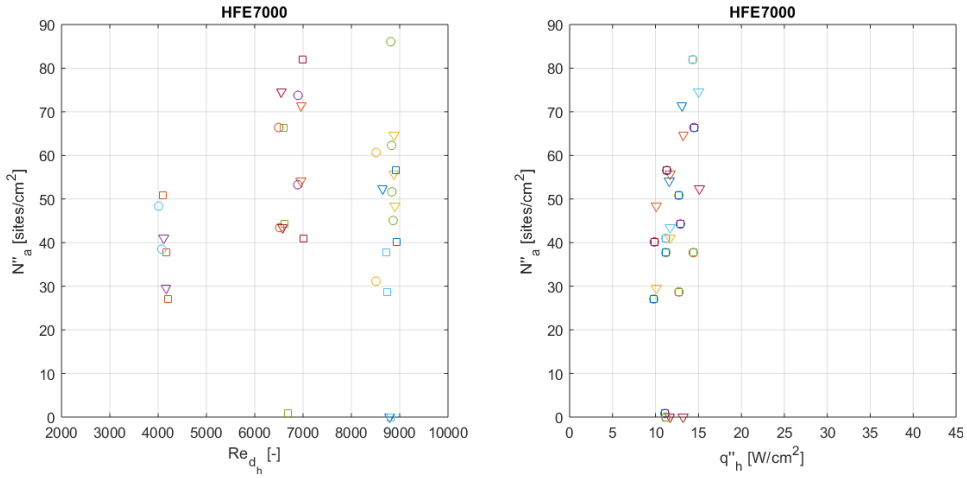

(b)

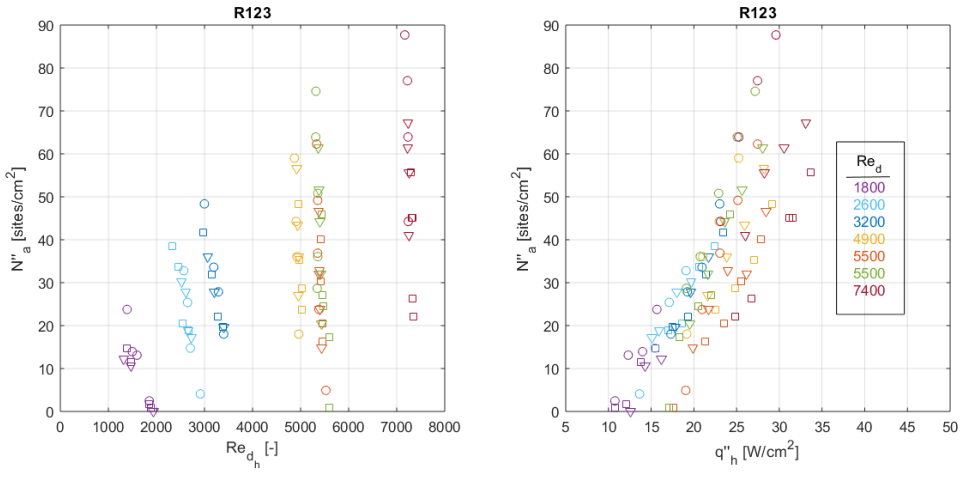

(c)

Figure C.4: Comparison of all N_a'' and q'' at different Re_d for (a) R245fa, (b) HFE7000, and (c) R123. Data at H2 are represented by circles, H3 by triangles, and H4 by squares.

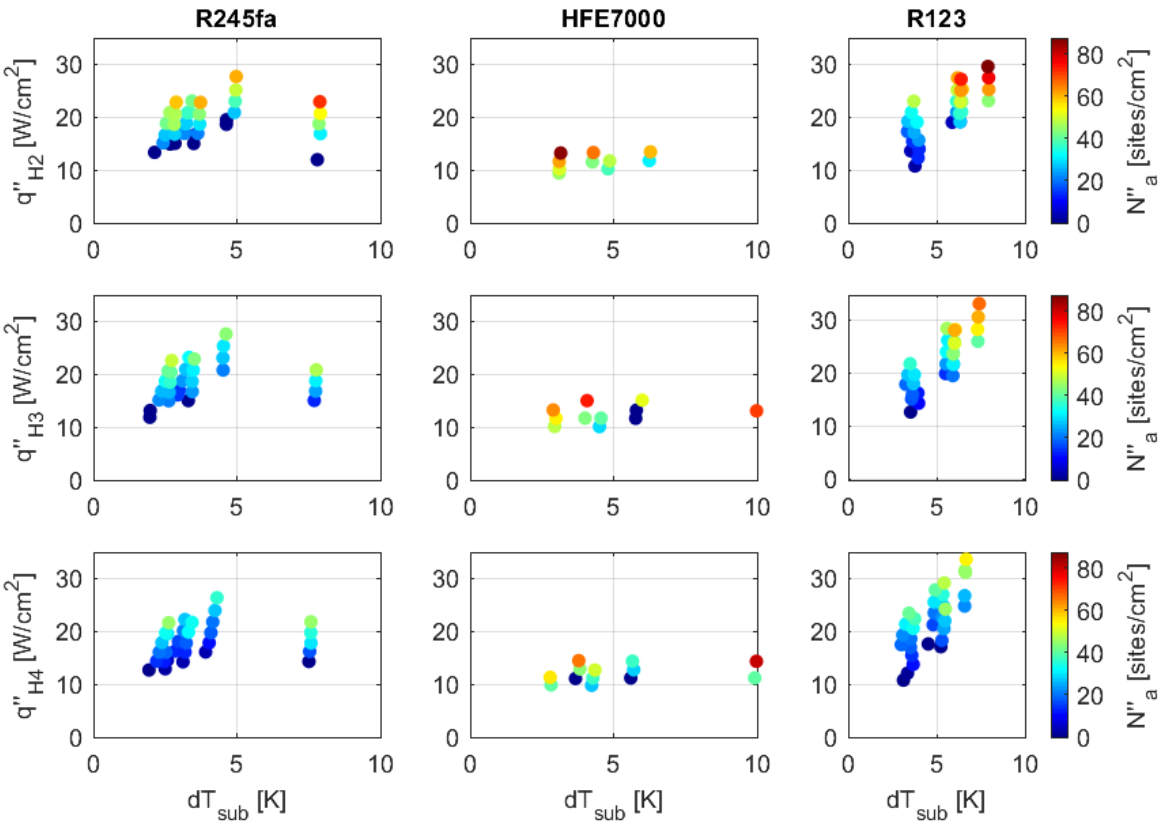

Figure C.5: Comparison of all N_a'' and dT_{sub} data where the columns split between fluids–R245fa, HFE7000, R123; and the rows split between heaters–H2, H3, H4

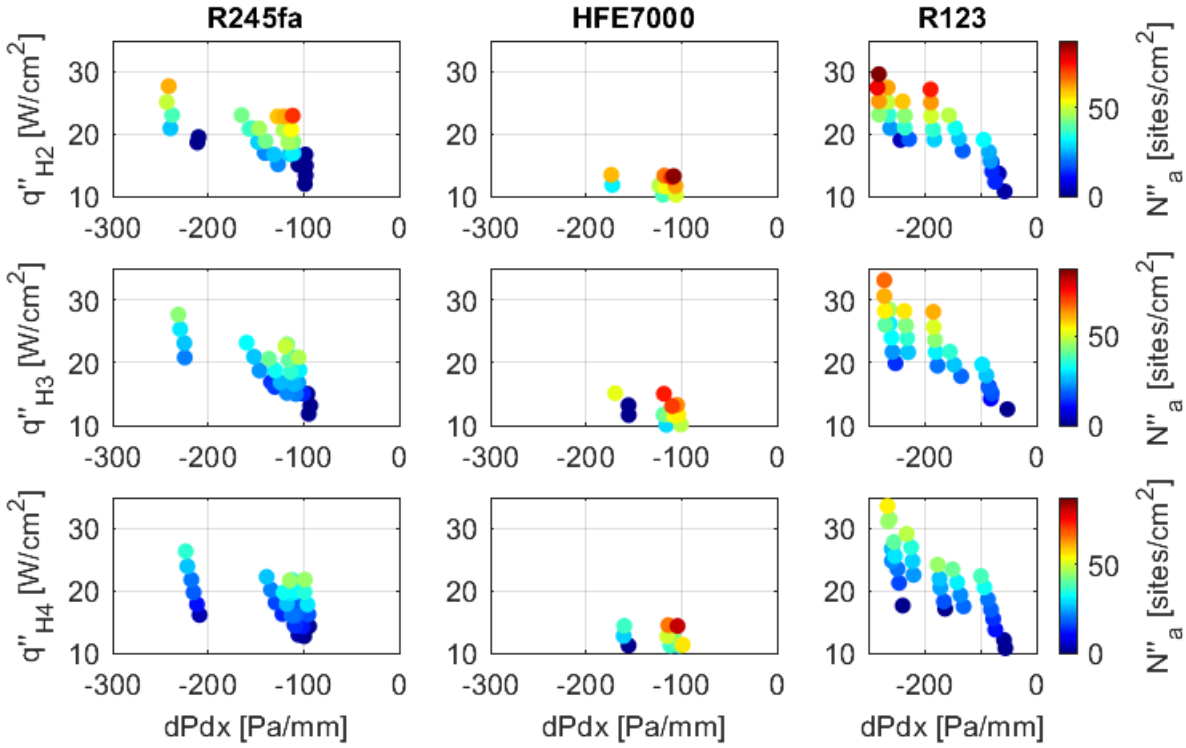

Figure C.6: Comparison of all N_a'' and $dPdx_{vid}$ data where the columns split between fluids–R245fa, HFE7000, R123; and the rows split between heaters–H2, H3, H4

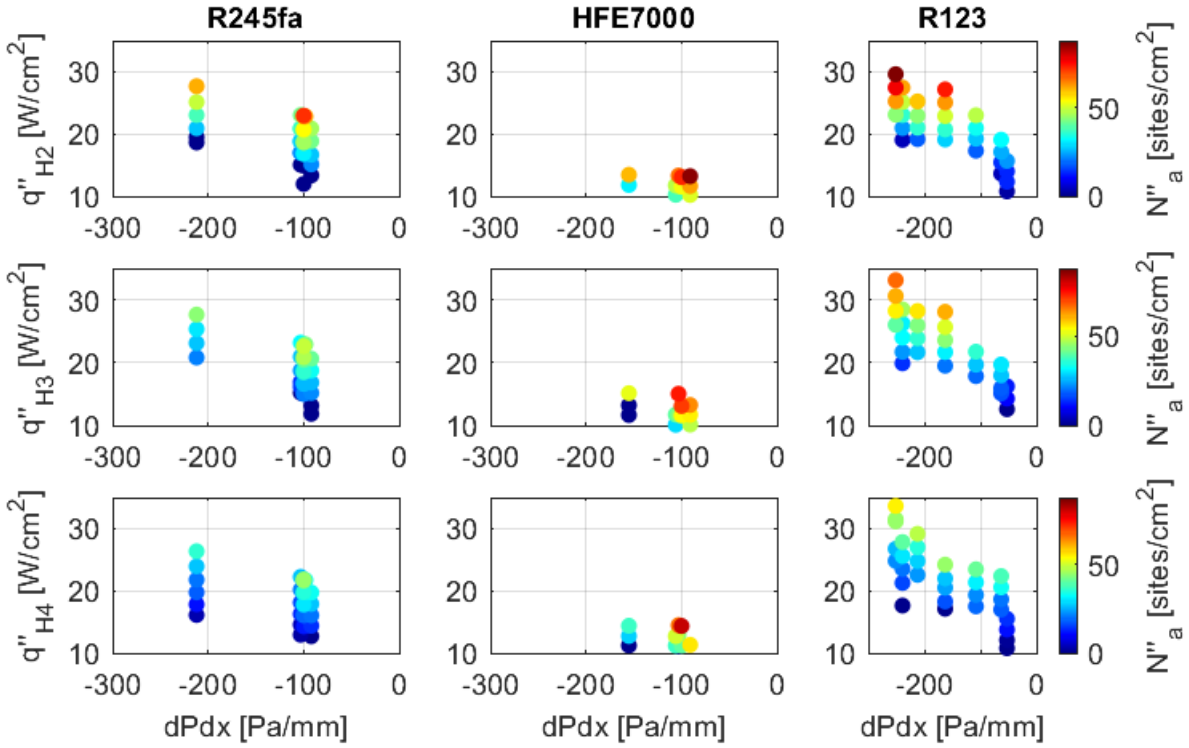

Figure C.7: Comparison of all N_a'' and $dPdx_{pre,vid}$ data where the columns split between fluids–R245fa, HFE7000, R123; and the rows split between heaters–H2, H3, H4

Appendix D

Nucleation Correlations

The correlations for active nucleation site density, N_a'', compared in Chapter 5 are presented here, with their supplemental relations, as they were implemented. All of the correlations for N_a'' have units [sites/cm^2].

D.1 Correlations of the form $N_a'' = f(T, R_c)$

Basu et al. [3]

$$N_a'' = \begin{cases} 3.4 \times 10^{-1}(1-\cos\theta)\Delta T_w^{2.0} & \text{for } \Delta T_{w,ONB} \leq \Delta T_w \leq 15 \text{ K} \\ 3.4 \times 10^{-5}(1-\cos\theta)\Delta T_w^{5.3} & \text{for } \Delta T_w > 15 \text{ K} \end{cases} \tag{D.1}$$

Benjamin and Balakrishnant [4]

$$N_a'' = 218.8\text{Pr}^{1.63}\theta_{bb}^{-0.4}\gamma^{-1}(\Delta T_{sat})^3 \, \frac{1 \text{ m}^2}{100^2 \text{ cm}^2} \tag{D.2a}$$

$$\text{where} \quad \theta_{bb} = 14.5 - 4.5 \times 10^6 \left(\frac{R_a P}{\sigma}\right) + 4 \times 10^{11} \left(\frac{R_a P}{\sigma}\right)^2 \tag{D.2b}$$

$$\gamma = \sqrt{\frac{k_w \rho_w c_{p,w}}{k_l \rho_f c_{p,l}}} \tag{D.2c}$$

Hibiki and Ishii [5]

$$N_a'' = \overline{N_n}\left\{1 - \exp\left(\frac{-\theta^2}{8\mu^2}\right)\right\}\left[\exp\left\{f(\rho^+)\frac{\lambda'}{R_c}\right\} - 1\right] \tag{D.3a}$$

where $\overline{N_n} = 47.2 \quad [\text{sites/cm}^2]$ (D.3b)

$$\mu = 0.722 \quad [\text{rad}] \tag{D.3c}$$

$$f(\rho^+) = -0.01064 + 0.48246\rho^+ - 0.22712(\rho^+)^2 + 0.05468(\rho^+)^3 \tag{D.3d}$$

$$\rho^+ = \log(\rho^*) = \log\{(\rho_f - \rho_g)/\rho_g\} \tag{D.3e}$$

$$\lambda' = 2.5 \times 10^{-6} \quad [\text{m}] \tag{D.3f}$$

$$R_c = \frac{2\sigma\{1 + (\rho_g/\rho_f)\}/P_f}{\exp\{h_{fg}(T_g - T_{sat}))/(RT_gT_{sat})\} - 1} \approx \frac{2\sigma T_{sat}}{\rho_g h_{fg}(T_w - T_{sat})} \tag{D.3g}$$

$$R = R_g(MW) \quad [\text{J/kg-K}] \tag{D.3h}$$

Kocamustafaogullari and Ishii [6]

$$N_a'' = \frac{N_a^*}{D_d^2}\,\frac{1\ \text{m}^2}{100^2\ \text{cm}^2} \tag{D.4a}$$

where $N_a^* = f(\rho^*)\ (R_c^*)^{-4.4}$ (D.4b)

$$f(\rho^*) = 2.157 \times 10^{-7}(\rho^*)^{-3.2}(1 + 0.0049\rho^*)^{4.13} \tag{D.4c}$$

$$\rho^* = (\rho_f - \rho_g)/\rho_g \tag{D.4d}$$

$$R_c^* = \frac{R_c}{D_d/2} \tag{D.4e}$$

$$R_c = \frac{2\sigma\{1 + (\rho_g/\rho_f)\}/P_f}{\exp\{h_{fg}(T_g - T_{sat}))/(RT_gT_{sat})\} - 1} \approx \frac{2\sigma T_{sat}}{\rho_g h_{fg}(T_w - T_{sat})} \tag{D.4f}$$

$$D_d = 2.5 \times 10^{-5}(\rho^*)^{0.9}\theta\left[\frac{\sigma}{g(\rho_f - \rho_g)}\right]^{1/2} \tag{D.4g}$$

$$R = R_g(MW) \quad [\text{J/kg-K}] \tag{D.4h}$$

Lie and Lin [7]

$$N_a'' = \left(80352 + 8034\Delta T_{sat}^{1.67} N_{conf}^{0.51}\right) \frac{1\ [\mathrm{m}^2]}{100^2\ [\mathrm{cm}^2]} \tag{D.5a}$$

$$\text{where} \quad N_{conf} = \frac{1}{d_h}\sqrt{\frac{\sigma}{g(\rho_f - \rho_g)}} \tag{D.5b}$$

Ren et al. [8]

$$N_a'' = 6.9 \times 10^5 \Delta T_w^{4.19} {\mathrm{Re}_{d_h}}^{-0.93} \exp\left(-0.05\mathrm{Ja}_{sub}\right) \frac{1\ [\mathrm{m}^2]}{100^2\ [\mathrm{cm}^2]} \tag{D.6a}$$

$$\text{where} \quad \mathrm{Ja}_{sub} = \frac{\rho_f c_{p,l} \Delta T_{sub}}{\rho_g h_{fg}} \tag{D.6b}$$

Wang and Dhir [9]

$$N_a'' = 5.0 \times 10^5 (1 - \cos\theta) D_c^{-6} \quad \text{where } D_c \text{ is in } \mu\mathrm{m} \tag{D.7a}$$

$$\text{where} \quad D_c = \frac{4\sigma T_{sat}}{\rho_g h_{fg} \Delta T_w} \frac{1 \times 10^6\ \mu\mathrm{m}}{1\ \mathrm{m}} \tag{D.7b}$$

Zhokhov [10], as referenced by Pioro et al. [12]

$$N_a'' = 5 \times 10^{-13} * R_c^{-3} \frac{1\ [\mathrm{m}^2]}{100^2\ [\mathrm{cm}^2]} \tag{D.8}$$

D.2 Correlations of the form $N_a'' = f(q'')$

Again, all N_a'' has units of [sites/cm^2]; heat flux, q'', has units [W/cm^2]; all other variables are in their base SI units.

Aoki [15]

$$N_a'' = 2.79(q'')^1 \tag{D.9}$$

Dhir and Liaw [16]

$$N_a'' \propto (q'')^{1.5} \tag{D.10}$$

Gaertner and Westwater [17]

$$N_a'' = 1.48e4(q'')^{2.13} \tag{D.11}$$

Hahne and Barthau [18] The data from Figure 6 in Hahne and Barthau [18] can be split into two regions as shown in Figure D.1

$$N_a'' = \begin{cases} 1.45 \times 10^3 (q'')^3 & \text{for } q'' < 0.5 \text{ W/cm}^2 \\ 4.53 \times 10^2 (q'')^{1.6} & \text{for } q'' > 0.5 \text{ W/cm}^2 \end{cases} \tag{D.12}$$

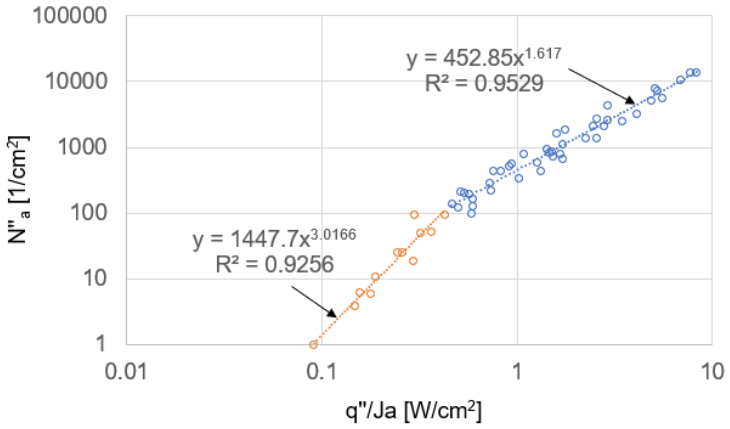

Figure D.1: Data extracted from Figure 6 of Hahne and Barthau [18] to establish $N_a'' = f(q''/Ja)$ regressions.

Kurihara and Myers [19]

$$N_a'' = 1.804 \times 10^{-3} \frac{\mu_l h_l^3}{\rho_g k_l^3} \text{Pr}^{2.67} \tag{D.13}$$

The conclusions by Luke and Cheng [20] did not suggest any correlations between N_a'' and q'', however Figure 8 from Luke and Cheng [20] does provide a general correlation of

$$N_a'' \propto (q'')^n \tag{D.14}$$

where n is 1.2 for propane nucleation on finely sandblasted and emery ground copper and $n = 2.55$ for propane on emery ground copper with a longer observation interval.

Mikic and Rohsenow [21]

$$N_a'' \propto (q'')^1 \tag{D.15}$$

Wang and Dhir [9]

$$N_a'' \propto (q'')^2 \tag{D.16}$$

Appendix E

Boiling Theory

E.1 Introduction

Boiling heat transfer is of significant importance to the modern world. A variety of devices rely on the heat transfer performance that is a result of a liquid boiling, including the fields of refrigeration, air conditioning, power generation, food processing, chemical synthesis, electronics cooling and many more. The concept of a boiling liquid is so commonplace that it would likely come as a surprise to most people that science does not really know how boiling works.

Seemingly the most common question being asked in the mechanical engineering field on this topic is *what factors contribute to boiling heat transfer?* Within this question, one is interested in the causes of bubble growth, the heat transfer mechanisms for a stationary bubble, the heat transfer mechanisms for a moving bubble, the effects of bubble coalescence, the precursors of critical heat flux, etc.; there are too many sub-inquiries to name even half of them. If all of the contributing factors were known, along with their interactions, one could design optimal devices at lower cost with superior performance.

Heat transfer mechanisms during ebullition are a main focus of research today; historically, one of the main focuses has been locating where and how bubbles formed. By the 1960s, the idea of bubble origin had become nearly immutable (i.e., bubbles formed from cavities and crevasses that had a pre-existing vapor). This theory of the pre-existing vapor (PEV) worked fairly well as an approximate theory; however, an increasing amount of experimental evidence suggests that bubble formation is more complex than previously thought. This led one researcher, in 1999, to write a paper entitled “What do we really

know about nucleate boiling?" [31].

What follows is a chronological review of research that has led to the current state of knowledge surrounding boiling theory as it pertains to heterogeneous bubble nucleation.[1]

E.2 The 1930s & Earlier

Prior to the 1930s[2], boiling was a problem of dimensional analysis. Studies were undertaken to discover which variables altered the relation between the heat flux and surface-to-liquid temperature difference. A brief history of these studies is provided by Drew and Mueller [54] in their 1937 "state of the art [review] of boiling". The relation between the heat transfer coefficient and surface-to-liquid temperature difference was thought to be of the form shown in Equation E.1 where the coefficient, a, depended on the fluid and the exponent, b, varied from study to study.

$$h = a(\Delta T)^b \tag{E.1}$$

The coefficient, a, in Equation E.1 was shown to vary from 0.505 for n-Butanol to 60.8 for water. Exponent b varied between 2.4 and 2.5, until a study of superior elaborateness suggested the exponent be equal to 4. All of the studies relating variables in Equation E.1 were done at atmospheric pressure because it was known that "lowering the boiling point by reducing the pressure lowers the coefficient" [54].

In 1931, Jakob and Fritz [55] showed that emery roughened surfaces temporarily in-

[1] Statistical mechanics is not included in this research since it can not be used as a predictive tool at this time. The works of Carey [48], Helrich [49], Israelachvili [50], Debenedetti [51] provide a good review of such behavior.

[2] While the value of any literature review is based on the thoroughness of its investigation, this review does not discuss the ontological ideas of Galileo, in the 1500s, through the 1800s. For a review of such material, see Mitrovic [52] and Bhavnani et al. [53]

creased heat transfer performance; after some time submerged in water, or left to oxidize, the boiling performance degraded. Temporary removal from the water saw renewed performance. The same phenomenon was seen with smooth surfaces. In addition, it was seen that liquid near the heater surface was superheated, as seen in Figure E.1.

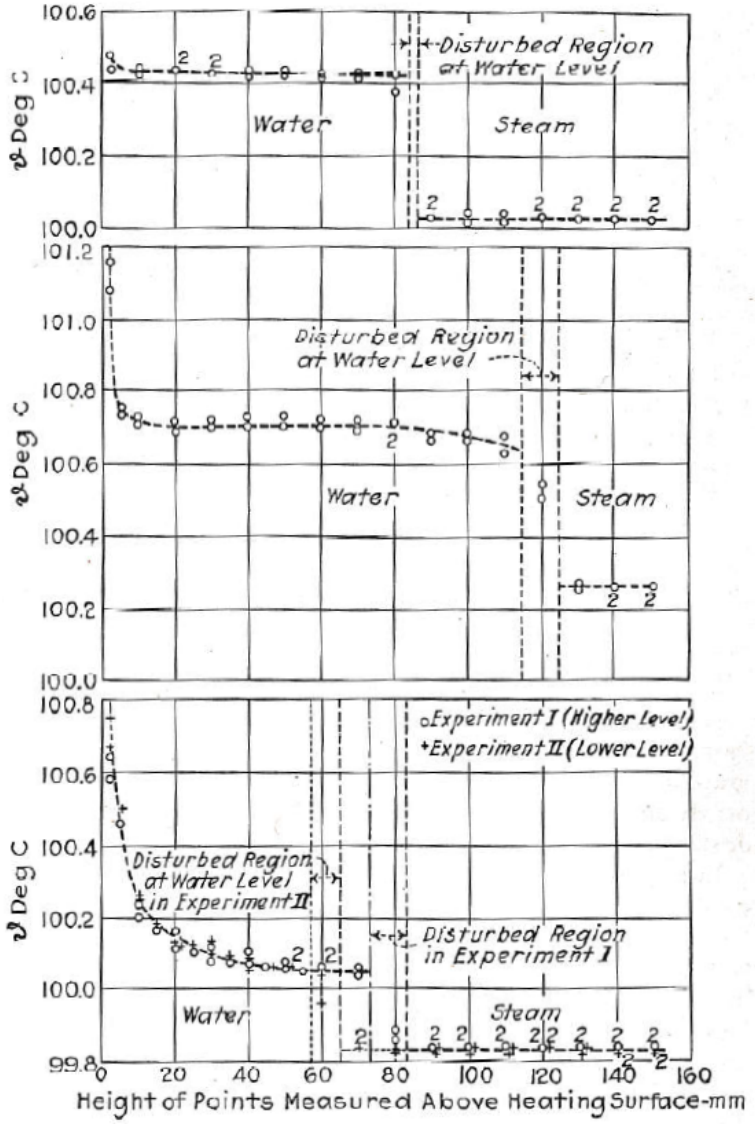

Figure E.1: Reproduction of Figure 12 from Jakob [2] showing that the liquid nearest to the heater surface approached the heater surface temperature, superheating above the saturation temperature of the bulk fluid. The three different plots reference different heat loads.

In the discussion that follows the article by Drew and Mueller [54], W. H. McAdams states that a four-fold improvement in heat transfer was seen after letting the test apparatus sit for four hours. This is the opposite behavior of that found by Jakob and Fritz [55], where the heat transfer performance degraded with time. It was theorized that "a slight deposit of foreign matter made the surface respond better" [54].

Three years later, in 1934, one of the first, if not the first, quantitative studies of the entire boiling curve was a Japanese paper presented by Nukiyama [56]. Nukiyama used Joule heating of various wires to study the interaction between the heat transfer rate and the surface temperature of the wire. It is from this study that the prototypical boiling curve was established [54], which has been reproduced in Figure E.2 with heat transfer rate in the y-axis and temperature departure on the x-axis. The main objective of

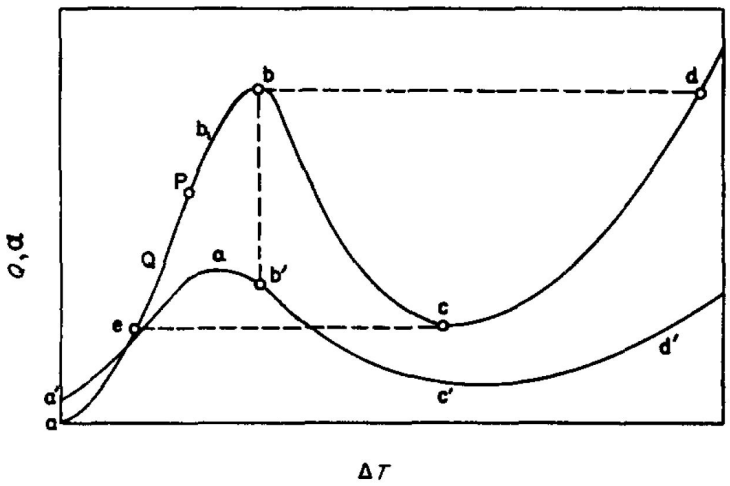

Figure E.2: Reproduction of Figure 2 from Nukiyama [56] showing the fundamental shape of a boiling curve with axes being the heat transfer rate, Q, versus ΔT, the difference between the surface and liquid temperatures.

Nukiyama was to investigate the peculiar heat transfer behavior of a fluid moving along path *bcd* of Figure E.2, from critical heat flux to film boiling, in addition to path *ce*, quenching from the point of minimum heat flux (known as the Leidenfrost Point). Little attention was given to the point at which boiling initiated, save for, "when the vaporization is mild,

the bubbles are seen first from the surface where there are scratches or impurities on the surface"[56].

Deferring to the authority of the review by Drew and Mueller [54], "in regard to the mechanism of nucleation boiling there is little add to the papers of Jakob and his followers"; the English translation of such papers was reviewed in Jakob [2]. This review begins with Equation E.2, which was proposed by W. Thomson (Lord Kelvin) to describe the curvature-driven pressure differences in a fluid. According to Lord Kelvin, the saturation pressure at the concave fluid surface, p_c, is not equal to the saturation pressure at a planar surface, p_s, but is lesser by the quantity given on the right side of Equation E.2. This quantity is driven by the surface tension, σ, radius of the concave surface, R, density of the saturated fluid, ρ', and the density of the saturated steam, ρ''.

$$p_c = p_s - \frac{2\sigma}{R}\frac{\rho''}{\rho' - \rho''} \tag{E.2}$$

From Equation E.2 it was recognized that, "in an absolutely pure liquid no vapor bubbles can originate at all, the initial diameter of such bubbles being infinitely small and the superheat infinitely high" [2]. Jakob goes on to say that practically, "water can be evaporated without considerable superheating if care is taken that there exist in the liquid sufficiently small curved surfaces on which the steam molecules can collect," referring to the textured surface of the containment vessel and bubbles attached to such surfaces. It is also mentioned that Bošnjaković was the first to connect the superheating of the liquid to the growth of a bubble. Jakob [2] investigated three different heater surfaces and the bubbles they created: unwetted surfaces[3] (e.g., a surface covered in a thin layer of oil), a half-wetted surface (e.g., a smooth surface), and what was called a "screen surface" where

[3] *Unwetted* and *wetted* are terms that describe the interfacial behavior of a liquid and a surface. A surface that is *unwetted* by water is traditionally known as hydrophobic, while a surface that is *wetted* by water is typically known as hydrophillic. The use of *unwetted* and *wetted* is simply the more general version of hydrophobic/hydrophillic behavior as it can be used to refer to any liquid.

roughness was imparted via sandblasting or the manufacture of 0.25 mm square cavities. The bubbles that these surfaces formed, respectively, can be seen in Figure E.3.

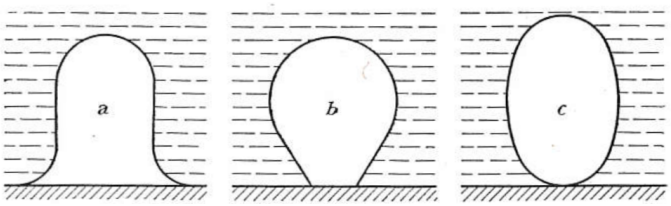

Figure E.3: Reproduction of Figure 8 from Jakob [2] showing the typical shapes of bubbles that form on differently wetted surfaces (a = non wetted surface, b = half-wetted surface, c = entirely wetted surface).

Bubbles on half-wetted surfaces are said to "originate at only a few small places.... these not being distinguished by any peculiarities whatsoever from the rest of the surface" [2]. At a minimum heat flux of 8.7 kW/m^2, there were five points on the surface where bubbles were forming, all of which were located at the edge of the heater. These five boiling points persisted as the heat flux increased, while others formed within the area of the heater. The middle of Figure E.4 shows a cross section of the heater; the heater is cylindrical in shape, the edge of the heater being some distance away from any mating surfaces.

It was photographically shown, multiple times by Jakob as summarized in Jakob [2], that rough surfaces develop more bubbles of smaller volume; the cause is hypothesized to be due to the adhesion of gas to the elements of roughness. The foundation of this thought likely stems from the paradox of Equation E.2 not allowing for ebullition when the bubble radius is zero.

Jakob goes on to recall his 1932 studies of the heat transfer coefficient as a function of time after a bubble has formed. It was found that the heat transfer coefficient induced by the generation of a bubble (within the first 1/100th of a second) could reach 230 $kW/m^2 - K$, as shown in Figure E.5. The generation of such bubbles were likened to an "explosion

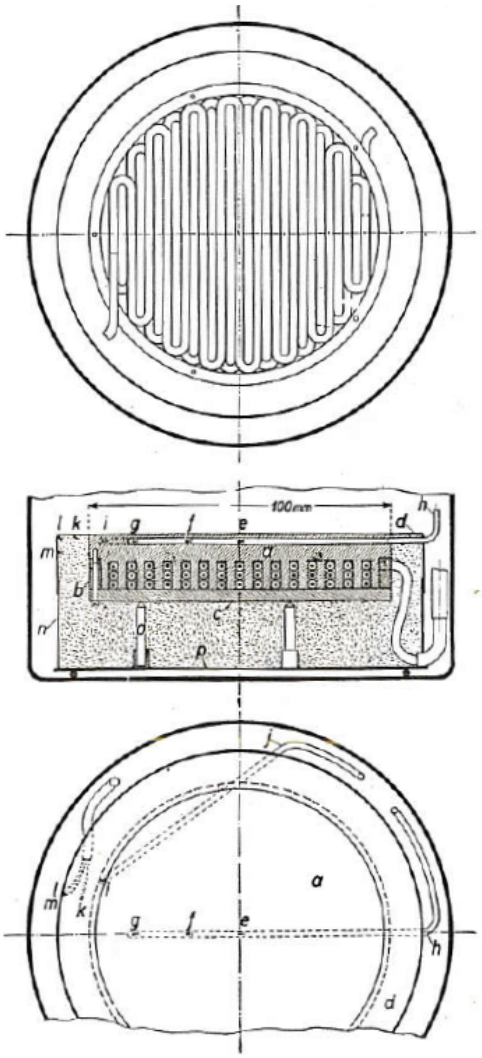

Figure E.4: Reproduction of Figure 7 from Jakob [2] showing the vertically-facing copper heater assembly. At the lowest heat flux there were five points where bubbles formed; all of these points were along the periphery of the heater surface (location *l*).

in the microscopic scale" [2]; it was assumed that bubbles are generally surrounded by a thin layer of liquid.

As of 1937 "it is by no means certain that all the variables with an important influence on the shape and position of the [boiling] curve are known. The most significant, as far as is known at present, is the character of the heating surface, although it is impossible to draw conclusions as to the effects of specific changes in surface" [54].

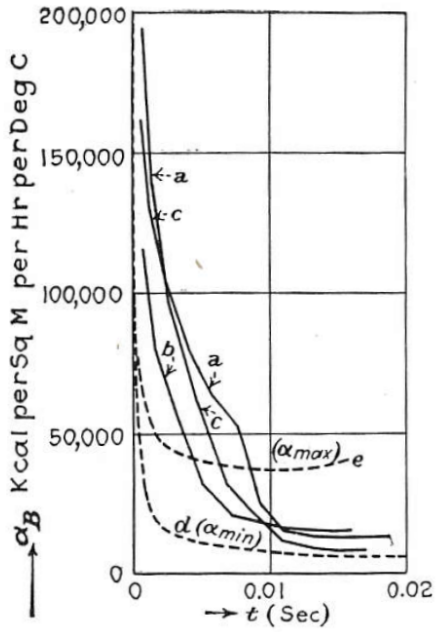

Figure E.5: Reproduction of Figure 17 from Jakob [2] showing the heat transfer coefficient as a function of time since bubbles a, b, and c formed. For reference, a heat transfer coefficient α_B of 1 $kcal/m^2 - hr - C$ is approximately equal to 1.16 $W/m^2 - K$. It is from this plot that bubble formation was thought to be akin to a micro-scale explosion, causing such high heat transfer coefficients at bubble inception.

E.3 The 1940s

A significant amount of the research done prior to 1940 was related to the heat transfer aspects of nucleation–trying to use dimensional analysis to discover those variables that influenced boiling heat transfer. By 1943, Dean [57] noticed this fact and stated that, "the formation of bubbles within liquids is a subject which has received surprisingly little attention from scientists". Dean echoed the realization of Jakob [2] whereby the "fundamental difficulty of bubble formation lies in the law relating pressure, surface tension, and bubble diameter" given in Equation E.3.

$$\Delta P = \frac{2\sigma}{R} \tag{E.3}$$

Here, ΔP is the difference in pressure between the inside and outside of a spherical bubble whose radius is R and has surface tension σ. Dean recognized that if Equation E.3 was valid down to the molecular scale, the "excess pressure inside the bubble would be 7500 atmospheres when $R = 1.9$ Å". Looking at such a situation from a perspective of molecules and their random thermal motion, the probability that enough molecules of sufficient energy would be near each other, in the body of the liquid, to form a bubble at that scale is small, but was studied in 1937 and 1941. According to Dean [57], "the results of the theory are not useful in practical cases as they lead to the conclusion that bubbles are not likely to form in liquids without many degrees of superheat or enormous negative pressures," though such theories were confirmed qualitatively.

In the years that followed, Dean [57] was remembered for his theory on boiling whereby nucleation was a result of the negative pressure at the center of a vortex. The pressure inside a bubble within an ideal rectilinear free vortex is the sum of the vortex pressure and the surface tension pressure given in Equation E.4, where Γ and r are the circulation rate and radial location from the center of the vortex, respectively.

$$P = \frac{-\Gamma^2 \rho}{8\pi^2 r^2} + \frac{2\sigma}{r} \tag{E.4}$$

In the case of a forced vortex, the first term in Equation E.4 would be replaced with $\omega^2 r^2 \rho/2$, where ω is the rate of rotation of the vortex. As a result of such research, Dean proposes that "bubbles can always be produced by active stirring or turbulent circulation of the liquid" [57]. Dean goes on to state that the use of many boiling chips is superior in performance due to the "turbulent motion of convective streams," supporting his theory, referred to as the Free-Eddy Theory by Bankoff et al. [58]. The conclusion of Dean [57] is that "bubbles can always be produced by active stirring or turbulent circulation of the liquid. This fact is well known though not often intentionally applied in practice." This

conclusion is related to the behavior of boiling chips whereby, "the use of many boiling chips actually produces considerable turbulent motion of convective streams when flasks are heated from below."

Another theory on how liquids boil was introduced by Frenkel in the 1920s and coalesced in his 1947 paper (Frenkel [59]). Frenkel proposed the idea of heterophase fluctuations. As it pertains to bubble nucleation in a liquid, this is the idea that statistical fluctuations in molecular movements will give rise to a Boltzmann distribution of vapor embryos of varying radii. The generic form of a Boltzmann distribution can be seen in Figure E.6. When the radius of these embryos reaches a critical radius and the thermody-

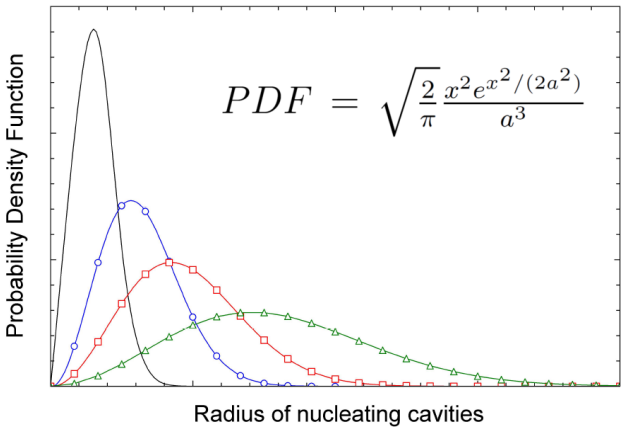

Figure E.6: Generic form of the Maxwell-Boltzmann distribution. Frenkel [59] refers to it as simply a Boltzmann distribution, however Kurihara and Myers [19], referencing the Frenkel paper, refers to it as the Maxwell-Boltzmann distribution shown here.

namic potential is sufficient, an embryo is capable of growing into a bubble.

E.4 The 1950s

The ideas of Frenkel were extended and more succinctly summarized by Clark [60]: "for a condition of iso-thermal fluctuations at constant pressure, the change in the Gibbs' free

energy per nucleus having an apparent spherical radius R is... given by" Equation E.5.

$$\frac{\Delta Z|_{P,T}}{n} = 4\pi\sigma(R^*)^2 \left[\left(\frac{R}{R^*} \right)^2 - \frac{2}{3} \left(\frac{R}{R^*} \right)^3 \right] \tag{E.5}$$

Here, R^* is the critical radius given by Equation E.6, which is derived from substituting the change in pressure from the Young-Laplace equation (Equation E.3) into the Clausius Clapeyron equation, assuming small superheats $T - T_{sat}$ and a liquid at saturation.

$$R^* = 2\sigma \frac{v_{fg}}{h_{fg}} \frac{T_{sat}}{T - T_{sat}} \tag{E.6}$$

After the derivation and theoretical background, Clark [60] found that the temperature at onset of nucleation was off by a factor of 100, but had the same general trend as experiment.

One of the popular goals in boiling theory has been the ability to predict the number of nuclei that will form per unit of heater surface area or unit volume of fluid. Based on the ideas of Volmer from 1939, authors such as Bernath [61] and Lamer and La Mer [62] developed an expression relating the amount of work needed for the formation of a vapor nucleus by summing the differing chemical potentials between vapor and liquid molecules:

$$W_n = \sum_{i=1}^{n_n} (\mu_i - \mu_L) = \sigma A_n - (P_n - P_L) V_n \tag{E.7}$$

Substituting expressions for the volume of the nucleus $V_n = \frac{4}{3}\pi r^3$ and the Young–Laplace equation for a spherical bubble, $r_n = \frac{2\sigma}{P_n - P_L}$, one arrives at Equation E.8.

$$W_n = \frac{16\pi\sigma}{3\left(P_n - P_L\right)^2} \tag{E.8}$$

It is then postulated that this energy could come from thermal fluctuations in the liquid,

similar to the hypothesis by Frenkel [59]. Bernath [61] goes on to discuss those factors that decrease the energy barrier, W_n, to creating a bubble:

1. Convex surfaces
2. Rough surfaces
3. Sharp-edged interactions
4. Presence of microscopic particles in liquid phase
5. Occluded Gasses

Lamer and La Mer [62] noted that as the vapor pressure of the nucleus (P_n) increased (corresponding to a small bubble) the work likewise increased. For $P_n \gg P_L$, the work to form an embryo is "indefinite because the great reduction in [radius] makes the concept of surface tension and a separate phase meaningless". Clark [60] later remarked that "if thermodynamic analysis were valid to near zero bubble size, which it is not, it would be expected that this pressure difference would become enormously large."

In a study on contact angle hysteresis Bartell and Shepard [63] showed that advancing liquid droplets were found to have air beneath them when moving across a surface with an array of pyramidal structures[4]. The experiment consisted of placing a drop of liquid on top of a surface covered with pyramidal structures, then slowly adding more liquid and observing the movement of the contact angle. It was postulated that the advancing water droplets contacted a downstream feature and continued to advance, trapping some volume of air beneath the water. This can be seen in Figure E.7. The quantity of entrapped air was found to be a function of the surface roughness, namely the slope of the pyramidal surface structures

Combining these ideas experimentally, Corty and Foust [64] used emery roughened surfaces, whose roughness was characterized by electron micrographs as well as a pro-

[4]Such pyramidal structures were used to produce a known, uniform, and macroscopic roughness. It was mentioned that each pyramidal face had its own sub-macro-scale roughness, however this was the same as the *smooth* surface without a pyramidal structure.

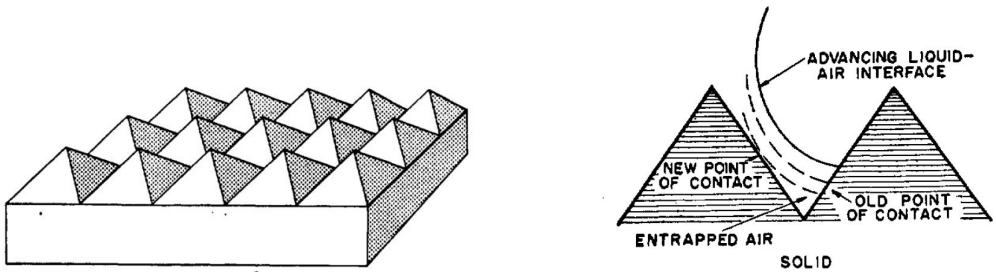

(a) (b)

Figure E.7: Reproductions of Figure 1 and Figure 3 from Bartell and Shepard [63] used a (a) pyramidal structured surface for testing contact angle hysteresis. (b) As the contact angle traverses the surface features it was hypothesized that air is entrapped by a liquid-air interface contacting a downstream face and rapidly changing geometry to form a stable contact angle. The liquid does not reach the bottom of the cavity, but rather it travels across the tops of the structures.

filometer, and counted the number of locations where bubbles were forming. It was found that the "lower knee of the boiling curve was reached at 10 to 20 bubbles/sq. in"[64]. Furthermore, it is postulated that boiling cavities are features with trapped vapor from previously departed bubbles.

A theoretical analysis by Bankoff [65], based on the minimization of Gibbs PV work required to create a vapor embryo, found that "unwetted cavities are preferred nucleation points; but the difficulties in filling these completely with liquid are so great that it is probable that nucleation almost always occurs at a pre-existing gaseous phase". Bankoff's analysis used a 1948 study by Fisher [66], which hypothesized that a pre-existing gaseous phase must exist at the bottom of a cavity; this hypothesis stemmed from the use of nucleation theory to predict premature cavitation of bubbles in a fluid under negative pressure. Bankoff [65] goes on to show that the amount of reversible work required for the formation of a vapor embryo on a convex surface projection is greater than the work required on a plane surface, both of which take more work than for an unwetted cavity.

To summarize the state of knowledge through 1956, a conference was held to discuss nucleation, bubble dynamics, and boiling heat transfer. Rohsenow suggested that nucle-

ation theory in ebullition could be split into the following three categories [58]:

1. Nucleation from the liquid phase due to statistical density fluctuations (homogeneous nucleation)
2. Nucleation from the solid surface in the absence of a gaseous phase
3. Nucleation from a pre-existing gaseous or vapor phase, which may or may not be stabilized on a solid surface

Homogeneous nucleation was considered only relevant to the initiation of bubble formation, but not the persistence of boiling. The critical bubble radius r^* for a bubble to cavitate homogeneously was given by Equation E.9, where σ, P'_G, and P_L are the surface tension, pressure within the bubble, and the local pressure external to the bubble, respectively.

$$r^* = \frac{2\sigma}{P'_G - P_L} \tag{E.9}$$

It was also discussed that studies at that time were merely capable of getting order-of-magnitude superheat measurements on glass surfaces at nucleation; higher precision was difficult due to the low superheats found with metal surfaces. Once nucleation began, superheats dropped significantly

The research by Dean [57] was discussed, whereby homogeneous nucleation could occur as a result of negative pressures at the center of a free vortex. As the editor summarizing the conclusions of the conference, Bankoff commented that the pressure at the center of a free vortex would be close to the external pressure [58]; he also noted that "none of the available experimental evidence has established its existence in any way". This last statement is intriguing since Clark [60] cites work done in 1955 whereby "cavitation bubbles are sometimes found to form away from a surface near the center of the boundary layer as a result of vortical eddies, suggesting that something in the nature of turbulence is important to the nucleation process." In contrast to cavitation bubbles,

Clark remarks that "bubbles formed as a result of heating at a surface have always been observed to form right at the surface."

This lead to the agreement that "nucleation from a pre-existing gaseous or vapor phase predominates in steady-state boiling and cavitation. The gaseous phase may be contained in cavities... or consist of microscopic bubbles suspended in the fluid either individually for a fluid saturated with gas or attached to solid particles" [58]. It was discussed that "both wetted and relatively nonwetted capillaries may function as nucleation centers, depending only on whether the liquid reaches the bottom of the cavity before the vapor pressure of the meniscus becomes great enough to satisfy the Gibbs requirement for mechanical equilibrium. Since the rate of penetration into unwetted cavities will naturally be less than into wetted cavities, these will be preferred nucleation points."

An interesting phenomenon was discussed whereby the heat flux of a surface is reduced until boiling stops at all but one nucleation site (all other wetted cavities are assumed to fill with liquid). If the heat flux is then increased, the surface superheat will return to its previous state; in addition, "reactivation of the nucleation centers proceeds radially out from this column of bubbles" and not from the previously active cavities. The explanation for such phenomenon is that as the remaining bubble grows, it covers neighboring nucleation sites. As the liquid from those sites comes into contact with the vapor inside the bubble, the liquid in the cavities evaporates, causing neighboring sites to be filled with vapor.

Following the conference, Bankoff went on to numerically solve for those parameters that would allow for gas entrapment in cavities and crevasses[5], similar to the experimental work done by Bartell and Shepard [63]. Two cases were studied: one where the liquid is displacing the gas in a groove, and the second where gas is displacing the liquid in

[5]a cavity is typically assumed to be a conical geometry, while a crevasse is assumed to be a wedge-shaped negative extrusion (e.g., a scratch) in a surface

the groove. Figure E.8 shows the necessary contact angle, θ, and the angle forming the crevasse, ϕ, necessary for zero gas to be entrapped. It was found that for $\theta > 180^\circ - 2\phi$ the fluid will not completely wet the groove and gas should be trapped beneath the liquid.

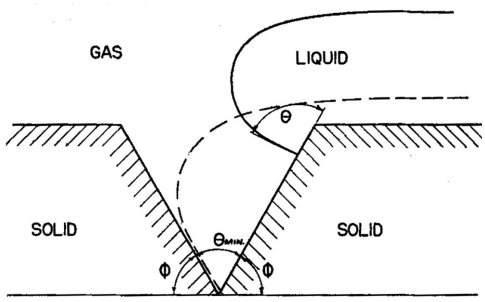

Figure E.8: Reproduction of Figure 1 from Bankoff [67]. This is the first numerical criteria to describe an idealized case of a liquid flow traversing surface discontinuities. For $\theta > 180^\circ - 2\phi$ the fluid will not completely wet the groove and entrapping gas.

The second case is shown in Figure E.9, where the gas is displacing the liquid. In this case, for $\theta < 2\phi$ the gas will be unable to displace the liquid that is at the bottom of the groove.

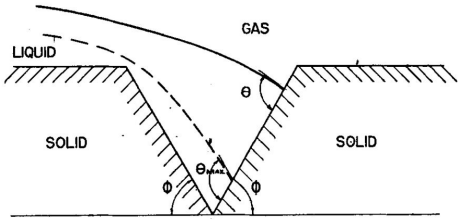

Figure E.9: Reproduction of Figure 2 from Bankoff [67]. This is the first numerical criteria to describe an idealized case of a liquid flow traversing surface discontinuities. For $\theta < 2\phi$ the gas will not be able to displace all of the liquid.

Both of these analyses assumed the surface was perfectly smooth and that the fluid curvature was not impacted by the geometry of the groove. One ramification of this theory is that when the contact angle is zero, there will be zero chance that gas will be entrapped. In addition, it was stated twice in Bankoff [67] that "we are considering displacement of gas only by travel of liquid across the grooves, and not by some other mechanism,

such as travel along the grooves."

It was not until 1959 that researchers, namely Clark et al. [27], used microscopes to observe active nucleation sites. A microscope was used to investigate where bubbles formed. The experiments comprised heaters that were made either of zinc or aluminum. Zinc was chosen due to its anisotropic nature; the zinc was processed such that a plane near that of maximum atomic density formed the heater surface. Different surface finishing techniques were used to reduce the number of nucleation sites to an observable quantity. It was found that polishing the surface[6] left scratches in the surface. The surface topology is described as consisting of smeared metal with a definite scratch pattern and a few pits [27]. Electropolishing broke up the continuous surface scratches and did not fill the pits on the surface. An attempt was made to look inside a pit to observe internal surface features, but the authors could not be certain that the micrograph was actually looking at the center of a pit; the surface resembled a honeycomb structure with "cells" of size 500 Å- 1000 Å.

The locations and number of observed nucleation sites can be found in Table E.1, which shows that most of the observed nucleation sites were pits, followed by scratches and the boundary between dissimilar materials.

Table E.1: Number of microscopically observed nucleation sites organized by feature believed to beneath the bubble from Clark et al. [27]

Nucleation Site Type	Number of Observations
Cavity / Pit	13
Scratch	3
Boundary between dissimilar materials	3
"Shifting speck of unidentified material"	1

The diameter or width of the nucleating features ranged from 2 μm to 70 μm. In no cases were there bubbles originating from grain boundaries. Based on additional data

[6]No grit size was provided nor roughness measurements taken

obtained by measuring heat flux and surface temperature, it was found that the polycrystalline zinc behaved no differently than the monocrystalline zinc. It is therefore determined that "nucleation sites are not regions of special atomic density in the hot solid. It follows also that the size of the grains cannot be important" [27]. It is noted that such a conclusion goes counter to that of Harrison and Levine [26], who found that the heat transfer performance of varying crystal faces do follow along unique heat transfer curves.

The following year, Gaertner and Westwater [17] provided the first count of active nucleation sites that was not done by visually surveying a field of active nucleation sites, as was standard practice at the time. Visually counting active nucleation sites is only a viable option at low heat fluxes when a countable number of sites are active. To overcome this limitation the authors electroplated their copper heater with up to 9 μm of nickel during the boiling process. It is claimed that vapor bubbles disturb the fluid near the nucleation site and thereby "push the plating solution away from the surface so that very little metal could plate these locations". After each run, the heater plate could be photographed and locations without plating could be counted as nucleation sites. As high as 1,130 nucleation sites per square inch could be obtained using this method.

A closer look at such cavities was done by Griffith and Wallis [68] who showed that the diameter of a cavity determines the superheat at nucleation, while the shape (and wettability) determines the stability. The nucleation site density, n/A, was related to the critical cavity size, r_c, using Equation E.10, as reported by Zeng and Klausner [13].

$$\frac{n}{A} = C_1 \left(\frac{1}{r_c}\right)^m \tag{E.10}$$

$$r_c = \frac{2\sigma T_{sat}}{\rho_v h_{fg} \Delta T_{sat}} \tag{E.11}$$

It was hypothesized that if there was a field of similarly sized conical cavities, they should

all nucleate at a given superheat and the boiling curve should be vertical. It was found that the slope of the boiling curve was large (though definitely not vertical) and that the superheat required for nucleation was in error by 17°C. The stability of a cavity depended on the prior history of that cavity; namely, if it had previously been degassed "it was found to be impossible to initiate boiling from the desired spots" [68]. Using the vapor pockets theory, it is assumed that the degassing "dissolved all the gas from the cavity before boiling began". It was also found that a cavity could be deactivated if the pressure was suddenly increased such that the liquid would be a few degrees subcooled. After increasing the pressure it was found that the cavity would no longer nucleate at the previous superheat; the hypothesis was that the decrease in pressure must have caused the cavity to become filled with liquid. Overall, it was found that Equation E.6 verified nucleation theory and was deemed "substantially correct" and that one parameter, namely R^*, is able to characterize boiling surface performance across all surface/liquid combinations.

Wettability had already been shown to be a considerable factor in the nucleation of bubbles prior to the end of the 1950s, but Harrison and Levine [26] showed that differing crystalline directions of monocrystalline copper presented differing wetting behaviors. Using stearic acid as the fluid, it was shown that the 100-direction had a steeper boiling curve than the 110 direction, for superheats between 38°F and 132°F, but also that the 110-direction nucleated first. Interestingly, the linear boiling curves for these two crystalline directions intersected at 75°F; the reason for this was postulated to be that the more non-wetting surface (100 direction) would have a higher thermal resistance during the natural convection regime, thus leading to a higher superheats for the same heat flux. Once nucleation began, the bubbles on the 100-surface would depart sooner, providing a steeper boiling curve.

E.5 The 1960s

Kurihara and Myers [19] summarizes the state of knowledge surrounding the origin of nucleation as of 1960. The following four ideas are proposed [19]:

1. *Molecular groups are formed by thermal fluctuations of molecules with energies corresponding to the new phase*
2. *Bubbles of sufficient size are formed by minute explosions of highly superheated liquid*
3. *Nuclei are foreign particles or pockets of dissolved gas*
4. *Nuclei consist of vapor or gas trapped in small crevices in a solid from which bubbles can form during boiling*

Perkins and Westwater [69] proposed that bubbles remain at a constant diameter during all but the last 20% of heat flux prior to CHF; Kurihara and Myers [19] reason that these bubbles must be nucleating in cavities and channels of that characteristic size. It was subsequently noted that only a small fraction of those correspondingly sized features were actually nucleating bubbles. This peculiarity follows the theory by Frenkel [59] of heterophase fluctuations following a Boltzmann distribution. Several reasons were given for being unable to verify this hypothesis, including the uncertainty about whether macro-scale contact angles corresponded to micro-scale contact angles, and the inability to count nuclei at higher heat fluxes.

High speed temperature measurements by Moore and Mesler [70] used a thermocouple capable of a one microsecond response time to measure fluctuations in temperature during the boiling process. This thermocouple was made using an Alumel wire insulated from a surrounding concentric tube made from Chromel P. A thin metal film made from Nichrome V was used to connect the two metals. This thermocouple provided an average reading across the tube with a diameter of 0.127 mm. As the surface was heated, the temperature fluctuations caused by bubbles near the thermocouple were measured; the

results of these measurements can be seen in Figure E.10. Photographically it was found

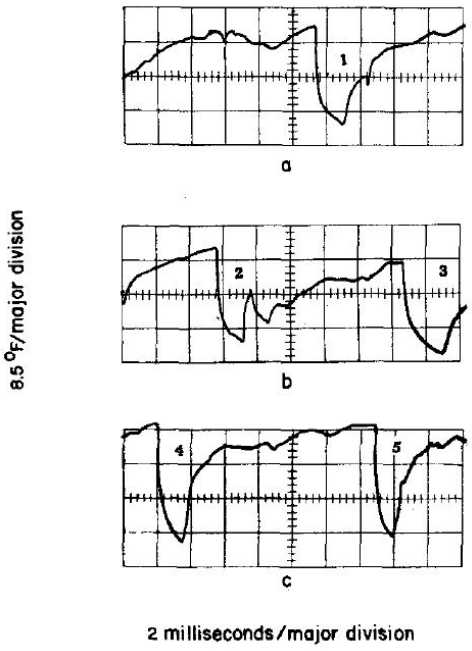

(a)

Drop	Average heat flux, B.t.u./(hr.)(sq. ft.)	Interval between max. and min. temperatures, msec.	ΔT max., °F.	Average period, msec.
1	135,000	1.80	24.2	14.3
2	135,000	1.51	23.6	14.3
3	135,000	2.28	22.6	14.3
4	202,000	1.46	29.3	8.8
5	202,000	1.12	27.6	8.8

Drop	Q/A, B.t.u./(sq. ft.)	Average heat flux over temp. drop, B.t.u./(sq. ft.)(hr.)	$f \cdot Q/A$, B.t.u./(sq. ft.)(hr.)	δ, min.
1	0.415	830,000	105,000	82
2	0.398	920,000	100,000	78
3	0.420	660,000	106,000	83
4	0.446	1,100,000	183,000	89
5	0.407	1,310,000	166,000	81

(b)

Figure E.10: Reproduction of Figure 3 and Table 1 from Moore and Mesler [70] showing (a) oscilloscope output of their thermocouple having a one-microsecond response time and (b) the heat flux, time response values, and other performance parameters. Note that 1,310,000 $Btu/hr - ft^2$ is equivalent to 413 W/cm^2 and the experimental fluid was water.

that bubbles did not show a preference to forming on the thermocouple itself. Using the research by Westwater [71] who showed that even at time scales as short as 0.1 milliseconds bubble formation could not be resolved, it was hypothesized that the downward spikes in temperature, seen in Figure E.10, begin when the bubble nucleates. The subsequent 2 milliseconds of temperature drop are a result of microlayer evaporation beneath the bubble. This is supported by estimation of the water layer thickness that would need to be evaporated to supply that same amount of energy (about 80 μm, incapable of being seen using traditional photographic methods of the time).

By 1961 it was becoming accepted that nucleation occurs in concave features, or reen-

trant features[7] and not convex or sharp features. As Kutateladze [72] states, "in some works on heat transfer with boiling an erroneous viewpoint of Kruzhilin has prevailed, namely that vapour bubbles rise on the projections of roughness." From the viewpoint of Kutateladze [72], the boiling phenomenon is completely probabilistic. With no uncertainty it is stated that the probability of a vapor bubble emerging is proportional to $\exp\left(\frac{1}{-\Delta T^2}\right)$ where ΔT is the surface superheat. A graphical representation of this is provided in Figure E.11.

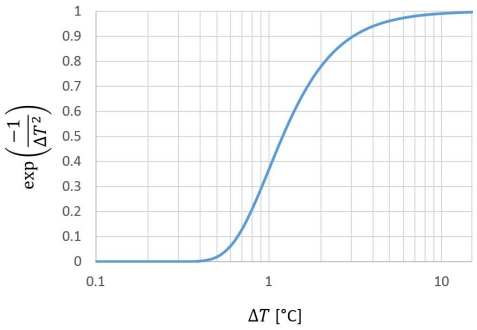

Figure E.11: According to Kutateladze [72], the probability of a bubble forming is proportional to $\exp\left(\frac{1}{-\Delta T^2}\right)$, as shown. Notice that the only variable of consequence is the surface superheat.

In addition, Kutateladze [72] reports that the reason why bubbles depart at different diameters is that the probabilistic behavior of such phenomena is described by Equation E.12 for a smooth surface, where D_0 is the bubble departure diameter and γ represents the specific weight.

$$D_0 = 0.02\theta\sqrt{\frac{\sigma}{\gamma_L - \gamma_v}} \tag{E.12}$$

Equation E.12 appears to show that the diameter of individual bubbles will be a constant, however it is asserted that the contact angle σ "cannot be considered as a distinct characteristic of a large area of a heating surface" and will therefore be variable at small length scales.

[7] where the diameter at the mouth of the cavity is smaller than some internal diameters.

More detail on Hsu [73] is provided due to the frequency with which it is referenced. In 1962, Hsu [73] comments that "it is now generally accepted that a cavity must be sharp enough to trap gases if it is to be a nucleation site" based on the previously discussed work of [19, 60, 64, 65, 71]. Hsu [73] assumes that boiling is not a problem of vapor generation, but a problem of bubble latency–the challenge was how to make the pre-existing vapor grow into larger bubbles. This transforms the problem into one of transient conduction from a warm liquid through a thermal boundary layer at the surface, in which there is a latent bubble.

To derive the temperature profile in the thermal boundary layer, a 1-D model was assumed for both the constant temperature and constant heat flux wall conditions. The differential equation for this case is shown in Equation E.13,

$$\frac{\partial \theta}{\partial t} = \alpha \frac{\partial^2 \theta}{\partial x^2} \tag{E.13}$$

where $\theta = T - T_\infty$ and α is the thermal diffusivity. The boundary conditions for Equation E.13 are shown in Table E.2.

Table E.2: Boundary equations for Equation E.13.

Constant Temperature	Constant Heat Flux
$\theta\big\vert_{t=0} = 0$	$\theta\big\vert_{t=0} = 0$
$\theta\big\vert_{y=\delta,t=0} = 0$	$\theta\big\vert_{y=\delta,t=0} = 0$
$\theta\big\vert_{y=0} = \theta_w$	$\left(\frac{\partial \theta}{\partial x}\right)_{x=\delta,t>0} = \frac{q}{K} = \text{const.}$

Solving the differential equation produces the expression for the dimensionless temperature inside the boundary layer:

For constant surface temperature:

$$\xi = \frac{\theta}{\theta_w} = \eta + \frac{2}{\pi} \sum_{n=1}^{\infty} \frac{\cos n\pi}{n} \sin n\pi\eta \exp(-n^2\pi^2\tau) \tag{E.14}$$

where

$$\theta_w = const., \quad \tau = \frac{\alpha t}{\delta^2}, \quad \eta = \frac{x}{\delta} \tag{E.15}$$

For constant heat flux:

$$\xi_b = \frac{\theta}{\frac{q\delta}{K}} = 2\sqrt{\tau} \sum_{n=0}^{\infty} (-1)^n \left[i\,erfc\frac{(2n+1)-\eta}{2\sqrt{\tau}} - i\,erfc\frac{(2n+1)+\eta}{2\sqrt{\tau}} \right] \tag{E.16}$$

where

$$\tau = \frac{\alpha t}{\delta^2}, \quad \eta = \frac{x}{\delta}, \quad \xi = \frac{\theta}{\frac{q\delta}{K}} \tag{E.17}$$

Since Hsu [73] postulated that the condition for bubble latency ends when the temperature at the bubble reaches a certain value, this means that Equation E.6 can be changed such that $\theta = \theta_b$ at $x = \delta - b$, where b is the height of the bubble nucleus. Substituting these variables into Equation E.6 and rearranging produces Equation E.18.

$$\theta_b = \theta_{sat} + \frac{2\sigma T_{sat}}{\lambda \rho_v r_n} \tag{E.18}$$

Combining this with the geometry of a truncated sphere (the assumed geometry of the spherical bubble nucleus) and non-dimensionalizing the equation produces:

$$\xi_b = \frac{\theta_b}{\theta_w} = \xi_{sat} + \left(\frac{2\sigma T_{sat} C_3}{\lambda \rho_v \delta \theta_w} \right) \frac{1}{1-\eta_b} = \xi_{sat} + \left(\frac{A C_3}{\delta \theta_w} \right) \frac{1}{1-\eta_b} \tag{E.19}$$

where

$$\xi = \frac{\theta}{\theta_w}, \quad \eta_b = \frac{x_b}{\delta}, \quad A = \frac{2\sigma T_{sat}}{\lambda \rho_v}, \quad \theta_w = T_w - T_\infty, \quad C_3 = 1 + \cos\varphi \tag{E.20}$$

and φ is the angle of the bubble wall with respect to the horizontal. Plotting Equation E.19 for the constant temperature case, or Equation E.16 for the constant heat flux case,

produces Figure E.12. The overlap of these curve with Equation E.21 defines the geometry of those cavities that are capable of bubble expansion.

$$\eta_b^* = \frac{(1+\xi_{sat}) \pm \sqrt{(1-\xi_{sat})^2 - \frac{4AC^3}{\delta\theta_w}}}{2} \tag{E.21}$$

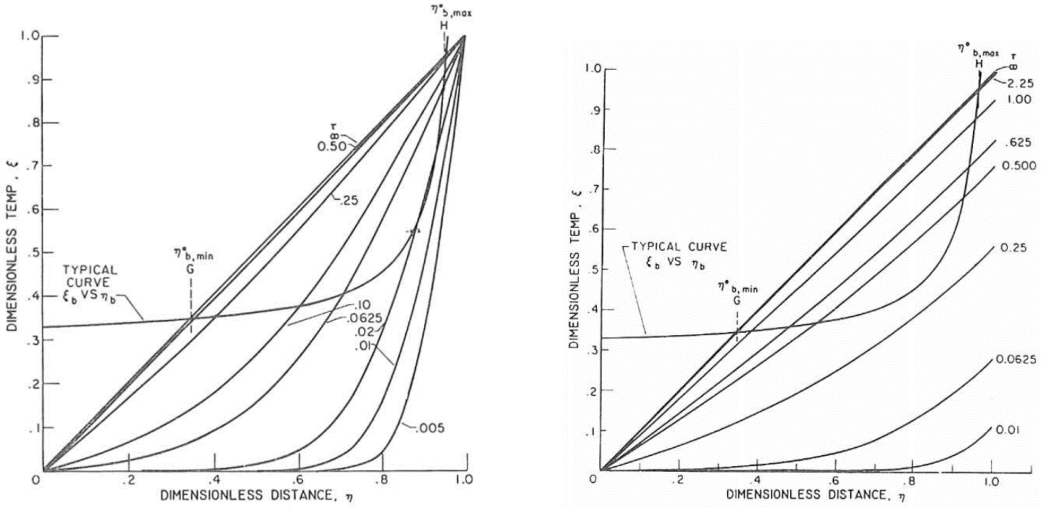

(a) Constant Temperature Surface (b) Constant Heat Flux Surface

Figure E.12: Reproduction of Figures 2 & 3 from Hsu [73], showing (a) the behavior of isothermal bubble growth when Equations E.14 and E.19 intersect and (b) the behavior of constant heat flux bubble growth when Equations E.16 and E.19 intersect. Conditions where the curves do not intersect correspond to cavities where bubbles cannot grow.

In addition, when the maximum radius curves of Figure E.12 intersect the non-dimensionalized temperature curve (ξ_b vs. η_b), there can be found a minimum temperature and heat flux necessary to initiate boiling. The equations for this behavior are as follows:

$$\theta_{w_0} = \theta_{sat} + \frac{2AC_3}{\delta} + \sqrt{\left(2\theta_{sat} + \frac{2AC_3}{\delta}\right)\left(\frac{2AC_3}{\delta}\right)} \tag{E.22}$$

$$q_0 = \frac{K}{q}\left[\theta_{sat} + \frac{2AC_3}{\delta} + \sqrt{\left(2\theta_{sat} + \frac{2AC_3}{\delta}\right)\left(\frac{2AC_3}{\delta}\right)}\right] \tag{E.23}$$

This means that if δ is known (the thermal boundary layer thickness) then the incipience point can be predicted. Alternatively, if the incipience point is known, then the wall temperature ($\theta_{w_0} = T_w - T_\infty$) and heat flux can be determined. Several examples of how this hypothesis could be used as a predictive tool were explained. Figure E.13 shows the model's behavior when predicting experimental data–namely, only those cavity sizes that are to the right of the curve in Figure E.13 should be able to nucleate. It can be seen that the model predicts the experimental data to a degree, though there is not enough data to confirm such a model. Figure E.13(c) does not seem to predict this behavior, though it is close to the average values of heat flux.

Rohsenow [74] reported on some of his earlier work with boiling metals that showed a unique behavior not seen in boiling non-metals; for a constant heat flux, the wall temperature would suddenly increase and subsequently decrease on a time scale of about two seconds. A typical time response can be seen in Figure E.14. Using a microphone, it could be heard that while at the lower temperature there was vigorous boiling, during the spike in temperature no noise could be heard, indicating that boiling had ceased. This instability was material dependent, but also material-finish dependent. While "mirror-finished nickel surfaces were [thermally] stable; the same surface etched was unstable" and experienced significant temperature spikes. In all cases of instability, once the heat flux surpassed a given value, the instability ceased. It was theorized that certain cavities would become inactive when the liquid metal reached the bottom of the cavity, thereby displacing the vapor. To circumvent the liquid's displacement of the vapor, doubly re–entrant cavities were tested in Marto and Rohsenow [75]; an image of such cavities can be seen in Figure E.15. Re-entrant cavities are theorized to halt the procession of the contact line at the lowest location of the inner–most hole, making them stable to the collapse of the vapor region.

It was shown that when boiling sodium at nearly constant pressure conditions, the

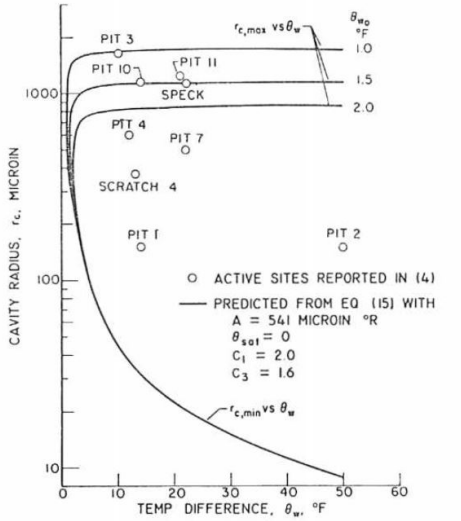

(a) Constant Temperature Surface

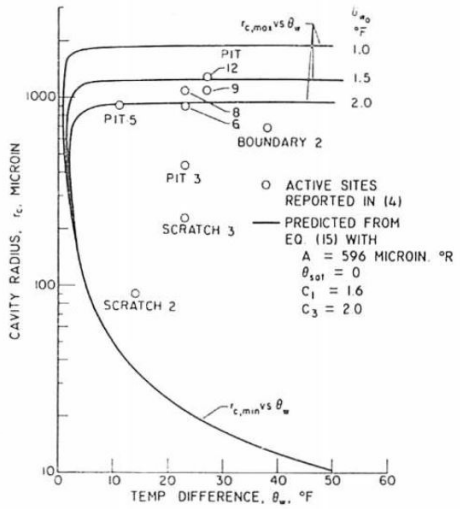

(b) Constant Temperature Surface

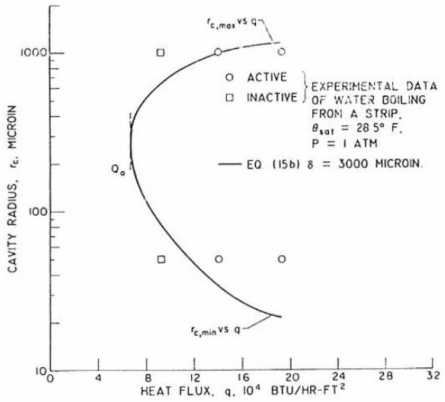

(c) Constant Temperature Surface

Figure E.13: Reproduction of Figures 6, 7 & 8 from Hsu [73]. (a) and (b) show the model's prediction of nucleation site radii at given superheats, while (c) shows the model's prediction of which radii would be activated as heat flux was increased.

doubly re-entrant surface produced the lowest superheat at boiling inception, approximately 9 $^{\circ}C$, when tested against a lapped surface, a mirror finished surface, and a surface with a mirror finish and artificial porous welds.

Toward the late 1960s and early 1970s, porous surfaces and surfaces with re–entrant cavities began being used widely in the refrigeration field by refining the external surface of thin–walled refrigerant tubes. Four such examples can be seen in Figure E.16.

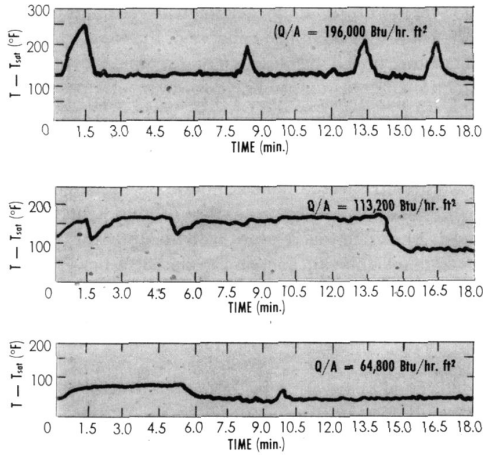

Figure E.14: Reproduction of Figure 11 from Rohsenow [74] showing the time scale of temperature spikes apparent in some boiling liquid metals. Above a certain heat flux, such instabilities ceased.

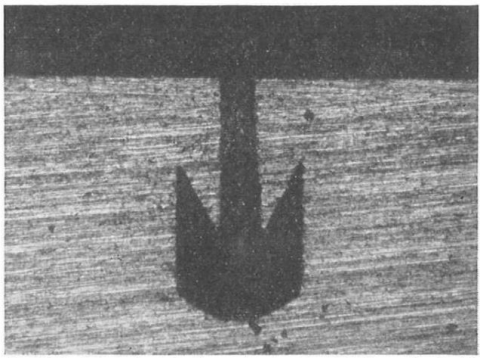

Figure E.15: Reproduction of Figure 3(f) from Marto and Rohsenow [75] showing a cut–away view of a doubly re-entrant cavity at 75× magnification. Such a cavity is created in two parts: first the depth of the hole is drilled; second, an insert is pressed in this hole creating the upward slope and central smaller hole. The cavities tested in Marto and Rohsenow [75] had a mouth diameter of 0.004 inches and a depth of 0.025 inches.

The surfaces in Figure E.16 were able to increase boiling performance (i.e., heat transfer performance) by 70% over a smooth surface.

Using thin film thermometers, Cooper and Lloyd [77] found that the surface temperature decay upon bubble nucleation was on the same scale as that reported by Moore and Mesler [70]. Cooper and Lloyd [77] used an array of thin film thermometers to detect the temperature profile at various distances from the nucleation site. Once again, with mea-

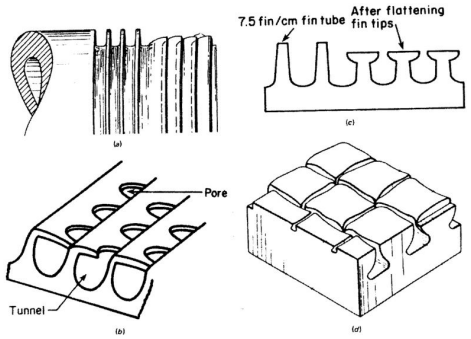

Figure E.16: Reproduction of Figure 6 from Webb [76] showing four patented boiling enhancements for thin–walled refrigeration tubes: (a) theorized by Webb and later patented by the Trane Corporation, (b) the Hitachi Thermoexcel-E^{TM} surface, (c) the Wieland GEWA-T^{TM} surface, (d) the Furukawa ECR-40^{TM} surface.

surements on the millisecond scale, the behavior as the bubble nucleated was unable to be discerned; however, the behavior of what seems to be an evaporating liquid-microlayer beneath the bubble was observed. To understand how this micro-layer forms, it was postulated that a bubble could form at a heated surface; the authors neglect hypothesizing whether the bubble forms in a cavity or just above the surface. As this rapidly forming bubble develops, it could push fluid away from the surface; however the no-slip boundary condition would leave a thin liquid layer beneath the rapidly forming bubble. If such a surface was a highly-nonwetting surface then perhaps the solid would not develop a liquid micro-layer as all of the liquid would be swept away. For a wetting surface such a liquid micro-layer could well exist.[8]

[8]Thus far several mentions of micro-layer evaporation have been made; it should be noted that these have thus far only been markers that a bubble had formed and that there was a liquid beneath at least a portion of the bubble. Mikic and Rohsenow [21] argue that micro-layer evaporation should not be weighted so heavily as a reason for bubble growth since the growth of bubbles is remarkably similar even when there exists no liquid micro-layer; therefore transient conduction from the liquid must be governing bubble growth.

E.6 The 1970s

In his review of boiling, Rohsenow [78] describes that when an inert gas is present, the fundamental equations used for predicting the critical bubble radius[9] are modified to include the partial pressure of the non-condensible gas, P_g:

$$\Delta P = P_v - P_L = \frac{2\sigma}{r} - P_g \tag{E.24}$$

$$T - T_{sat} = \frac{R_v T^2}{P_L h_{fg}} \left(\frac{2\sigma}{r} - P_g \right) \tag{E.25}$$

where R_v is the universal gas constant, P_v is the vapor pressure inside the bubble, and P_L is the pressure outside the bubble. These equations can be compared to previously derived equations that have been rearranged for comparison as Equations E.9 and E.6 where the ideal gas law is assumed to simplify Equation E.6:

$$\Delta P = P_v - P_L = \frac{2\sigma}{r} \tag{E.9}$$

$$T - T_{sat} = \frac{v_{fg}}{h_{fg}} \frac{2\sigma}{r} \tag{E.6}$$

Without citation, Rohsenow [78] then states that "for most cavities it is shown by many different experiments that Equation E.6, with r the cavity radius, predicts the required superheat for bubble growth in a uniformly superheated system." Equation E.26 was used to define the temperature and gradient at a surface inside a tube.

$$\frac{q}{A} = h \left(T_w - T_{liq} \right) = -k_l \left(\frac{\partial T}{\partial y} \right)_{y=0} \tag{E.26}$$

[9] this is the radius above which a bubble will grow and below which a bubble will collapse

Combining Equation E.6 and Equation E.26, a transient conduction model similar to that of Hsu [73] was proposed. Figure E.17 shows dashed lines for the temperature profile near the wall, and a solid line denoted T_g^*, depicting Equation E.6, which denotes the radius of critical cavities as a function of distance from the wall. The intersection of these lines provides those cavity radii that will grow. This is the same logic as Hsu [73].

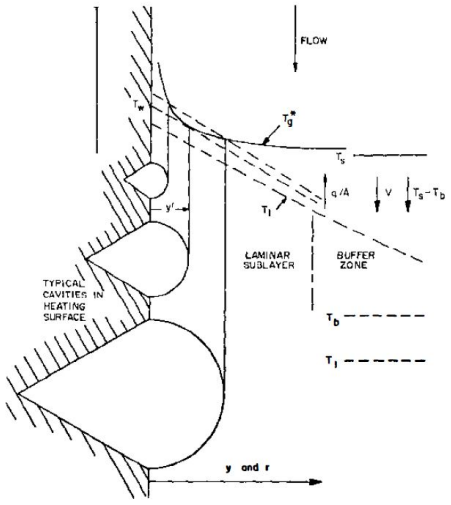

E.6

Figure E.17: Reproduction of Figure 3 from Rohsenow [78] showing a series of dashed lines representing the temperature distribution in the thermal boundary layer. Curve T_g^* is a plot of Equation E.6 and is a function of cavity radius versus distance from the wall. It is hypothesized that when the outer radius of a pre-existing bubble reaches a critical temperature, given by Equation E.6, it will begin to grow.

It is claimed that this correlation works for convective situations, but underpredicts when the convection coefficient is low or when using liquids with high thermal conductivities, such as liquid metal; the underpredicting of liquid metals is because "the slope of the temperature curve (dotted lines of Fig. E.17) is very small, so the point of tangency occurs beyond the size where cavities exist, requiring superheats higher than those predicted." [78]

Continuing his review of boiling, Rohsenow [78] discusses the factors affecting boiling performance as they were understood in 1971. Table E.3 shows the direction in which

the boiling curve (heat flux versus superheat) is shifted as a result of altering a nominal surface/fluid combination using the factor on the left.

Table E.3: Many variables were understood to affect boiling performance by 1971. It is because of the numerous variables that correlation and prediction of boiling phenomena was difficult. Column two shows the direction in which the boiling curve would shift as a result of the factor in column one. A brief reason is shown in column three as described by Rohsenow [78].

Factor	Boiling Curve Shift	Reason
Increased Pressure	$\leftarrow$	Governed by Equation E.6
Decreased Surface Roughness	$\rightarrow$	"Presumably because active cavity sizes are smaller on the smoother surfaces" [78]
Aging	$\rightarrow$	Chemical reactions causing the vapor-containing cavities to shrink
Surface coatings or deposits	$\rightarrow$	Adds another conduction layer
Non-condensible gases	$\leftarrow$	Come out of solution when the surface becomes hot
Hysteresis	$\rightarrow$	Well-wetting liquids deactivate cavities
Vertically oriented heating surface	$\uparrow$	Increased natural convection
Agitation	$\uparrow$	Similar manner as increasing the velocity.
Subcooling	$\leftrightarrow$	$\leftarrow$ for flow inside horizontal tube. $\rightarrow$ for flow over a flat plate
Nonwet surfaces	$\rightarrow$	Larger bubbles cover more of the heater's surface area
Gravitational Field	$\times$	No reported affect

Cornwell [79] provided interesting experimental insights into some of the nucleation theories that had been proposed prior to 1977. Many people had previously combined the Clausius-Clapeyron equation with the Young-Laplace equation to get Equation E.27 for the critical radius of a cavity, above which bubbles could form.

$$r_c = \frac{2\sigma T_{sat}}{\rho_g h_{fg} \Delta T_{sat}} \tag{E.27}$$

Summarizing the evidence used to support this hypothesis, Cornwell states that "this evidence is either based on a few randomly selected sites on a natural surface or on artificially produced sites and is at variance with earlier reports of cavity sizes an order of magnitude greater" [79]. To experimentally investigate how cavity radius correlates with bubble nucleation, Cornwell [79] slowly increased the heat flux and marked the locations of nucleation on a screen so they could later be analyzed under a scanning electron microscope (SEM) at $16,000\times$ magnification. The locations of interest were later found by noticing a "small annular brown stain caused by a minute amount of silica deposition due to the bubble action" in the location of nucleation.[10] Figure E.18 shows information relating to each nucleation site. These data have been shown in tabular form so that the "Type of Site" information would not be omitted. This information is difficult to identify once the numerical data has been plotted. A legend for the letters in column four can be seen in Table E.4.

Table E.4: Legend for the lettered symbols in column four of Figure E.18.

Reference Letter	Positively Identified	Photographed	Mean Radius Measured
A	$+$	$+$	$+$
B	$+$	$+$	$-$
C	$\approx$	$+$	$\approx$
D	$-$	$+$	$-$

Looking more closely at the data in Figure E.18, Cornwell notes that "14 [of the nucleation sites] were in craters or scratches, presumably due to the slight shelter afforded from the surrounding liquid turbulence".. It is interesting that 68 locations on the heater produced air bubbles; seven of these spots went on to produce vapor bubbles; four of those seven were unstable and later stopped nucleating. The assumption was that vapor must have been present in those cavities, but too much escaped during the vapor bub-

[10] It is reported that this identification technique had previously been shown to work by Heled and Orell

Site	q (kW/m^2)	ΔT_{sat} (°C)	Location Certainty	r_c (μm)	Type of Site	Site Extinction	Air bubble Site
1	27·9	6·8	A	5	Pit - deep in parts	24	
2	28·1	7·2	A	2·5	Largest cavity in crater (80μm dia)	28	✓
	28·1	7·2	B	-	Alternately with above crater	28	✓
3	28·5	7·7	B	-	Many pits in crater (120μm dia.)	28	✓
4	29·0	8·0	A	6	End of groove (12μm wide)		✓
5	29·0	8·1	C	2	Pit in shallow groove (35μm wide)	24	
6	29·0	8·1	A	6	Pit - deep in parts	24	
7	29·0	8·3	B	-	Many pits in crater (200μm dia.)		
8	29·0	8·3	A	4	Pit - deep central part of 4μm dia.	24	
9	29·2	8·3	A	2·5	Pit - deep and undercut	46	
10	29·2	8·8	C	4	Shallow pit in scratch	36	
11	29·6	8·8	A	4·5	Pit - deep and undercut	24	
12	29·6	9·0	A	2	Pit - deep central part		
13	29·6	9·0	D				✓
14	29·6	9·0	C	-	Site under metal fragment		
15	29·6	9·0	B	-	Crater at end of scratch(60μm dia.)	24	
16	29·6	9·0	A	3	Pit - deep in parts	28	
17	29·6	9·0	A	2·5	Pit - deep in parts		
18	29·6	9·0	A	5·5	Pit - elongated and deep 6x18μm		
19	29·6	9·0	A	2·5	Pit - deep in parts	46	
20	29·6	9·0	C	1·5	Pit at end of groove (20μm wide)	46	
21	29·6	9·0	B	-	Elongated pit about 8μm wide		✓
22	29·6	8·8	D				
23	29·5	8·8	A	2·5	Pit - deep in parts		
24	29·5	8·8	D				
25	29·5	8·8	A	1·5	Deep pit in crater (50μm dia.)		
26	29·5	8·8	D				
27	29·5	8·7	A	2	Pit - undercut in parts		
28	29·5	8·8	A	2	Deep part of groove 4μm wide		
29	29·5	8·8	B	-	Area with porous appearance		
30	29·5	9·0	A	2	Pit - deep in parts		
31	32·7	9·0	A	2	Pit - deep part of 0·5μm dia.		
32	32·7	9·1	D			36	
33	33·9	9·3	A	3	Pit - deep in parts		
34	34·3	9·5	A	2	Pit - deep in parts		
35	35·0	9·6	D				
36	35·1	9·6	A	1	Pit in crater (15μm dia.)		
37	35·1	9·6	A	2·5	Pit - well defined round hole		
38	35·1	9·5	D				
39	35·1	9·5	C	1	Two possible sites in area		
40	35·1	9·5	C	1	Number of possible sites in area		
41	35·1	9·5	A	1·5	Elongated pit - deep one end		
42	35·1	9·5	A	1·5	Pit - largest in crater (90μm dia.)	46	✓
43	38·5	9·7	A	1	Pit situated in fold on surface		
44	44·6	10·2	A	2·5	Pit - deep part of 2μm dia.		
45	44·6	10·5	A	1·5	Pit - deep part in scratch		
46	44·6	10·6	D				
47	44·6	10·7	C	1	Number of possible sites in area		
48	44·6	10·7	D				
49	44·6	10·6	D				
50	44·6	10·6	A	1	Pit - in shallow crater (25μm wide)		

Figure E.18: Reproduction of Table 1 from Cornwell [79] showing the individual descriptions of nucleation sites. The nucleation sites have been arranged in order of heat flux (the same order as they were found). If a cavity stopped nucleating, this time was marked in terms of when another cavity began nucleating as shown in column seven. Column eight identifies whether these nucleation sites were also sites were air had previously nucleated.

ble's departure, leaving the cavities unstable or latent. As a result, only three of the 34 persistent nucleation spots had verifiable pre-existing vapor or gas.[11]

[11]It could also be possible that such locations were somehow sinks for air to dissolve out of the liquid, thereby forming a bubble that had nothing to do with there being air in the cavity itself.

Figure E.19 shows the ability of Equation E.27 to predict the temperature at which various nucleation cavities will start nucleating. While the data are intersected by the plot of Equation E.27, it would be difficult to use such an equation as a predictive tool. Equation 2 in Figure E.19 is a modification of Equation E.27, shown in Equation E.28, to account for dissolved air.

$$\Delta T'_{sat} = \frac{T_{sat}}{\rho h_{fg}} \left(\frac{2\sigma}{r_c} - P_a \right) \tag{E.28}$$

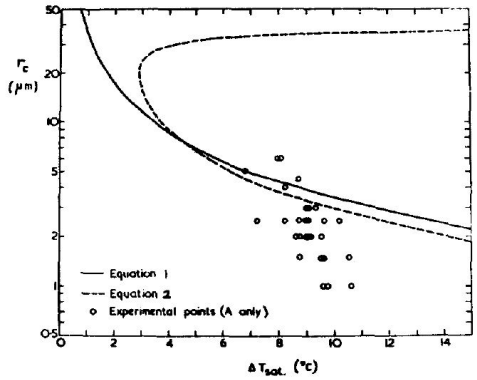

Figure E.19: Reproduction of Figure 5 from Cornwell [79] showing the ability of Equation E.27 (Equation 1 in the figure) to predict the experimental data. Equation 2 in the figure is a modification from Equation 1, but is secondary to the argument that the theory does not do a good job at predicting experimental data.

E.7 The 1980s

By the 1980s it is being accepted that the growth of one bubble does not exist independent of neighboring bubbles. One early investigation is one by Chekanov, as reported by Sultan and Judd [80], where two artificial cavities were formed in a 20 μm thick layer of permalloy. Photoelectric signals[12] displayed when bubbles had formed at each site. Further analysis showed that the "time elapsed between the start of bubble growth at two

[12]Sultan and Judd [80] does not give any more detail about this measurement technique

neighboring nucleation sites" varied as random variables that followed a gamma distribution shown in Equation E.29, where $P(\tau)$ is the probability density function, λ is a scaling variable, ν is a shape parameter, and τ the time elapsed.

$$P(\tau) = \frac{\lambda\,(\lambda\tau)^{\nu-1}\exp\left(-\lambda\tau\right)}{\Gamma\left(\nu\right)} \tag{E.29}$$

It was found that ν was a function of distance between the two artificial nucleation cavities. For $\nu > 1$ (distances of less than three bubble diameters), the growth of one bubble inhibited the bubble growth at the neighboring cavity. The opposite is true for distances greater than three bubble diameters from the primary bubble. The reason behind this interaction was postulated to be a result of "acoustic action and hydrodynamic mixing".

In their study of bubble formation interactions, Sultan and Judd [80] used two copper probes to measure the electrical conductance of the volume surrounding the probe-tip. Figure E.20 shows the probe assembly used to detect and cross-correlate bubble behaviors. The assembly in Figure E.20 was placed above a heater assembly (copper block with cartridge heaters to provide a heat flux). After the probe assembly was lowered so that it touched the heater assembly, it was then raised 0.25 *mm* above the heater assembly. The entire probe was moved until Probe 1 indicated the presence of a bubble. Probe 2 was then moved radially from Probe 1 until it also indicated the presence of a bubble. Based on the cross-correlation of these signals, a theory was proposed whereby as a bubble expands, it pushes a volume of superheated liquid in front of the bubble. This can be seen in Figure E.21. Due to the increased amount of hot liquid, heat is transferred back to the solid along a ring, radially displaced from the nucleation site. Superimposing such a ring heat source with the temperature profile in the solid under a nucleating bubble, a radially varying temperature profile is generated that predicts the time lag for varyingly separated nucleation cavities.

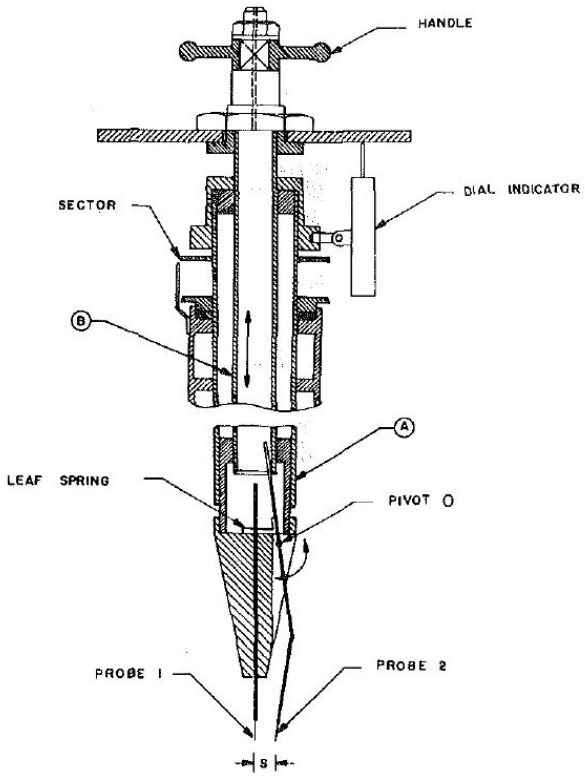

Figure E.20: Reproduction of Figure 2 from Sultan and Judd [80] showing the bubble detection probe assembly. The probe was lowered until it touched the heater surface, then raised 0.25 *mm* above the surface. Probe 1 and Probe 2 used electrical conductance (with a 11 kHz, 10 V signal) to detect when a bubble was present. Probe 2 could be moved radially away from Probe 1 until the electrical conductance indicated another bubble. Cross-correlation was then used to measure the interaction between nucleation sites.

In 1981, Messina and Park [81] investigated boiling performance from surfaces where pits were artificially etched with varying geometries. Among their observations were that vortices, acting like "small tornados" moved across the surface, activating nucleation sites; most did not remain active for long periods of time. Perhaps more interestingly, it was also found that "poorly formed [i.e., jagged–edged] or very shallow pits... generally caused a significant increase in heat transfer". The interesting nature of this observation is that "no previous investigations have considered artificial pits as shallow as those of the

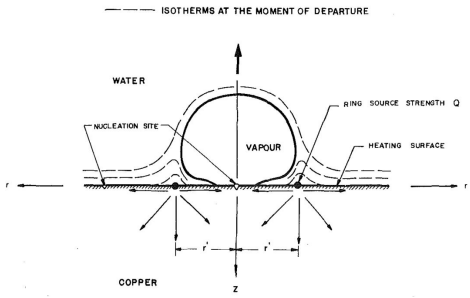

Figure E.21: Reproduction of Figure 7 from Sultan and Judd [80] showing the ring source of heat at bubble departure. It is this ring that induces thermal waves in the heater surface. When the peak of the thermal wave contacts a suitable nucleation cavity a subsequent bubble will grow.

present investigation to be efficient nucleation sites. It is nonetheless apparent... that the pits acted as sources of bubble nuclei." For reference, the ratio of depth–to–diameter for pits exhibiting such anomalous behavior was 0.030, with an average diameter of 0.0358 cm.

Some of the lowest superheats at the onset of heterogeneous nucleation were seen by Nakayama et al. [82] when studying porous surfaces. To study this behavior. Nakayama et al. [82] minimized the number of parameters by creating a surface with many tunnels capped by triangular pores. Figure E.22 shows such a surface where the tunnels are parameterized by height H_t, width W_t, and spacing λ_t; the pores by pitch λ_o and having an inscribed circle of diameter d_o. The parameters shown in Figure E.22 were varied in accordance with Table E.5, where A_r is the real surface area derived from cross-sectional photographs and A is the projected base area of the specimen. Surfaces used for experiment varied from the idealized case and can be seen in Figure E.23. The performance of these surfaces can be seen in Figure E.24; the wall superheat was measured by extrapolation of thermocouple readings below the heater surface. It can be seen that the porous surfaces nucleate at surface superheats $10\times$ lower than the plain surfaces. Where boiling curves overlap, namely Figures E.24(a) and E.24(c), it can be seen that the smaller pore

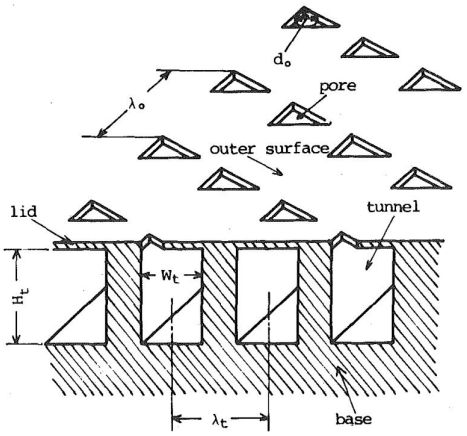

Figure E.22: Reproduction of Figure 1 from Nakayama et al. [82] showing an idealization geometry of a porous surface.

Table E.5: Dimensions for the idealized geometry shown in Figure E.22, where all lengths have units of millimeters.

Fluid	Surface No.	d_o	λ_o	λ_t	H_t	W_t	A_r/A
Water	W-1	0.20	0.60	0.60	0.62	0.25	2.93
	W-2	0.14	0.72	0.50	0.50	0.20	3.40
	W-3	0.08	0.72	0.50	0.60	0.15	3.70
R-11	R(11)-1	0.10	0.70	0.55	0.40	0.25	3.36
	R(11)-2	0.06	0.70	0.55	0.40	0.25	3.36
	R(11)-3	0.04	0.70	0.55	0.40	0.25	3.36
Liquid Nitrogen	LN-1	0.20	0.72	0.40	0.40	0.18	3.33
	LN-2	0.12	0.72	0.40	0.50	0.14	3.71
	LN-3	0.09	0.72	0.40	0.56	0.16	4.05
	LN-4	0.06	0.72	0.40	0.52	0.18	4.05
	LN-5	0.03	0.72	0.40	0.56	0.18	4.09

diameters perform better at lower superheats, while larger diameters perform better at higher superheats.

Three heat transfer mechanisms were proposed [82] to explain this quality of performance.

1. *Convective heat transfer from the outer surface enhanced by agitating force of bubble forma-*

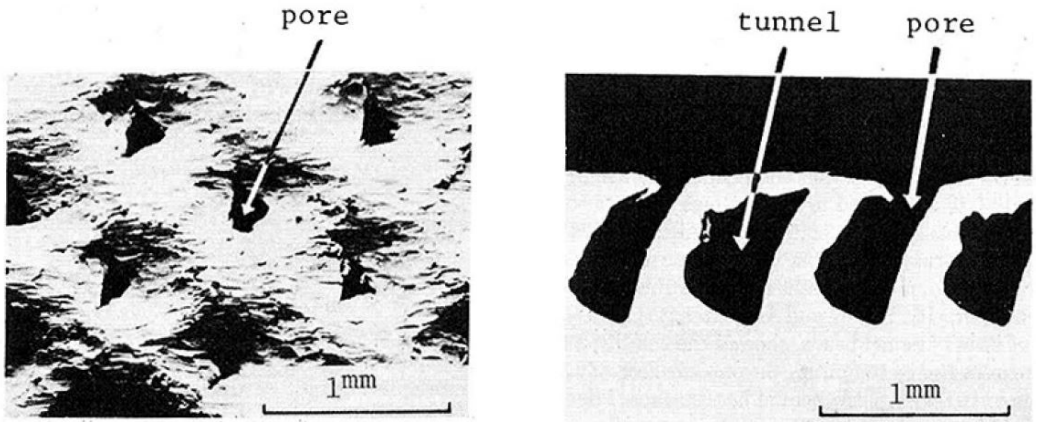

(a) Plan view (b) Cross-sectional view

Figure E.23: Reproduction of Figure 2(a) & 2(b) from Nakayama et al. [82] displaying the cross section and plan view of the idealized geometry shown of Figure E.22.

tion

2. *Vaporization of liquid near the outer surface into growing bubbles*
3. *Vaporization of liquid in the tunnels*

It was deduced that "vaporization of liquid in the tunnels" was the dominant heat transfer mechanism by reasoning that the other two mechanisms would be present for a plain heat transfer surface. In a corresponding paper, Nakayama et al. [83] hypothesized that bubbles formed via evaporation in the corners of the tunnel, thus increasing the pressure inside the tunnels. The model used to predict the formation of these bubbles follows from the combination of the Clausius–Clapeyron equation, the Young–Laplace equation, and the equation for an ideal gas. An eight step process can be used to predict the heat transfer from some of the experimental surfaces; the available results show good agreement with the proposed heat transfer theory.

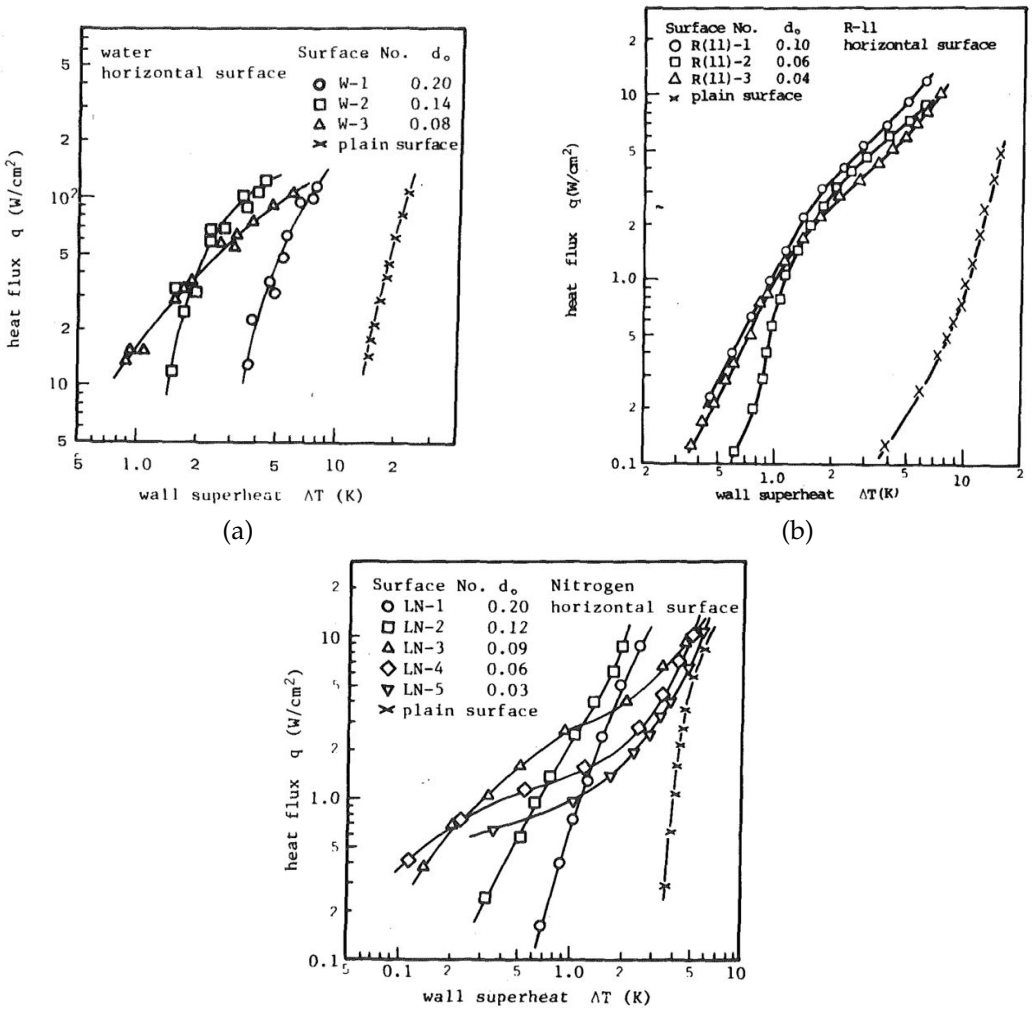

Figure E.24: Reproduction of Figure 3(a) - (c) from Nakayama et al. [82] exhibiting the performance characteristics of the porous surfaces for three different fluids: (a) water, (b) R-11, (c) liquid nitrogen

E.8 The 1990s

Majumdar and Bhushan [84] reports that the measured surface variation in slope and curvature are highly dependent on resolution of the measurement instrument, while the variation in height is often dependent on the length of the specimen that is capable of being scanned. For these reasons, fractal geometry would be better suited to describing

surface features of certain materials. Those materials formed by natural processes (i.e., fracture of a solid, deposition of materials, or solidification of a solid [84]) will produce fractal geometries. For those materials that are further processed by biased processes (e.g., directional lapping, rolling, milling, grinding), their geometry will be non-fractal only to the length scale affected by the machining. Examples of materials found to be fractal in geometry include stainless steel, glass, and sandstone.

The temperature variations in the surface as a result of bubble nucleation was looked at more closely by Kenning [22]. Using thermochromic liquid crystals, it was found that poorly wetting liquids created smaller bubbles more frequently, resulting in stable hot and cold regions in the surface. For well–wetting surfaces, bubbles would form less often, be of larger volume and producing more significant temperature variations in the heater. The temperature variations were found to be confined within the projected area of the bubble, as opposed to spreading to twice the bubble diameter as suggested by Mikic and Rohsenow [21]. Such temperature variations had become important partly due to the research by Zeng and Klausner [13], who showed that the nucleation site density was not solely predicted by the critical cavity radius and ΔT above saturation. Unfortunately, the confounding variables were unable to be determined.

By the 1990s, the volume of papers from research on "how does liquid boil" started getting overwhelmed by empirical research discussing the performance of various enhanced surfaces. This is partly because it was becoming accepted knowledge that boiling was a result of pre-existing vapor–this was the leading section about nucleate boiling in a review of boiling theory by Dhir [85]. In addition, computing capacity and manufacturing techniques were advancing at a quick pace, allowing for a wide array of empirical experimentation. It was at this time that a paper titled *What do we really know about nucleate boiling?* was authored by Kenning [31] to discuss the "mismatches between accepted models for bubble nucleation, growth, and heat transfer in nucleate boiling and the ex-

perimental evidence." One example being a study reported where a stainless steel surface was plated with copper from a thickness of 2 μm to 1 mm. As the plating grew thicker (the surface state remained constant) the heat transfer coefficient increased by approximately 50% and "was related by simple models to the penetration distance associated with the bubble frequency". The idea that bulk properties of the wall could have a significant affect on heat transfer and bubble nucleation had previously not been included in boiling correlations, but was noted to be of significant importance at a boiling conference held in 1994, as reported by Shoji [86].

E.9 The 2000s

At the beginning of the 21st century, research began trying to understand boiling from the chaos theory perspective, shown in Figure E.25. From this approach, the temporal and spatiotemporal dynamics are used, rather than the average behavior of the system.

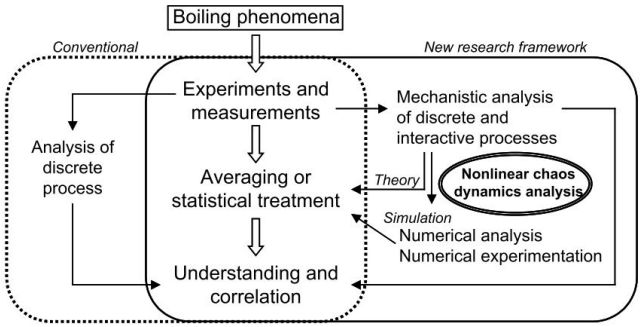

Figure E.25: Reproduction of Figure 3 from Shoji [86] depicting the conventional approach to studying boiling phenomena compared to the chaos theory approach whereby nonlinear dynamics are theorized to be of significant importance.

Shoji [86] reports that the intermittent boiling from a conical cavity required greater superheats than the relatively stable boiling from reentrant or cylindrical cavities. In addition, the depth of the cylindrical cavity (varying between 5 μm and 100 μm) has a

strong impact on the boiling behavior, while the diameter has little influence. It was also determined that the complexity of the temperature fluctuations beneath the cavity increase with increasing cavity depth. Several other examples of boiling phenomena exhibiting complex behavior were provided [86]; however, even using this new approach, "the physical mechanisms of boiling phenomena are still not yet fully understood". He goes on to say, "that actual boiling phenomena, even in simple systems, are complex, far beyond the capabilities of our detection techniques and analysis tools." One example is the characterization of surface features; it is known that the height of surface roughness is inadequate to fully represent a surface, however the "better and more plausible" fractal representation has yet to be validated.

Dinh et al. [87] used a 130 μm thick glass surface coated with a layer of titanium (140 nm thick with rms roughness of $\pm$ 4 nm) to be used as a heater via Joule heating. The titanium was known to quickly oxidize in the presence of water when heated. Even when heated in air, the moisture was enough to produce sub-micron scale "oxide islands" (typical size was 600 $\times$ 600 nm^2). As the heater became more aged, the nucleation site density increased, when compared to a fresh heater. It was found that the contact angle for HPLC water was 60° – 75° and was constant between the pure and oxidized surfaces; yet, the nucleation behavior was very different. On the clean surface, bubbles nucleated at a superheat of 10 – 15 K with a heat flux of 50 kW/m^2. In an experimental run where the heat flux was doubled from 280 kW/m^2 to 560 kW/m^2, it was seen that "new nucleation sites were found to appear quite randomly rather than concentrated with surface areas of comparatively higher temperatures". According to classical nucleation theory, an atomically smooth heater should approach the behavior of homogeneous boiling requiring superheats of 300 K to nucleate, rather than 15 K. Perhaps one could then ask, "if nanoscopic features of the surface can effect and control heterogeneous nucleation... what is the role, if any, of micron–scale, and macroscopic roughness?" [88]

Having personally shown several aspects that do not comport with the classical theories of nucleation, including the pre–existing vapor theory, Dinh et al. [87] describes three other potential ideas worth considering. First, reporting on the work of Tien and coworkers who performed experiments on atomically smooth heaters, it was found that as the heater became smaller, higher nucleation temperatures were required. They hypothesized that a vapor film formed immediately upon activating the heater. Second, looking back at the work of Frenkel from the 1940s, "Frenkel related the reduced nucleation barrier to large wetting angles in hydrophobic islands." Therefore, it is at these hydrophobic islands where nucleation starts. How these hydrophobic islands cause change in the local contact angle is still unknown. Third, there is the idea of nanobubbles and hydrophobic centers by Ishida and coworkers, and Tyrrell and Attard. This is the idea that hydrophobic surfaces are covered with nanoscopic close packed bubbles, which were investigated using an atomic force microscope. It was found to be possible to remove such bubbles, but they appeared to regrow, prompting such researchers to theorize that "the hydrophobic surface is acting as a nucleation site for air in effectively supersaturated water". It is uncertain how much of an influence the AFM probe might have had on the fluid surroundings being measured.

Investigations into the nucleation process during flow through micro-channels was done by Liu et al. [89]. Using an ultra-high-speed camera, they were able to visualize (looking downward at an upward facing heater) bubbles typically formed, "near but not exactly at the edges (corners) on the channel bottom surface". An image of this location can be seen in Figure E.26; from this perspective it is not possible to tell whether the bubble is touching the bottom surface of the heater. Qu and Mudawar [90] also reference the majority of bubbles initially forming on the bottom wall *near* a corner (though some formed on the side wall) but none formed at the hottest location, namely, in the corner

where the sidewall meets the base of the heater[13]; in addition, Qu and Mudawar [90] go on to say that bubbles initially formed at the outlet of the micro–channels, where the micro–channels ended and the outlet (oriented at 90 degrees from the micro–channels) began.

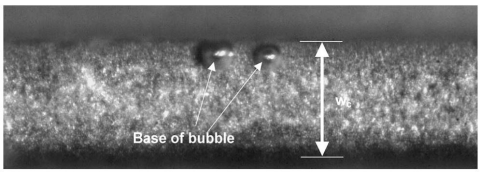

Figure E.26: Reproduction of Figure 3 from Liu et al. [89] showing the location of bubbles that were first to nucleate in a microchannel of dimensions 275 μm wide by 636 μm deep.

Mitrovic [52] describes how to make an ideal boiling surface based on the theoretical work of Hsu [73], which was expanded upon by Mikic and Rohsenow [21]. It was defined that an ideal boiling surface is one that follows Equation E.30, where the product of the heat flux, q, and the thermal resistance, R, is equal to the wall superheat, ΔT, which is equal to a constant.

$$q \cdot R = \Delta T = const \tag{E.30}$$

The physical behavior of such a surface is one where an increase in heat flux is always accompanied by a comparable decrease in thermal resistance, maintaining a constant wall superheat (i.e., the boiling curve is vertical, on the traditional heat flux versus wall superheat axes). Recall that the transient conduction model by Hsu [73] relied on the intersection of two curves (the bubble temperature and the liquid temperature) to predict from which cavity radii bubbles were able to grow. When the curve of bubble temperature first intersects the line of liquid temperature at the surface, there is only one point of contact.

[13]In micro–channel studies, it is typical for there to be multiple micro–channels in parallel in the same test section, cut into the same block of copper or silicon. While it was noted that the *majority* of bubbles initially formed on the bottom surface, incipience occurred with only one or two bubbles in any given micro–channel

This means that only one cavity radius is able to nucleate. Any further increase in liquid temperature would result in more cavities becoming active at the expense of more work to increase the liquid temperature. Mitrovic [52] therefore reasons that the ideal boiling surface is one where all of the cavities are at the same radius. Experimental verification of this theory was tested using R11 and a hexagonally packed array of uniform radius cavities as shown in Figure E.27. It can be seen that the vertical nature of the boiling curve is achieved starting at a heat flux of 20 kW/m^2 through 150 kW/m^2. The verticality of the boiling curve ceases at 60 kW/m^2, while the heat flux was decreasing.

An interesting study was done by Pesse et al. [91] in 2005 to investigate the vapor trapping ability of a micro–machined rectangular cavities. The parameters of the study can be seen in Table E.6. In this study, micro–machined channels were machined in silicon, which were then capped with glass, leaving one end open; a schematic of this setup can be seen in Figure E.28. With the cavities initially filled with air, deionized water was exposed to the channels at one end of the cavities. The liquid-vapor interface was monitored over time. Varying surface treatments of the silicon were used to modify the contact angle between the DI water and silicon. The static contact angle varied between zero and 90 degrees.

Table E.6: Experimental parameters from Pesse et al. [91] whereby micro–machined channels in silicon, which were capped with glass to simulate nucleation cavities, were tested for their vapor trapping ability.

Parameter	Units	Minimum	Maximum
Cavity Width	μm	5	50
Cavity Depth	μm	50	500
Contact Angle	deg	$\sim$0	$\sim$60

It was found that "all the microchannels with rectangular cross–sections tested in this study were completely flooded given sufficient time. The time taken to completely flood the microchannel varied from seconds, to minutes, to hours to even days" [91]. This is

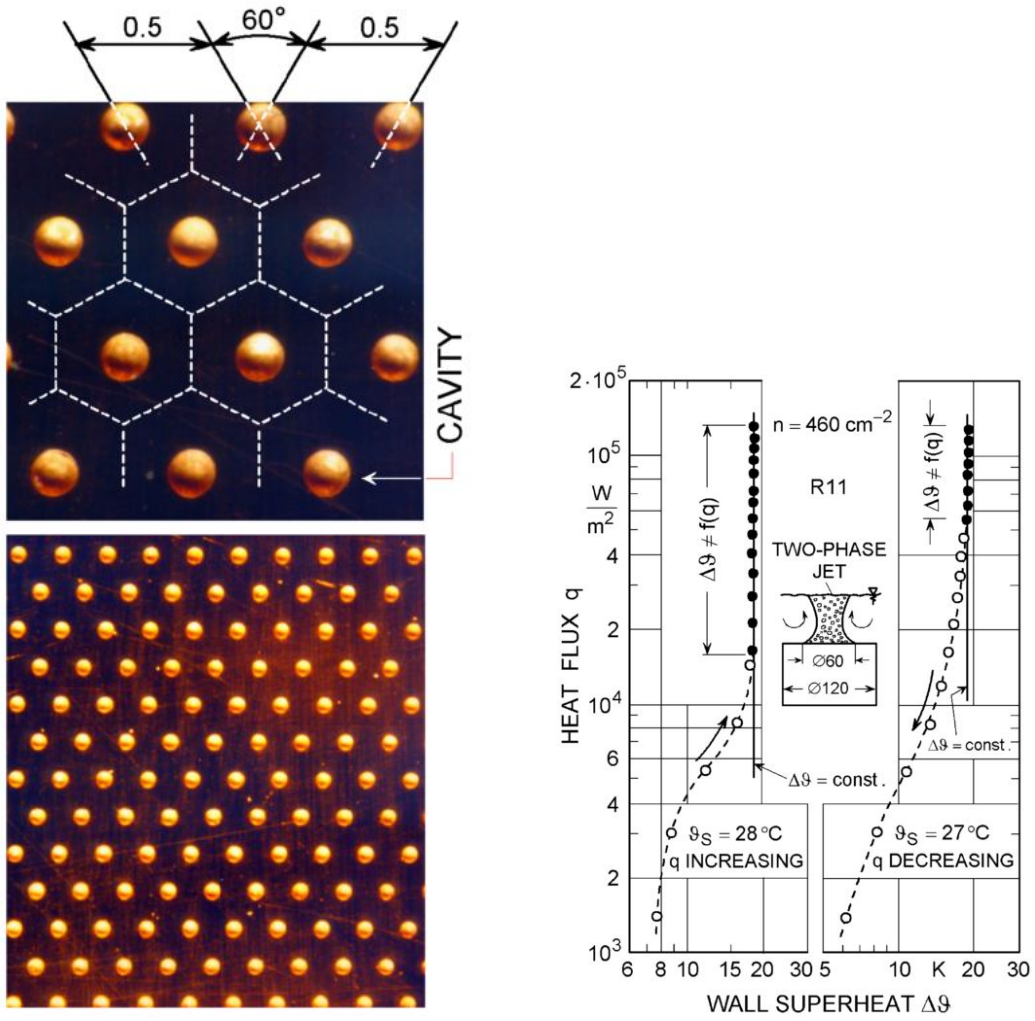

(a) (b)

Figure E.27: Reproduction of Figure 5 and Figure 6 from Mitrovic [52], (a) and (b) respectively, showing the (a) hexagonally etched arrays of uniformly dimensioned cavities and (b) the heat transfer performance. The diameter of these cavities was 180 μm, depth was 120 μm, and the density was 460 cavities/cm^2.

remarkable since the prevailing thought was that steep sloped cavities were preferred for trapping vapor. It was seen that increasing the cavity depth, cavity cross sectional area, and/or contact angle all act in such a way as to increase the time for a cavity to fill with liquid, but in all cases, every cavity filled with liquid given enough time. It should be repeated that all contact angles were less than 90 degrees. It is uncertain whether the

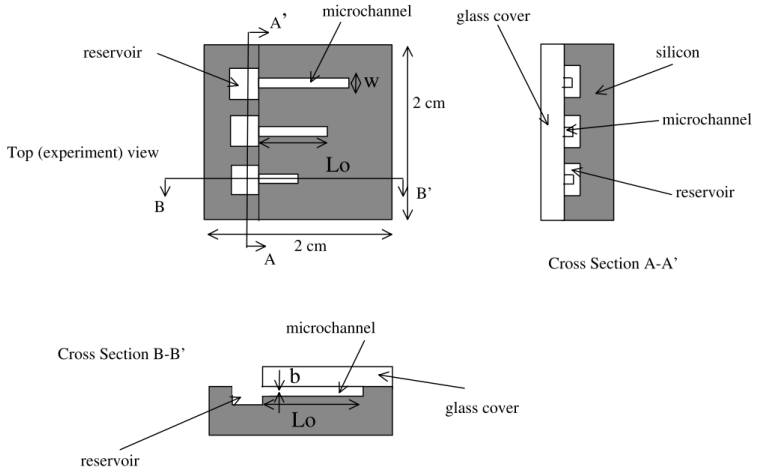

Figure E.28: Reproduction of Figure 2(b) from Pesse et al. [91] showing the closed-end silicon microchannels, capped with glass and left open on one end for a reservoir of DI water.

same results would be seen with nonwetting fluids. The implications of these results being that, if a wetting fluid is left in contact with a heater surface for sufficient amount of time, there will be no microscale features containing trapped gas or vapor.

Also in 2005, Carey and Wemhoff [92] detail another mismatch between classical boiling theory and experiments using highly wetting liquids and/or extremely smooth surfaces (surfaces that are expected to nucleate homogeneously): sudden heating of a surface can often cause bubbles to form via homogeneous nucleation. In work by Andrews and O'Horo, it was found that bubbles were not forming in contact with the surface, but away from the surface in a homogeneous manner; this is significant since the liquid is superheated the most where it contacts the surface, yet the bubble is not forming in that location. One proposed mechanism for this behavior is that the long-range attractive forces of the solid wall are affecting the state of the liquid molecules near the wall. Using a Redlich–Kwong fluid model, an equation of state was derived to predict the local fluid state near the wall; this model was based on the work of Gerweck et al. [93]. In the model by Carey and Wemhoff [92], the near–wall attractive forces between the fluid and

the solid were included using the Lennard–Jones potential function shown in Equation E.31, where $C_{\phi,fs}$ is the attractive force potential coefficient, and D_m is the mean effective diameter of a fluid molecule.

$$\phi_{fs}(r) = -\frac{C_{\phi,fs}}{r^6}\left[1 - \frac{D_m^6}{r^6}\right] \tag{E.31}$$

The characteristic length scale used for non–dimensionalization can be seen in Equation E.32, where k_B is Boltzmann's constant.

$$L = \left(\frac{k_B T_c}{P_c}\right)^{1/3} \tag{E.32}$$

It was found that "the pressure and spinodal temperature differ from the bulk values only in the region very close to the solid surface. The density similarly differs significantly from the bulk value only in the region very close to the solid surface." The term *very close to the solid surface* was found to be "within a few nanometers of the wall". The behavior of pressure and temperature near the wall for saturated liquid water at atmospheric pressure on a gold substrate can be seen in Figure E.29. As the reduced distance from the wall ($z_r = z/[k_b T_c/P_c]^{1/3}$) decreases, both the pressure and spinodal temperature increase, the former being more gradual than the latter.

As a result of the increasing spinodal temperature near the wall, the near–wall fluid must be superheated to a higher degree before nucleation. Figure E.30 shows an experimental verification of this theory. The text boxes to the right of the plot in Figure E.30 show the observations of Rembe, which closely mirror the predicted behavior of Carey and Wemhoff [92]. As the temperature profile of the liquid increases in time, it eventually intersects with the spinodal temperature curve. As soon as this happens, boiling commences. Because the temperature profile of the liquid is fairly flat in its distribution, this intersection occurs away from the wall, giving evidence to why homogeneous boiling

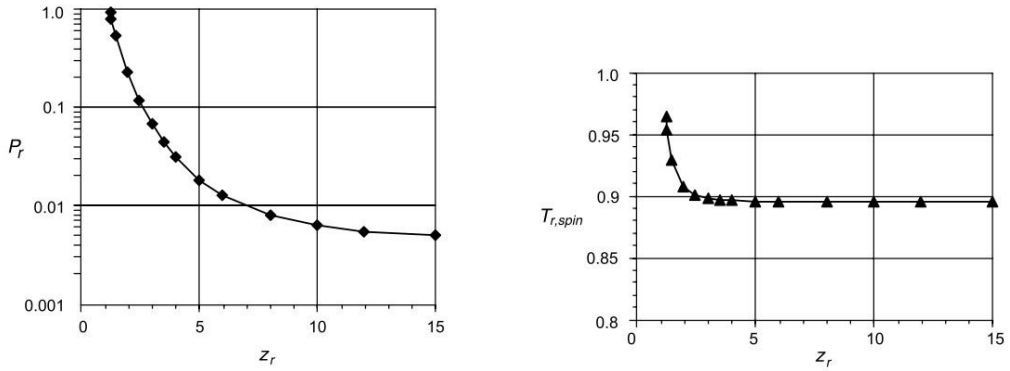

Figure E.29: Reproduction of Figure 4 from Carey and Wemhoff [92] depicting the near–wall effects of pressure and temperature due to intermolecular long–range forces. (a) The reduced pressure ($P_r = P/P_c$) increases more gradually as the wall near, in comparison to the (b) sharp increase in spinodal temperature

occurs in some cases.

It was also noted that it is possible for a fluid to traverse the spinodal curve without boiling, such as in cases of rapid transient heating. In these cases, "the temperature profile could continue to increase creating a region of superspinodal fluid."

In 2005, a paper was published by Qi and Klausner [94] on the comparison between gas nucleation and pool boiling from artificial cavities (a subsequent paper, Qi and Klausner [95], looked into the same behavior for natural surfaces). It was observed that "during the boiling mode, there is significant ebullition around the periphery of the silicon test surface" causing strong convective currents that suppressed boiling incipience. A schematic of the test section can be seen in Figure E.31. It was additionally noted that, as opposed to gas nucleation experiments where cylindrical cavities were always stable, for pool boiling, artificial cavities were not always seen to be stable and depended on the wall superheat.

In 2007, the latest thorough review of electrohydrodynamics (EHD) was authored by Laohalertdecha et al. [96] detailing the efforts to enhance heat transfer using EHD. Elec-

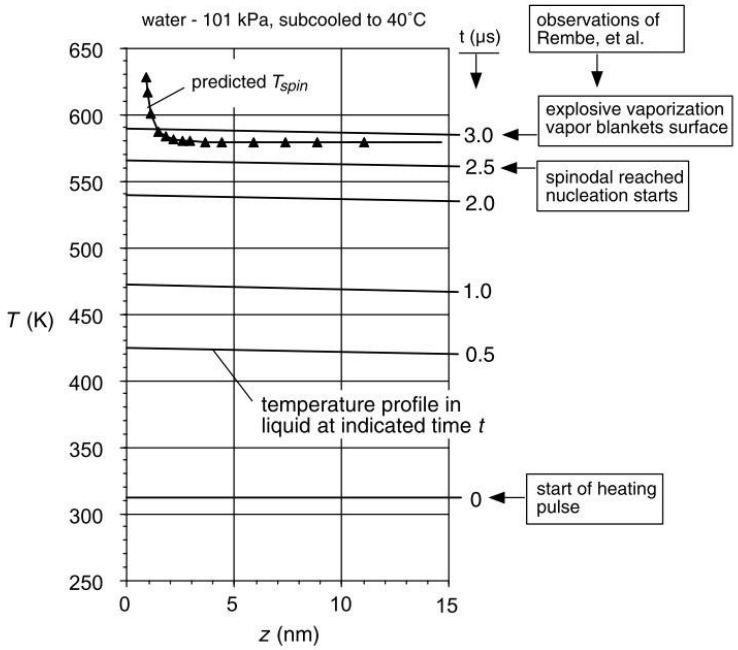

Figure E.30: Reproduction of Figure 10 from Carey and Wemhoff [92] showing an experimental verification of the derived Redlich–Kwong equation of state predicting an increase in spinodal temperature near the wall. During sudden heating, such as that in an ink–jet printer, the fluid temperature increases near the wall, faster than away from the wall. Once this temperature profile intersects the spinodal temperature curve, homogeneous boiling occurs. Note that this location is indeed away from the wall.

trohydrodynamics uses "either a DC or an AC high-voltage low-current electric field, applied in the dielectric field medium flowing between a charged and a receiving (grounded) electrode" [96]. The single-phase heat transfer implementation of EHD has been shown to provide a 20 fold increase in heat transfer rate while only incurring a 3 fold increase in pressure drop during fully developed laminar flow. Laohalertdecha et al. [96] provides the following mechanisms for enhancing two-phase heat transfer using EHD:

- *movement of vapor bubbles on the heated surface due to Maxwell stress*
- *spreading of the vapor bubble base over the heat transfer surface*
- *increasing the number of bubbles by breaking up large bubbles, thereby decreasing the bubble detachment diameter and creating more turbulence*

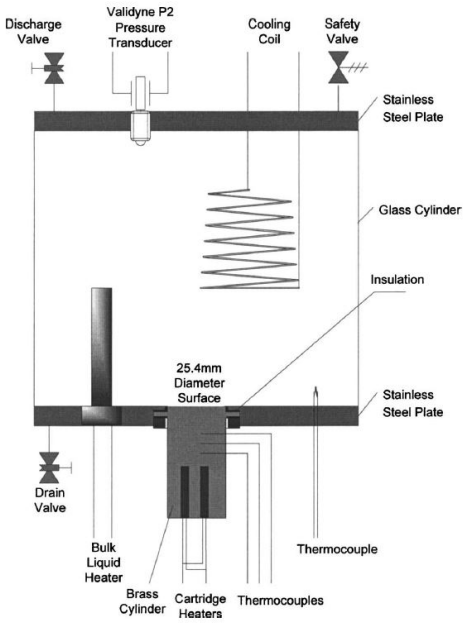

Figure E.31: Reproduction of Figure 4 from Qi and Klausner [94] showing a fairly typical pool boiling setup. Worth noting is that thermal energy is transferred from cartridge heaters through a volume of brass. Artificial cavities were created in silicon; the silicon was then cemented to the top surface of the brass using a high-conductivity cement. From the periphery of the silicon surface, significant boiling was occurring–enough that the convective currents spread across the top surface of the heater, suppressing boiling behavior. No more detailed image of the cemented surface was provided.

- *elimination of boiling hysteresis, thereby decreasing the degree of the superheat required to start nucleate boiling*
- *improving the transitional and minimum film boiling conditions by destabilizing the blanketing vapor film*
- *improving the wetting of the heating surface due to the decrease of surface tension*
- *introducing the waves and perturbations at the surface of a boiling liquid, due to the instability of the vapor/liquid interface*

One particular study mentioned was by Neve and Yan [97], who tested the boiling behavior of R114 on the exterior of common passively enhanced tubes (Thermoexcel-HE, Thermoexcel-C, Gewa-T, Low fin) and a smooth tube. Also applied between the

tube an exterior shell was an voltage that varied between 0 kV/mm and 4.5 kV/mm. It was found that the heat transfer coefficient for the smooth tube was doubled, and the enhanced tubes performed even better. Figure E.32 shows the typical performance of EHD enhancement for boiling on the exterior of a horizontally mounted tube. Note that for an applied potential of 3 kV/mm, the onset of nucleate boiling is decreased by 75%, from a superheat of 2.8 K to 0.7 K; for half that potential (1.5 kV/mm) the decrease in superheat is 50%.

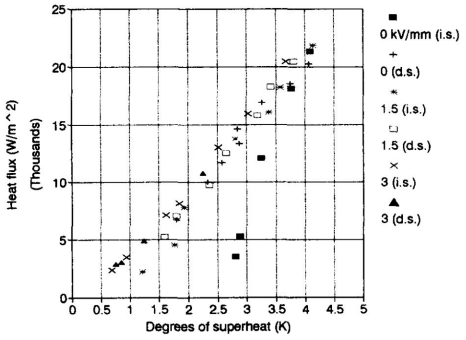

Figure E.32: Reproduction of Figure 6 from Neve and Yan [97] showing the performance of a Gewa-T enhanced tube with varying voltages applied between the enhanced tube and exterior shell (between which was the boiling fluid). It can be seen that the onset of nucleate boiling occurs at a superheat close to 0.7 K for 3 kV/mm applied voltage, and a superheat of 1.2 K for an applied voltage of 1.5 kV/mm. Note, "i.s." and "d.s." stand for increasing superheat and decreasing superheat, respectively.

E.10 The 2010s

In a series of papers, Bon and Klausner [23], Bon [24], and Bon et al. [25] found that heat transfer was slightly greatest for metal surfaces with decreased planar density, and silicon surfaces with increased planar density; the precise magnitude of such improvement is uncertain. The conditions necessary for the onset of nucleation were not studied in great enough detail to make any generalizations regarding the influence of crystallographic direction. One characteristic that was shown to greatly impact nucleation onset

was the whether or not hysteresis was present in the boiling data. As the heat flux is slowly increased, a surface transitions from convective heat transfer to nucleate boiling. If conditions are right, a metastable state can exist beyond the typical transition point where the liquid will maintain the performance of convectively boiling; upon some perturbation, the metastable state will instantly revert to the expected nucleation versus superheat curve. In their studies, the authors found that some surfaces showed significant hysteresis whereby the surfaces reached superheats 30°C above their expected values. A characteristic plot showing this behavior is shown in Figure E.33. Surfaces that exhibited no hysteresis were theorized to have been affected by "edge bubble nucleation which can be attributed to poor bonding between the encapsulating epoxy and the substrate" [23].

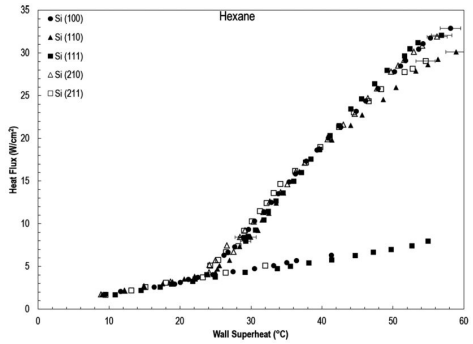

Figure E.33: Reproduction of Figure 4 from Bon et al. [25]. There are two regimes of importance in this plot: at low heat flux there exists data along a line of low slope; as the heat flux is increased, data populates along a line of increased slope. Data on the line of lower slope, but right of the intersection of the two lines, exist in a metastable state and will revert to the line of higher slope, at constant heat flux. In this plot surface Si (210) symbolized by open triangles shows no hysteresis; it was theorized that this was due to boiling along the edge of the heater. Other surfaces overshoot the intersection by as much as 30°C .

In 2011, Legay et al. [98] conducted a thorough literature review regarding the heat transfer influence of acoustic vibrations. The idea that sound vibrations could enhance heat transfer was first derived in the 1950s, but the significance the phenomenon was not fully grasped until the 2000s. There are two ranges of acoustic frequency of interest when

discussing acoustic heat transfer enhancement. Starting at the upper threshold of human hearing ($\sim$ 20 kHz) and having a range up to approximately 1 MHz exists what is known as power ultrasound. Such a wave has the ability to "modify the medium where it propagates" [98], for example by cavitating gas or vapor bubbles or by generating temperature gradients. Cleaning equipment and polymer welding operates in this regime. The other regime is frequencies higher than one megahertz, known as low power ultrasound. For these frequencies, the acoustic waves possess less power and do not affect the medium in which they propagate. According to Legay et al. [98], low power ultrasound is typically used in "medical diagnosis or nondestructive material control". Heat transfer study in the low power ultrasound regime is "very scarce".

"Acoustic streaming" is a phenomenon where there exists a momentum gradient in the fluid, caused by the acoustic waves, that preferentially heats up liquid near the emitter– further away from the acoustic source the temperature is less because the acoustic waves have dissipated in energy. A second phenomenon is known as "acoustic cavitation" where gas or vapor bubbles form in the presence of an oscillating pressure field. When a bubble exists for only one cycle, it is referred to as a transient cavity. Conversely, when a bubble continues to exist for many cycles, perhaps oscillating about a constant size, it is referred to as a stable cavity. When a gas bubble is formed and then collapses, the gas has to be dissolved into the liquid, which takes a finite amount of time, thus the collapse is not as dramatic as a vapor bubble. When vapor is cavitated and then collapses, all of the vapor recondenses into a liquid, leading to a violent collapse of the bubble; such bubbles have been known to collapse in 10^{-7} seconds with a local pressure above 190 MPa [98].

Acoustics can influence a boiling surface by creating small bubbles near a surface, disrupt their location thereby disturbing the boundary layer, and increasing convective heat transfer and delaying film boiling. Experimental verification that ultrasound can improve heat transfer has been mixed. Both Legay et al. [98] and Krishnan et al. [99] report

on authors that found improvements to be meager and not sufficient to be economically viable, while reporting on others that found no sufficient increase in heat transfer.

E.11 Other Boiling Phenomena

This last section is devoted to a topic that could easily be obscured by a chronological review and involves boiling at mating surfaces. When researchers design a boiling experiment, there is almost always a fluid enclosure that makes contact with the heater surface via an o-ring or some other sealing method. There exists one way around such a phenomenon whereby one suspends a thin-film heater in the middle of a fluid volume, however this has been used only sparingly as most experiments have used heater wire or cartridge heaters to provide a known heat flux through a long copper cylinder. It is common, when designing pool boiling experiments, that there be a minimum distance between the edge of the heater and the edge of the fluid enclosure; this is to avoid such edge-nucleation from interfering with the experiment of interest. Reading articles closely, a few of them give insight into this phenomenon, though often as a sidenote. Chyu and Mghamis [100] is the only known paper that tries to explain this and does so using the standard PEV theories of Hsu [73] and Bergles and Rohsenow [101].

E.11.1 Boiling at mating surfaces

Looking more closely at the 1931 paper by Jakob and Fritz [55], one will see that bubbles first formed on the edge of their circular heater plate. A schematic of the test assembly is shown in Figure E.34. It was noted that at low heat fluxes, bubbles would form on the periphery of the heater surface despite it always being colder than the center of the heating surface. An additional point of initial bubble generation was located where thermocouple θ_o' enters copper plate c. Initial testing had been done without the circular groove, c_1, and

it was found that bubbles formed at the solder joint between c and f regardless of how smoothly the solder was applied.

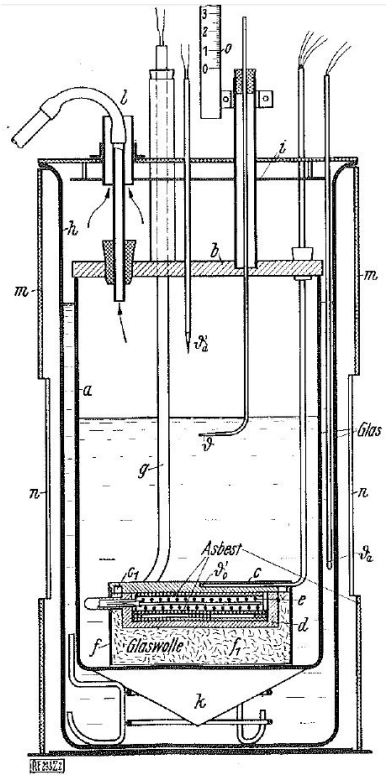

Legend

a : Glass vessel
b : Cover
c : Copper plate
c_1 : Circular groove
d : Brass body
e : Heating coil
f : Nickel plate coating
f_1 : Glass wool
g : Pipe for the power supply lines
h : Glass vessel
i : Cover
k : Nickel funnel
l : Steam exhaust
m : Aluminum foil glued asbestos case
n : Openings for review
o : Scale
θ : Thermocouple
θ_a : Thermocouple
θ'_d : Thermocouple
θ'_o : Thermocouple

Figure E.34: Reproduction of Figure 2 from Jakob and Fritz [55] showing their experimental setup. The copper plate, c, has a circular groove, c_1 machined about its periphery to limit radial heat conduction to the edge of the plate. Despite this effort the location of primary bubble generation was the edge of the heater surface.

For this to align with the PEV theory of boiling, the copper boiling surface would have had to have uniquely-sized vapor cavities dispersed along the periphery of the heater. One could say that the manufacture of the heater plate introduced uniquely-sized cavities along the periphery of the heater that are not present elsewhere on the surface. This may be true, however such macroscopic machining processes would likely introduce macroscopic cavities incapable of holding a vapor pocket.

Corty and Foust [64] reported an interesting phenomenon regarding the formation of bubbles. The process began by boiling a liquid on a surface, then lowering the heat flux

until the all nucleation sites disappeared. After 10-15 minutes, the surface superheat was increased to 40°C or 50°C without bubbles forming (superheats of 25°C were typical for vigorous boiling). Further superheating caused sudden "vigorous nucleate boiling" starting with a randomly located nucleation site, then spreading concentrically around this point. It is later suggested that "oscillations and pressure surges may create increased supersaturation in neighboring cavities, allowing nucleation to take place there" providing a means for propagation of nucleation sites.

In Gaertner and Westwater [17][14], it is mentioned that a fairly large heater surface is required "to prevent boiling at the gasket situated at the edge of the... disk". Figure E.35 shows the experimental setup from Gaertner and Westwater [17]. Another location of nucleation was at the junction between the two inch diameter boiling surface, and the nine inch diameter copper fin[15]. In fact, nucleation at this junction was present no matter how small the heat flux. This is another example of nucleation preferentially occurring where two materials meet (copper–copper & glass–rubber in Gaertner and Westwater [17]) , similar to the studies by Jakob and Fritz [55] (copper–nickel), Clark et al. [27] (aluminum–Duco cement), and Mcgillis et al. [102] (copper–epoxy).

[14]This study used electroplating during ebullition to later count the number of nucleation sites that had been active

[15]The nine inch diameter copper fin was annular in shape and no details were provided for how the fin was connected to the boiling surface.

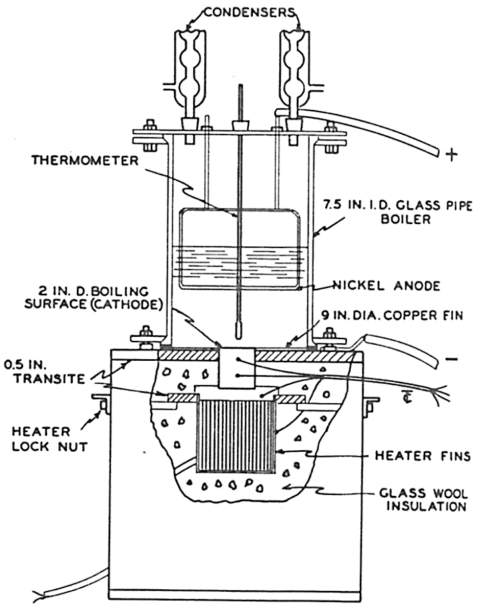

Figure E.35: Experimental setup from Gaertner and Westwater [17]. It was found that the surface heat flux to the two inch diameter boiling surface was not constant; the area formed from the central 1.5 inch diameter portion showed a flat heat flux profile. The annular fin (see "9 IN. DIA. COPPER FIN") conducted heat away, leaving the external perimeter of the heater cooler.